Title

DNA-Based Engineering Strategies to Dissect Complex Signaling Environments within the Adult Neural Stem Cell Niche

Permalink

https://escholarship.org/uc/item/1955c0q4

Author

Scheideler, Olivia Jean

Publication Date

2019

Peer reviewed|Thesis/dissertation

DNA-Based Engineering Strategies to Dissect Complex Signaling Environments within the Adult Neural Stem Cell Niche

By

Olivia Jean Scheideler

A dissertation submitted in partial satisfaction of the
requirements for the degree of
Joint Doctor of Philosophy
with the University of California, San Francisco
in
Bioengineering
in the
Graduate Division
of the
University of California, Berkeley

Committee in Charge:

Professor David Schaffer, Co-Chair
Professor Lydia Sohn, Co-Chair
Professor Zev Gartner, UCSF
Professor Liwei Lin

Spring 2019

Abstract

DNA-Based Engineering Strategies to Dissect Complex Signaling Environments within the Adult Neural Stem Cell Niche

by

Olivia Jean Scheideler

Doctor of Philosophy in Bioengineering

University of California, Berkeley

Professor David Schaffer, Co-Chair

Professor Lydia Sohn, Co-Chair

Stem cell niches are discrete anatomical microenvironments that present a rich collection of extrinsic factors to govern stem cell behavior. In particular, these niche signals – including soluble cues, extracellular matrix (ECM) associated signals, and cues from neighboring cell types – play critical roles in balancing stem cell self-renewal and differentiation. This balance ensures that tissues can maintain homeostatic tissue turnover while also adapting to external demands, such as injury, inflammation, and infection, to name but a few. Recapitulating the complex signaling dynamics of the stem cell niche *in vitro* has proven to be a challenging, yet necessary, task for dissecting and understanding the underlying mechanisms that instruct stem cell fate decisions. The resulting biological insight, in turn, accelerates stem cell applications to the clinic by informing the development of cell replacement therapies to regenerate injured or diseased cell types.

The emergence of innovative engineering strategies within the field has helped elucidate both the key signaling components and mechanisms of niche-directed stem cell behavior (Chapter 1). As these diverse networks continue to be explored, engineering strategies are evolving concurrently to facilitate the study of more complex niche signaling environments *in vitro*, where multiple inputs are coordinating with each other across time and space to guide resident stem cells. Mapping the dynamic relationships between niche signaling nodes requires developing methods and platforms that provide multiplexed, spatiotemporal control. In this dissertation, we address this technological challenge by drawing inspiration from one of biology's most robust, functional nano-building block materials, i.e. DNA, as a means to achieve such control. We demonstrated the resulting technology's utility for investigating stem cell biology by applying these DNA-based engineering strategies to study hippocampal adult neural stem cells (NSCs), a powerful cell type within the mammalian brain that gives rise to adult neurogenesis and holds promising therapeutic potential for treating neurodegenerative diseases, such as Alzheimer's and Parkinson's disease. Specifically, we capitalized on DNA's rapid yet highly specific Watson-Crick base-pairing, ease

of programmability, remarkable stability, and the added advantage that biology has evolved already a collection of enzymes for targeting and modifying DNA.

We first highlighted the unprecedented multiplexing capabilities imparted by DNA, assembling heterogeneous cell communities (up to four distinct cell types) with single-cell precision. We spotted onto a glass surface unique 20-base pair oligonucleotides that hybridize with complementary strands that are each tethered to the surface of different cell types. With this capability, we were able to position strategically single NSCs alongside different astrocyte neighbors that present opposing juxtacrine cues and, thus, tease apart the juxtacrine signaling hierarchy within the NSC niche (Chapter 2). While this approach offers a simple solution for multiplexing by simply modifying the sequence of surface-patterned oligo, we drastically improved the throughput and resolution of DNA surface patterns through the use of photolithography, converting our previously time-intensive and serial method to an inherently parallel one that captures the spatial dimension of niche-driven signaling due to the tight spatial control afforded by lithography (Chapter 3). Additionally, in this work, we expanded the patterning capabilities to include solid-phase cues in addition to cells, empowering additional investigations into the role that spatial presentation plays in how single NSCs resolve competing solid-phase ligands. Finally, we concluded by presenting parallel strategies for integrating temporal control into our DNA-based system by implementing various classes of nucleases and programming nuclease-targeting sequences into our patterned oligo strands (Chapter 4).

In summary, we have developed a repertoire of DNA-instructive engineering methods that we employed to elucidate the complex signaling dynamics of the NSC niche but can be widely applied to other stem cell microenvironments or translated to other tissue systems. Together, these tools assemble more mimetic *in vitro* models through multiplexed control over different cell types and solid-phase ligands as well as robust spatial and temporal control.

Acknowledgements

To my advisors, Dave and Lydia, I would like to thank you both first and foremost for allowing me to be a part of both of your labs and for agreeing to pursue this unprecedented, collaborative thesis. I greatly appreciate your patience as I carved out my project "niche" as well as your relentless support and encouragement throughout the highs and lows of my PhD. I feel so extremely blessed to call both of your labs my home – within each, I never fail to be inspired by the passion, drive, and creativity of fellow lab mates.

I would also like to thank Professor Zev Gartner and Professor Liwei Lin for being a part of my thesis and qualifying exam committee and for taking the time to meet with me countless times over the course of my PhD. To Professor Gartner, I am particularly grateful for your support and guidance through my qualifying exam.

I would like to extend a special thank you to Professor Seung-Wuk Lee for agreeing to chair my qualifying exam, for allowing me to participate in his class as a graduate student instructor and, more importantly, for his unwavering support from my very first year as a PhD student. Your enthusiasm for science and engineering is contagious, and I greatly enjoyed developing the phage-monitoring Android app during my rotation in your lab.

To the best program administrator on campus, Kristin Olson, thank you for all of your help throughout the years, answering my random questions, chatting with me in your office, running a 5K with me, etc. But, on top of all of that, thank you for making the Bioengineering department feel like home.

To my parents, my grandma, and my sister, you are *the* most important part of my life. Your relentless love, support, and encouragement have enabled me to tackle school head-on and to conquer the challenges of graduate school. Thank you for supporting me and helping keep things in perspective.

And to my husband, Will, some of my favorite memories of graduate school include our coffee breaks and walks around campus, not to mention our competition during intramural soccer for the "Most Valuable Scheideler" award. You ground me, motivate me, support me, and I am so extremely grateful that, in our journey through life together, graduate school marks another shared chapter.

Lastly, I would like to acknowledge my funding sources, the National Science Foundation Graduate Research Fellowship (NSF GRFP), the Siebel Scholars Foundation, and the PEO Foundation, which enabled me to focus my efforts on pushing my research projects forward.

Table of Contents

Chapter 1: Emerging Engineering Strategies for Studying the Stem Cell Niche

This chapter is in part a postprint of a paper submitted to and accepted for publication as

Scheideler, O.J., Sohn, L.L., Schaffer, D.V. Emerging engineering strategies to study the stem cell niche. In: Turksen K. (eds) Biology in Stem Cell Niche. Stem Cell Biology and Regenerative Medicine. Springer, Cham.

1.1 Stem Cells and Regenerative Medicine

Stem cells have drawn great attention from the biomedical community as diverse players that assume central roles in development, tissue homeostasis, and tissue regeneration (*1*). Defined by their ability to self-renew and differentiate into mature cell lineages, stem cells can be generally categorized into three main subtypes: embryonic stem cells (ESCs), induced pluripotent stem cells (iPSCs), and adult stem cells (ASCs). ESCs and iPSCs share similarities in their morphology, proliferation, and ability to differentiate into cell types from any of the three germ layers: endoderm, ectoderm, and mesoderm. However, ESCs and iPSCs differ in their point of origin. While ESCs are derived from the inner cell mass of mammalian blastocysts, iPSCs are generated via reprogramming of somatic cells through the retroviral introduction of key factors, such as the four Yamanaka factors Oct3/4, Sox2, c-Myc, Klf4 (*2*). ASCs, in contrast, generate a more limited or restricted number of cell lineages that help mediate cell turnover within adult tissues. ASCs populations, which by convention and contrary to their name can be derived from adult or fetal tissue, include, but are not limited to, hematopoietic stem cells (HSCs), neural stem cells (NSCs), satellite muscle stem cells, epidermal stem cells, and intestinal stem cells (ISCs).

Collectively, stem cells offer exciting therapeutic potential for replacing diseased and injured cell populations through regenerative medicine and tissue engineering strategies. These approaches include transplantation of stem cells and their differentiated progeny as well as stimulation of endogenous stem cell populations (i.e. ASCs). The clinical success of both these approaches hinges on the ability to control stem cell behavior, in particular through precise regulation of stem cell expansion and differentiation. For *ex vivo* stem cell therapies, a major challenge is producing cells of high purity, yield, and quality. In the case of endogenous cell stimulation, the ability to target specific stem cell niches to support endogenous repair represents another major hurdle (*3, 4*). To date, considerable progress has been made in developing therapies based on stem and progenitor cells in the hematopoietic system. The use of HSCs has found encouraging success in treating conditions such as autoimmune diseases and blood defects (*5, 6*). The primary challenge in stem cell research is to extend this clinical success to other stem cell systems. Therefore, it has become clear that, before stem cells can become a viable therapeutic agent, the complex mechanisms regulating their behavior must be deconstructed.

1.2 Stem Cells and Their Niches

Efforts within the past few decades have demonstrated that stem cells localize within physiological domains referred to as "niches" – a concept that Schofield first formulated in 1978 to describe the bone-marrow microenvironment of HSCs (*7-9*). Since this time, a multitude of studies have confirmed the existence of a variety of microenvironments that house stem cells. For instance, NSCs have been found within the subventricular zone (SVZ) of the lateral ventricles and the subgranular zone of the hippocampal dentate gyrus of the adult mammalian brain (*10-12*). Epidermal stem cells have been shown to reside in a distinct anatomical location called the hair follicle bulge (*13-16*), muscle stem cells localize between basal lamina and the periphery of myofiber plasma membrane (*17-19*), and ISCs have been suggested to reside at the +4 position of the crypt base as well as the crypt base itself (*20-22*). In addition to being described by their anatomical locations, stem cell niches are also defined by their functional properties (*7, 23*). In response to physiological or pathological circumstances or demands, niches play an integral role in coordinating stem cell behavior to maintain homeostasis and stimulate repair (*23*).

The niche's regulatory role is the result of a dynamic interplay of signaling components that include soluble cues, surrounding extracellular matrix (ECM)-associated cues, and neighboring niche constituent cells (*4*). These signals manifest in various ways, including biophysical signals in the form of the stiffness and topography of imposing ECM in addition to biochemical cues, such as secreted paracrine factors as well as ECM-sequestered growth factors and cytokines (*24-27*). Understanding the mechanisms by which these signals modulate stem cell behavior is an essential step in clinically translating stem cell therapies. Specifically, exploring the length and time scales over which individual signals and combinations of signals modulate stem cell behavior has increasingly become a research thrust within the field. *In vitro* models that mimic aspects of *in vivo* niche microenvironments have facilitated this investigation and have been made possible through an extensive breadth of novel engineering strategies. In this initial chapter, we examine the various strategies employed for recapitulating stem cell-ECM and stem cell-niche cell interactions, with a particular focus on more recent engineering strategies that have progressed in parallel with the field's growing knowledge of stem cell behavior.

1.3 Stem Cell-ECM Interactions

The ECM is an intrinsically complex, heterogeneous physical structure that plays key roles within stem cell niches. In addition to supporting cellular adhesion, the ECM presents biophysical cues related to the material's physical properties as well as biochemical cues in the form of insoluble ligands. Stem cells actively and dynamically probe this matrix by applying traction forces to "sense" these instructive inputs and subsequently respond by altering their cytoskeleton, adjusting focal adhesions, and remodeling the ECM via degradation and deformation (*28-30*). This bidirectional communication is a major topic of interest, as studies have collectively demonstrated that the niche's ECM directly and indirectly regulates key stem cell behaviors, such as adhesion, proliferation, differentiation, and migration (*28, 31-33*).

1.3.1 Stem Cell Adhesion to Niche ECM via Integrins

The ECM is an intricate three-dimensional (3D) architecture comprised of diverse biomolecules, including proteins, polysaccharides, proteoglycans, morphogens, cytokines, and growth factors (*34*). The composition of this ECM is unique to a given stem cell niche but, despite their considerable structural diversity, similarities among niches have been noted. One common feature is stem cell localization adjacent to basal lamina or basement membranes, which have specialized ECM structures rich in laminins, collagens, proteoglycans, and other important adhesive proteins (tenascin, fibronectin, nidogen, etc.) (*35, 36*). For example, NSCs within the SVZ contact finger-like extensions of basal lamina (termed “fractones”), which extend from surrounding vasculature (*37, 38*). Similarly, ISCs inhabit the crypts of intestinal villi, where they share an interaction with the gut epithelial basement membrane (*35*), a physical fusion of basal and reticular laminas. Likewise, muscle satellite stem cells reside under the basal lamina of myofibers, and interfollicular epidermal stem cells lie adjunct to the encasing basal lamina in the hair follicle bulge (*15, 18*).

Integrins are a well-characterized family of heterodimeric cell surface receptors that mediate stem cell adhesion to this common interface (*28, 39*). These receptors consist of two transmembrane chains (18 α- and 8 β-subunits), which combine to form more than 24 different integrins (excluding splice variants) (*40*). Examples of integrins in stem cell niches include α5β1 integrin, a laminin receptor expressed by some NSCs, and α8β1, which mediates hair follicle stem cell binding to the ECM protein nephronectin. Many integrins also possess the capability to recognize the Arg-Gly-Asp (RGD) tripeptide motif within their ligands. Stem cells assemble these nanoscale integrin complexes into macroscale focal adhesions (*41*). These adhesions are proposed to play a large role in translating extracellular ECM protein stimuli into intracellular biochemical signals (a process referred to as mechanotransduction), ultimately leading to global changes in cell morphology as well as regulating gene expression to modulate cellular behavior (*42*). This complex cascade of signaling events, initiated from the binding of ECM ligands to focal adhesions, exerts tension onto the cell’s cytoskeleton and induces stress on the nucleus, as the cytoskeleton is connected to the nuclear envelope (*43*). As a result, nuclear remodeling occurs, which asserts force back onto the cytoskeleton and alters focal adhesions. The subsequent “inside-out” signaling allows cells to manipulate the clustering of integrins to their membrane, increasing or decreasing binding of their integrin receptors (*44*). Therefore, focal adhesions represent a key mediator of dynamic spatial and temporal interactions between the environment and intracellular signaling (*42*). Disruption to this integrin-based interaction can result in stem cells exiting their niche via differentiation or apoptosis (*45*). Some integrin signaling pathways under investigation are the Ras/MAPK, RhoA/ROCK, and P13K/Akt pathways. YAP and TAZ have also recently been identified as key downstream transcription factors sensitive to mechanical cues (*28, 43, 46*).

Integrin signaling has also been shown to interface with growth factor-initiated pathways (*39*). In neural progenitor cells, for example, the addition of fibroblast growth factor upregulated the expression of β1 integrins, which is believed to enhance cell responsiveness to its ECM (*39, 44*). Another example of growth factor-integrin interplay was suggested for mesenchymal stem cells (MSCs) – multipotent adult stromal cells of a mesodermal lineage. The activation of MSC α5β1 integrins on stretched fibronectin fibers promoted osteogenesis; however, inhibition of the epidermal growth factor receptor on the same stretched fibers decreased osteogenesis from 41% to 27% (*35*). As an example in ESCs, it is hypothesized that platelet-derived growth factor receptor coordinates with collagen IV-integrin α1/β1/αv to induce differentiation toward smooth muscle cells (*40*).

1.3.2 Cadherins, Another Class of Adhesion Receptors

While adhesion via integrins is a recurring theme in a majority of the stem cell niches, HSCs and likely other stem cells rely on another adhesion protein to interface indirectly with their physical microenvironment. Specifically, HSCs interact with an intermediate cell type, osteoblasts, to anchor themselves to the inner surface of the trabecular bone (*47*). This physical cell coupling relies on the recruitment of cadherins and catenins, proteins that assemble to form intercellular adheren-junction complexes (*38, 48*). Cadherins have been demonstrated to regulate stem cell behavior in a manner similar to that of integrins. For instance, in the testis stem cell niche of *Drosophila melanogaster*, N-cadherin assists in orienting stem cells for asymmetric division within the niche (*49*). In the *Drosophila* ovary niche, loss of N-cadherin results in the retreat of stem cells from the niche (*49*). In mammalian systems, N-cadherin-mediated anchoring of NSCs to ependymal cells lining the ventricle has been implicated in regulating the quiescence of NSCs within the SVZ niche. Upon the degradation of this cell-cell adhesion, NSCs translocate from the ependymal cells towards the blood vessels, enhancing their interaction with ECM and initiating their activation (*49*).

1.3.3 Molecular Sequestering of Growth Factors and Cytokines by ECM

In addition to mediating stem cell adhesion, the ECM acts as a reservoir for growth factors and cytokines (*50*). Immobilization is achieved through non-covalent binding to ECM proteins, proteoglycans, and glycoasminoglycans (*51, 52*). Specifically, ECM proteins possess intrinsic binding domains that facilitate the spatial localization of these regulatory factors (*52, 53*). Collagen II binds through its von Willebrand domain to transforming growth factor β 1 and bone morphogenetic protein 2 (*54*). Similarly, fibronectin harbors a heparin II domain that binds molecules such as vascular endothelial growth factor and platelet-derived growth factor (*54*). These factors can either be released to establish local morphogen gradients or instigate signaling from a bound state (*50*). Liberation of these molecules occurs by either proteolytic degradation of the ECM or cell-generated forces.

While some growth factors directly bind ECM proteins, many others harbor domains that bind to heparan sulfate, a glycosaminoglycan consisting of a linear polysaccharide that attaches to core proteins to form heparan sulfate proteoglycans (HSPGs) (*55, 56*). In addition to organizing the presentation of these ligands, HSPGs play a functional role in modulating signaling. They assist in bridging growth factors with their receptors and can serve as co-receptors, influencing growth factor activity by biasing activation thresholds and binding specificities (*53, 55, 57*). HSPGs also assist in extending signaling duration through the inhibition of receptor-mediated endocytosis (*54, 58, 59*).

1.4 Seminal Engineering Strategies - Establishing a Foundation

An increased understanding of the regulatory role that native ECM plays within stem cell niches has been achieved through the synergistic efforts of biologists, materials scientists, engineers, chemists, and physicists (*34*). Early investigations clearly established the importance and the associated mechanisms by which ECM composition, matrix rigidity, topography (both nano- and micro-), porosity, ligand presentation, and control of cell geometry regulate stem cell behavior (*51, 60*). These findings were realized with the aid of engineering techniques that re-created static representations of stem cell-ECM interfaces. Materials with pre-defined topographies, patterned peptide sequences, and fixed mechanical properties represent only a few of these early approaches, and these initial studies were critical advances that stimulated interest in dissecting the surrounding physical microenvironment within the stem cell niche. The following sections highlight a variety of early, landmark engineering strategies pursued for studying the role that ECM elements play within the niche.

1.4.1 Micro/Nanofabrication Techniques for Generating Pre-Printed Topographies

Topography is an inherent characteristic of ECM that has been investigated as an instructive cue that guides the formation of focal adhesions and cytoskeletal tension (*41*). The complex, heterogeneous composition of the niche's ECM contributes to an intricate blend of structural features, including pores, protrusions, ridges, and grooves (*61*). Deconstructing the biophysical responses to these physiological topographies has required a reductionist approach due to the complexity of the dynamic bi-directional interactions between stem cells and ECM. Thus, many efforts have focused on recapitulating single-feature architectures *in vitro* and observing how these static systems affect stem cell behavior.

Studying the effects of static topographies requires a platform that must be precise and reproducible on the micro- and nanoscale. A wide spectrum of fabrication methods – including photolithography, soft lithography, dip-pen nanolithography, and electron-beam lithography – have been used in these platforms (*61, 62*). Posts and grooves are two examples of structures that have been heavily investigated. Studies have not only manipulated the overall scale of these features (macro vs. micro vs. nano) but also varied the physical aspect ratios of these structures. Ahn and colleagues, for instance, employed ultraviolet (UV)-assisted capillary-force lithography to generate polyurethane nanoposts (Figure 1.1a) (*63*). They then investigated how varying post-to-post distances (i.e. post densities) at the micron scale influenced human mesenchymal stem (hMSC) cell fate, and subsequently discovered that certain topographies biased the process of hMSC differentiation. In particular, a greater nanopost separation (i.e. a post-to-post distance of 5.6 μm) favored osteogenic differentiation, whereas adipogenesis was maximized at a smaller post-to-post separation (2.4 μm) (*63*). Motemani *et al.* also investigated the effect of nano-columnar surfaces, created using glancing angle deposition, on hMSCs (*64*). Nanoscale columns were fabricated in vertical, slanted, and chevron geometries from titanium dioxide (TiO_2), a common implant material, by sputtering titanium at an oblique angle and using substrate rotation to bias the columnar growth direction before annealing to oxidize the films. Following plating of MSCs on these surfaces, unique nano-sized pseudopodia extensions were observed and suggested to cause cytoskeletal tension and trigger mechanotransduction, though additional studies would be required to confirm these assumptions (*64*). While the focus was not on hMSC differentiation but rather on cell morphology and cytocompatibility, this work does yield a promising technique for future studies in exploring the effects of nanoscale topographies on stem cell behavior (*64*). In contrast, Fu *et al.* engineered elastomeric micropost arrays of varying post heights (0.97 μm, 6.1 μm, and 12.9 μm) for generating different mechanical substrate rigidities (1,556 nN/μm, 18.16 nM/μm, 1.90 nN/μm) (Figure 1.1b) (*65*). Single hMSCs were adhered to islands of different post heights and cell traction forces were tracked over a 7-day period. A strong correlation between osteogenic and adipogenic lineage commitment and traction forces suggested that MSC contractile state could be used as a noninvasive predictor of hMSC differentiation (*65*).

In addition to posts, considerable work has explored the effects of grooves on stem cell behavior, and in particular the effects of groove depth, groove pitch, and terrace widths. For example, Béduer and colleagues used conventional soft-lithography techniques to assess how adult NSCs responded to imposed micro-patterned polydimethylsiloxane (PDMS) surfaces with varying terrace and groove widths (5 μm-5 μm, 10 μm-10 μm, 20 μm-20 μm, 10 μm-60 μm, respectively) (Figure 1.1c) (*66*). They found that smaller groove separations lowered differentiation rates and hindered the number of neurite extensions from differentiated neurons, despite promoting a high degree of cellular alignment (*66*). Recknor and colleagues also examined the effects of a micro-patterned polystyrene groove topography as a guidance cue for neural progenitor cells (NPCs) (*67*). Rather than modulating the physical dimensions of the grooves, however, Recknor *et al.* studied the synergistic effects of a 16 x 13 x 4 μm (width/mesa width/groove) groove depth pattern in conjunction with a chemical and a biological cue (*67*). Specifically, NPCs were co-cultured on a confluent monolayer of cortical astroctyes, which resided on top of a laminin-coated, micro-patterned polystyrene substrate. The resulting microenvironment was found to enhance NPC neuronal differentiation selectively (*67*).

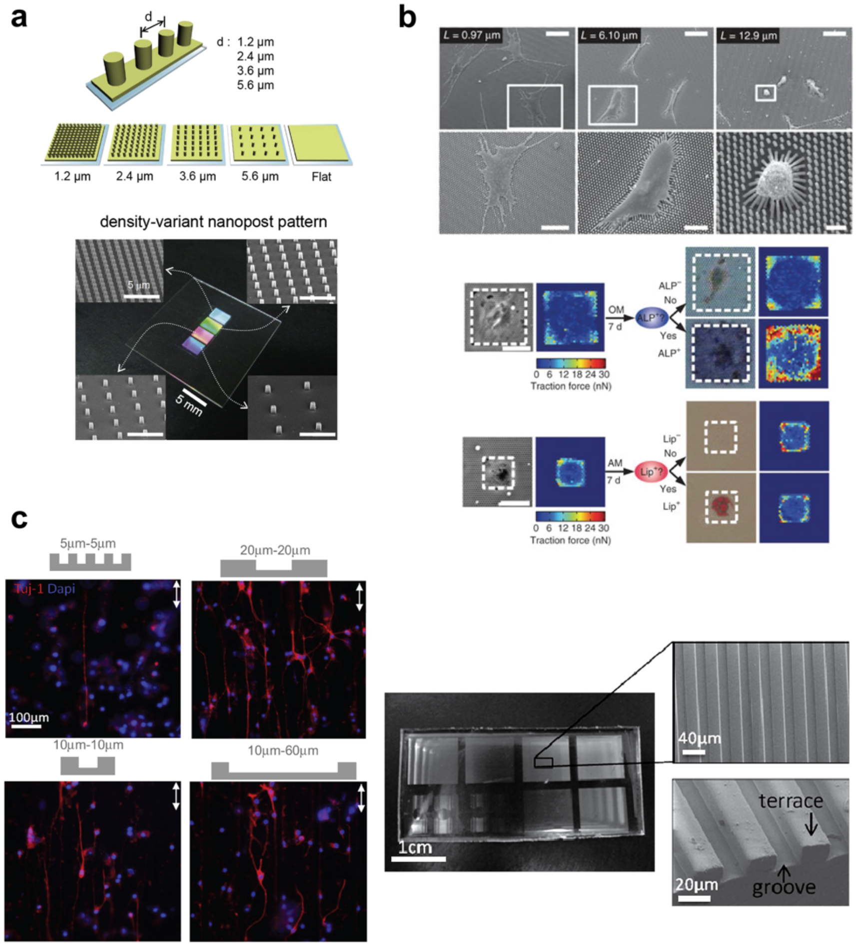

Figure 1.1 Engineering strategies for generating static, pre-printed topographies. Panel **a**: polyurethane nanoposts of varying densities fabricated using UV-assisted capillary force lithography (*63*). Panel **b**: SEM images of hMSCs cultured on islands of different PDMS micropost height arrays (top); brightfield micrographs and traction force maps of hMSCs exposed to osteogenic or adipogenic medium (bottom) (*65*). Panel **c**: micropatterned PDMS grooves applied towards influencing NSC differentiation; cells stained for neuronal marker Tuj-1 (red) and nuclei (blue) (*66*).

Many other creative approaches, including techniques for constructing 3D structures, have also been pursued in engineering models of ECM topology. To start, Christopherson *et al.* revealed that modulations to nanofiber diameters were sufficient for biasing NSC proliferation and differentiation (Figure 1.2a) (*68*). Specifically, they fabricated laminin-coated polyethersulfone fiber mesh matrices exhibiting a range of average fiber diameters (283±45 nm, 749±153 nm, and 1452±312 nm). An increase in fiber diameter in the presence of fibroblast growth factor-2, a mitogen that promotes stem cell maintenance, induced a decrease in NSC proliferation rate and migratory activity (*68*). When cultured in differentiation conditions, on the other hand, NSCs tended toward a glial lineage on the 283-nm fibers as cells displayed a better ability to spread randomly along the nanofiber matrix. For the larger fiber diameters, NSCs were restricted to extending along single fibers, promoting a neuronal lineage (*68*). Though correlations have been observed between topographies and cell behavior, the mechanisms of shape regulation remain elusive. Another such innovative study involves preparing porous honeycomb polystyrene scaffolds by casting the polymer under humid conditions to form hexagonally arranged pores (*69*). Kawano and colleagues used this system to dissect the influence cellular- and subcellular-scaled pore sizes have on hMSC behavior (*69*). For pore sizes smaller than the cell (1.6 μm), osteospecific differentiation was prominent. In contrast, myospecific differentiation was associated with larger pore sizes (3.8 μm) (*69*). Along the same lines, hMSCs were cultured on TiO_2 nanotubes of different pore diameters - 30, 50, 70, and 100 nm (*70*). The self-assembled, highly-ordered nanotube arrays were created by anodization, where different diameters were a result of manipulating anodizing potentials (5-20 V) (Figure 1.2b). With this platform, Oh *et al.* demonstrated that hMSC elongation increased with nanotube diameter and correlated with differentiation into an osteogenic lineage (*70*). Moreover, a saturation effect of hMSC differentiation was observed as diameters approach 100 nm. Finally, Das *et al.* drew inspiration from collagen by engineering helical, silica nanoribbons covalently modified with RGD to mimic collagen fibril structure (Figure 1.2c) (*71*). They probed the role that different periodicities (63.5±5 nm vs. 110±15 nm) had in directing the lineage commitment of hMSCs and found that helical nanoribbons with smaller periodicity induced a strong commitment to the osteoblast lineage (*71*).

To increase the throughput of topographical investigations, novel on-chip systems that encompass various dimensions and architectural complexities within a single platform have been developed. Yim *et al.* fabricated one such system, which they termed the Multi-ARChitecture (MARC) chip (Figure 1.3) (*72*). By utilizing nanoimprinting lithography, they generated not only a variety of isotropic (1 μm pillars, 2 μm holes, 1.8 μm concave and convex lenses) and anisotropic (2 μm and 250 nm gratings) features but also hierarchical, composite structures of 2 μm lines and 250 nm dimples on top of 2 μm gratings (*72*). Neuronal differentiation of human embryonic stem cells (hESCs) was studied with this system. When hESCs grew on laminin-coated PDMS replicas of these MARC chips, grating topographies favored neuronal differentiation, whereas isotopic patterns favored the glial lineage (*72*).

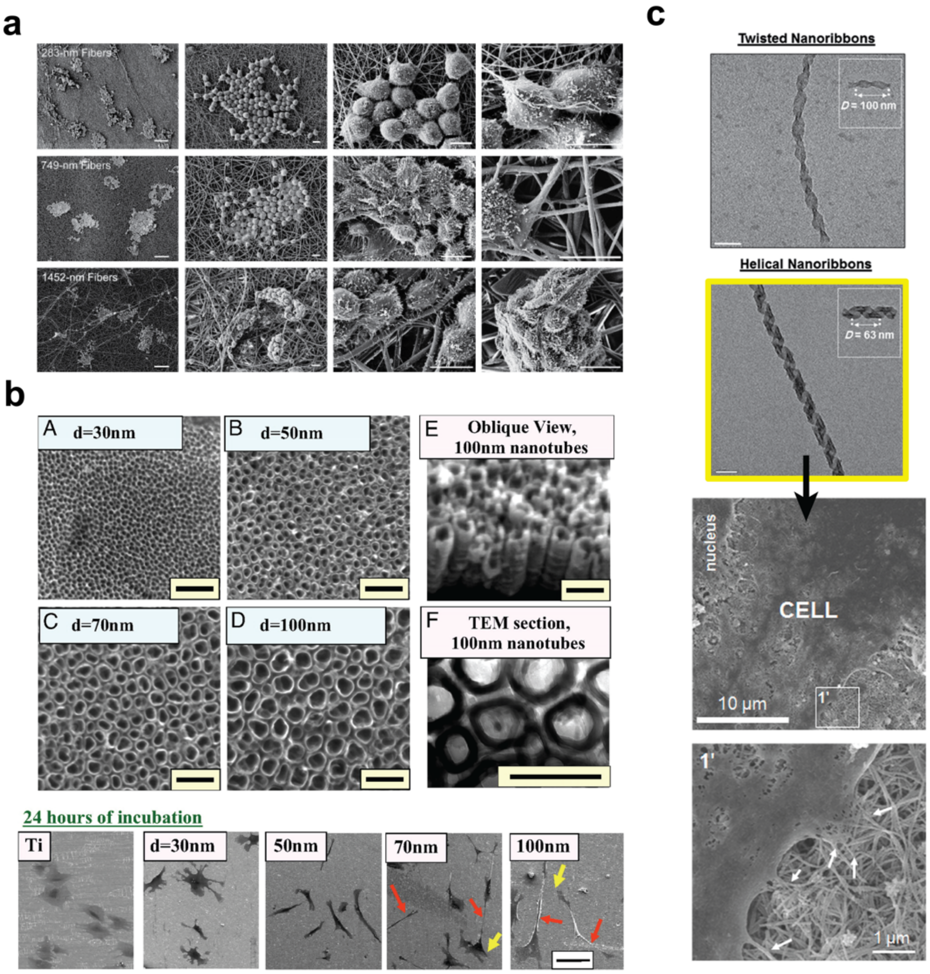

Figure 1.2 Engineering strategies for generating 3D static topographies. Panel **a:** SEM images of NPCs cultured on nanofibers of varying diameter (*68*). Panel **b**: SEM images of TiO_2 nanotubes of different pore diameters and hMSCs cultured on nanotube surfaces (*71*). Panel **c**: SEM images of silica-RGD nanoribbons with twisted and helical morphologies (top); SEM images of hMSCs cultured on grafted helical nanoribbon substrate, exhibiting extended filopodia-like structures (bottom) (*70*).

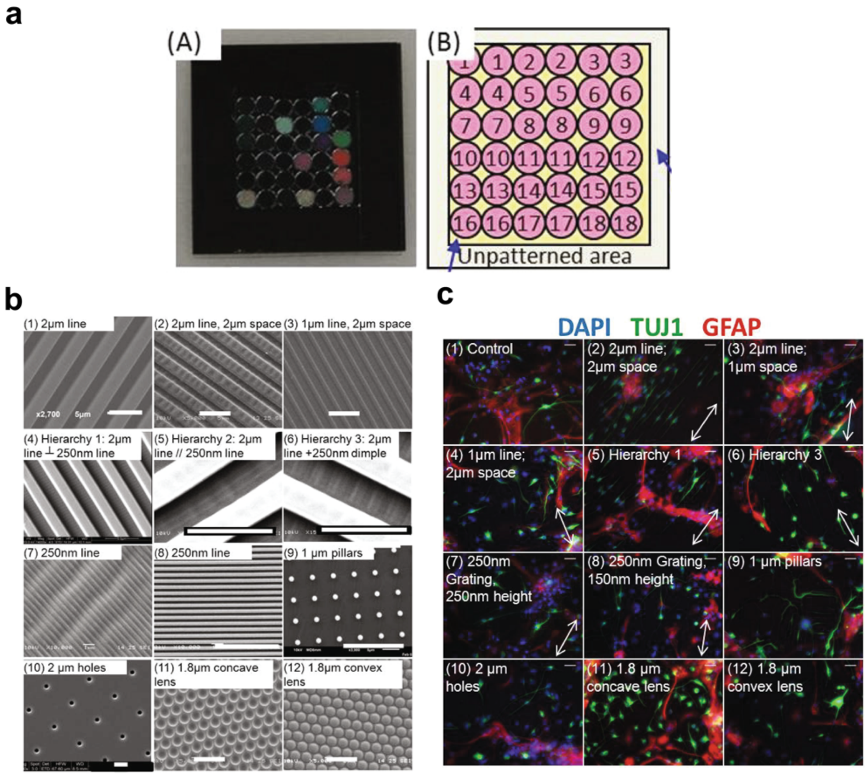

Figure 1.3 MARC chip for high-throughput topographical investigation of hESC neural differentiation. Panel **a**: schematic overview of chip design (*72*). Panel **b**: SEM images of single and multi-architectural PDMS patterns (*72*). Panel **c**: immunostaining of hESC for neuronal (Tuj1, green) and astrocytic (GFAP, red) lineages on the different topographies (*72*).

1.4.2 Micropatterning Techniques to Relate Stem Cell Shape to Behavior

Micropatterning techniques have been developed to control cell shape on a single-cell level to understand better how cytoskeletal state orchestrates stem cell behavior. The pioneering works of Ingber and Whitesides paved the way for the development of a multitude of chemical patterning techniques, important tools for dissecting the relationship between stem cell shape and response (*73-75*). These two groups demonstrated the ability to engineer cellular geometry through microcontact printing, a technique in which an elastomeric stamp is used to transfer, for example, square or rectangular patterns (2-80 µm) of self-assembled monolayers of alkanethiols onto a gold substrate (*75*). An ECM component, such as laminin, can then be deposited onto the alkanethiol micro-islands and thereby be selectively adsorbed onto the printed regions, while the gold substrate remains adhesion-resistant. Though this platform was initially explored with hepatocytes, analogous efforts have extended into the stem cell field. A seminal effort by McBeath and colleagues helped elucidate the molecular basis of cell shape-mediated effects on hMSC commitment to an adipogenic or osteogenic fate (*76*). Microcontact-printed fibronectin islands of 1,024 and 10,000 µm^2 areas were used to control cell shape. The smaller islands promoted more rounded morphologies in contrast to the larger islands, which stimulated well-spread morphologies. Using this system, they discovered that hMSC differentiation was mediated by RhoA signaling with lineage specification occurring through the RhoA effector, ROCK (*76*).

RhoA activity, though capable of displacing soluble factor signaling, was found to be dependent on cell shape. A rounded morphology was necessary for adipogenesis and, similarly, a spread-out morphology was needed for osteogenesis. ROCK, on the other hand, was found to be downstream of these instructive signals. hMSCs with constitutively-active ROCK become osteoblasts, regardless of cell shape (*76*). This landmark study highlights the importance of cell mechanics as an inductive cue for stem cell differentiation.

More recent efforts have focused on further dissecting the relationship between stem cell shape and behavior, resulting in the development of additional innovative materials. For example, Peng *et al.* patterned a polyethylene glycol (PEG) hydrogel with gold micro-islands conjugated with RGD peptides (*77*). They investigated the effect that different anisotropic patterns (circle, square, triangle, and star) and rectangles of varying aspect ratios (1, 1.5, 2, 4, 8, and 16) had on single rat MSC differentiation (Figure 1.4a). They found that cell-shape perimeter could be used as a simple parameter for predicting stem cell differentiation in the case of anisotropic patterns; however, isotropic patterns exhibited a non-monotonic osteospecific differentiation as a function of aspect ratio (*77*). A similar study investigating the influence of cell shape on lineage commitment was conducted by Kilian *et al.*, who also harnessed microcontact printing (*78*). MSCs were cultured on three shapes with pentagonal symmetry but different curvatures: 1) flower shape with large convex curves; 2) pentagon with straight edge lines; and 3) star shape with concave edges and sharp vertices (Figure 1.4b) (*78*). The subtle geometric differences were sufficient to generate strikingly different differentiation profiles through varying degrees of actin-myosin contractility (*78*). In general, pointed features between concave regions resulted in enhanced stress filaments and increased myosin contractility. Additionally, these local shape cues were associated with pathways promoting osteogenesis (*78*).

Connelly *et al.* also utilized microcontact printing in their system to generate patterned, polymer-brush surfaces for investigating the role of cell-ECM interactions in regulating human epidermal stem cell differentiation (*79*). Circular micro-islands of collagen were prepared with diameters ranging from 20-50 μm, thereby enabling the capture of single epidermal stem cells and control over cell spreading (Figure 1.4c) (*79*). More importantly, this platform enabled the researchers to dissect how changes to cytoskeletal organization influenced differentiation. This was achieved by altering individual parameters of the microenvironment systematically through the addition of actin-disrupting agents, such as latrunculin A, ROCK inhibitor Y27632, blebbistatin, and cytochalasin D. Connelly and colleagues thereby demonstrated that cell shape guides the initiation of differentiation more strongly than other factors, such as adhesive area, ECM composition, or ECM density (*79*).

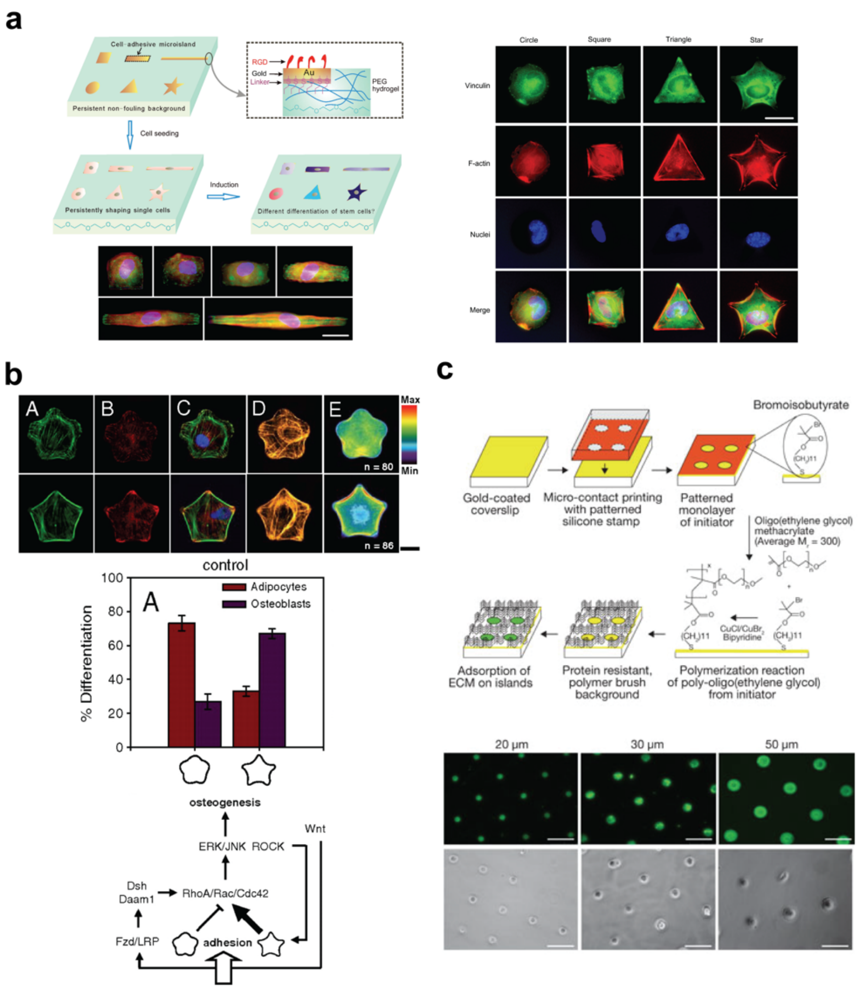

Figure 1.4 Strategies for engineering stem cell shape. Panel **a**: RGD-conjugated gold microislands of different anisotropic geometries patterned onto PEG hydrogels (left); immunostaining of single rat MSCs under different geometrical shape constraints (*77*). Panel **b**: immunofluorescent images of single MSCs stained for F-actin (green), vinculin (red), and nuclei (blue) on flower and star shape patterns created by microcontact printing (*78*). Panel **c**: microcontact printing schema for generating circular collagen microislands of different diameters applied towards studying single primary human keratinocytes (*79*).

1.4.3 Soft Matter Hydrogel Systems with Predefined Characteristics

Great strides have also been made in the development of biomimetic hydrogel systems – both naturally-derived and synthetic – that recapitulate biofunctionality as well as key mechanical properties of the stem cell niche (*80-83*). Hydrogel matrices have been utilized as a platform for presenting specific biological moieties to stem cells *in vitro*, such as cell adhesion ligands and growth factors (in both soluble and tethered fashions) (*81, 84-86*). Strategies to explore the effects of tethered ligand type, ligand density, ligand flexibility, and ligand spatial patterns have been at the forefront of these recent studies. The RGD peptide motif (arginine-glycine-aspartic acid), a major binding site of fibronectin and other ECM proteins, is one integrin-binding ligand that has been frequently studied, tethered to many hydrogel matrices, and applied to a wide spectrum of stem cell systems. For example, Salinas and Anseth investigated hMSC attachment and viability when RGD peptides conjugated to PEG hydrogels were presented via two covalent mobilization schemas: pendant tethering with a spacer arm sequence (aka mono-functionalization) or dually attached with a loop-like structure (i.e. di-functionalization) (Figure 1.5a) (*87*). In short, they found that hMSCs demonstrated lower viability in the dually-tethered gel in addition to a lower expression level of αvβ3 integrins, most likely due to steric hindrance from the two links that prevented hMSCs from binding to the RGD motif through their integrins (*87*). The use of a spacer arm sequence for immobilizing RGD was offered as a solution for overcoming integrin inaccessibility.

Building on earlier work with fibroblasts (*88*), Lam and Segura investigated another mode of RGD presentation by exploring the effects of RGD clustering on guiding the behavior of encapsulated mouse MHCs within 3D hyaluronic acid hydrogels (Figure 1.5b) (*89*). While it did not play a significant role in altering MHC proliferation, varying the distribution of the bioactive signals did have an effect on cell spreading and integrin expression. Homogenous gels (i.e. gels that display the lowest level of RGD clustering) induced a low degree of spreading. As signal clustering increased, so did the degree of MHC spreading. Furthermore, the expression of cell integrins also varied. For example, the number of cells that expressed α2 and β1 integrins was significantly higher in gels with the lowest amount of clustering and, conversely, α3 integrins were more prominent in the highly-clustered gels (*89*). Along similar lines, Wang and colleagues explored the effect of five RGD nanospacings from 37 to 124 nm on PEG hydrogels on MSCs lineage commitment (Figure 1.5c) (*90)*. These underlying nanopatterns were obtained by grafting RGD peptides onto patterned gold nanodots, enabling single nanodot-integrin interactions. With this platform, the authors observed that cell circularity (i.e. area multiplied by 4π and divided by square of perimeter) increased in response to increases in RGD nanospacing (*90*). Furthermore, under solely osteogenic or adipogenic differentiation conditions, increases in RGD nanospacings translated to an increase in the extent of respective osteogenic and adipogenic differentiation of MSCs. In the case of co-induction conditions, however, osteogenesis was found to be more sensitive to RGD nanospacings, as more MSCs pursued an osteogenic fate as nanospacings increased (*90*).

Elucidating the effect of ECM composition has also been a recent interest in the field. Battista *et al.* dissected the role that material structure and molecular-binding domain density have in controlling embryoid body growth, cavitation, and differentiation of mESCs (*91*). Semi-interpenetrating polymer networks consisting of collagen type I fibers, fibronectin, and laminin were modulated to produce scaffolds of varying physical properties and compositions. Cellular adhesion cues from laminin in the 3D scaffold were found to guide EB differentiation into cardiac-tissue lineages, while the addition of fibronectin cues induced dose-dependent differentiation into epithelial lineage without the addition of soluble factors (*91*). In addition, high-throughput microarray systems have been developed to allow for the simultaneous screening of ECM factors, both individually and combinatorially, to better investigate the complexity of the stem cell niche's ECM. Jongpaiboonkit *et al.* generated 3D PEG hydrogel arrays to screen for both individual and combinatorial effects of various ECM features: cell-adhesion ligand type, ligand density, and ECM degradability (*85*). This group focused primarily on the fibronectin-derived Arg-Gly-Asp-Ser-Pro (RGDSP) and laminin-derived Ile-Lys-Val-Ala-Val (IKVAV) sequences. Additionally, degradability was induced by photocrosslinking PEG-diacrylate chains with varying concentrations of dithiothreitol (DTT), resulting in “DTT bridge” with ester bonds prone to hydrolytic degradation (*85*). Other high-throughput techniques have involved adopting robotic spotting printing technologies. For example, Flaim *et al.* presented an ECM microarray platform that deposits an array of ECM molecule mixtures (*92*). 32 combinations were investigated with varying collagen I, collagen III, collagen IV, laminin, and fibronectin compositions (Figure 1.5d) (*92*). This method can be expanded to include a vast range of insoluble and soluble ECM cues.

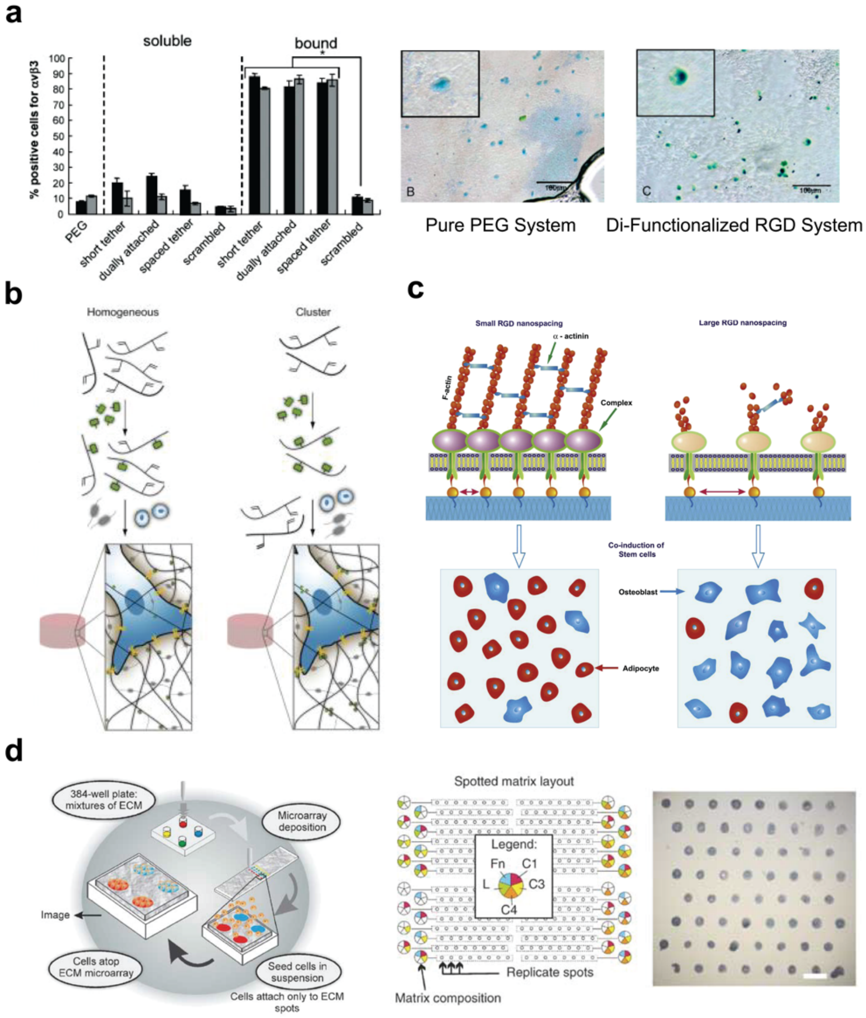

Figure 1.5 Engineering ligand presentation in hydrogel systems. Panel **a**: investigating the effects of RGD tethering via two mobilization schemas, i.e. mono- vs. di-functionalization, on hMSC attachment. hMSCs stained for nuclei (blue) and αvβ3 cell surface integrin (green) (*87*). Panel **b**: schematic of RGD clustering within hyaluronic acid hydrogels (*89*). Panel **c**: the effect of small vs. large RGD nanospacing on MSC differentiation (*90*). Panel **d**: ESCs cultured on an ECM microarray platform consisting of varying ECM compositions (*92*).

Biochemical information within the ECM has thus been a focus of numerous studies, however, hydrogels have also enabled major strides in the field’s understanding of how mechanical properties regulate and affect stem cell function. In particular, the elastic modulus (or stiffness) of the substrate has been widely explored. The initial landmark study utilized a collagen-coated polyacrylamide gel with tunable cross-linking properties, correlating to varying matrix stiffnesses as low as 0.1 kPa to 40 kPa (*33*). With this system, the physiological stiffnesses characteristic of brain, muscle, and bone were recapitulated *in vitro* and presented to naïve MSCs. The resulting differentiation of MSCs into tissue-specific cell types along with corresponding altered gene expression patterns demonstrated the significance that matrix mechanical properties have in the stem cell niche (*33*).

Gilbert and colleagues extended this initial strategy to illustrate the potency that substrate elasticity has on muscle stem cell self-renewal and cell fate (*93*). In doing so, they engineered a tunable PEG hydrogel system covalently cross-linked with laminin in which stiffness could be controlled by varying the PEG polymer percentage in the precursor solution. Muscle stem cells cultured on soft PEG gels with an elastic modulus that mimicked adult murine skeletal muscle (~12 kPa) was found to enhance muscle stem cell survival when compared to cultures on traditional, stiff polystyrene surfaces (~10^6 kPa) (*93*). Substrate rigidity also influenced Myogenin expression (a transcription factor expressed by differentiated muscle stem cells). Soft substrates demonstrated a 3-fold decrease in Myogenin-positive cells. Additionally, muscle stem cells cultured on PEG substrates most closely tuned to their native muscle niche stiffness (as opposed to brain or cartilage) were found to retain the greatest stemness (*93*).

While many studies that investigate the effects of substrate stiffness on stem cell behavior (including the aforementioned studies) employ model systems that yield thin layers of tunable hydrogels coated on a rigid substrate, Saha *et al.* highlighted one potential problem with this approach (*94*). Soft polyacrylamide hydrogels are prone to equi-biaxial compressive stress when exposed to an aqueous environment due to osmotic pressure difference. The ensuing instability causes the formation of sharp folds (i.e. creases) as a result of induced buckling of the polyacrylamide surfaces. The authors emphasized that these surface creases must be characterized and controlled as they influence stem cell behavior (*94*). NSCs were demonstrated to migrate towards the folds and adopted mature neuronal and astrocytic phenotypes when compared to NSCs that were uniformly attached and differentiated when cultured on smooth and stable polyacrylamide surfaces (*94*). Therefore, instable surface creasing of polyacrylamide substrates (and potentially other soft hydrogel systems) may bias stem cell mechanotransduction studies (94). This highlights the need for well-characterized and tightly controlled synthesis of soft-matter substrates. An overview of other key studies investigating the importance of matrix elasticity in stem cell biology are described in a number of extensive reviews (*45, 51, 60, 95*).

1.5 Second Generation Engineering Strategies - Increased Complexity with a Focus on Spatiotemporal Control

Engineered microenvironments are thus clearly valuable tools for dissecting how the ECM affects stem cell fate decisions, and there have been increasing advances in elucidating how these extrinsic cues modulate core transcriptional networks (*79*). As demonstrated in the above section, initial engineering strategies in the stem cell field focused primarily on recapitulating *static* representations of the niche ECM. More recent engineering strategies, however, have evolved to emulate the dynamic interaction between stem cells and their physical environment. The creation of platforms with increasingly sophisticated structural and functional complexity is helping to bridge a gap between *in vitro* systems and what are likely highly dynamic *in vivo* physiological environments. In particular, the ability to engineer and incorporate tightly-coupled spatial and temporal control into these platforms has become a key objective of the field. The following section provides an overview of these emerging second-generation engineering strategies.

1.5.1 Biomaterials with Tunable Properties

An increased interest in mimicking the dynamic properties of the stem cell niche's ECM has spurred the development of smart biomaterials – ones whose properties can be manipulated by external stimuli (*96*). Light, temperature, pH, electric fields, small molecules, and shear stress represent a variety of "triggers" that have been employed to induce changes in stiffness, topography, and adhesion (*96*). These *in situ* perturbations are powerful tools because they allow for the investigation of spatial and temporal ECM cues, providing a deeper insight into stem cell behavior.

1.5.2 Spatiotemporal Control Over Topography

To complement landmark studies with pre-printed substrates, in recent years, topographic presentation has evolved toward materials with active and tunable topographies. Shape-memory polymers represent one class of active materials that have been employed for probing stem cell response to localized topographical changes, and studies involved with such polymer systems have provided insights into the dynamics of cytoskeletal organization and mechanotransductive signaling events (*97*). These systems have relied primarily on the use of temperature as a temporal control for switching topography from a primary temporary pattern to a secondary permanent pattern. Davis *et al.* was one of the first groups to harness this effect (*98*). They utilized a thermally-responsive polyurethane polymer substrate with end-linked thiol-ene crosslinks that was programmed to change from a lamellar surface to a flat surface upon a temperature transition from 30°C to 37°C (*98*). More recent techniques have extended this strategy a step further by demonstrating the capability to switch between two distinct patterns. Le *et al.* established this dual-shape capability by developing a poly(ε-caprolactone) surface in which the primary pattern was formed with replica molding, while the secondary pattern was generated by mechanically deforming the substrate at 130°C using a second replica mold and, subsequently, cooling it to 78°C (*97*). With this technique, a combination of pattern transformations was introduced to hMSCs: micron-sized cube arrays to hexnuts, cylinders to boomerangs, and channels to planar surface (Figure 1.6a) (*97*). Though pattern versatility was evident, there were significant challenges, including a lack of pattern reversibility and a high transition temperature of 40°C (resulting in cell toxicity).

Gong *et al.* illustrated another approach for utilizing shape-memory systems (*99*). They engineered a four-stage shape memory platform with tunable microgrooves (Figure 1.6b). To start, poly(ε-caprolactone) was modified with A allyl alcohol as a plasticizer, shifting the shape-memory recovery function to within the physiological range of 32°C- 41°C. Two different dynamic surfaces were then pursued. The first modulated microgroove depth, increasing from 0 to 1.7 μm, 3.5 μm, and 4.9 μm at 32, 35, 38, and 41°C, respectively. The other surface transitioned from a temporal microgroove with a width of 9 μm at 32°C to 7, 4.5, and 3.1 μm at the same increasing temperature set-points. The changes in the first surface induced parallel upward forces, which had little to no effect on cultured rat bone marrow MSCs (*99*). The latter, convergent force from the second surface, however, greatly affected cytoskeletal arrangement and biased differentiation fate towards a myogenic lineage (*99*). In a final example, Tseng *et al.* translated shape-memory polymers into 3D by utilizing an electrospun scaffold whose fibrous architecture transitioned from a strain-aligned state to its original random fiber arrangement upon thermal activation (Figure 1.6c) (*100*). This controllable change in scaffold architecture exhibited desirable shape recovery properties as well as cytocompatibility for human adipose-derived stem cells. Moreover, the recovery rate of the scaffold could be controlled by modulating the chemical composition of the polyurethane scaffold, which comprised of hard segments of polyhedral oligomeric silsesquioxane and soft segments of polylactide/caprolactone copolymer (resulting in an increase in the glass transition temperature or decrease in hydrophilicity) (*100*). These shape-memory-actuated materials, while still in the early stages of development, offer exciting potential for supporting further in-depth studies of stem cell regulation.

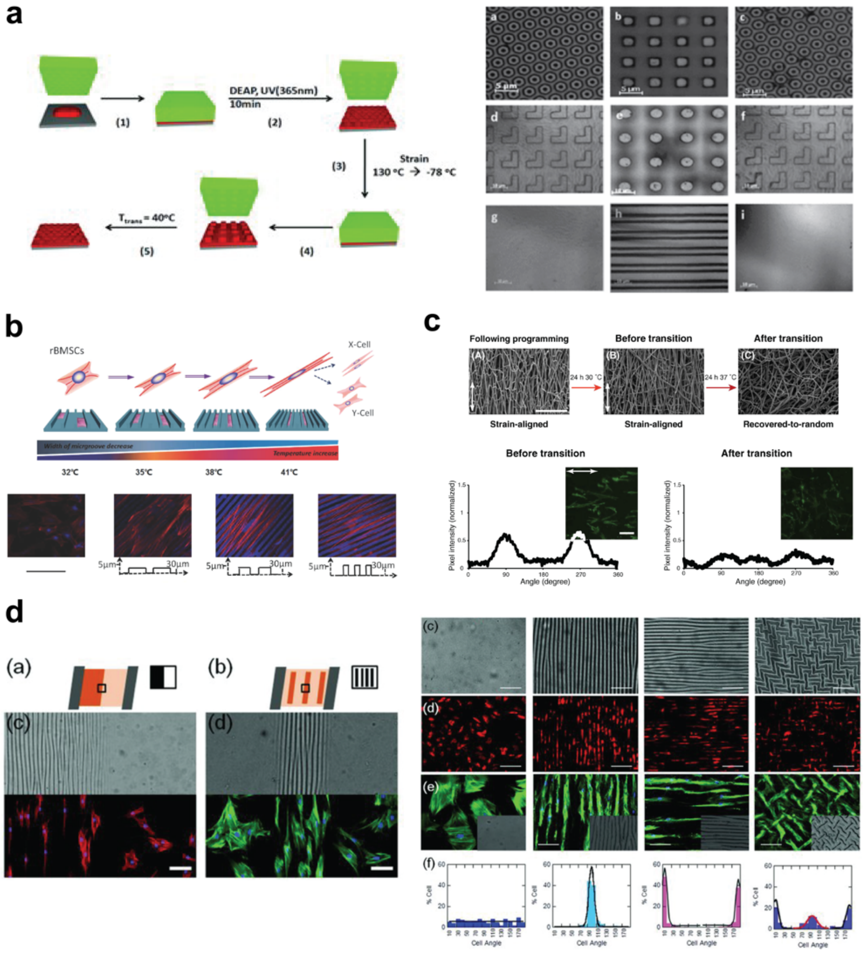

Figure 1.6 Engineering dynamic topographies with spatiotemporal control. Panel **a**: schematic for fabricating thermally-responsive poly(ε-caprolactone) topographies (*97*). Panel **b**: four-stage shape memory platform with tunable microgrooves applied towards studying MSC behavior; cells immunostained for F-actin (red) and nuclei (blue) (*99*). Panel **c**: dynamic switching from fiber-aligned state to random fiber orientation via a cytocompatible temperature increase (top); cells stained with phalloidin (green) to visualize actin (bottom) (*100*). Panel **d**: spatial control of lamellar patterns dictated by mask applied during UVO treatment (right); illustration of quadruple topographical switching from flat to lamellar patterns at 90 degrees to lamellar at 180 degrees to zigzag patterns (right); live hMSCs labeled with CellTracker red, and fixed cells stained for F-actin (green) and nuclei (blue) (*101*).

While thermally-induced shape-memory polymers offer considerable advances, another means of creating quasi-static topography was demonstrated through a technique that combined strain-induced buckling of PDMS substrates with plasma oxidation. Guvendiren *et al.* introduced a strategy for fabricating versatile, high-fidelity, and reversible lamellar wrinkling patterns (Figure 6d) (*101*). To obtain this, PDMS sheets were stretched uniaxially, followed by exposure to ultraviolet/ozone (UVO). This exposure created stiff regions that resulted in perpendicular buckling when the strain was released. With this system, hMSCs were exposed to four changing patterns, starting with a flat, unpatterned surface to lamellar with 90-degree patterns to lamellar with 180-degree patterns and, finally, to zigzag patterns. hMSCs responded to these *in situ* dynamic patterning switches through changes in cell orientation angle (*101*). Key advantages of this system include the ability to modulate pattern amplitude and periodicity by altering the degree of strain release. Moreover, spatial control of topographies could be regulated by selectively exposing the surface to UVO with different shadow-mask patterns. One disadvantage, however, is that high hMSC proliferation could lead to "masking" of the triggered topographical change. In other words, as culture time and cell division increases, cellular alignment to induced topographies diminishes (*101*).

Photo-induced manipulation of surface topography is another powerful approach that enables high spatial and temporal control. In comparison to its shape-memory polymer counterparts, light-responsive materials can be operated at standard physiological temperature (37°C) as well as undergo countless sequential alterations that are not pre-determined, as long as phototoxicity does not occur. Kirschner *et al.* engineered one such system – a photodegradable PEG-based hydrogel platform in which topographical cues can be formed *in situ* by user-controlled spatial erosion (*102*). Specifically, photolithographic techniques were used to pattern features (such as anisotropic channels and isotropic square patterns) on a photolabile gel, where pattern depths could be controlled by modulating the time of UV exposure (10 mW/cm^2). Moreover, sequential patterning steps could be applied to alter surface topography concurrently during cell culture. hMSCs were cultured on this tunable surface and demonstrated reversible changes in cell morphology and alignment (*102*). Similar to the shape-memory materials, only initial studies have been conducted with this system. Future perspectives involve using this system for better understanding how stem cells respond to real-time changes of ECM topographical cues within their niches.

1.5.3 Spatiotemporal Control Over Matrix Stiffness

In addition to modulating topography, light has also been used as a tool for creating dynamic cultures of switchable substrate stiffnesses. Yang *et al.* synthesized a phototunable hydrogel that incorporates a poly(ethylene glycol) di-photodegradable acrylate crosslinker (*103*). Upon controlled exposure to UV light, the initially stiff hydrogel (Young's modulus of 10 kPa) transitioned into a soft hydrogel with a modulus of 2 kPa (Figure 1.7a). With this system, they investigated the effects of mechanical dosing and mechanical memory on hMSCs (*103*). In statically soft gels, hMSCs retained the capability to differentiate into both adipogenic and osteogenic lineages. However, upon mechanical dosing (i.e. culturing the cells on stiff substrates at variable time frames before *in situ* softening of the hydrogel), differentiation became biased towards osteogenic lineages. Specifically, cells were cultured from 1 day to 10 days on stiff substrates prior to transitioning to soft hydrogels. The longer hMSCs were cultured on the stiff substrate, the more biased the cells became towards osteogenesis (*103*). Transcriptional coactivators that play a key role in mechanotransduction, YAP and TAZ, were found also to persist in the nucleus (i.e. mechanical memory) even after cells were transitioned to soft substrates, suggesting that hMSCs retain information about past ECM states (*103*). This system helped uncover a temporal aspect of stem cell mechanotransduction, where brief periods of mechanical dosing resulted in reversible activation of YAP and longer periods resulted in constitutive YAP nuclear localization (*103*).

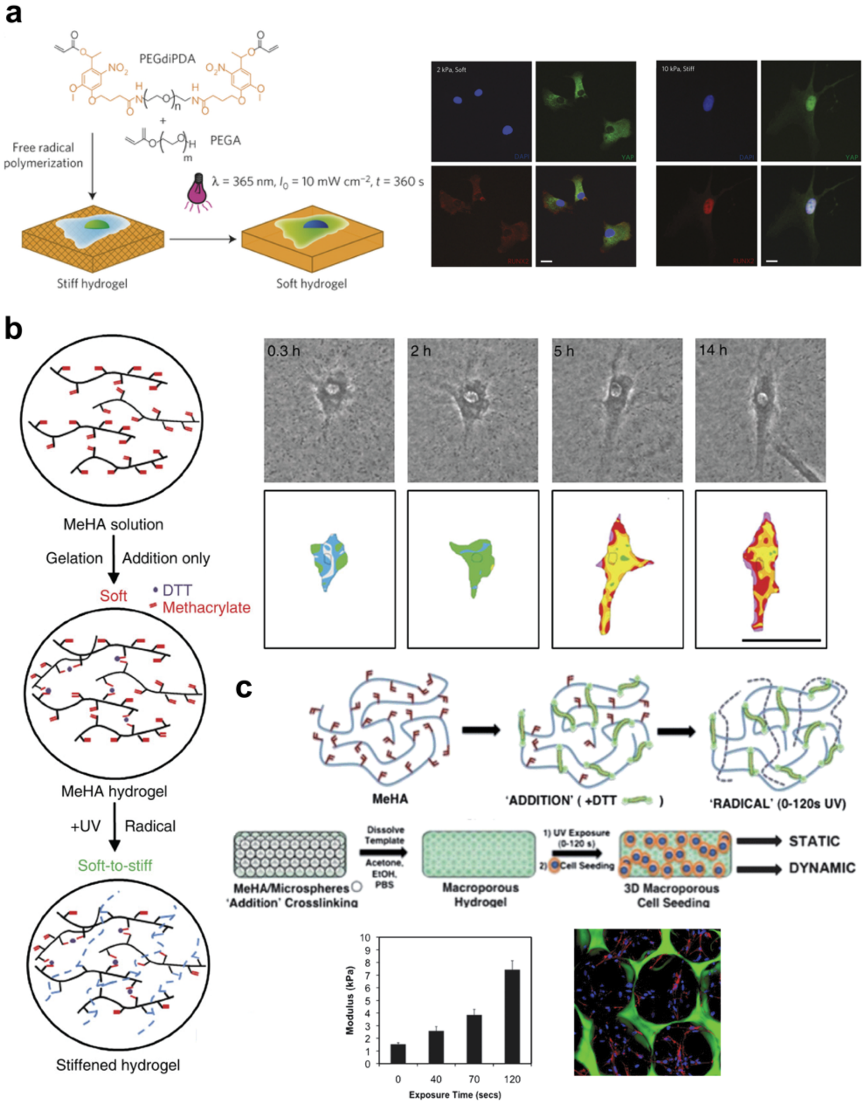

Figure 1.7 Engineering strategies for dynamic control over substrate stiffness. Panel **a**: illustration of photodegradable hydrogel system (top); immunostaining of hMSCs for YAP (green) and RUNX (blue) localization (bottom) (*103*). Panel **b**: crosslinking schematic (left) and traction stress maps of single hMSC during *in situ* stiffening (right) (*104*). Panel **c**: crosslinking schematic for generating porous hydrogel architectures; changes in bulk compressive moduli in responsive to UV crosslinking exposure times; hMSCs stained for actin (red) and nuclei (blue); porous hydrogels stained with FITC (green) (*86*).

In an analogous fashion, Guvendiren *et al.* engineered a complementary strategy for *in situ* hydrogel stiffening in the presence of hMSCs – a system characterized by fast kinetics, long-term stability, and structural uniformity (Figure 1.7b) (*104*). This approach is potentially biologically relevant since matrix stiffening has been generally associated with key biological phenomena, such as disease and tissue development. To develop this dynamic substrate, hyaluronic acid macromers were functionalized with methacrylates, which react with thiols and radicals for crosslinking. Gelation was obtained through the addition of DTT, providing an initial stiffness of 3 kPa. Further, secondary crosslinking was achieved through a photoinitiator and subsequent UV light exposure for two minutes at 10 mW/cm^2, increasing the matrix modulus to 30 kPa. This temporal stiffening not only can be tuned by exposure time but also can be achieved via sequential exposures during cell culture (*104*). The use of DTT, however, poses a potential caveat for this hydrogel system as it may impact hMSC redox state.

Marklein and colleagues extended this photoactivated crosslinking approach to study hMSC behavior in 3D porous hydrogels, investigating the importance of the magnitude, context, and timing of presented stiffness stimuli (*86*). In their work, Marklein *et al.* generated a macroporous architecture by initially crosslinking methylated hyaluronic acid around a hexagonally-organized template of microspheres (Figure 1.7c). These hydrogels were triggered to stiffen from 2.6 kPa to 12.4 kPa, either on Day 2 or 7 of a 14-day culture. These variable mechanics were controlled by UV exposure (10 mW/cm^2) and found to affect the secretion profiles of cytokine and angiogenic factors (*86*). In particular, hMSCs cultured on hydrogels that were stiffened on Day 2 (i.e. transitioned to the stiffer substrate sooner) displayed a greater reduction in key angiogenic factors and cytokine molecules compared to samples stiffened on Day 7. In contrast, morphology, proliferation, and differentiation did not exhibit significant dependence on stiffness dynamics (*86*).

Yoshikawa *et al.* explored a different approach to achieving a dynamically tunable hydrogel platform (*105*). In lieu of using light as a stimulus, changes in viscoelastic properties were achieved through subtle pH changes and subsequently manipulating hydrophobic and interchain interactions. In this study, the pH-responsive polymer films consisted of a triblock ABA-type hydrogel, where A represented poly-(2-(diisopropylamino)ethyl methacrylate) and B represented poly(2-(methacryloyloxy)ethyl phosphorylcholine) (*105*). By narrowly adjusting the pH range between 7 to 8 – a range that does have the potential to affect cellular function – the stiffness of the copolymer could be reversibly transitioned between 1.4 kPa to 40 kPa. Mouse myoblasts were used as a model system for this study, where morphological changes and cell adhesion strength were evaluated in relation to dynamic modulations of substrate stiffness (*105*). While recent efforts have demonstrated the capability of either dynamic stiffening or softening of gels, a significant advance within the field would be a system that allows for reversible switching with cues that are inert to cells. This level of control would enable more complex investigations of the effects of stiffness pulses at different temporal onsets and durations.

1.5.4 Dynamic Control of Integrin-Based Focal Adhesions

Achieving precise control over the spatiotemporal presentation of ECM bioactive ligands has warranted the development of additional sophisticated engineering strategies. As illustrated in the previous sections, cell-adhesive ligands are key mediators of cell-matrix interactions and, thus, stem cell function. While previous strategies investigated the influence of pre-patterned peptides that mimic the active domains of key ECM components in a static fashion, several groups have recently fabricated smart biointerfaces that control the activation and de-activation of these integrin-based signals.

Photolabile protecting groups are an attractive approach for achieving dynamic control over the formation of stem cell focal adhesions, which activate downstream signaling cascades. Weis *et al.* pursued this approach by anchoring "caged" RGD peptides to self-assembled monolayers of alkanethiols on a gold substrate (Figure 1.8a) (*106*). To ensure only specific cell attachment to RGD-anchored SAMs, oligo(ethylene glycol) groups were conjugated to the SAMs lacking tethered peptides, providing a non-biofouling background. This system was applied to study how RGD peptide density influenced the differentiation of myoblasts (myofiber precursors) (*106*). With an initial surface RGD density ~17%, few cells attached to the substrate. However, upon a 3-minute light exposure, the maximum surface RGD density was unmasked, and integrin-mediated myoblast interaction with the substrate was thus enabled. Light exposure for 3 minutes was applied at different time points during the culture timeframe: 1 hour, 6 hours, 24 hours, and 48 hours. Myogenic differentiation – analyzed via sarcomeric myosin expression and the formation of multi-nucleated myotubes – was more prominent when cells were exposed to high-density RGD peptides during earlier culture times (*106*). This discovery highlights the importance of temporal presentation of ECM ligands, motivating additional exploration of their relationship to dynamic mechanical cues.

Another approach for achieving dynamic ligand manipulation during stem cell culture was demonstrated by Kloxin *et al* (*107*). Photolabile tethers consisting of a photodegradable acrylate monomer were conjugated to the fibronectin epitope Arg-Gly-Asp-Ser (RGDS) within a nondegradable PEG-based hydrogel. Upon irradiation, the photolytic removal of RGDS moieties locally modified peptide presentation within the 3D microenvironment (Figure 1.8b) (*107*). The importance of persistent RGDS signaling on hMSC viability and differentiation was investigated by photolytically removing RGDS on Day 10 of a 21-day culture. In response to the temporal changes, hMSCs were found to downregulate the expression of αvβ3 integrins, while increasing the production of glycosaminoglycans as well as type II collagen, both of which are key markers of chondrogenic differentiation (*107*).

While photoresponsive materials have proved very effective for achieving spatiotemporal control over ligand presentation, Kasten *et al.* demonstrated an alternate technique for probing stem cell mechanotransduction: the use of magnetic forces to induce integrin response (*108*). This strategy drew inspiration from earlier efforts, which utilized ferromagnetic microbeads coated with synthetic RGD peptides. These materials were employed for applying controlled mechanical loads to fibronectin receptors without inducing global changes to cell shape (*109*). In this particular application, however, Kasten and colleagues coupled paramagnetic microbeads to hMSC integrins by coating beads with an antibody specific for the β1 integrin subunit (Figure 1.8c) (*108*). A custom magnetic device with an average magnetic field strength of 0.015 Tesla was then applied to the culture system, thereby inducing the displacement of the magnetic beads, which subsequently applied a drag force on stem cell integrin receptors, created mechanical stress, and temporarily distorted the cell membrane. This study was also tested in conjunction with three different types of substrates: polystyrene, RGD-functionalized, and fibronectin-coated surfaces (*108*). Differentiation markers associated with adipogenic (i.e. PPARγ), osteogenic (i.e. ALP), and chondrogenic lineages (i.e. Sox9) were investigated in addition to released soluble factors relating to angiogenesis (i.e. VEGF) and osteogenesis (i.e. collagen I). Kasten and colleagues observed that VEGF expression increased in response to short-term integrin stress stimulated by the magnetic field when hMSCs were cultured on RGD peptides and fibronectin but not on polystyrene (*108*). Collagen I expression, in contrast, was upregulated when hMSCs were cultured on polystyrene but not the other two surfaces (*108*). These initial results not only highlighted the dynamic ability to control integrin stress through a magnetic field but also emphasize the importance of multifactor interactions of ECM-niche components.

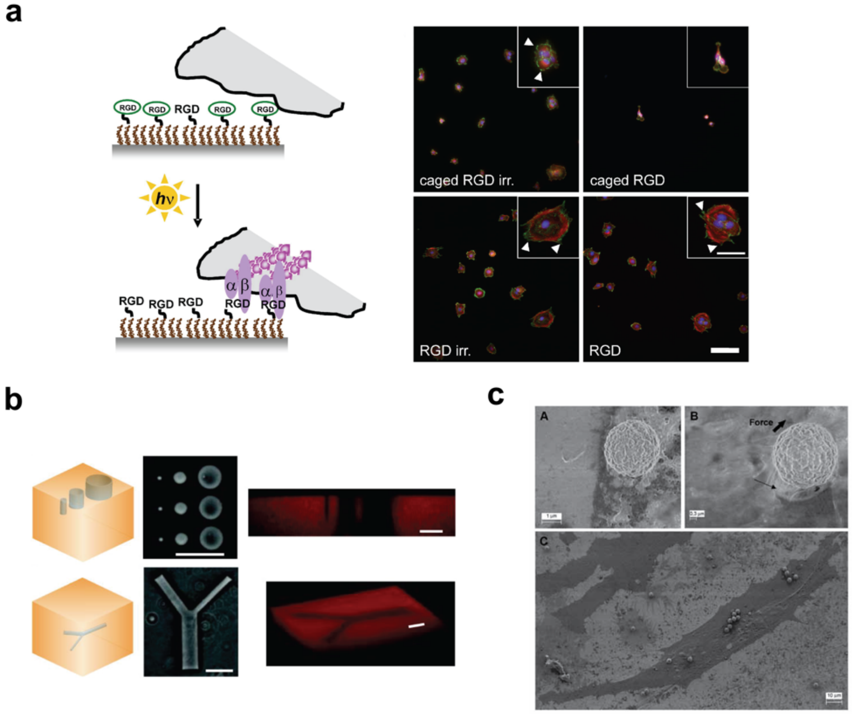

Figure 1.8 Engineering strategies for *in situ* modulation of ligand presentation and hydrogel degradation. Panel **a**: schematic illustrating ligand tethering and UV irradiation to release caged RGD molecules; myoblasts stained for actin (red), vinculin (green), and nuclei (blue) (*106*). Panel **b**: 3D photopatterning of surface features, such as various sizes of microwells and a bifurcation channel, within a photodegradable hydrogel (*107*). Panel **c**: SEM images of paramagnetic beads attached to MSC β1 integrin subunit (*108*).

1.6 Dissecting Cell-Cell Interactions within the Stem Cell Niche

Cellular components within the stem cell niche serve as another key source of instructive inputs for regulating stem cell quiescence, proliferation, and cell-fate determination (*4, 48, 110, 111*). The spectrum of intercellular communication that takes place within these niches encompasses a stem cell's interactions with other stem cells, stem cell progeny, and neighboring niche cells. Cell-cell signaling among these parties is achieved through various means: release of secreted soluble factors between neighboring cells (paracrine signaling), release of factors back to the same cell (autocrine signaling), cell-surface ligand-receptor binding between cells in direct contact (juxtacrine signaling), the transmembrane flux of signals through intimate gap junctions, and potentially mechanical interactions between cells.

The importance of cellular interactions and organization within stem cell niches was first demonstrated in early studies involving *Drosophila* germline stem cells (GSCs). Investigations of the ovary and testes niches showed that stemness and differentiation are balanced by critical communication between stem cells and their non-stem cell niche neighbors (*112-114*). In the female fly, for instance, GSCs populate the anterior end of the ovariole and interact with three somatic cell types. GCSs indirectly adhere to the niche by intimately associating with cap cells via adherens junctions, cell-cell connections that form via homotypic cadherin binding (*115*). During asymmetric division, the daughter cell that maintains this adhesion also retains its stem cell identity, whereas the daughter cell lacking adhesion differentiates into a cystoblast (*116*). Terminal filament cells and inner germarium sheath cells (also referred to as escort cells) augment this maintenance of stem cell phenotype by repressing the key differentiation gene bag-of-marbles (bam). This repression is achieved through the secretion of cytokines by terminal filament cells, which signal the cap and escort cells to produce bone morphogenic protein (Bmp) ligands that bind with receptors that act to downregulate bam in GSCs (*116*). The *Drosophila* testis, though a more complex microenvironment, shares similar hallmarks with the ovary niche. Only GSCs that contact adjacent hub cells within the apex of the testis self-renew. Hub cells also secrete Upd, which stimulates GSC adhesiveness and prevents surrounding cells from outcompeting GSCs for niche contact (*116*). Moreover, somatic cyst progenitor cells indirectly activate the Bmp pathway by secreting Gbb and Dpp, repressing differentiation yet again. These examples illustrate the balance of communication between stem cells and non-stem cell niche neighbors.

The degree of interaction between stem cells and other cellular players is particular to the stem cell niche under investigation. For instance, muscle satellite stem cells remain relatively isolated and quiescent as they reside near basal lamina of muscle fibers (*48*). Not until activation do they proliferate and fuse with one other to form differentiated myotubes. Hematopoietic stem cells, on the other hand, tightly associate with not only osteoblasts that line the endosteal surface of the trabecular bone but also endothelial cells that line blood vessels (*115*). Similarly, NSCs closely associate with endothelial cells of surrounding vasculature, neighboring astrocytes, microglia, and in some cases ependymal cells (*110, 117*). Epithelial stem cells that reside in a specialized “bulge” structure within hair follicles, in contrast, encounter periodic stimuli from specialized mesenchymal cells, referred to as dermal papilla (DP). Specifically, the regeneration of hair follicles exposes resident stem cells to dynamic, perpetual cycles of growth (anagen), regression (catagen), and rest (telogen). During the anagen stage, massive cell death occurs below the bulge area for all cells except DP. The basement membrane then shrinks and draws DP into close contact with stem cells within the bulge. This close association is believed to be necessary for re-activating hair follicle regeneration, thereby initiating a brief telogen phase followed by rapid anagen phase (*118*). As a final example, intestinal stem cells populate the crypt base of intestinal villi and drive rapid cell turnover of the epithelial lining of the small intestine and colon (*21*). Within this niche, stem cells receive a complex array of signals from neighboring epithelial and stromal cells – paneth cells, goblet cells, and transit-amplifying cells, to name but a few. Renewal of the epithelium is orchestrated by a complex array of cellular signals, which ultimately drive budding transit-amplifying cells to differentiate into mature lineages, such as enteroendocrine cells, tuft cells, and absorptive enterocytes. These committed cells migrate out of the crypt and up to the base of the villi (*21*).

While the well-studied *Drosophila* niches are not as complex as vertebrate niches, the insights obtained from these lower organism counterparts were essential in stimulating more rigorous investigations of key regulatory cellular signals. These efforts have exposed a sophisticated interplay of signaling factors. Diffusible growth factors represent one class of secreted soluble signals that can positively or negatively regulate stem cell behavior within the niche – the effects of which are under strict spatial and temporal constraints (*4*). For example, in the SVZ of the lateral ventricles, endothelial cells from surrounding vasculature produce a variety of paracrine factors that modulate key aspects of neurogenesis. The production of vascular endothelial growth factor, for instance, has been found to promote NSC self-renewal within the adult rat brain (*119-121*). Also, the secretion of brain-derived neurotrophic factor (BDNF) has been suggested to direct NSC proliferation and balance the rates of neuroblast migration and differentiation in adult neurogenic niches (*121-123*). In addition to these growth factor examples, endothelial cells are capable of secreting other types of short-range signals. For example, the chemokine stromal cell-derived factor-1 (SDF-1) is believed to regulate the migration and survival of SVZ neural progenitor cells. Additionally, the secreted glycoprotein pigment epithelium-derived factor (PEDF) promotes NSC self-renewal within the murine SVZ (*121, 124*). These secreted factors have complex but essential functions in regulating stem cell behavior. Thus, engineering strategies for identifying and dissecting these paracrine signals is a key objective within the field.

Integral membrane proteins that mediate juxtacrine (i.e. cell-cell contact dependent) signaling are another important class of molecules. For example, Ephrin receptor tyrosine kinases (Ephs) and their membrane-bound ephrin ligands allow for bidirectional communication between ligand-expressing and ligand-receiving cells (*125*). Several studies have investigated Eph-ephrin signaling within adult NSC and intestinal stem cell niches. A and B subclass ephrins and Eph receptors have, for example, been suggested to regulate proliferation negatively within the adult SVZ of the lateral ventricles (*126*). In the adult hippocampal niche, the presentation of ephrin-B2 by hippocampal astrocytes induces neuronal differentiation of NSCs (*127*). Eph-ephrin has also been implicated in coordinating migration and proliferation of stem cells within the intestinal epithelium (*125*). Notch receptors and their Delta-like or Jagged family ligands represent another key signaling pathway active between juxtaposed cells in adult stem cell niches (*128*). For instance, niche ependymal cells and astrocytes in the early postnatal SVZ express Jagged1, which activate Notch1 and inhibit differentiation of neural progenitors (*128*). Specifically, forced Notch1 activation was found to increase NSC proliferation, whereas Notch1 repression promoted cell cycle exit (*129*). Additionally, inactivation of the Notch/RBPJκ signaling pathway in adult hippocampal stem cells resulted in the depletion of Sox2-positive neural precursors and long-term suppression of hippocampal neurogenesis (*130*). Therefore, Notch is viewed as a regulator of cell cycle progression that also prevents premature NSC depletion (*131*). Recent *in vivo* studies also revealed that Notch also plays an instructive role in biasing NSCs towards an astrocytic fate within the hippocampus (*132*). While Notch signaling has been demonstrated to play a crucial role in NSC maintenance in the adult dentate gyrus, it also been shown to participate in regeneration of muscle. Notch is active in quiescent muscle satellite cells; however, upon injury, muscle stem cells experience a downregulation of Notch signaling and accordingly exit their quiescent state (*128, 133*).

1.7 Early Approaches for Studying Stem Cell-Niche Cell Interactions In Vitro

A diverse spectrum of engineering strategies has emerged in the stem cell field for modeling and dissecting heterotypic cellular interactions within stem cell niches. Early efforts focused primarily on the use of bulk co-culture studies for elucidating the effects of cell-cell juxtacrine signaling and soluble paracrine factors. To study juxtacrine signaling, co-culture systems have seeded two or more cell types onto the same monolayer culture, yielding random heterotypic interactions. To study soluble paracrine factors, permeable transwell inserts have often been employed to separate two cell populations while allowing for the diffusion of soluble factors between cells. Additionally, applying conditioned media – i.e. medium that has been cultured with one cell type that contains paracrine factors – to stem cell cultures can achieve a similar result to the transwell system, with the caveat that particularly labile factors can undergo decay in conditioned medium. In either case, the degree of cell-cell signaling can be controlled by adjusting the cell numbers for each population (*134*). Often, both direct co-cultures and transwell co-cultures are conducted in parallel to isolate the paracrine from juxtacrine effects.

This two-pronged strategy has proved useful in a variety of studies. Ottone and colleagues, for instance, employed this approach for investigating how cell-cell contact-dependent signaling of vascular epithelium governs NSC behavior (*135*). In doing so, they pursued both co-cultures and transwell cultures of NSCs with three types of murine endothelial cells: primary brain microvascular endothelial cells, brain microvascular endothelial cell line, and conditionally immortalized pulmonary endothelial cells. Direct cell contact between NSCs and all three cell types through bulk co-culture studies was found to induce cell-cycle arrest in the G_0-G_1 phase and thereby promote quiescence (*135*). To assess whether this outcome resulted from contact-dependent signaling, cell-cycle profiles of transwell cultures were conducted in parallel and compared with NSC monocultures. Similar results between these two culture systems indicated that the observed quiescence was, indeed, a result of juxtacrine signaling from endothelial cells (*135*). In addition, this study showed that NPCs cultured in contact with epithelial cells as opposed to cultured in transwells failed to produce differentiated progeny, instead maintaining multipotent GFAP$^+$Sox2$^+$ markers (*135*). Song *et al.* also exploited the advantages of the two co-culture systems to study how niche cell types within the hippocampus affect neurogenesis (*136*). When NSCs were plated in primary neuron-enriched cultures, they observed an increase in oligodendrocyte production and a lack of neurogenesis. In contrast, NSCs cultured on a feeder layer of primary hippocampal astrocytes displayed a 10-fold increase in the percentage of differentiated neurons compared to control laminin-coated surfaces. To elucidate whether hippocampal astrocytes instructed neuronal fate commitment via paracrine or membrane-bound factors, NSCs were cultured in medium conditioned by astrocytes and found to result in a lower level of neurons (*136*). These parallel cultures indicated that hippocampal neurogenesis stems from a mixture of soluble and contact-dependent cues. Later work by Ashton *et al.* revealed that the juxtacrine signal responsible for neurogenesis was ephrin-B2 (*127*).

Dual co-culture approaches have also played an integral role in helping dissect the contributions of neighboring niche cell types in influencing the behavior of other adult stem cell types. For example, Loibl *et al.* utilized this strategy for studying whether endothelial progenitor cells (EPCs) promoted angiogenesis through the induction of a pericyte-like phenotype in MSCs, which can be identified by an upregulation of CD146, NG2, αSMA, and PDGFR-β (*137*). In a method analogous to that of Ottone *et al.*, cell-cell crosstalk was investigated by comparing direct co-cultures to transwell cultures and single-cell type control cultures. After three days in the different cultures, they reported an approximate 15-fold increase of CD146 expression for the direct co-culture vs. only a three-fold and two-fold increase for single and transwell cultures, respectively (*137*). A similar but less pronounced trend in gene expression was observed for NG2. Additionally, for αSMA and PDGFR-β, MSCs in direct co-cultures were better able to maintain expression while the other cultures demonstrated decreases in expression (*137*). These findings suggest that EPCs play a key role in mediating differentiation of MSCs into pericytes through cell-cell juxtacrine interactions (*137*). Moreover, these findings (along with those of Ottone and Song) highlight the major role that direct co-cultures and transwell co-cultures have in elucidating the effects of cellular interactions within stem cell niches.

1.7.1 Patterned Bulk Stem Cell Co-Cultures

While random bulk co-cultures are useful tools for studying cellular interactions that may occur within the stem cell niche, there has been significant work in developing patterned co-culture systems. These platforms are motivated by two key advantages. The first is the enhanced spatial control for more precise manipulation of heterotypic cellular interactions. The second is the high reproducibility of patterning techniques, which ensures consistent cellular localization across multiple experiments for statistical analysis (*138*). These spatially-defined *in vitro* culture systems are also deemed by some as more accurate predictors of heterotypic cell-cell effects as they better mimic the inherently structured cellular organization of *in vivo* microenvironments (*139*).

Soft-lithography techniques are broadly utilized for fabricating such platforms, where success depends upon one cell type preferentially attaching to patterned regions comprised of a particular type of ECM and a second cell type preferring the unpatterned regions (*138, 140*). Rodriguez *et al.* demonstrated this strategy by combining microcontact printing with avidin-biotin chemistry to generate hMSC and human umbilical vein endothelial cell (HUVEC) co-cultures of various geometrical interfaces at both the multicellular and single-cell level (Figure 1.9a) (*140*). This specific strategy relied on the patterning of three distinct regions: adhesive, nonadhesive, and dynamically adhesive. Microcontact printing was first utilized to pattern regions of fibronectin, a cell-adhesive material, followed by the printing of neutravidin, an initially non-adhesive material. Pluronic F127 was physisorbed onto the remaining non-patterned regions to produce a nonbiofouling background. For cell patterning, the first population was seeded onto the substrate and attached to the fibronectin areas. Neutravidin was then dynamically switched from non-adhesive to adhesive upon addition of biotinylated fibronectin, which allowed for the selective patterning of the second cell type (*140*). Fukuda *et al.* employed an analogous strategy by utilizing capillary force lithography and layer-by-layer assembly of polyelectrolytes to demonstrate the capacity to establish patterned co-cultures of ESCs and NIH-3T3 fibroblasts (Figure 1.9b) (*141*). Specifically, glass substrates were patterned with cell-resistive hyaluronan (HA) utilizing capillary force lithography. This was achieved by placing a PDMS mold on top of a spin-coated thin film of HA and subsequently allowing capillary action to create a positive replica of the PDMS mold. Fibronectin was then deposited onto the HA-patterned substrate and adsorbed to the bare glass-exposed regions. ES cells then selectively adhered to the fibronectin patterns. In order to accommodate the secondary cell type, fibroblasts, collagen was deposited onto the surface, adhered to the HA regions, and switched the regions to cell-adhesive (*141*). Such patterned co-cultures offer useful platforms for studying fundamental stem cell biology and even exploring various tissue engineering strategies, though they rely upon selectivity of ECM proteins that may, in many other cases, be somewhat promiscuous in their cell adhesive properties.

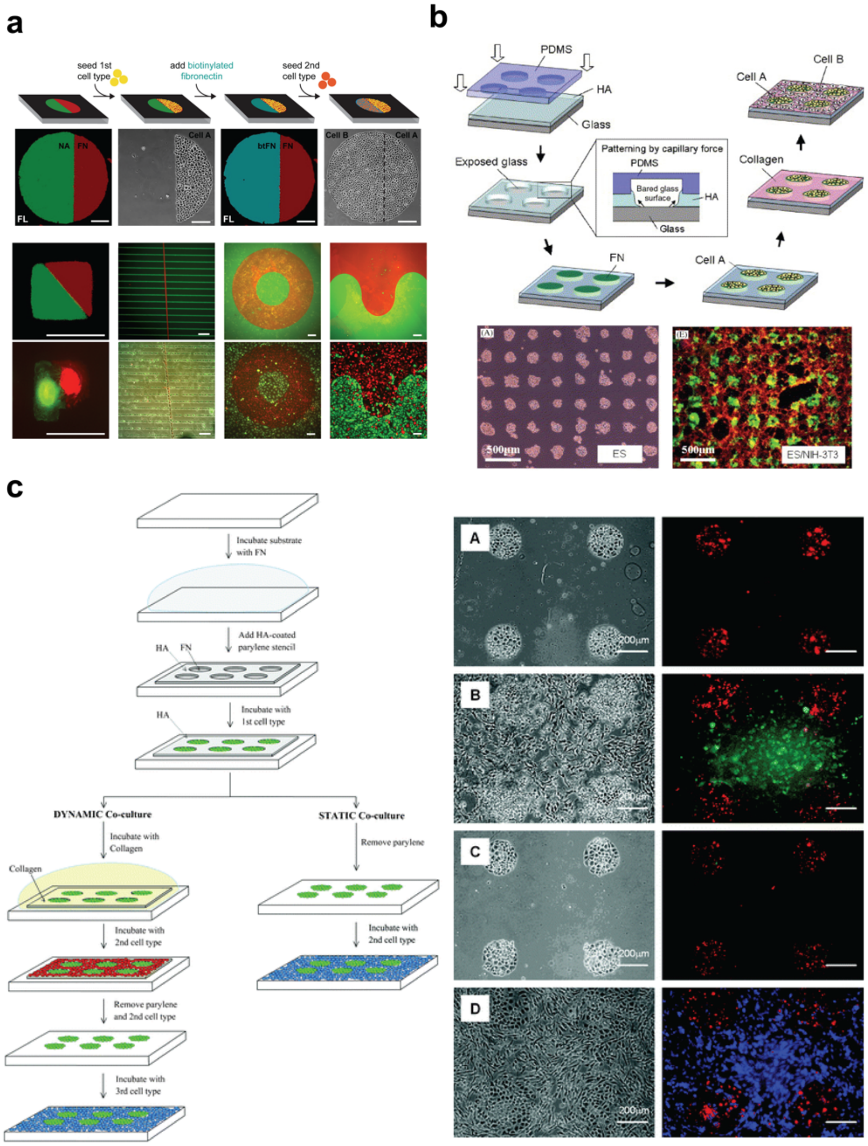

Figure 1.9 Patterned bulk co-culture strategies. Panel **a**: patterning schematic for generating bulk and single-cell patterned co-culture systems; two MSC populations labeled with either CellTracker red or CellTracker green (*140*). Panel **b**: schematic illustrating the use of capillary force lithography and layer-by-layer deposition for generating ESC (green) and NIH-3T3 (red) co-culture on a patterned HA/collagen surface (*141*). Panel **c**: schematic for patterning static and dynamic co-cultures of mESCs (red), AML12 cells (green), and NIH-3T3 cells (blue) (*142*).

Another engineering approach for controlling heterotypic cellular interactions involves the utilization of microfabricated elastomer stencils, which are advantageous because they do not rely on patterning of ECM components. In this approach, stencils with a distinct pattern are coupled to a substrate, thereby physically blocking cellular adhesion to specific regions upon seeding of the first cell type. The stencil is removed to expose the previously covered underlying substrate, and the second cell type is seeded. Wright *et al.* employed this strategy for creating static and dynamic co-cultures of mouse ES cells with fibroblasts and/or hepatocytes (*142*). The static co-culture was achieved by attaching a reversibly sealed parylene-C stencil with hole patterns of diameters ranging from 40 to 200 μm to a fibronectin-coated PDMS substrate. Upon attachment of ES cells to the exposed hole regions, the stencil was gently peeled off. AML12 hepatocyte cells were subsequently seeded on the cell micropatterned surface, filling in the unpatterned regions. In the case of the dynamic co-culture, the authors demonstrated the capacity for temporal regulation of cell-cell interactions, though efficiencies of the process were not noted. Specifically, ES cells were cultured with fibroblasts and hepatocytes in a sequential manner, thereby exposing ES cells to two different cell types (Figure 1.9c) (*142*). Unlike the static platform that accommodated only two cell types, the dynamic platform utilized a parylene-C stencil initially treated with hyaluronic acid. ES cells were then seeded within the open hole patterns of the micro-stencil. To support the second cell type, collagen was absorbed onto the HA-coated stencil, switching the non-patterned regions from cell repulsive to adhesive. Finally, ES cells were exposed to a secondary support cell by completely removing the stencil and seeding the third cell type (*142*). This dynamic strategy has potential not only to elucidate how cues from other niche cells act independently, but also for dissecting how these disparate cues may act in a combinatorial and hierarchical manner. Additionally, Wright and colleagues claim that hole patterns on the parylene-C stencils could be fabricated down to a 3 μm diameter and can easily be adapted to support single-cell studies (*142*). These methods make elastomer stencils a powerful and unique engineering strategy for controlling heterotypic cellular interactions beyond two cell types.

1.7.2 Patterned 3D Stem Cell Co-Cultures

The push toward 3D patterned co-cultures has also been of recent interest within the stem cell field as they better emulate native cellular microenvironments within *in vivo* tissue niches. The drive from 2D to 3D has led to the development of many new engineering strategies. While micropatterning techniques generally manipulate cell-surface adhesion to obtain cellular patterns, this strategy cannot be applied for the formation of cell spheroids. Thus, additional approaches are required. Microfluidic methods encompass one such approach for generating patterned 3D co-cultures. Torisawa *et al.*, for instance, illustrated the ability to generate co-culture spheroids with various compositions and geometries (Figure 1.10a) (*143*). Their technique involved the fabrication of a two-layered PDMS device with two microchannels separated by a semi-porous membrane of polycarbonate. The top channel was dedicated to guiding the relative positions of the two cell types via laminar streams, thereby hydrodynamically focusing the cell populations into the bottom layer and ultimately controlling the geometry of the multicellular spheroids. Spatial control of these 3D co-cultures was achieved by changing the geometry of the bottom microchannel. With this system, Torisawa and colleagues patterned spheroids within a straight 200 μm channel, juxtaposing mouse ES cells with hepatocarcinoma HepG2 cells (*143*). They demonstrated that ESC differentiation within the patterned co-culture spheroids revealed regional differentiation dependent upon initial cell-cell positioning. This microfluidic system was shown also to be compatible with other cell types and generated a variety of 3D co-culture spheroid patterns of breast cancer cells with HUVECs and monkey kidney cells. The capability of recapitulating more complex co-cultures was presented by patterning up to five distinct groups of cells (i.e. five alternating lines of cells with a total width of 1 mm that formed contacting spheroids after 3 days of culture) through the use of a five-inlet top channel (*143*).

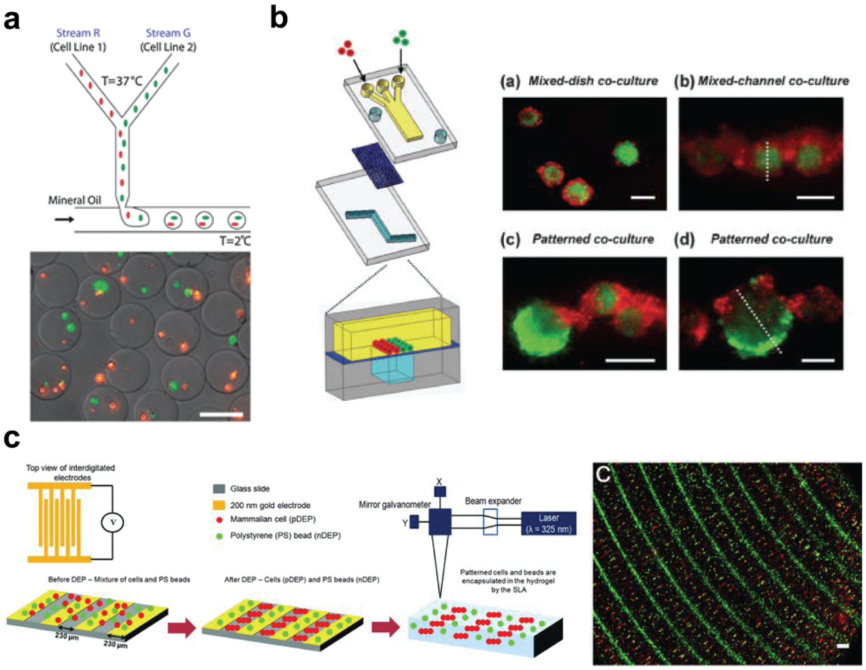

Figure 1.10 Microfluidic strategies for generating patterned bulk co-cultures. Panel **a**: encapsulation of fluorescently labeled populations of mESCs into agarose microgels and formation of embryoid bodies after 4.5 days of culture (*144*). Panel **b**: fluorescent images comparing 3D mixed dish vs. patterned mESC spheroid co-cultures generated from a two-layered microfluidic device (*143*). Panel **c**: patterning of mESCs (red) and polystyrene beads (green) using spiral electrodes (*145*).

Droplet microfluidics is another promising technique for generating high-throughput 3D cell co-cultures. Tumarkin and colleagues utilized this technology to synthesize microgel emulsions that served as "micro-reactors", in which discrete numbers of cells were compartmentalized to enhance heterotypic cellular interactions (Figure 10b) (*144*). The encapsulation of two different cell populations in agarose droplets was achieved using a T-junction microfluidic device. Co-encapsulation was tested on two populations of mESCs, where one was fluorescently labeled with a green cell tracker and the other labeled with a red cell tracker. Cells were suspended in agarose solution and supplied to the microfluidic device. Despite relying on random Poisson seeding, the relative cell numbers encapsulated from each population could be roughly controlled by tuning the ratio of flow rates for the cell suspensions. To generate droplets, a carrier phase of mineral oil containing 3%(wt) of Span 80 surfactant was introduced perpendicular to the cell streams. Downstream of the junction, droplets were collected and cooled to induce gelation of the microgels, and analysis was conducted using optical microscopy and flow cytometry. Encapsulated cells not only demonstrated the ability to form embryoid bodies but also demonstrated viability approaching 80% at the end of a 4.5-day culture (*144*). These results are useful first steps, showing the viability of the technique for precisely encapsulating two different cell populations. Limitations of this strategy, however, include a practical restriction to two cell types due to Poisson statistics, an inability to control cell stoichiometry directly, and potential difficulties in extending the approach to adhesion-dependent cells.

The ability to control the assembly of heterotypic cellular interactions in 3D has also been demonstrated by Bajaj and colleagues utilizing a different microfluidic technique (*145*).

Dielectrophoresis (DEP), in combination with stereolithography and custom-made electrodes, was used to pattern and encapsulate two distinct populations of mouse ESCs within poly(ethylene glycol) diacrylate hydrogels of tunable stiffnesses (Figure 10c) (*145*). DEP refers to the induced motion of electrically polarizable entities (such as cells) when exposed to an electric field gradient (*146*). Without dielectrophoretic forces, the two different cell populations exhibited minimal cell contact. However, upon inducing DEP by energizing the electrodes with an AC voltage, cell-cell contacts were stimulated and led to pearl chain geometries. In addition to patterning cells, Bajaj *et al.* extended this strategy to organize spheroids of cells spatially within hydrogels (*145*). This method holds potential for enabling more robust investigations of stem cell-niche cell communication.

While microfluidics has been a key technology for generating *in vitro* platforms for studying juxtacrine signaling within stem cell niches, it has also played a pivotal role in elucidating the effects of paracrine signaling. Unlike standard cell-culture platforms, which are prone to unequal distributions of secreted factors, microfluidic devices utilize laminar flow to impose precise control of soluble factor profiles (*147*). Microfluidic gradient generators, for example, have been employed for exogenous delivery of soluble factors (i.e. growth factors and cytokines) to stem cell cultures (*148, 149*). Flow has also been used to modulate the distribution of secreted factors from niche cells to stem cells (*150, 151, 152*). Moreover, another advantage of using microfluidics is the ability to isolate soluble factors for downstream analysis (*147*).

1.8 Shifting Focus to Single-Cell Resolution and Artificial Niches

The aforementioned bulk co-culture systems (both random and patterned) have yielded valuable insight into the effects of cellular signaling within stem cell niches. However, there are a number of additional features that would be advantageous to address. Micropatterned surfaces enable spatial control of cellular interactions yet can restrict cell motility and proliferation to chemically patterned regions (*134*). Additionally, the ability to pattern more than two cell types remains a challenge. Microfluidic platforms, on the other hand, introduce shear forces, which may affect and bias stem cell behavior. Another significant concern with bulk co-culture systems is the difficulty in discerning each cell type's relative contribution to overall behavior (*153*). In an attempt to address the latter issue, there is a growing focus within the stem cell field on developing engineering strategies that operate at the single-cell level. These types of systems allow for more focused and robust analyses of the effects of juxtacrine and paracrine signaling. Moreover, they hold potential for shedding insight onto the heterogeneity of intercellular interactions (*147*).

1.8.1 Microfluidic Approaches for Single-Cell Co-Cultures

The microfluidic field has fostered the development of a multitude of strategies to capture and pair different cell types at a single-cell resolution. Skelley and colleagues presented a technique for individually pairing thousands of mouse ESCs with mouse embryonic fibroblasts at an efficiency approaching 70% (*154*). Their microfluidic device consisted of a dense array of passive hydrodynamic traps, referred to as weirs, that operated via a three-step loading protocol (Figure 1.11a) (*154*). Each weir was comprised of a larger front-side cup optimized to accommodate two cells and a smaller back-side capture cup for temporary capture. mESCs were first flown toward the smaller back-side cups. Once cells fully occupied these cups, the flow direction was switched, and the captured mESCs were rapidly transferred to the large front-side cup. Fibroblasts were then flown in the same direction, trapped, and loaded adjacent to the captured mESCs (*154*). Though these authors focused on applying the system to enhance cellular fusion, this platform also holds potential for elucidating the effects of heterotypic cellular interactions on dictating stem cell behavior, though attachment-dependent cells may pose a challenge.

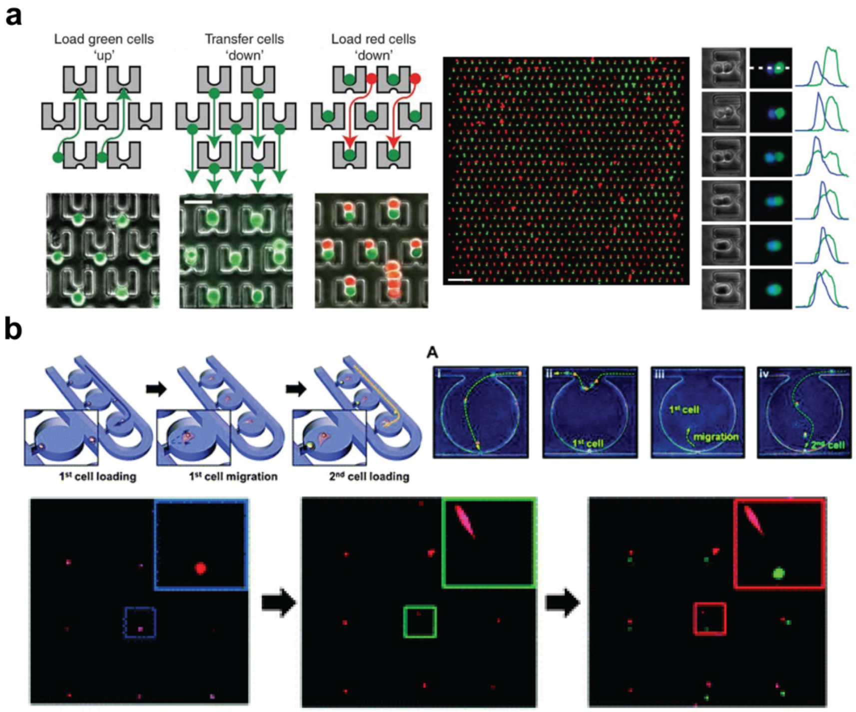

Figure 1.11 Single-cell co-cultures using microfluidics. Panel **a**: cell-loading schematic for capturing Cell Tracker-labeled mouse 3T3s (red and green) (left); fusion of a paired green fluorescent protein-expressing mESC (green) and Hoerchst-stained mouse embryonic fibroblast (blue) (right) (*154*). Panel **b**: overview of single-cell pairing protocol in which sequential trapping of mouse embryonic fibroblasts (red) and mESCs (green) is achieved (*155*).

Hong *et al.* developed another microfluidic device that performed heterotypic cell pairing at a single-cell level and supported the culture and tracking of cell pairs over multiple generations (*155*). Rather than employing weir-based hydrodynamic traps, they relied on trapping junctions that implemented self-variable fluidic resistance to generate high-efficiency cell groupings (Figure 1.11b) (*155*). The basic principle of this approach is that, once cells enter the individual culture chamber and are trapped by small junctions located at the bottom of these chambers, fluidic flow resistance increases and blocks additional cells from infiltrating the chamber. Following capture of the first cell, cells are incubated to allow for migration away from the junction, resetting the traps to an "active" state and allowing for the capture of a second cell type (*155*). Advantages of this device include high-throughput and minimized physical constraint to cell growth, allowing for multiple cell divisions and migration. Hong and colleagues applied this system for the single-cell co-cultures of mouse embryonic fibroblasts and mESCs as a proof-of-concept (*155*).

Other microfluidic-based tools with considerable spatial control over sequential trapping and pairing of heterotypic single-cell pairs have been developed but not yet implemented within the stem cell field. The adoption of these emerging technologies offers potential for shedding light on the role of specific cellular interactions within stem cell niches. Dura *et al.* presented a deformability-based, cell-pairing device which utilized weir-based traps, similar to Skelley and colleagues (*156*). However, upon capturing the first cell type, a transient increase in flow rate squeezed the arrested cells into the larger double-cell traps through constriction by flow-induced deformation (Figure 1.12a) (*156*). The second cell type was captured consecutively in a similar fashion. An advantage of this system is that paired cells were secured within the traps, allowing for the device to be disconnected and applied for other off-chip applications, while retaining cell pairing integrity. Dura *et al.* also developed methods for pairing heterotypic cells of different sizes by tuning the geometry of the trapping structures (*156*). Finally, the ability to pair triplets of cells was illustrated, where one red fluorescently-labeled NIH3T3 fibroblast was sandwiched between two green fluorescently-labeled fibroblasts (*156*).

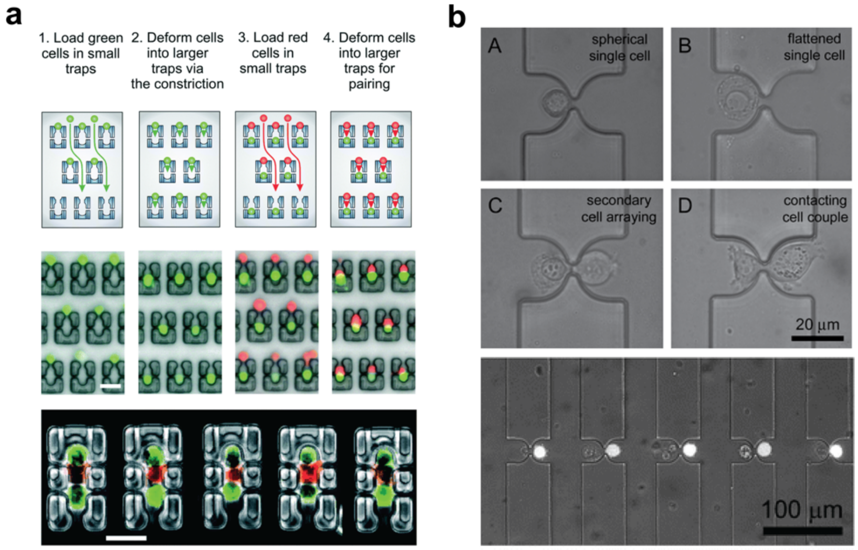

Figure 1.12 Examples of additional microfluidic platforms with potential applications for studying stem cell-niche cell interactions. Panel **a**: loading protocol for pairing cells into traps possessing lock-in features (top); two-component and three-component pairings demonstrated (bottom) (*156*). Panel **b**: heterotypic single cell co-culture arrays, pairing one unlabeled SW480 cell with one fluorescently labeled with calcein AM (*157*).

Frimat *et al.* demonstrated another microfluidic approach for inducing single-cell co-culture contacts for studying the formation of gap junctions (Figure 1.12b) (*157*). To start, a microfluidic circuit based on differential fluidic resistance directed single cells into an array of trap structures within a superimposed serpentine channel. To capture a second single cell adjunct to the first, a second trapping structure was designed using a mirrored configuration. Despite the heterogeneous size characteristics of the cells employed (HT29 colon carcinoma cells, MCF-7 epithelial-like breast cancer cells, and SW480 epithelial cells), these cells were captured at an efficiency approaching 81% with 96% of cells retained within these traps during the first two days (*157*).

1.8.2 Artificial Stem Cell-Niche Cell Signaling Approaches

The precise manipulation of different cell types remains an ongoing challenge within the field. While micropatterning and microfluidics enable more precise spatial control over the design of *in vitro* platforms, other approaches for dissecting cellular communication within the niche have been pursued. These approaches involve analyzing the natural complexity of cellular interactions and re-engineering more simplified versions *in vitro*. One notably powerful approach involves the immobilization of key cell surface ligands (cadherins, EpCAM, delta-1, jagged-1, and ephrins) to biomaterials as a means of mimicking communication from a secondary cell type.

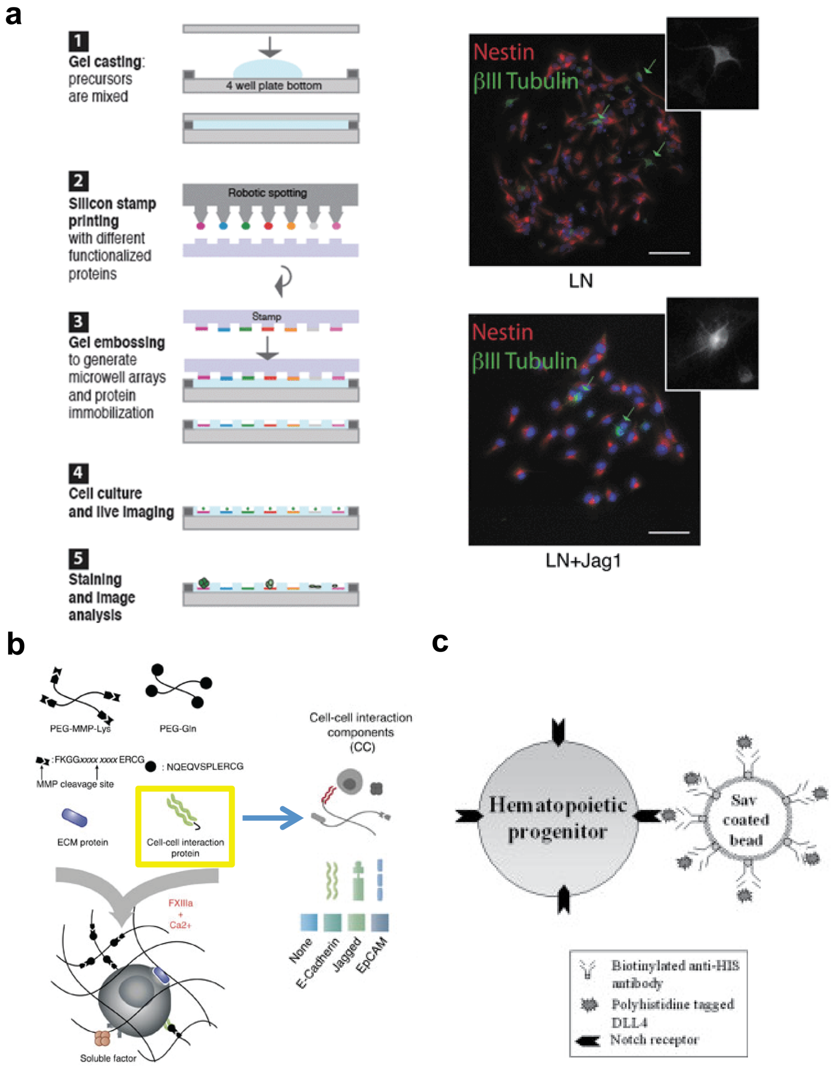

Figure 1.13 Strategies for engineering artificial niches microenvironment that mimic cell-cell interactions. Panel **a**: overview of steps for fabricating microarrayed artificial niches (left); representative images of NSC cultures immunostained for Nestin (red) and βIII-tubulin (green) on hydrogels co-functionalized with Laminin-1 alone or Jagged-1 and Laminin-1 (right) (*158*). Panel **b**: cell-cell interaction components incorporated into 3D microarray platform in combination with other factors (i.e. matrix elasticity, proteolytic degradability, cell density, ECM component, and soluble factors) for studying mESC behavior (*159*). Panel **c**: illustration of DLL4-coated microbead interacting with Notch receptor on HSCs (*160*).

Roccio and colleagues demonstrated the fabrication of a microarrayed artificial niche platform dedicated to better understanding the role that the Notch ligand, Jagged-1, has on regulating single NSC behavior (Figure 1.13a) (*158*). A robotic spotter was utilized to immobilize the protein of interest to the bottom of PEG-based hydrogel microwells. Tethered Jagged-1 was found to increase survival and neurosphere-forming efficiency of single NSCs. They also assessed the potential synergistic effects of Jagged-1 in combination with Laminin-1 (though no additive effect was observed) (*158*). In another system developed by the same group, a 3D-niche microarray system was presented that expanded the cell ligand repertoire to include E-cadherin and EpCAM – not to mention a plethora of other key niche factors, including control over ECM stiffness, ECM components, soluble factors, cell density, and ECM degradability (Figure 1.13b) (*159*).

An additional approach for developing functionalized biomaterials for mimicking cellular interactions was demonstrated by Taqvi *et al*. Magnetic microbeads were functionalized with the notch ligand, Delta-like ligand 4 (DLL4), thus, creating a synthetic alternative to niche stromal cells that communicate with HSCs (*160*). Functionalization was achieved by first coating magnetic polystyrene microbeads with streptavidin. These beads were then washed and incubated with a biotinylated histidine tag antibody and, again, with the histidine-tagged DLL4 protein (schematic illustrated in Figure 1.13c) (*160*). This biomaterial-based artificial Notch-signaling system was utilized for investigating the induction of T-cell differentiation in HSCs (*160*). This approach offers a simplified alternative to modifying niche stromal cells genetically to express Notch ligands followed by co-culture. More importantly, this system enables more thorough investigation of the effects of Notch ligand-receptor interaction. Quantitative and temporal studies are enabled by, respectively, tuning the ligand-cell ratio and duration of signaling. For instance, Taqvi *et al.* found that a 1:1 bead-to-cell ratio generated a significantly higher T-cell differentiation efficiency when compared to a 5:1 functionalized bead-to-cell ratio (*160*).

1.9 Conclusions and Future Directions

Understanding the complexity of stem cell behavioral regulation remains a formidable challenge, and insights into the underlying mechanisms will greatly enable the development of stem cell-based therapies. The successful control of stem cell expansion and differentiation *ex vivo* in addition to the targeted activation of endogenous stem cell populations demands a comprehensive understanding of the regulatory role of environmental (i.e. niche) signals. Accordingly, the development of innovative engineering strategies for recapitulating key facets of stem cell-ECM interactions and stem cell-niche interactions has been instrumental in providing deeper insights into how stem cells respond to extrinsic cues at a molecular level.

Within the past few decades alone, the stem cell field has made tremendous progress in understanding these niche principles through initial strategies that focused primarily on fabricating static representations of niche ECM features (i.e. topography, matrix elasticity, ligand presentation, etc.) and bulk co-culture studies of heterotypic cellular interactions (i.e. paracrine and juxtacrine signaling). However, the desire to mimic dynamic *in vivo* niche phenomena has spurred the evolution of more sophisticated second-generation engineering tools. The push to incorporate spatiotemporal control into biomaterial systems has enabled an unprecedented ability for probing stem cell response to dynamic changes in the duration or intensity of presented ECM cues. In the case of studying niche cellular interactions, the robust isolation of single-cell co-cultures and the development of artificial cell-signaling platforms allows for more controlled and reproducible study of cell-cell interactions.

As our knowledge of stem cell biology continues to expand, we anticipate that engineering strategies will also progress. Biomaterials with not only tunable but also reversible properties will be key for dissecting how stem cells respond to ECM-related signaling dynamics. For instance, biomaterials engineered to allow reversible stiffening *and* softening will be a significant advancement within the field. Additionally, platforms that allow for the ability to investigate combinations of ECM cues simultaneously and at different temporal onsets will be valuable for obtaining a more comprehensive understanding of stem cell niches that can ultimately be applied to accelerate the development of clinical applications. For studying the role of intercellular communication within stem cell niches, high-throughput strategies for creating precise cellular communities of more than two cell types at a single-cell resolution will reveal potential juxtacrine/paracrine signaling hierarchies. Another important advance would include engineering strategies that control the timing of cellular interactions to understand the duration of contact that is necessary to bias stem cell behavior towards a desired fate. With these advanced strategies in hand, the stem cell field will be better positioned to make stem cell therapies a clinical reality.

1.10 References

1. Sun Y, Chen CS, Fu J. Forcing stem cells to behave: a biophysical perspective of the cellular microenvironment. Annu Rev Biophys. 2012;41:519–42. doi:10.1146/annurev-biophys-042910-155306.
2. Takahashi K, Yamanaka S. Induction of pluripotent stem cells from mouse embryonic and adult fibroblast cultures by defined factors. Cell. 2006 Aug 25;126(4):663–76. doi: 10.1016/j.cell.2006.07.024.
3. Lane SW, Williams DA, Watt FM. Modulating the stem cell niche for tissue regeneration. Nat Biotechnol. 2014 Aug 5;32(8):795–803. doi:10.1038/nbt.2978.
4. Vazin T, Schaffer DV. Engineering strategies to emulate the stem cell niche. Trends Biotechnol. 2010 Mar;28(3):117–24. doi:10.1016/j.tibtech.2009.11.008.
5. Liu B, Shu S, Kenny TP, Chang C, Leung PSC. Stem cell therapy in autoimmune rheumatic diseases: a comprehensive review. Clin Rev Allergy Immunol. 2014 Oct;47(2):244–57. doi: 10.1007/s12016-014-8445-8.
6. Daley GQ. The promise and perils of stem cell therapeutics. Cell Stem Cell. 2012 Jun 14;10(6):740–9. doi: 10.1016/j.stem.2012.05.010.
7. Voog J, Jones DL. Stem cells and the niche: a dynamic duo. Cell Stem Cell. 2010 Feb 5;6(2):103–15. doi:10.1016/j.stem.2010.01.011.
8. Iwasaki H, Suda T. Hematopoietic stem cell biology. In: Kondo M, editor. Stem cell biology and regenerative medicine. Totowa, NJ: Humana Press; 2010. p. 37–56.
9. Scholfield R. The relationship between the spleen colony-forming cell and the haemopoietic stem cell. Blood Cells. 1978;4(1-2):7-25.
10. Fuentealba LC, Obernier K, Alvarez-Buylla A. Adult neural stem cells bridge their niche. Cell Stem Cell. 2012 Jun 14;10(6):698–708. doi:10.1016/j.stem.2012.05.012..
11. Miller FD, Gauthier-Fisher A. Home at last: neural stem cell niches defined. Cell Stem Cell. 2009 Jun 5;4(6):507–10. doi:10.1016/j.stem.2009.05.008.

12. Gage FH. Mammalian neural stem cells. Science. 2000 Feb 25;287:1433–8. doi: 10.1126/science.287.5457.1433.
13. Taylor G, Lehrer MS, Jensen PJ, Sun TT, Lavker RM. Involvement of follicular stem cells in forming not only the follicle but also the epidermis. Cell. 2000 Aug 18;102(4):451–61. doi:10.1016/S0092-8674(00)00050-7.
14. Gambardella L, Barrandon Y. The multifaceted adult epidermal stem cell. Curr Opin Cell Biol. 2003 Dec;15(6):771–7. doi:10.1016/j.ceb.2003.10.011.
15. Tumbar T, Guasch G, Greco V, Blanpain C, Lowry WE, Rendl M, et al. Defining the epithelial stem cell niche in skin. Science. 2004 Jan16;303(5656):359–63. doi: 10.1126/science.1092436.
16. Fuchs E. Skin stem cells: rising to the surface. J Cell Biol. 2008 Jan 28;180(2):273–84. doi: 10.1083/jcb.200708185
17. Boonen KJM, Post MJ. The muscle stem cell niche: regulation of satellite cells during regeneration. Tissue Eng Part B Rev. 2008 Dec;14(4):419–31. doi:10.1089/ten.teb.2008.0045.
18. Kuang S, Gillespie MA, Rudnicki MA. Niche regulation of muscle satellite cell self-renewal and differentiation. Cell Stem Cell. 2008 Jan 10;2(1):22–31. doi:10.1016/j.stem.2007.12.012.
19. Yin H, Price F, Rudnicki MA. Satellite cells and the muscle stem cell niche. Physiol Rev. 2013 Jan;93(1):23–67. doi:10.1152/physrev.00043.2011.
20. Takeda N, Jain R, LeBoeuf MR, Wang Q, Lu MM, Epstein JA. Interconversion between intestinal stem cell populations in distinct niches. Science. 2011 Dec 9;334(6061):1420–4. doi:10.1126/science.1213214.
21. Barker N. Adult intestinal stem cells: critical drivers of epithelial homeostasis and regeneration. Nat Rev Mol Cell Biol. 2014;15:19–33. doi:10.1038/nrm3721.
22. Clevers H. The intestinal crypt, a prototype stem cell compartment. Cell. 2013 Jul 18;154(2):274–84. doi: 10.1016/j.cell.2013.07.004.
23. Scadden DT. The stem-cell niche as an entity of action. Nature. 2006 Jun 29;441(7097):1075–9. doi:10.1038/nature04957.
24. Spradling A, Drummond-Barbosa D, Kai T. Stem cells find their niche. Nature. 2001 Nov 1;414: 98-104. doi:10.1038/35102160.
25. Moore KA, Lemischka IR. Stem cells and their niches. Science. 2006 Mar 31;311(5769):1880–5. doi:10.1126/science.1110542
26. Jones DL, Wagers AJ. No place like home: anatomy and function of the stem cell niche. Nat Rev Mol Cell Biol. 2008 Jan;9(1):11–21. doi:10.1038/nrm2319.
27. Discher DE, Mooney DJ, Zandstra PW. Growth factors, matrices, and forces combine and control stem cells. Science. 2009 Jun 26;324(5935):1673–7. doi:10.1126/science.1171643.
28. Gattazzo F, Urciuolo A, Bonaldo P. Extracellular matrix: A dynamic microenvironment for stem cell niche. Biochim Biophys Acta. 2014 Aug;1840(8):2506–19. doi:10.1016/j.bbagen.2014.01.010.
29. Khetan S, Guvendiren M, Legant WR, Cohen DM, Chen CS, Burdick JA. Degradation-mediated cellular traction directs stem cell fate in covalently crosslinked three-dimensional hydrogels. Nat Mater. 2013 May;12(5):458–65. doi:10.1038/nmat3586.
30. Vincent LG, Engler AJ. Stem cell differentiation: post-degradation forces kick in. Nat Mater. 2013 May;12(5):384–6. doi:10.1038/nmat3636.

31. Rozario T, DeSimone DW. The extracellular matrix in development and morphogenesis: a dynamic view. Dev Biol. 2010 May 1;341(1):126–40. doi:10.1016/j.ydbio.2009.10.026.
32. Tibbitt MW, Anseth KS. Dynamic microenvironments: the fourth dimension. Sci Transl Med. 2012 Nov 14;4(160):160ps24. doi:10.1126/scitranslmed.3004804.
33. Engler AJ, Sen S, Sweeney HL, Discher DE. Matrix elasticity directs stem cell lineage specification. Cell. 2006 Aug 25;126(4):677–89. doi:10.1016/j.cell.2006.06.044.
34. Tam RY, Owen SC, Shoichet MS. ECM-inspired chemical cues: biomimetic molecules and techniques of immobilization. In: Brennan AB, Kirschner CM, editors. Bio-inspired materials for biomedical engineering. Hoboken, NJ: John Wiley & Sons, Inc.; 2014. p. 7-24.
35. Li ACY, Thompson RPH. Basement membrane components. J Clin Pathol. 2003 Dec; 56(12): 885–887.
36. Potten CS, Booth C, Pritchard DM. The intestinal epithelial stem cell: the mucosal governor. Int J Exp Path.1997;78:219–43. doi :10.1046/j.1365-2613.1997.280362.x.
37. Kazanis I, Lathia J, Moss L, ffrench-Constant C. The neural stem cell microenvironment. StemBook, ed. The Stem Cell Research Community, StemBook. 2008 Aug 31;1–26. http://www.stembook.org.
38. Marthiens V, Kazanis I, Moss L, Long K, ffrench-Constant C. Adhesion molecules in the stem cell niche--more than just staying in shape? J Cell Sci. 2010 May 15;123:1613–22. doi:10.1242/jcs.054312.
39. Campos LS, Decker L, Taylor V, Skarnes W. Notch, epidermal growth factor receptor, and beta1-integrin pathways are coordinated in neural stem cells. J Biol Chem. 2006 Feb 24;281(8):5300–9. doi:10.1074/jbc.M511886200.
40. Xiao Q, Zeng L, Zhang Z, Hu Y, Xu Q. Stem cell-derived Sca-1+ progenitors differentiate into smooth muscle cells, which is mediated by collagen IV-integrin alpha1/beta1/alphav and PDGF receptor pathways. Am J Physiol Cell Physiol. 2007 Jan;292(1):C342–52. doi:10.1152/ajpcell.00341.2006.
41. Dalby MJ, Gadegaard N, Oreffo ROC. Harnessing nanotopography and integrin-matrix interactions to influence stem cell fate. Nat Mater. 2014 Jun;13(6):558–69. doi:10.1038/nmat3980.
42. Geiger B, Spatz JP, Bershadsky AD. Environmental sensing through focal adhesions. Nat Rev Mol Cell Biol. 2009 Jan;10(1):21–33. doi:10.1038/nrm2593.
43. Guilluy C, Osborne LD, Van Landeghem L, Sharek L, Superfine R, Garcia-Mata R, et al. Isolated nuclei adapt to force and reveal a mechanotransduction pathway in the nucleus. Nat Cell Biol. 2014 Mar 9;16(4):376–81. doi:10.1038/ncb2927.
44. Ross RS. Molecular and mechanical synergy: cross-talk between integrins and growth factor receptors. Cardiovasc Res. 2004 Aug 15;63(3):381–90. doi:10.1016/j.cardiores.2004.04.027.
45. Watt FM, Huck WTS. Role of the extracellular matrix in regulating stem cell fate. Nat Rev Mol Cell Biol. 2013 Aug;14(8):467–73. doi:10.1038/nrm3620.
46. Dupont S, Morsut L, Aragona M, Enzo E, Giulitti S, Cordenonsi M, et al. Role of YAP/TAZ in mechanotransduction. Nature. 2011 Jun 9;474(7350):179–83. doi: 10.1038/nature10137.
47. Zhang J, Niu C, Ye L, Huang H, He X, Harris S, et al. Identification of the haematopoietic stem cell niche and control of the niche size. Nature. 2003 Oct 23;425:836–41. doi:10.1038/nature02041.

48. Fuchs E, Tumbar T, Guasch G. Socializing with the neighbors: stem cells and their niche. Cell. 2004 Mar 19;116(6):769–78. doi:10.1016/S0092-8674(04)00255-7.
49. Long KR, ffrench-Constant C. Neural stem cell quiescence comes to an un-sticky end. Nat Cell Biol. 2014 Jul 1;16(7):625–7. doi:10.1038/ncb3003.
50. Brzoska E, Ciemerych MA, Przewozniak M, Zimowska M. Regulation of muscle stem cells activation: the role of growth factors and extracellular matrix. Vitam Horm. 2011 Jan;87:239-76. doi:10.1016/B978-0-12-386015-6.00031-7.
51. Reilly GC, Engler AJ. Intrinsic extracellular matrix properties regulate stem cell differentiation. J Biomech. 2010 Jan 5;43(1):55–62. doi:10.1016/j.jbiomech.2009.09.009.
52. Rodda AE, Meagher L, Nisbet DR, Forsythe JS. Specific control of cell–material interactions: Targeting cell receptors using ligand-functionalized polymer substrates. Prog Polym Sci. 2014 Jul;39(7):1312–47. doi: 10.1016/j.progpolymsci.2013.11.006.
53. Kim S-H, Turnbull J, Guimond S. Extracellular matrix and cell signaling: the dynamic cooperation of integrin, proteoglycan and growth factor receptor. J Endocrinol. 2011 May;209(2):139–51. doi: 10.1530/JOE-10-0377.
54. Zhu J, Clark R a F. Fibronectin at select sites binds multiple growth factors and enhances their activity: expansion of the collaborative ECM-GF paradigm. J Invest Dermatol. 2014 Apr;134(4):895–901. doi: 10.1038/jid.2013.484.
55. Hudalla GA, Murphy WL. Biomaterials that regulate growth factor activity via bioinspired interactions. Adv Funct Mater. 2001 May 24;21(10):1754-1768. doi:10.1002/adfm.201002468.
56. Turnbull J, Powell A, Guimond S. Heparan sulfate: decoding a dynamic multifunctional cell regulator. Trends Cell Biol. 2001 Feb;11(2):75–82. doi:10.1016/S0962-8924(00)01897-3.
57. Sarrazin S, Lamanna WC, Esko JD. Heparan sulfate proteoglycans. Cold Spring Harb Perspect Biol. 2011 Jul;3(7):1-33. doi: 10.1101/cshperspect.a004952.
58. Conway A, Schaff DV. Biophysical regulation of stem cell behavior within the niche. Stem Cell Res Ther. 2012; 3(6):50. doi: 10.1186/scrt141.
59. Bishop JR, Schuksz M, Esko JD. Heparan sulphate proteoglycans fine-tune mammalian physiology. Nature. 2007 Apr 26;446(7139):1030–7. doi:10.1038/nature05817.
60. Guilak F, Cohen DM, Estes BT, Gimble JM, Liedtke W, Chen CS. Control of stem cell fate by physical interactions with the extracellular matrix. Cell Stem Cell. 2009 Jul 2;5(1):17–26. doi:10.1016/j.stem.2009.06.016.
61. Mendes PM. Cellular nanotechnology: making biological interfaces smarter. Chem Soc Rev. 2013 Dec 21;42(24):9207–18. doi:10.1039/c3cs60198f.
62. Tsimbouri P, Gadegaard N, Burgess K, White K, Reynolds P, Herzyk P, et al. Nanotopographical effects on mesenchymal stem cell morphology and phenotype. J Cell Biochem. 2014 Feb;115(2):380–90. doi:10.1002/jcb.24673.
63. Ahn EH, Kim Y, Kshitiz, An SS, Afzal J, Lee S, et al. Spatial control of adult stem cell fate using nanotopographic cues. Biomaterials. 2014 Mar;35(8):2401–10. doi:10.1016/j.biomaterials.2013.11.037.
64. Motemani Y, Greulich C, Khare C, Lopian M, Buenconsejo PJS, Schildhauer TA, et al. Adherence of human mesenchymal stem cells on Ti and TiO2 nano-columnar surfaces fabricated by glancing angle sputter deposition. Appl Surf Sci. 2014 Feb 15;292:626–31. doi: 10.1016/j.apsusc.2013.12.022.

65. Fu J, Wang YK, Yang MT, Desai RA, Yu X, Liu Z, et al. Mechanical regulation of cell function with geometrically modulated elastomeric substrates. Nat Methods. 2010 Sept; 7(9):733-739. doi: 10.1038/nmeth.1487.
66. Béduer A, Vieu C, Arnauduc F, Sol J-C, Loubinoux I, Vaysse L. Engineering of adult human neural stem cells differentiation through surface micropatterning. Biomaterials. 2012 Jan;33(2):504–14. doi: 10.1016/j.biomaterials.2011.09.073.
67. Recknor JB, Sakaguchi DS, Mallapragada SK. Directed growth and selective differentiation of neural progenitor cells on micropatterned polymer substrates. Biomaterials. 2006 Aug;27(22):4098–108. doi: 10.1016/j.biomaterials.2006.03.029.
68. Christopherson GT, Song H, Mao H-Q. The influence of fiber diameter of electrospun substrates on neural stem cell differentiation and proliferation. Biomaterials. 2009 Feb;30(4):556–64. doi: 10.1016/j.biomaterials.2008.10.004.
69. Kawano T, Sato M, Yabu H, Shimomura M. Honeycomb-shaped surface topography induces differentiation of human mesenchymal stem cells (hMSCs): uniform porous polymer scaffolds prepared by the breath figure technique. Biomater Sci. 2014;2(1):52. doi: 10.1039/C3BM60195A.
70. Oh S, Brammer KS, Li YSJ, Teng D, Engler AJ, Chien S, et al. Stem cell fate dictated solely by altered nanotube dimension. Proc Natl Acad Sci U S A. 2009 Feb 17;106(7):2130–5. doi: 10.1073/pnas.0813200106.
71. Das RK, Zouani OF, Labrugère C, Oda R, Durrieu MC. Influence of nanohelical shape and periodicity on stem cell fate. ACS Nano. 2013 Apr 23;7(4):3351–61. doi: 10.1021/nn4001325.
72. Yim EKF, Ankam S, Moe AAK, Chan LYT. Effect of spatial arrangement of substrate topography on neuronal differentiation of stem cells. The 15th International Conference on Biomedical Engineering IFMBE Proceedings. Goh J, editor. Cham: Springer International Publishing. 2014;43:60–3. doi: 10.1007/978-3-319-02913-9_16.
73. Singhvi R, Kumar A, Lopez GP, Stephanopoulos GN, Wang DI, Whitesides GM, et al. Engineering cell shape and function. Science. 1994;264(5159):696-8. doi: 10.1126/science.8171320.
74. Xia Y, Whitesides GM. Soft lithography. Annu Rev Mater Sci. 1998; 28:153-84. doi: 10.1146/annurev.matsci.28.1.153.
75. Whitesides GM, Ostuni E, Takayama S, Jian X, Ingber DE. Soft lithography in biology and biochemistry. Annu Rev Biomed Eng. Aug 2001; 3:335-373. doi: 10.1146/annurev.bioeng.3.1.335.
76. McBeath R, Pirone DM, Nelson CM, Bhadriraju K, Chen CS. Cell shape, cytoskeletal tension, and rhoA regulate stem cell lineage commitment. Dev Cell. 2004 Apr;6(4):483–95. doi: 10.1016/S1534-5807(04)00075-9.
77. Peng R, Yao X, Ding J. Effect of cell anisotropy on differentiation of stem cells on micropatterned surfaces through the controlled single cell adhesion. Biomaterials. 2011 Nov;32(32):8048–57. doi: 10.1016/j.biomaterials.2011.07.035.
78. Kilian KA, Bugarija B, Lahn BT, Mrksich M. Geometric cues for directing the differentiation of mesenchymal stem cells. Proc Natl Acad Sci U S A. 2010 Mar 16;107(11):4872–7. doi: 10.1073/pnas.0903269107.
79. Connelly JT, Gautrot JE, Trappmann B, Tan DW-M, Donati G, Huck WTS, et al. Actin and serum response factor transduce physical cues from the microenvironment to regulate

epidermal stem cell fate decisions. Nat Cell Biol. 2010 Jul;12(7):711–8. doi: 10.1038/ncb2074.

80. DeForest CA, Anseth KS. Advances in bioactive hydrogels to probe and direct cell fate. Annu Rev Chem Biomol Eng. 2012 Jan;3:421–44. doi: 10.1146/annurev-chembioeng-062011-080945.
81. Saha K, Irwin EF, Kozhukuh J, Schaffer D, Healy KE. Biomimetic interfacial interpenetrating polymer networks control neural stem cell behavior. J Biomed Mater Res A. 2007 Apr; 81(1):240-9. doi: 10.1002/jbm.a.30986.
82. Lutolf MP, Hubbell JA. Synthetic biomaterials as instructive extracellular microenvironments for morphogenesis in tissue engineering. Nat Biotechnol. 2005;23(1):47–55. doi: 10.1038/nbt1055.
83. Rice JJ, Martino MM, De Laporte L, Tortelli F, Briquez PS, Hubbell JA. Engineering the regenerative microenvironment with biomaterials. Advanced Healthcare Materials. 2013; 2(1):57–71. doi: 10.1002/adhm.201200197.
84. Lutolf MP, Gilbert PM, Blau HM. Designing materials to direct stem-cell fate. Nature. 2009 Nov 26;462(7272):433–41. doi: 10.1038/nature08602.
85. Jongpaiboonkit L, King WJ, Murphy WL. Screening for 3D environments that support human mesenchymal stem cell viability using hydrogel arrays. Tissue Eng Part A. 2009 Feb;15(2):343–53. doi: 10.1089/ten.tea.2008.0096.
86. Marklein RA, Soranno DE, Burdick JA. Magnitude and presentation of mechanical signals influence adult stem cell behavior in 3-dimensional macroporous hydrogels. Soft Matter. 2012;8(31):8113-20. doi: 10.1039/C2SM25501D.
87. Salinas CN, Anseth KS. The influence of the RGD peptide motif and its contextual presentation in PEG gels on human mesenchymal stem cell viability. J Tissue Eng Regen Med. 2008 Jul;2(5):296–304. doi: 10.1002/term.95.
88. Maheshwari G, Brown G, Lauffenburger DA, Wells A, Griffith LG. Cell adhesion and motility depend on nanoscale RGD clustering. J Cell Sci. 2000 May; 113 (Pt 10): 1677–86.
89. Lam J, Segura T. The modulation of MSC integrin expression by RGD presentation. Biomaterials. 2013 May;34(16):3938–47. doi: 10.1016/j.biomaterials.2013.01.091.
90. Wang X, Yan C, Ye K, He Y, Li Z, Ding J. Effect of RGD nanospacing on differentiation of stem cells. Biomaterials. 2013 Apr;34(12):2865–74. doi: 10.1016/j.biomaterials.2013.01.021.
91. Battista S, Guarnieri D, Borselli C, Zeppetelli S, Borzacchiello A, Mayol L, et al. The effect of matrix composition of 3D constructs on embryonic stem cell differentiation. Biomaterials. 2005 Nov;26(31):6194–207. doi: 10.1016/j.biomaterials.2005.04.003.
92. Flaim CJ, Chien S, Bhatia SN. An extracellular matrix microarray for probing cellular differentiation. Nat Methods. 2005 Feb;2(2):119–25. doi: 10.1038/nmeth736.
93. Gilbert PM, Havenstrite KL, Magnusson KEG, Sacco A, Leonardi NA, Kraft P, et al. Substrate elasticity regulates skeletal muscle stem cell self-renewal in culture. Science. 2010 Aug 27;329(5995):1078-1081. doi: 10.1126/science.1191035.
94. Saha K, Kim J, Irwin E, Yoon J, Momin F, Trujillo V, et al. Surface creasing instability of soft polyacrylamide cell culture substrates. Biophy J. 2010 Dec 15;99(12):L94-6. doi: 10.1016/j.bpj.2010.09.045.

95. Kshitiz, Park J, Kim P, Helen W, Engler AJ, Levchenko A, et al. Control of stem cell fate and function by engineering physical microenvironments. Integ Biol (Camb). 2012 Sep;4(9):1008–18.
96. Higuchi A, Ling QD, Kumar SS, Chang Y, Kao TC, Munusamy MA, et al. External stimulus-responsive biomaterials designed for the culture and differentiation of ES, iPS, and adult stem cells. Prog Polym Sci. 2014 May;39(9):1585–613. doi: 10.1016/j.progpolymsci.2014.05.001.
97. Le DM, Kulangara K, Adler AF, Leong KW, Ashby VS. Dynamic topographical control of mesenchymal stem cells by culture on responsive poly(ε-caprolactone) surfaces. Adv Mater. 2011 Aug 2;23(29):3278–83. doi: 10.1002/adma.201100821.
98. Davis KA, Burke KA, Mather PT, Henderson JH. Dynamic cell behavior on shape memory polymer substrates. Biomaterials. 2011 Mar;32(9):2285–93. doi: 10.1016/j.biomaterials.2010.12.006.
99. Gong T, Zhao K, Yang G, Li J, Chen H, Chen Y, et al. The control of mesenchymal stem cell differentiation using dynamically tunable surface microgrooves. Adv Healthc Mater. 2014 Mar 20;1–12. doi: 10.1002/adhm.201300692.
100. Tseng LF, Mather PT, Henderson JH. Shape-memory-actuated change in scaffold fiber alignment directs stem cell morphology. Acta Biomater. 2013 Nov;9(11):8790–801. doi: 10.1016/j.actbio.2013.06.043.
101. Guvendiren M, Burdick JA. Stem cell response to spatially and temporally displayed and reversible surface topography. Adv Healthc Mater. 2013 Jan;2(1):155–64. doi: 10.1002/adhm.201200105.
102. Kirschner CM, Anseth KS. In situ control of cell substrate microtopographies using photolabile hydrogels. Small. 2013 Feb 25;9(4):578–84. doi: 10.1002/smll.201201841.
103. Yang C, Tibbitt MW, Basta L, Anseth KS. Mechanical memory and dosing influence stem cell fate. Nat Mater. 2014 Jun;13(6):645–52. doi: 10.1038/nmat3889.
104. Guvendiren M, Burdick JA. Stiffening hydrogels to probe short- and long-term cellular responses to dynamic mechanics. Nat Commun. 2012 Jan;3:792. doi: 10.1038/ncomms1792.
105. Yoshikawa HY, Rossetti FF, Kaufmann S, Kaindl T, Madsen J, Engel U, et al. Quantitative evaluation of mechanosensing of cells on dynamically tunable hydrogels. J Am Chem Soc. 2011 Feb 9;133(5):1367–74. doi: 10.1021/ja1060615.
106. Weis S, Lee TT, del Campo A, García AJ. Dynamic cell-adhesive microenvironments and their effect on myogenic differentiation. Acta Biomater. 2013 Sep;9(9):8059–66. doi: 10.1016/j.actbio.2013.06.019.
107. Kloxin AM, Tibbitt MW, Anseth KS. Synthesis of photodegradable hydrogels as dynamically tunable cell culture platforms. Nat Protoc. 2010 Dec;5(12):1867-87. doi: 10.1038/nprot.2010.139.
108. Kasten A, Müller P, Bulnheim U, Groll J, Bruellhoff K, Beck U, et al. Mechanical integrin stress and magnetic forces induce biological responses in mesenchymal stem cells which depend on environmental factors. J Cell Biochem. 2010 Dec 15;111(6):1586–97. doi: 10.1002/jcb.22890.
109. Wang N, Butler JP, Ingber DE. Mechanotransduction across the cell surface and through the cytoskeleton. Science. 1993 May 21;260(5111):1124-1127.
110. Rezza A, Sennett R, Rendl M. Adult stem cell niches: cellular and molecular components. Curr Top Dev Bio. 2014;107:333-72. doi: 10.1016/B978-0-12-416022-4.00012-3.

111. Ohlstein B, Kai T, Decotto E, Spradling A. The stem cell niche: theme and variations. Curr Opin Cell Biol. 2004 Dec;16(6):693–9. doi:10.1016/j.ceb.2004.09.003.

112. Xie T. A niche maintaining germ line stem cells in the Drosophila ovary. Science. 2000 Oct 13;290(5490):328–30. doi:10.1126/science.290.5490.328.

113. Yamashita YM, Fuller MT, Jones DL. Signaling in stem cell niches: lessons from the Drosophila germline. J Cell Sci. 2005 Feb 15;118(Pt 4):665–72. doi:10.1242/jcs.01680.

114. Fuller MT, Spradling AC. Male and female Drosophila germline stem cells: two versions of immortality. Science. 2007 Apr 20;316(5823):402–4. doi:10.1126/science.114086.

115. Jones DL, Wagers AJ. No place like home: anatomy and function of the stem cell niche. Nat Rev Mol Cell Biol. 2008 Jan;9(1):11–21. doi:10.1038/nrm2319.

116. Losick VP, Morris LX, Fox DT, Spradling A. Drosophila stem cell niches: a decade of discovery suggests a unified view of stem cell regulation. Dev Cell. 2011 Jul 19;21(1):159–71. doi:10.1016/j.devcel.2011.06.018.

117. Miller FD, Gauthier-Fisher A. Home at last: neural stem cell niches defined. Cell Stem Cell. 2009 Jun 5;4(6):507–10. doi:10.1016/j.stem.2009.05.008.

118. Tumbar T, Fuchs E. Epithelial hair follicle stem cells. In: Lanza R, Gearhart J, Hogan B, Melton D, Pedersen R, Thomas ED, et al, editors. 2nd ed. Essentials of stem cell biology. London: Academic; 2009. p. 189-97.

119. Jin K, Zhu Y, Sun Y, Mao XO, Xie L, Greenberg DA. Vascular endothelial growth factor (VEGF) stimulates neurogenesis in vitro and in vivo. Proc Natl Acad Sci U S A. 2002 Sep 3;99(18):11946–50. doi:10.1073/pnas.182296499.

120. Shen Q, Wang Y, Kokovay E, Lin G, Chuang SM, Goderie SK, et al. Adult SVZ stem cells lie in a vascular niche: a quantitative analysis of niche cell-cell interactions. Cell Stem Cell. 2008 Sep 11;3(3):289–300. doi:10.1016/j.stem.2008.07.026.

121. Porlan E, Perez-Villalba A, Delgado AC, Ferrón SR. Paracrine regulation of neural stem cells in the subependymal zone. Arch Biochem Biophys. 2013 Jun;534(1-2):11–9. doi:10.1016/j.abb.2012.10.001.

122. Leventhal C, Rafii S, Rafii D, Shahar A, Goldman SA. Endothelial trophic support of neuronal production and recruitment from the adult mammalian subependyma. 1999;464:450–64. doi:10.1006/mcne.1999.0762.

123. Bath KG, Akins MR, Lee FS. BDNF control of adult SVZ neurogenesis. Dev Psychobiol. 2012 Sep;54(6):578–89. doi:10.1002/dev.20546.

124. Ramírez-Castillejo C, Sánchez-Sánchez F, Andreu-Agulló C, Ferrón SR, Aroca-Aguilar JD, Sánchez P, et al. Pigment epithelium-derived factor is a niche signal for neural stem cell renewal. Nat Neurosci. 2006 Mar; 9(3):331–9. doi: 10.1038/nn1657.

125. Holmberg J, Genander M, Halford MM, Annerén C, Sondell M, Chumley MJ, et al. EphB receptors coordinate migration and proliferation in the intestinal stem cell niche. Cell. 2006 Jun 16;125(6):1151–63. doi:10.1016/j.cell.2006.04.030.

126. Genander M, Frisén J. Ephrins and Eph receptors in stem cells and cancer. Curr Opin Cell Biol. 2010 Oct;22(5):611–6. doi:10.1016/j.ceb.2010.08.005.

127. Ashton RS, Conway A, Pangarkar C, Bergen J, Lim K-I, Shah P, et al. Astrocytes regulate adult hippocampal neurogenesis through ephrin-B signaling. Nat Neurosci. 2012 Oct;15(10):1399–406. doi: 10.1038/nn.3212.

128. Koch U, Lehal R, Radtke F. Stem cells living with a Notch. Development. 2013 Feb;140(4):689–704. doi:10.1242/dev.080614.

129. Breunig JJ, Silbereis J, Vaccarino FM, Sestan N, Rakic P. Notch regulates cell fate and dendrite morphology of newborn neurons in the postnatal dentate gyrus. Proc Natl Acad Sci U S A. 2007 Dec 18;104(51):20558-63. doi: 10.1073/pnas.0710156104.
130. Ehm O, Goritz C, Covic M, Schaffner I, Schwarz TJ, Karaca E et al. RBPJk-dependent signaling is essential for long-term maintenance of neural stem cells in the adult hippocampus. J Neurosci. 2010 Octo 13; 30(41):13794-807. doi: 10.1523/JNEUROSCI.1567-10.2010.
131. Ables JL, Breunig JJ, Eisch AJ, Rakic P. Not(ch) just development: Notch signaling in the adult brain. Nat Rev Neurosci. 2011 May; 12(5): 269-283. doi: 10.1038/nrn3024.
132. Gaiano N, Fishell G. The role of notch in promoting glial and neural stem cell fates. Annu Rev Neurosci. 2002; 25:471-90. doi: 10.1146/annurev.neuro.25.030702.130823.
133. Bjornson CR, Cheung TH, Liu L, Tripathi PV, Steeper KM, Rando TA. Notch signaling is necessary to maintain quiescence in adult muscle stem cells. Stem Cells. 2012 Feb;30(2):232-242. doi: 10.1002/stem.773.
134. Rosenthal A, Macdonald A, Voldman J. Cell patterning chip for controlling the stem cell microenvironment. Biomaterials. 2007 Jul;28(21):3208–16. doi: 10.1016/j.biomaterials.2007.03.023.
135. Ottone C, Krusche B, Whitby A, Clements M, Quadrato G, Pitulescu ME, et al. Direct cell – cell contact with the vascular niche maintains quiescent neural stem cells. Nat Cell Biol. 2014 Nov;16(11):1045-1056. doi: 10.1038/ncb3045.
136. Song H, Stevens CF, Gage FH. Astroglia induce neurogenesis from adult neural stem cells. Nature. 2002 May 2;417(6884):39–44. doi: 10.1038/417039a.
137. Loibl M, Binder A, Herrmann M, Duttenhoefer F, Richards RG, Nerlich M, et al. Direct cell-cell contact between mesenchymal stem cells and endothelial progenitor cells induces a pericyte-like phenotype in vitro. Biomed Res Int. 2014 Jan 20;2014:395781. doi: 10.1155/2014/395781.
138. Kaji H, Camci-Unal G, Langer R, Khademhosseini A. Engineering systems for the generation of patterned co-cultures for controlling cell-cell interactions. Biochim Biophys Acta. 2011 Mar;1810(3):239–50. doi: 10.1016/j.bbagen.2010.07.002.
139. Khademhosseini A, Suh KY, Yang JM, Eng G, Yeh J, Levenberg S, et al. Layer-by-layer deposition of hyaluronic acid and poly-L-lysine for patterned cell co-cultures. Biomaterials. 2004 Aug;25(17):3583–92. doi: 10.1016/j.biomaterials.2003.10.033.
140. Rodriguez NM, Desai RA, Trappmann B, Baker BM, Chen CS. Micropatterned multicolor dynamically adhesive substrates to control cell adhesion and multicellular organization. Langmuir. 2014 Feb 11;30(5):1327–35. doi: 10.1021/la404037s.
141. Fukuda J, Khademhosseini A, Yeh J, Eng G, Cheng J, Farokhzad OC, et al. Micropatterned cell co-cultures using layer-by-layer deposition of extracellular matrix components. Biomaterials. 2006 Mar;27(8):1479–86. doi: 10.1016/j.biomaterials.2005.09.015.
142. Wright D, Rajalingam B, Selvarasah S, Dokmeci MR, Khademhosseini A. Generation of static and dynamic patterned co-cultures using microfabricated parylene-C stencils. Lab Chip. 2007 Oct;7(10):1272–9. doi: 10.1039/B706081E.
143. Torisawa Y, Mosadegh B, Luker GD, Morell M. Microfluidic hydrodynamic cellular patterning for systematic formation of co-culture spheroids. Integr Biol (Camb). 2009 Dec;1(11-12):649-54. doi: 10.1039/b915965g.

144. Tumarkin E, Tzadu L, Csaszar E, Seo M, Zhang H, Lee A, et al. High-throughput combinatorial cell co-culture using microfluidics. Integr Biol (Camb). 2011 Jun;3(6):653–62. doi: 10.1039/c1ib00002k.
145. Bajaj P, Marchwiany D, Duarte C, Bashir R. Patterned three-dimensional encapsulation of embryonic stem cells using dielectrophoresis and stereolithography. Adv Healthc Mater. 2013 Mar;2(3):450–8. doi: 10.1002/adhm.201200318.
146. Martinez-Duarte R. Microfabrication technologies in dielectrophoresis applications – a review. Electrophoresis. 2012 Nov;33(21):3110–32. doi: 10.1002/elps.201200242.
147. Guo F, French JB, Li P, Zhao H, Chan CY, Fick JR, et al. Probing cell-cell communication with microfluidic devices. Lab Chip. 2013 Aug 21;13(16):3152–62. doi: 10.1039/c3lc90067c.
148. Chung BG, Flanagan LA, Rhee SW, Schwartz PH, Lee AP, Monuki ES, et al. Human neural stem cell growth and differentiation in a gradient-generating microfluidic device. Lab Chip. 2005 Apr;5(4):401–6. doi: 10.1039/B417651K.
149. Park JY, Kim SK, Woo DH, Lee EJ, Kim JH, Lee SH. Differentiation of neural progenitor cells in a microfluidic chip-generated cytokine gradient. Stem Cells. 2009 Nov;27(11):2646–54. doi: 10.1002/stem.202.
150. Blagovic K, Kim LY, Voldman J. Microfluidic perfusion for regulating diffusible signaling in stem cells. PLoS One. 2011;6(8):e22892. doi:10.1371/journal.pone.0022892.
151. Ellison D, Munden A, Levchenko A. Computational model and microfluidic platform for the investigation of paracrine and autocrine signaling in mouse embryonic stem cells. Mol Biosyst. 2009 Sep;5(9):1004–12. doi: 10.1039/b905602e.
152. Song X, Kong B, Li D. A new tool for probing of cell-cell communication: human embryonic germ cells inducing apoptosis of SKOV3 ovarian cancer cells on a microfluidic chip. Biotechnol Lett. 2008 Sep;30(9):1537–43. doi: 10.1007/s10529-008-9725-2.
153. Bogdanowicz DR, Lu HH. Multifunction co-culture model for evaluating cell – cell interactions. Methods Mol Biol. 2014;1202:29–36. doi: 10.1007/7651_2013_62.
154. Skelley AM, Kirak O, Suh H, Jaenisch R, Voldman J. Microfluidic control of cell pairing and fusion. Nat Methods. 2009 Feb;6(2):147–52. doi: 10.1038/nmeth.1290.
155. Hong S, Pan Q, Lee LP. Single-cell level co-culture platform for intercellular communication. Integr Biol (Camb). 2012 Apr;4(4):374–80. doi: 10.1039/c2ib00166g.
156. Dura B, Liu Y, Voldman J. Deformability-based microfluidic cell pairing and fusion. Lab Chip. 2014 Aug 7;14(15):2783–90. doi: 10.1039/c4lc00303a.
157. Frimat JP, Becker M, Chiang YY, Marggraf U, Janasek D, Hengstler JG, et al. A microfluidic array with cellular valving for single cell co-culture. Lab Chip. 2011 Jan 21;11(2):231–7. doi: 10.1039/c0lc00172d.
158. Roccio M, Gobaa S, Lutolf MP. High-throughput clonal analysis of neural stem cells in microarrayed artificial niches. Integr Biol (Camb). 2012 Apr;4(4):391–400. doi: 10.1039/c2ib00070a.
159. Ranga a, Gobaa S, Okawa Y, Mosiewicz K, Negro a, Lutolf MP. 3D niche microarrays for systems-level analyses of cell fate. Nat Commun. 2014 Jul;5:4324. doi: 10.1038/ncomms5324.
160. Taqvi S, Dixit L, Roy K. Biomaterial-based notch signaling for the differentiation of hematopoietic stem cells into T cells. J Biomed Mater Res A. 2006 Dec 1;79(3):689–97. doi: 10.1002/jbm.a.30916.

Chapter 2: Interrogating cellular fate decisions with high-throughput arrays of multiplexed cellular communities

This chapter is in part a postprint of a paper submitted to and accepted for publication as

Chen, S., Bremer, A.W., Scheideler, O.J., Na, Y.S., Todhunter, M.E., Hsiao, S., Bomdica, P.R., Maharbiz, M.M., Gartner, Z.J., Schaffer, D.V. Interrogating cellular fate decisions with high-throughput arrays of multiplexed cellular communities. Nature Communications 7, 10309 (2016).

2.1 Introduction

Networks of interacting cells regulate the biology and pathology of all mammalian tissues, including positive-negative selection in adaptive immune responses (*1*), tumor-stromal-vascular interactions during cancer progression (*2*), and stem cell-niche interactions during development and adulthood (*3*). Within these intercellular signaling networks, the relative number and spatial organization of diverse cell types contributes to the behavior of the system as a whole (*4*). The capacity to reconstitute *in vitro* these networks of interacting cells, or cell communities, would offer new insights into the logic and dynamics of collective cell-decision making.

The stem cell niche is an example of a cell community containing a diversity of interacting cells that orchestrate tissue development, maintenance, and repair (*3*). Within this milieu, spatially-restricted extracellular signals guide stem cell self-renewal and differentiation (*5*). These include juxtacrine signals that require cell-cell contact, lipoprotein ligands with limited diffusion, molecules that bind proteoglycans or matrix, and soluble close-range signals (*6, 7*). For example, adult neural stem cells (NSCs) (*8-10*) in the brain generate new neurons to modulate learning and memory, a process tightly regulated by a repertoire of neighboring cells (astrocytes, neurons, endothelial cells, etc.) that present a spectrum of signals (Eph-ephrin (*11*), Notch-Delta (*12*), Wnt (*13*), Shh (*14*), etc.). Elucidating the quantitative dynamics by which such disparate, local cues instruct sometimes mutually exclusive cell fate decisions would advance stem cell biology and regenerative medicine.

A number of methods have been developed to study networks of interacting cells. Trans-well and monolayer co-culture systems have yielded insights into intercellular signaling (*13, 15*), but in general they cannot control the stoichiometries or contact times of close-range cell-cell interactions, do not extend beyond two cell types, and do not permit the longitudinal study of precisely defined groups of cells. Microfluidic and micropatterned platforms (Chapter 1) offer improved throughput and the capacity for single-cell analysis but are typically inefficient and incapable of robust manipulation of more than two cell types at the single-cell level, and restrict cell motility and proliferation (*16, 17*).

To study communication within cellular communities with improved efficiency and resolution, we engineered a high-throughput, patterned co-culture platform and investigated the effects of close-range signaling interactions on single NSC fate decisions. Our system integrates four key design criteria: 1) positional control over single cells to study their heterogeneous behaviors (**single-cell resolution**); 2) the capacity to simultaneously pattern multiple cell types to examine the logic of cell-cell communication within a niche (**multiplexing)**; 3) longitudinal cell observation to reveal the dynamics of processes such as differentiation (**long-term lineage tracing)**; and 4) robust, scalable, reproducible system performance for statistical analysis (**large sample size)**.

With this DNA-based patterning platform, we demonstrate the unprecedented capability of reconstituting cellular communities comprised of up to four heterotypic cell types at high-throughput and with single-cell resolution. Moreover, we highlight the significantly improved efficiencies of this patterning technique over random Poisson loading as well as exhibit the strength of our system in manipulating cellular interactions by varying the initial position of patterned cell pairs, which translates to control over cell-cell contact. We then establish the promise of this platform by modeling and investigating complex cell signaling networks. Specifically, by patterning communities of NSCs with a niche cell that expresses the Notch ligand and another that expresses the Eph ligand, this platform enables us to dissect how NSCs resolve the simultaneous presentation of competing juxtacrine signals that promote different cell fates.

2.2 Results

2.2.1. DNA-Based Patterning Platform Overview

We fulfill the four design requirements mentioned above using a two-step patterning procedure. First, arrays of cell-adhesive "microislands" are generated on a non-adhesive background surface. Second, we prepare a programmably-adhesive substrate by printing short oligonucleotides within each microisland, which can capture multiple cell types that present complementary DNA strands temporarily tethered to their cell membranes. The result is a geometrically-organized, precisely-defined community of interacting cells for biological investigation (Figure 2.1).

2.2.2 Fabrication of Cell-Adhesive Microislands

In greater detail, to prepare cell-adhesive microislands, we harnessed ultraviolet-ozone (UVO) patterning to etch cell-adhesive microisland features into a non-adhesive polyhydroxyethylmethacrylate (polyHEMA) film coating an aldehyde-functionalized glass slide (Figure 2.1a). Unlike other non-fouling biomaterials, polyHEMA could be deposited as a thick film and was stable for at least 7 days (Figure 2.1b, Supplementary Figure 2.1). The resulting array of visible microislands (Figure 2.1d) obviated the need for alignment markers in subsequent printing steps, simplified image registration on consecutive days, and offered a means for lineage tracing. Importantly, these microislands restricted close-range cellular signals to confined communities, yet their size could be tuned to provide space for cell migration and division as needed.

2.2.3 DNA-Programmed Assembly for Heterotypic Cell Patterning

To generate a programmably-adhesive surface, we rely on DNA-programmed assembly (*18-20*), a technique wherein DNA oligonucleotides are chemically incorporated into cell membranes to allow "velcro"-like attachment to substrates functionalized with the complementary sequences. We use direct microscale writing of DNA strands within the adhesive microislands for single-cell capture (Figure 2.1c). We printed up to four orthogonal DNA sequences as cell-sized spots within each microisland (Figure 2.1d), but additional sequences would enable the capture of even more cell types. After stabilization of DNA to the surface by reductive amination (Figure 2.1c box), each cell type is modified with unique lipid-conjugated complementary oligonucleotides, addressing the cell type to a specific DNA spot in the array. Cells are then serially flowed over the surface within the confines of a polydimethylsiloxane (PDMS) flow cell. Intervening washes remove unbound cells to reveal cellular communities with precisely-defined composition and relative spacing (Figure 2.1e).

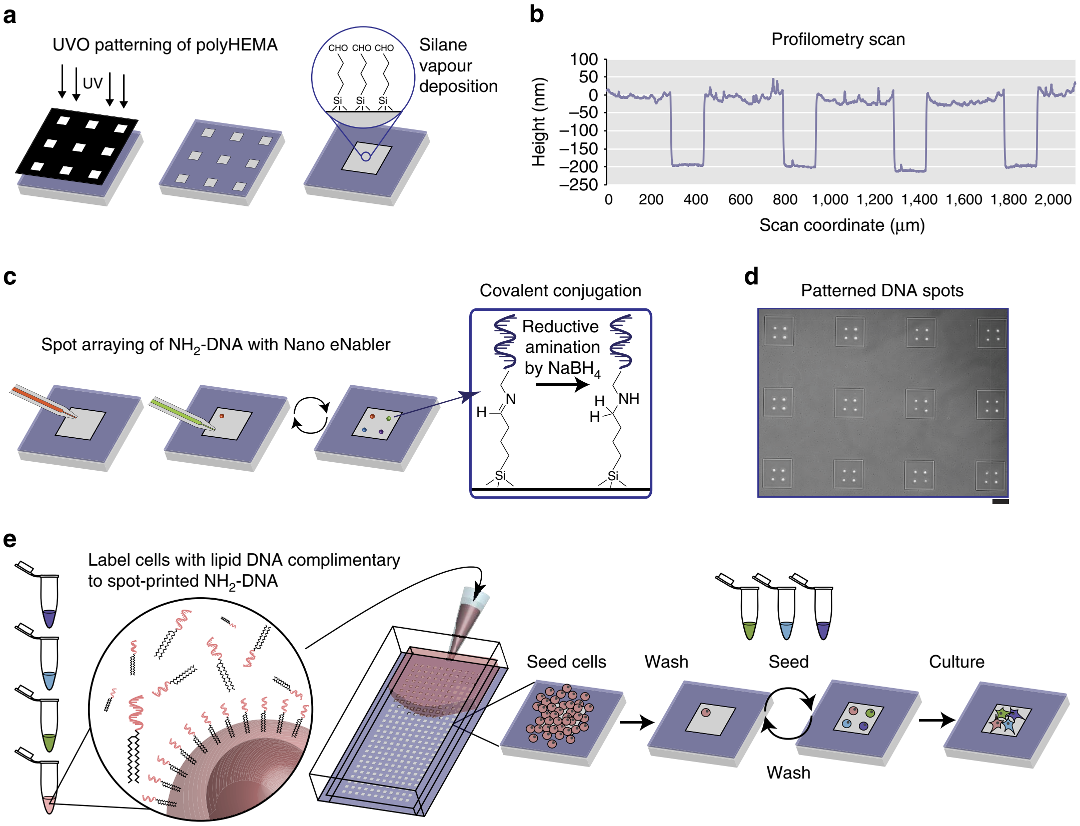

Figure 2.1 Two-step patterning process and single-cell tethering workflow. (a) Microisland patterns were produced by UVO (185 nm) patterning into thin polyHEMA coatings (<0.5 μm). An aldehyde-functionalized organic silane was then vapor deposited to prepare for DNA printing. (b) Profilometry measurements show representative microisland features of 200 nm. (c) Spot arraying of NH_2-terminated oligonucleotides within each microisland was performed using the Nano eNabler system. After arraying of single-cell sized spots, the entire slide underwent reductive amination using $NaBH_4$. (d) Representative image of four-component printed DNA patterns (scale bar: 100 μm). (e) Multiple cell populations are labeled with distinct DNA molecules presenting sequences complementary to the microisland DNA strands, washed, and passed through a PDMS flow cell affixed to the patterned slides either sequentially at a density of ~800,000 cells cm^{-2} or in mixed solutions at a density of ~400,000 cells cm^{-2}. Untethered cells are washed away, and the process is repeated for each cell type.

This method for building arrays of cellular communities provides tunable control over the number, identity, and initial placement of individual cells, along with the ability to define the size and shape of a community's spatial constraints (Figure 2.2). For example, altering the number of DNA spots printed within a microisland determines the number of cells within each community. Moreover, printing either identical or orthogonal DNA sequences – which are highly multiplexable due to the large number of orthogonal, 20-mer oligonucleotides – dictates the capture of cells from the same or different populations (Figure 2.2a). To demonstrate control over cell number and composition, we printed between one to four DNA sequences within each adhesive microisland. In parallel, we labeled four separate populations of MCF10A human mammary epithelial cells (each colored with a different cell tracker dye) with four complementary DNA strands, which addressed each population to the corresponding DNA spot within the microisland arrays (Figure 2.2a, 2.2b). Capture efficiencies were high, though occasional DNA spots neglected to capture a cell or captured more than one of the same cell-type. To enable quantitative comparison to standard Poisson loading used in microfluidic and micropatterned platforms, a single population – or a mixture of two, three, or all four cell populations – was seeded onto microislands lacking printed DNA at a low cell/surface area ratio (Supplementary Figure 2.2). In every case, loading efficiency was higher using DNA-programmed assembly, with improvements over Poisson loading exceeding an order of magnitude for seeding with two or more cell types (Figure 2.2c, 2.2d). For communities of four cell types, we achieved a nearly 25% yield compared to zero microislands seeded with the desired four cells for Poisson loading – at least a 195-fold improvement (Figure 2.2d).

2.2.4 Tunable Control of Cell-Cell Contact During Differentiation

In addition to controlling cell identities and numbers, altering the photomask used to etch polyHEMA during UVO patterning offers control over the size and shape of a community's spatial constraints (Figure 2.2e). Moreover, the initial position of each cell within the community can be controlled by precise placement of each DNA spot within the microislands, allowing geometric arrangement of cells with programmed cell-to-cell distances (Figure 2.2f). Control over these variables is important as spatial constraints determine the frequency and duration of cell-cell interactions – key determinants of cell fate decisions in the stem cell niche (*21*). To examine how patterning distances regulate cell-cell contact probability and duration (Figure 2.3a), we arrayed pairs of adult NSCs and primary astrocytes at intercellular distances ranging from 50 – 125 μm and conducted live imaging over 48 hours. Both the percentage of cell pairs that came into contact, as well as the total cell-cell contact time, increased the closer the NSC-astrocyte pairs were initially patterned (Figure 2.3b, 2.3c). In contrast, cells cultured without confinement in microislands – as would occur in standard co-cultures – experienced reduced interactions and often migrated away from one another (Supplementary Figures 2.3-2.5). These results demonstrate the advantage of this system to directly control cell-cell distances and confinement geometry, which lies in stark contrast to previously-reported high-throughput co-culture systems that cannot control these parameters simultaneously (*16,17,21*).

We next applied the platform to investigate NSC fate decisions in response to model niche cells. First, we compared NSC behavior when co-cultured with cortical astrocytes over 6 days under two conditions: in bulk co-culture or with single astrocytes in microisland arrays (Figure 2.3d, Supplementary Figure 2.6). Patterns of differentiation and proliferation were quantified by recording initial and final cell counts for each microisland (Figure 2.3d-f). Overall, NSCs exhibited greater neuronal differentiation (i.e. expression of beta-tubulin III, or Tuj1) after 6-day culture in microislands when compared to bulk co-cultures ($p < 0.05$, Student's t-test) (Figure 2.3e). This observation applied to bulk co-cultures having low cell density equivalent to the overall cell density across the entire patterned substrate surface area (500 cells cm^{-2}) and high cell density equivalent to cell density within each microisland (5000 cells cm^{-2}). Additionally, NSCs that underwent neuronal fate commitment proliferated to a greater extent than NSCs that developed into glial fibrillary acidic protein (GFAP)-positive astrocytes ($p = 8e^{-4}$, Student's t-test) (Figure 2.3f), an interesting phenomenon also observed *in vivo* (*22*).

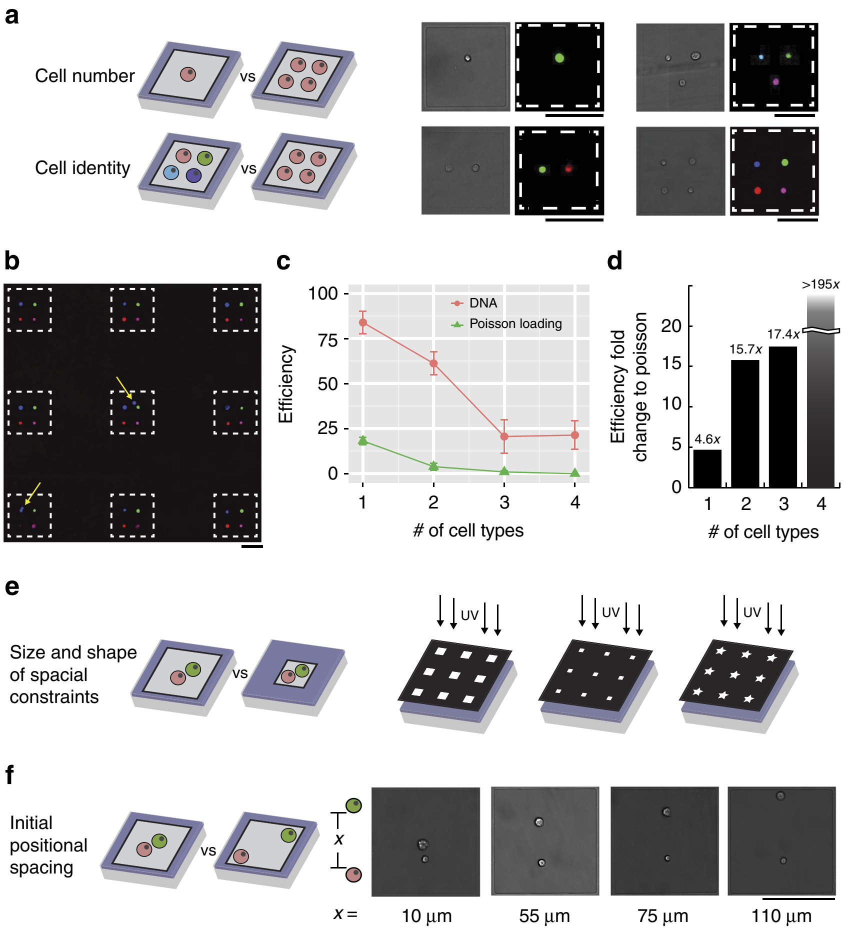

Figure 2.2 Customizable capabilities of two-step surface-patterning platform for modulating cellular interactions. (a) Both cell number and identity can be precisely controlled. (b) As an example of the latter, four MCF10A cell populations, each colored with a different dye, were labeled with distinct DNA strands and arrayed onto microislands printed with four of the complementary DNA oligonucleotides. Seven out of the 9 displayed microislands possessed the correct cellular community, with yellow arrows indicating microislands containing incorrect cellular components. (c) Using this DNA-based cell tethering, the efficiency of exact MCF10A cell patterning (red circles) was considerably higher than the same four cell populations plated at a low cell/surface ratio for random Poisson seeding (green triangles) of single-, double-, triple-, and quadruple-cell communities. (d) Efficiency, or fold improvement, of our DNA patterned compared to Poisson loaded arrays. (e) Variations to the microisland features for further modulation of cell-cell communication can be achieved by changing the size and shape of the photomask used during UV etching. (f) DNA printing enables precise control over the initial cell positions of NSC-astrocyte (bottom cell-top cell) pairs. All error bars are s.e.m. and n=4. All scale bars: 100 μm.

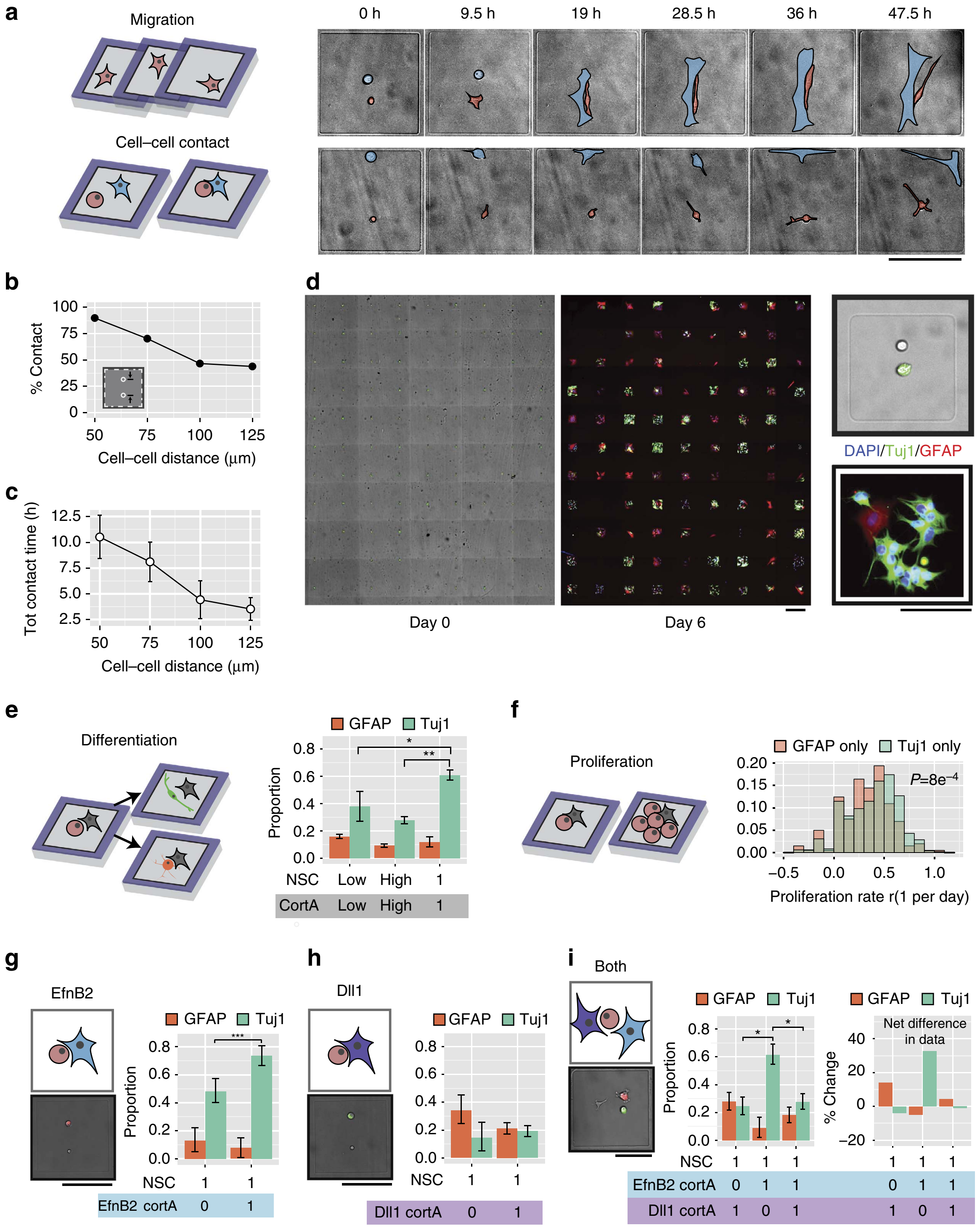

Figure 2.3 Arrays of cellular communities yield insights into cell dynamics and NSC differentiation, proliferation, and signal arbitration of opposing juxtacrine signals at the single-cell level. (a) Migration and cell-cell contact for each microisland can be tracked with timelapse microscopy. Representative 48-hr timelapse images illustrating the dynamics of two NSC-astrocyte pairs initially patterned at different separations. NSC highlighted in red, and astrocyte highlighted in blue. (b) Percent of cellular communities that showed contact increased as the initial distance separating NSC and astrocyte decreased. (c) Total contact times also increased as initial cell-cell distance

decreased. (d) Cell communities could be repeatedly imaged over long timescales with subsequent visualization of differentiation markers. Representative, stitched montages of NSCs (upper) and cortical astrocytes (lower, green) immediately after patterning (left), then upon immunostaining after 6 days for the neuronal marker Tuj1 and astrocyte marker GFAP (right). Higher magnification of a representative adhesive microisland shows that all progeny of this particular single NSC founder differentiated into Tuj1$^+$ neurons. (e) NSC differentiation can be tracked for each community. When patterned with single naïve astrocytes, NSCs exhibited enhanced Tuj1 differentiation and similar GFAP differentiation when compared to low-density and high-density bulk co-cultures. (f) Microisland confinement enabled analysis of proliferation rates. Proliferation rates (r) for Tuj1-biased lineages (lineages in which no GFAP cells were present) were higher than proliferation rates for GFAP-biased lineages ($p=8e^{-4}$). (g) NSCs patterned with a single hEfnB2-overexpressing astrocyte exhibited enhanced Tuj1$^+$ differentiation. (h) NSCs patterned with a single hDll1-overexpressing astrocyte displayed low Tuj1 expression. (i) When a single NSC was in the presence of both a Dll1-astrocyte and an EfnB2 astrocyte, the Dll1 phenotype (i.e. reduced Tuj1) dominated. The left graph represents immunostained proportions of NSCs in each condition, and the right graph depicts immunostaining changes compared to NSCs patterned 1:1 with a naïve cortical astrocyte. All error bars are 95% confidence intervals; all p values obtained from t-test. ***$p < 0.001$, **$p < 0.01$, *$p < 0.05$. All scale bars: 100 μm.

2.2.5 NSCs "listen" to Dll1 when Presented with Dll1 and EfnB2

In vivo, stem cells are exposed to conflicting signals that induce mutually-exclusive fate decisions. For example, Notch and Eph receptors play critical roles in mediating different cell fate decisions in the NSC niche. Notch signaling promotes the maintenance or self-renewal of early NSCs (*12,22*), and we recently discovered that the cell surface ligand ephrin-B2 (EfnB2) presented from neighboring astrocytes induces neuronal differentiation of NSCs (*11*). As both signals are presented to NSCs in the adult niche, they likely compete to regulate stem cell fate specification – a dynamic process that our system is ideally suited to investigate at the single-cell level. Therefore, we engineered primary cortical astrocytes as model niche cells to express either EfnB2 or Delta-like 1 (Dll1) translationally coupled to a nuclear-localized fluorescent protein (Supplementary Figures 2.7, 2.8).

We measured the distribution of cell fate decisions arising from NSCs patterned with EfnB2-astrocytes, Dll1-astrocytes, or both engineered cell types. Supplementary Table 2.1 provides a detailed overview of the density of events that we obtained for our different community compositions (n=44 for 1 NSC + 1 EfnB2, n=106 for 1 NSC + 1 Dll1, n=57 for 1 NSC + 1 EfnB2 + 1 Dll1). When NSCs were cultured alone with EfnB2-astrocytes, Tuj1 expression in NSCs increased, indicating a bias towards neuronal differentiation ($p < 0.001$, Student's t-test) (Figures 2.3g), and NSC proliferation rates decreased (Supplementary Figure 2.9), as anticipated based on our prior work (*11*). In contrast, Dll1-astrocytes biased NSCs towards low Tuj1 expression (Figures 2.3h), consistent with its role in maintaining stem cell identity (Supplementary Figure 2.10). In the presence of both EfnB2- and Dll1-expressing astrocytes, NSCs adopted the Dll1-responding phenotype of low Tuj1 expression ($p < 0.05$, Student's t-test) (Figure 2.3i). Analogously, the distributions of percent Tuj1+ cells island^{-1} and the total number of Tuj1$^+$ cells produced were similar when NSCs were cultured with an astrocyte expressing Dll1-alone or a Dll1 astrocyte plus an EfnB2 astrocyte (Supplementary Figure 2.11b). These results suggest that, in dynamic niche microenvironments, competing juxtacrine signals from Dll1 and EfnB2 may be interpreted by NSCs as a Dll1 signal.

2.3 Discussion

Here, we report an *in vitro* platform that tackles the shortcomings of current co-culture techniques and enables the investigation of more complex biological questions that address the role of cell-cell communication during NSC fate decisions. Using a combination of UV and DNA-based patterning, we establish a high-throughput system for generating multiplexed arrays of cellular communities having up to four cell types. These communities can be assembled with single-cell resolution and efficiencies at least 195-fold higher than practically achievable with Poisson loading. We demonstrate robust control over community composition with regards to cell number, identity, and positioning and apply the method to study NSC behavior and cell fate decisions in response to single and multiple signals presented from the surface of model niche cells. Our results reveal a potential signaling hierarchy between EfnB2 and Dll1 ligands during NSC differentiation.

In addition to exploring the effects of competing juxtacrine ligands, we anticipate that future applications of this technology include increasing the complexity of cellular communities by incorporating niche cell types that contribute other juxtacrine and/or paracrine signals, introducing patterned protein cues, expanding the platform to generate three-dimensional niches, and quantitative real-time analysis of signaling. Together, these various approaches will yield a more complete understanding of how the logic and dynamics of intercellular signaling networks regulate the collective behaviors of cellular communities.

2.4 Methods

Substrate Preparation

Slides were initially coated with polyHEMA to generate a non-adhesive, background surface within which adhesive features could be patterned. First, polyHEMA (Sigma) was dissolved in a sonicator for 1 hour at 10 mg mL^{-1} in 100% ethanol. 150 μL of polyHEMA solution was then drop casted onto Nexterion AL (Schott) slides and allowed to dry under a clean polystyrene dish lid to block dust and slow the drying process. Slow drying over 1 hour at room temperature was helpful in reducing ridges on the surface, resulting in a glossy and flat polyHEMA film. To create cell-adhesive microislands within the polyHEMA film, UVO patterning was performed using a custom quartz mask (Photosciences Inc) and a UV-Ozone cleaner (Jelight). The quartz mask contains four 19 x 15 grids of clear square features (either 141 x 141 μm or 200 x 200 μm) arranged with a 500 μm pitch – all of which are aligned within the spatial dimensions of a Millipore 4-well EZ slide. Similar to water purification techniques that employ UV light to reduce organic contaminants, this deep UV patterning technique is thought to act through 185 nm light interacting with water and dissolved oxygen to create highly reactive hydroxyl radicals within the liquid layer, which then attack the organic polymer (*23*). The very short half-life of these radicals ensures that only the clear square features are etched into the polyHEMA film. To achieve this patterning, the quartz mask was first cleaned using acetone and then irradiated in the UVO cleaner for 5 minutes at a distance of 5 cm to remove organic residues. A 160 uL drop of DI water was deposited across the chrome side of the mask, and the polyHEMA-coated side of the slide was lowered onto the wetted chrome surface slowly to avoid bubble formation. Water was necessary to provide an insulating layer from the ozone generated within the UVO machine. Excess water was pressed out gently and blotted off using a lint-free TexWipe. The mask-slide assembly was then inverted onto two small stands within the machine to prevent slipping of the slide relative to the mask. This results in the polyHEMA-coated slide facing upward with the chrome mask separating the slide from the UV source, controlling for the selective passing of the UV light. The slide was then illuminated for 5 minutes. Exposure times of less than 5 minutes resulted in an incomplete etch (Supplementary Figure 2.1b). After illumination, the slide was detached gently from the mask by flooding the surrounding area with DI water and using tweezers to slowly pull the slide up from the mask. The slide was then rinsed with DI water, dried under nitrogen gas, and immediately placed under vacuum. With the exception of the three- and four-component experiments, all experiments employed the smaller 141 μm square size.

Because the illumination may have scavenged the organic aldehyde groups originally present on the Schott Nexterion AL slide, we reconstituted the slide with trimethoxysilane aldehyde (UCT, PSX-1050) by chemical vapor deposition in a plastic vacuum chamber under house vacuum for 1 hour. Within this chamber, 100 μL of the silane was heated in a metal heat block at 110°C. After deposition, the slide was vacuum-sealed with a FoodSaver sealer and stored at room temperature until the DNA printing step.

DNA spots of controlled sizes were printed within the adhesive microislands using a Nano eNabler system (Bioforce Nano, Ames Iowa). First, 5'-NH_2-modified oligonucleotides were diluted to 1.5 mM in a 4X inking buffer (20% trehalose, 0.4 mg mL^{-1} N-octylglucoside pH 9.5, 900 mM NaCl, 90 μM Na Citrate). Surface patterning tools (SPTs; BioForce Nano) of different sizes (30S and

10S versions) were cleaned by a UVO cleaner and loaded with 0.4 µL of the DNA inking solution. 30S SPTs were used to print the 12-13 µm astrocyte-tethering spots. Spots for tethering NSCs were smaller (7-8 µm) and were printed using the 10S SPTs. These distinct, orthogonal DNA solutions were printed within close proximity of each other (10~20 µm gap). The SPTs and slides were loaded into the machine, and the humidity was allowed to equilibrate to 55-60% before printing. After DNA printing was complete, the slide was dried in a 120°C oven for 1 minute and vacuum sealed.

The printed DNA strands formed Schiff C=N bonds with the surface aldehyde. To convert the hydrolysable Schiff bases to single C-N bonds, reductive amination was performed by treatment with sodium borohydride (Sigma, 0.25% in PBS, supplemented with 0.25% LiCl) for 1 hour at room temperature. Li^+ ions were added to increase efficiency of BH_4^- as a reducing agent. This step also reduced unreacted aldehyde groups on the surface to non-reactive primary alcohols. Slides were stored under vacuum at room temperature until the cell-tethering step.

Lipid-DNA Conjugates

5'-OH oligonucleotides (sequences in Supplementary Table 2.2) were synthesized on controlled pore glass (CPG, Glen Research) on an Applied Biosystems Expedite 8909 DNA synthesizer, as developed elsewhere. A synthetic phosphoramidite (MMT-Amino Modifier C6, Glen Research) was then resuspended in anhydrous acetonitrile (Fisher Scientific) according to vendor instructions and added to the oligonucleotides using the synthesizer. Free amine groups were generated by removing the MMT group with Deblocking Mix (Glen Research), followed by an acetonitrile wash. The CPG with oligonucleotide-amine groups was then transferred from synthesis columns to Eppendorf tubes. A C16 fatty acid (Hexadecanoic acid, Sigma-Aldrich) was conjugated to oligonucleotides by adding 1mL of a dicholoromethane (DCM, Fisher Scientific) solution containing 200 mM fatty acid, 400 mM N,N-diisopropylethylamine (DIPEA, Sigma-Aldrich), and 200 mM diisopropylchlorophosphoramidite (DIPC, Sigma-Aldrich). Eppendorf tubes were wrapped in parafilm, secured with a cap locker, and placed on a shaker overnight. The next morning, CPG beads were rinsed with a series of DCM and N,N-dimethylformamide (DMF, Sigma-Aldrich) washes and dried in a speedvac. Next, the lipid-conjugated DNA was cleaved from the CPG solid support by adding a small amount of a 1:1 mixture of ammonium hydroxide/40% methylamine (AMA, both from Sigma-Aldrich), sealing and cap-locking the tubes, and incubating at 70°C for 15-30 minutes. After cooling to RT, AMA was evaporated overnight using a speedvac. The resulting cleaved DNA/CPG was resuspended in 700µL of triethylamine acetic acid (TEAA, Fisher Scientific) and passed through a 0.2 µm Ultrafree centrifugal filter (Millipore) to remove the CPG solid support from the cleaved DNA solution. This DNA solution was next transferred to a polypropylene vial and carried through reversed-phase high-performance liquid chromatography (HPLC) to purify the desired lipid-modified DNA product. HPLC was performed with an Agilent 1200 Series HPLC system equipped with a diode array detector monitoring at 260 and 300 nm. A C8 column (Hypersil Gold, Thermo Scientific) was used with a gradient between 8 and 95% acetonitrile over 30 minutes with the pure fractions collected manually at the ~12-minute mark. Fractions were lyophilized, followed by three cycles of resuspension in distilled water and further lyophilization to remove residual TEAA salts. Fatty Acid-DNA concentrations were determined using a Thermo-Fisher NanoDrop 2000 series and measuring absorbance at 260 nm. Lipid-DNA stock solutions were resuspended at 250µM and stored at -20°C, with aliquots suspended in 1X

PBS to make a 5µM working solution. CoAnchor strands were generated in similar fashion with exception to the lipid conjugation occurring on the 3' end.

Characterization of DNA-Strand Incorporation onto Cells

We quantified absolute numbers of DNA strands incorporated per cell using two types of DNA: NHS-conjugated (*25*) 20-bp oligonucleotides (purchased from Adheren, Inc.) and lipid-modified (*19*) 100-bp oligonucleotides.

First, the NHS-DNA was prepared by adding 1.2 µL of activator to 175 µL of DNA solution, and the mixture was allowed to react at room temperature for 20 minutes. During this reaction, we detached NSCs and astrocytes, counted cells, and added 2 x 10^6 NSCs or 1 x 10^6 astrocytes into each of three tubes. We resuspended each cell pellet with 100 µL of PBS (as a negative control), 176 µL NHS-DNA, or 60 µL of lipid DNA (5.5 mM). The NHS-DNA was reacted with cells for 20 minutes, and the lipid DNA was incubated with cells for 15 minutes. After the reactions, the cells were diluted with 1% BSA in PBS and washed three more times. We then hybridized Alexa 488 complementary strands to the DNA-labeled cells by resuspending in 50 µL of complementary Alexa 488-conjuated DNA at 1 ng μL^{-1} and incubating on ice in the dark for 30 minutes. Cells were washed 3x with 1% BSA in PBS and resuspended in a 1 mL volume before assessment on a Beckman Coulter FC 500 flow cytometer. Beads from an Alexa 488 Quantum MESF bead kit (Bang's Laboratories) were used to calibrate the total number of fluorophores conjugated to the cell surface.

Because our measurements showed that lipid DNA was superior in the extent of DNA incorporation onto both NSCs and astrocytes (Supplementary Table 2.3), we used lipid DNA for all subsequent experiments.

Cell Culture

Adult rat neural stem cells (NSCs) isolated from the hippocampi of 6-week-old female Fischer 344 rats (160-170 g) (*26*) were used for stem cell signaling experiments. To promote NSC adhesion, tissue culture polystyrene plates were coated with poly-L-ornithine (Sigma) overnight at room temperature and 5 µg mL^{-1} of laminin (Invitrogen) overnight at 37°C. Cells were cultured in monolayers in DMEM/F-12 high-glucose medium (Life Technologies) containing N-2 supplement (Life Technologies) and 20 ng mL^{-1} recombinant human FGF-2 (Peprotech), which supports self-renewal and proliferation. Medium was changed every other day, and cells were passaged using Accutase upon reaching ~80% confluency.

Rat primary cortical astrocytes from the cortices of embryonic day 19 Sprague-Dawley rats were purchased from Invitrogen (Cat. No. N7745-100). The cells were expanded on tissue culture plates in DMEM containing 4.5 g L^{-1} glucose and 15% fetal bovine serum (Invitrogen) and initially exhibited a doubling time of approximately 9 days. The cells were then adjusted to maintenance on poly-L-ornithine/laminin coated tissue culture plates in DMEM/F-12 high-glucose containing N-2 supplement, 10% fetal bovine serum and 1% penicillin/streptomycin (Gibco). Medium was changed every 2-3 days, and cells were passaged with 0.25% trypsin/EDTA as required upon reaching 100% confluency.

Human mammary epithelial (MCF10A) cells were cultured in DMEM/F12 (Invitrogen), supplemented with 5% horse serum (Invitrogen), 1% penicillin/streptomycin (Invitrogen), 0.5 μg mL^{-1} hydrocortisone (Sigma), 100 ng mL^{-1} cholera toxin (Sigma), 10 μg mL^{-1} insulin (Sigma), and 20 ng L^{-1} recombinant human EGF (Peprotech). Similarly, medium was changed every other day, and cells were passaged with 0.25% trypsin/EDTA upon reaching 80% confluency.

hDll1 and mEfnB2 Cell Lines

To create astrocyte cell lines overexpressing key signaling ligands, we infected astrocytes with lentiviral vectors carrying a multicistronic cassette containing either hDelta1 (*12*) or hEphrinB2 (*11*), an NLS tagged fluorophore (mCherry or Venus), and Puromycin resistance (Supplementary Figure 2.7). Between each coding sequence is a viral 2A peptide that self-cleaves after translation, resulting in a 1:1 stoichiometry of expression.

Plasmid DNA is transfected into HEK 293T cells in the log phase of growth, along with third-generation lentiviral helper plasmids (RSV Rev, MDL gag/pol, and VSVG) using polyethylenimine (PEI) at 4:1 ratio (4 μg PEI:1 μg DNA). Media is collected at 44 hours and 68 hours after transfection, pooled, filtered with a 0.45 μm syringe filter, and centrifuged in a SW28 swinging bucket rotor in a Beckman Dickinson ultracentrifuge (2 hours, 24k rpm, 4°C). A 20% sucrose layer at the bottom of each tube provides effective separation of the viral pellet from the 293T media so that the final viral suspension is free of 293T contaminants. After centrifugation, the media and sucrose layer are aspirated, and the pellet is resuspended in sterile PBS, aliquoted, and frozen at -80°C. Infectious titers are determined by infecting astrocytes with serial dilutions of the virus, assessing infection rates by flow cytometry, and back-calculating the viral concentration using the Poisson distribution. The addition of polybrene (4 μg mL^{-1}) was essential for enabling lentiviral infection for cortical astrocytes.

To generate cell lines, cortical astrocytes were infected at MOI of 3 with 4 μg mL^{-1} polybrene. The day after infection, the media was supplemented with 10 μg mL^{-1} puromycin for 7 days through feedings and passages. For further isolation of high expressing cells, we sorted the population by FACS using a MoFlo Cell Sorter, gating for positively fluorescent cells for both mCherry and Venus. After sorting, cells were replaced, expanded, and aliquots were frozen at passages 15-18. Before each experiment, astrocytes were thawed from the same stock.

Due to the 2A peptide linker, the NLS-XFP fluorescence could be used as a readout of ligand expression for each cell, which we confirmed by two-color immunoflow (Supplementary Figure 2.8). To prepare cells for this analysis, astrocytes expressing NLS-mCherry hEfnB2 and NLS-mCherry hDll1 were detached from the plate using a brief Accutase treatment (instead of Trypsin to avoid excessive cleavage of membrane proteins). FBS-containing media was used to quench the enzymes, and 1 x 10^6 cells were fixed using 2% PFA and 1% BSA for 15 minutes. Cells were pelleted at 300 g for 5 minutes and washed 2x with PBS. Cells were blocked for 15 minutes in blocking buffer (5% donkey serum, 1% BSA, 0.1% triton-x-100 in PBS) and then stained with 100 μL of 1:50 rabbit polyclonal IgG for hDelta1 (sc-9102, Santa Cruz) or 1:100 rabbit polyclonal IgG for EfnB2 (HPA008999, Sigma) for 1 hour on a rocking shaker at room temperature. Cells were washed 3x with blocking buffer and then incubated in 100 μL of 1:250 Alexa 488 donkey anti-rabbit secondary antibody (Jackson Immunochemical) in the dark for 1 hour on a rocking shaker at room temperature. Cells were washed 2x in PBS and resuspended to < 500 cells μL^{-1} for assessment on the Guava easyCyte 6HT. Before collecting data, fluorescence compensation was performed using 488 labeled Quantum MESF beads (Bang's Laboratories) and unstained NLS-mCherry astrocytes.

Cell-Tethering Experiments

Slides were sterilized under a germicidal UV lamp in the laminar flow hood for 15 minutes. PDMS flow cells were plasma oxidized for 1 minute (to make the surface hydrophilic) and then sealed on top of the polyHEMA patterns for each well of a four-well chamber. A nontoxic grease marker was used to line off the inlet and outlet of each flow cell to ensure that flow travels through, and not around, the flow cells. 20 µL of 2% BSA (in PBS) was added to each flow cell for 1 hour to block nonspecific cell attachment.

NSCs and astrocytes were then detached and prepared at 4 x 10^6 and 2 x 10^6 cells, respectively, in PBS. Cells were labeled with 5 µM lipid DNA for 10 minutes at room temperature and, in some cases, 5 µM of a second, Co-Anchor lipid DNA strand was successively introduced to anchor the first strand into the cell membrane (also followed by a 10-minunte incubation step). Following incubation, cells were washed 4x with PBS with 3-minute spins at 300 g to pellet the cells in between washes. Cells were resuspended in 2% BSA (in PBS) to a final concentration of 4 x 10^7 NSCs mL^{-1} or 2 x 10^7 astrocytes mL^{-1} and stored on ice until ready for patterning. For some experiments, cell populations were combined before injecting the cell suspension (20 µL) into the flow cell. For all of the cell settling and washing steps, the slide was kept at 4°C to improve strand hybridization and slow down cellular metabolism during the lengthy experimental steps.

The cells were allowed to settle to the surface for 10 minutes and were then cycled through the well by adding 3 µL of cell suspension at the inlet, pipetting cells up at the outlet, and then adding the cell suspension back to the inlet. By cycling 15-20x, we enhanced the probability of hybridization between matched pairs of surface-bound and cell-conjugated strands. Excess cells were washed away slowly, then vigorously, with progressively larger volumes of PBS. Gaskets from 4-well Millipore EZ slides were then fastened onto the slide without removing flow cells. DMEM/F-12 with 10 µg mL^{-1} laminin was flowed through the flow cells, and the slide was incubated at 37°C and 5% CO_2 for 10-30 minutes before high-throughput imaging on the ImageXpress Micro (IXM) high-throughput automated imager. Each well was imaged in its entirety using a 10X objective with transmitted light illumination and/or fluorescent illumination. After imaging, mixed differentiation media (50% conditioned media from NSCs in the log-phase of growth, 1% FBS, 1 µM retinoic acid (Enzo Life Sciences), 1% pen/strep in DMEM/F-12 media) was added through the flow cells and used to fill the rest of the wells. Cells could then be carried through culture and, due to the transient nature of the DNA tethering (DNA linkages generally break down within hours), free to migrate and interact within their confined community over time.

Fluorescent Labeling of MCF10As for Efficiency Experiments

Up to four distinct MCF10A cell populations were labeled with CellTracker fluorescent dyes (Life Technologies) prior to cell tethering and patterning. CellTracker Green CMFDA, CellTracker

Deep Red, CellTracker Violet BMQC, and CellTracker Red CMPTX were prepared to a 10 mM concentration in DMSO. 4 x 10^6 MCF10As were resuspended in each CellTracker dye (0.1 µM for Green, 5 µM for Deep Red, 10 µM Violet, 5 µM Red) in 1X PBS for 10 minutes and subsequently washed 2x with PBS. Subsequent cell tethering steps were conducted as normal.

Poisson-Loading of MCF10A Populations into Microislands

Up to four populations of MCF10As were labeled with distinct CellTracker fluorescent dyes for 10 minutes (as described in detail in the above section). Cells were then washed 2x with 1X PBS and prepared as a mixed population. Cells from each population were prepared at a concentration of 5 x 10^5 cells mL^{-1} – a concentration that was previously determined by investigating a range of cell concentrations (1.25 x 10^6 cells mL^{-1} to 5 x 10^5 cells mL^{-1}) and analyzing which concentration supplied an optimal singe cell per microisland coverage. 20 µL of the mixed cell population was then injected into the PDMS flow cell and allowed to settle. Slides were imaged with the IXM and quantified for efficiencies. Microislands that contained exactly one cell type from each population was considered to be efficient.

Data Analysis

Acquired images for each well (a 7 x 14 grid) were tiled to form a whole-well montage in MetaXpress. These montages were rotated with bilinear interpolation in ImageJ, scaled with consistent scalings for each set of experiments, and then converted to 8-bit. Centroid coordinates for the upper left adhesive microisland were manually determined and recorded in a spreadsheet. These values were then inputted into a custom Matlab script, which cropped the images around each microisland and stored these images in an aligned array. A custom Matlab GUI, which displays the images from the array in succession, was used to record cell counts for day 0 images and immunostained images (Supplementary Figure 2.12). Mean and integrated intensity values for nuclear NLS-Venus fluorescence were determined by automated segmentation using Otsu and Minimum Error thresholding, followed by end-user error correction for low-intensity cases.

Cell counts were compiled in a Matlab data structure, which was then filtered to remove sites that were uncountable (due to poor image quality, overlapping cells that make quantification impossible, or imperfections in polyHEMA) and sites in which all NSCs died by day 6. The proliferation rate for each site was calculated according to the following equation:

$$C_f = C_i * 2^{rt}$$

where C_i is the initial NSC count at day 0, C_f is the final count of NSC-derived progeny, and t is the time elapsed in days. We note that this definition of proliferation includes the effects of apoptosis on cell counts. These data were then ported into R for statistical analyses and plotting using the ggplot2 package. Error bars for proportion data were generated using the MultinomialCI package on raw cell counts. A complete description of calculation metrics can be found in Supplementary Note 2.1.

Immunostaining

On day 5-6 of differentiation, flow cells were removed, and the cells were fixed with 4% PFA for 10 minutes at room temperature. The cells were washed 3x with PBS and then blocked in blocking buffer (PBS with 5% donkey serum and 0.3% Triton-X-100) for 1 hour. The cells were stained overnight at 4°C on a rocking shaker with 1:1000 mouse monoclonal IgG for beta-tubulin III (Tuj1) (T8578, Sigma) and 1:1000 rabbit polyclonal IgG for glial fibrillary acidic protein (GFAP) (ab7260, Abcam), diluted in blocking buffer. The next day, the antibody solution was removed, cells were washed 3x with PBS and then incubated in the dark for 1-2 hours at room temperature on a rocking shaker with secondary antibodies, 1:250 Alexa Fluor 488 donkey anti-mouse IgG (H+L) and 1:250 Cy3 donkey anti-rabbit (H+L) (all Jackson Immunochemical) in blocking buffer. After secondary incubation, cells were washed 3x with PBS (with 1:1000 DAPI in the second wash) and kept in PBS until imaging.

Timelapse Experiments

NSCs and astrocytes were tethered onto DNA spots in polyHEMA-patterned and non-polyHEMA-patterned substrates, as described above. After cell tethering and washes, mixed differentiation media supplemented with 10 μg mL^{-1} laminin was flowed through the flow cells, and excess media was added to the wells. The slide was then imaged with transmitted light on the IXM using a 10X objective at 30-minute intervals for 44 hours. During imaging, an environmental control chamber maintained the slide at 37°C with a continuous supply of 5% CO_2. Movies from 50-60 sites were collected for each of 2-3 wells in each type of substrate.

Timelapse movies were analyzed manually. For each pair of patterned cells, we recorded moments of contact and disengagement, division and death events, and the final and maximum distances between cell nuclei and membranes. The total contact time and number of contact events are calculated from these data.

Flow Cell Production

Simple PDMS flow cells were produced using a 200 μm-thick mold created by stacking two white tough-tags and a piece of clear tape. Using a razorblade, the sticker stack is cut to 31 mm x 6 mm and affixed to the bottom of a 10 cm petri dish. Sylgard 184 (Ellsworth Adhesive) prepolymer is mixed with its curing agent at a 10:1 ratio, and 12 g of the mixture is poured onto the mold. PDMS is cured at 80°C for 1 hour, and flow cells are cut to 1 x 0.8 cm.

2.5 Acknowledgements

We thank Dr. Mary West, Wanichaya Ramey, Dr. Lukasz Bugaj, Dr. Dawn Spelke, Dr. Randolph Ashton, Jorge Santiago, David Ojala, Dr. Alyssa Rosenbloom, Robert Weber, and Max Coyle. This work was funded by NIH grants R21 EB014610, R01 ES020903, DP2 HD080351-01, and DOD grant W81XWH-13-1-0221. Y.S.N was supported by the Samsung Scholarship. O.J.S. was supported by the National Science Foundation Graduate Research Fellowship.

2.6 Supplemental Information

2.6.1 Supplementary Figure 2.1 – PolyHEMA Patterning Characterization

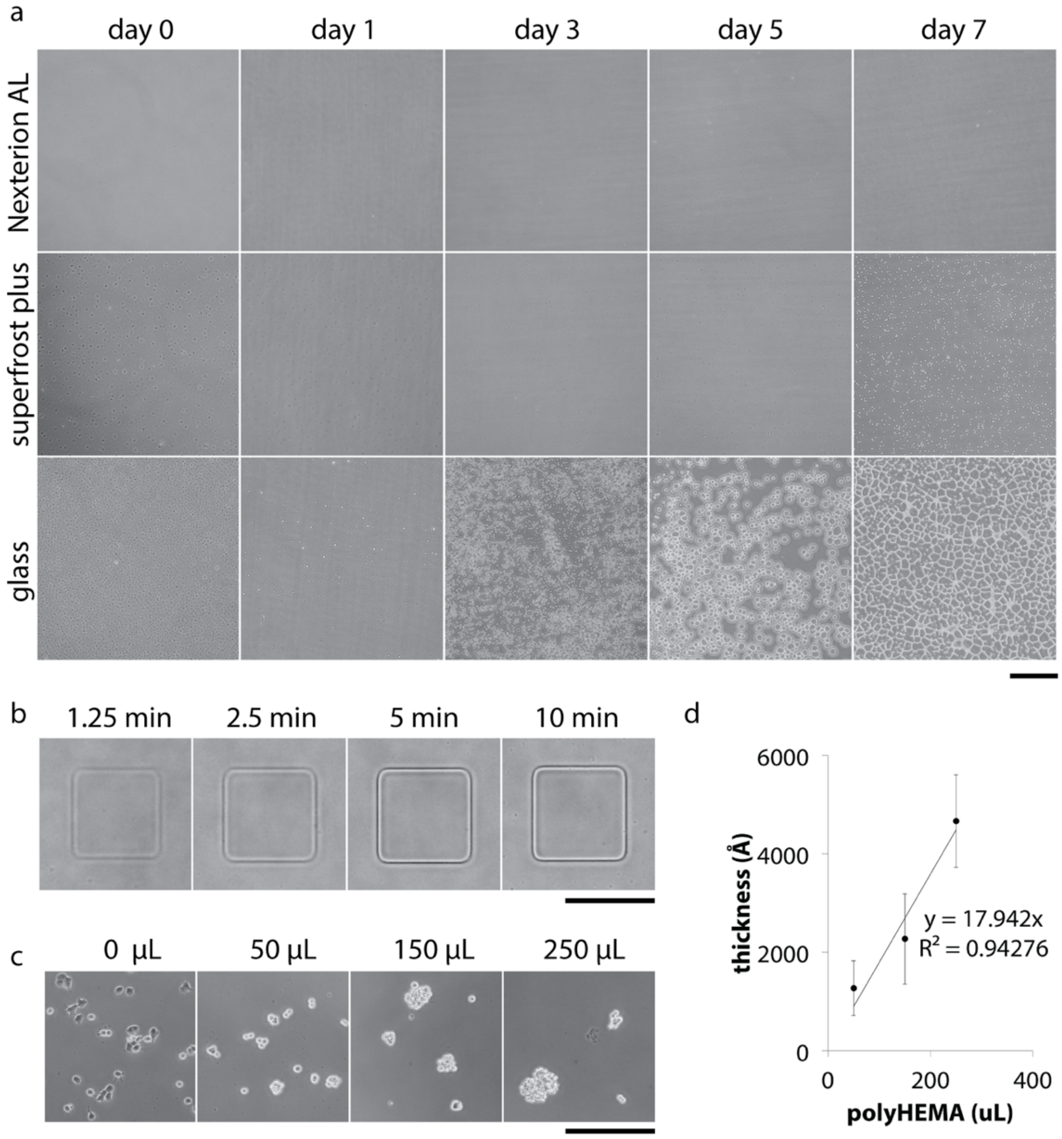

Supplementary Figure 2.1 (a) Optimizing substrate chemistry strongly enhanced polyHEMA stability in aqueous solutions. Schott Nexterion AL slides performed well relative to other options with little to no degradation over 7 days. PolyHEMA coated on plain glass slides began to detach after one day, while SuperFrost+ slides displayed slight improvement with little observable detachment until day 5. (b) Phase contrast microscopy showed that 5 minutes of deep UV illumination was sufficient to etch through our standard thickness of polyHEMA coatings (150 µL of 10 mg mL^{-1} polyHEMA). (c) PolyHEMA was effective at blocking cell adhesion down to 50 µL slide^{-1}. (d) The thickness of polyHEMA coating was modulated by depositing different volumes of polyHEMA solution (10 mg mL^{-1}). Profilometer measurements were performed at 9 different locations sampled over the entirety of two coated slides for each deposition. All scale bars: 200 µm.

2.6.2 Supplementary Figure 2.2 – Overview of Experimental Poison Loading of MCF10As into Microislands

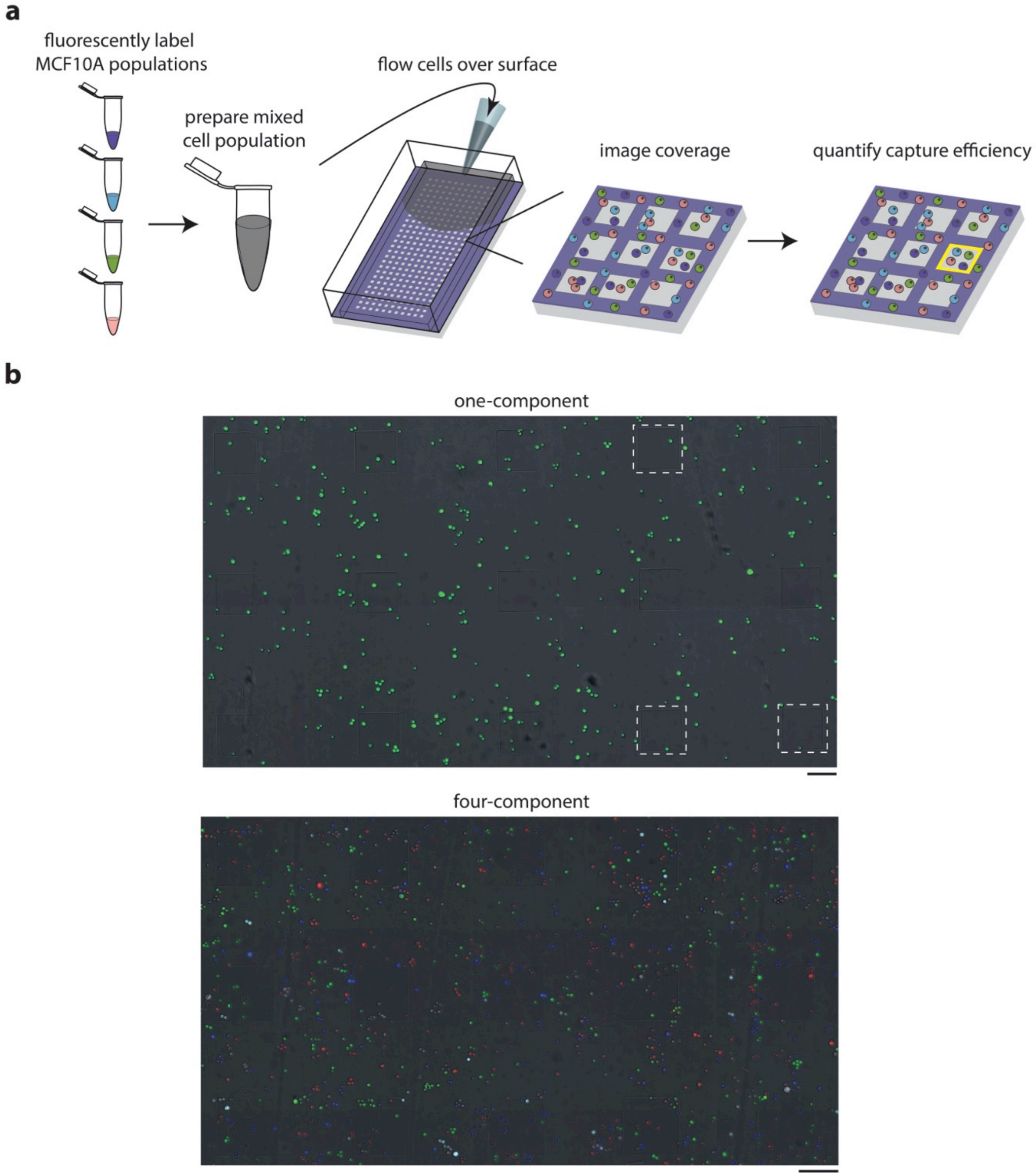

Supplementary Figure 2.2 (a) Schematic for conducting Poisson-loading experiment with 4 distinct, fluorescently-labeled MCF10A populations. (b) Representative one-component (top) and four-component (bottom) images of microislands that contain cells seeded using random Poisson loading. White, dashed boxes indicate microislands that possess the correct cellular components. All scale bars: 100 µm.

2.6.3 Supplementary Figure 2.3 – Confinement to Small Adhesive Microisland Sustains Intercellular Contact for Extended Times

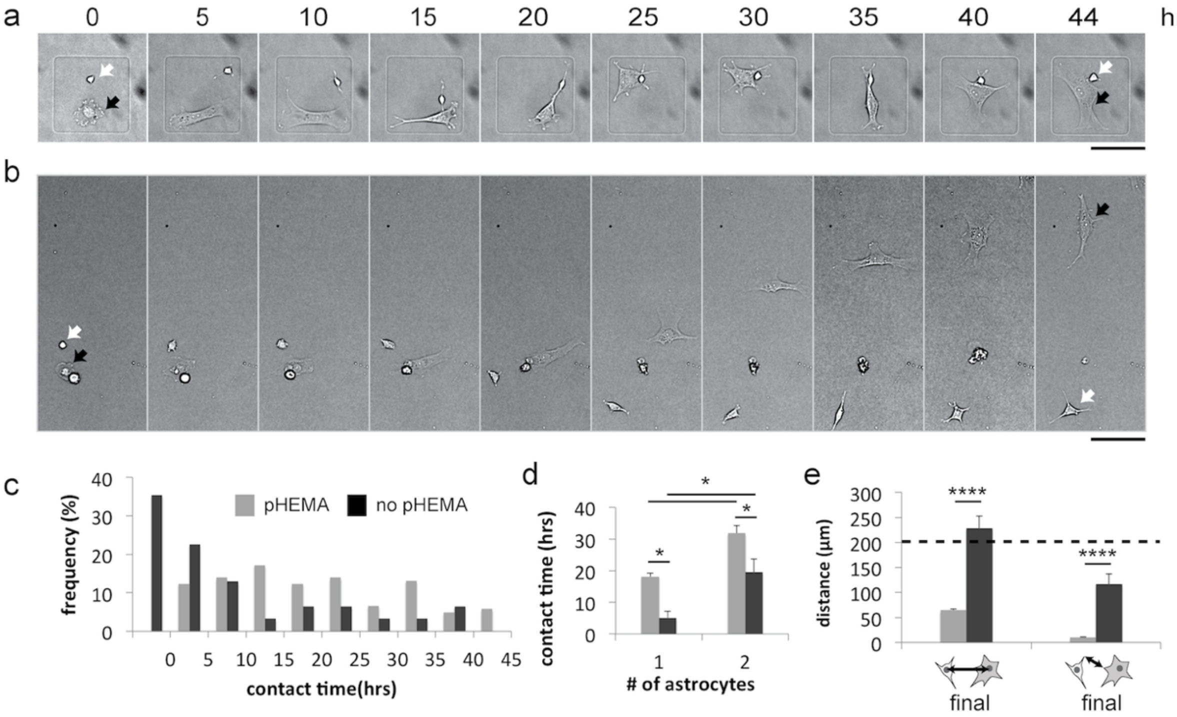

Supplementary Figure 2.3 (a) 141 x 141 μm adhesive microislands enabled extensive membrane contact between patterned NSCs (white arrow) and patterned astrocytes (black arrow). (b) On standard aldehyde slides lacking adhesive microislands, patterned NSCs and astrocytes migrated up to hundreds of microns away from each other over the course of 2 days. (c) Histograms of total contact times between patterned single NSCs and astrocytes showed that, without polyHEMA confinement, almost 35% of pairs made no contact at all. (d) The total amount of time that a NSC made contact with a single astrocyte was substantially increased with polyHEMA microisland confinement, and the addition of a second astrocyte further increased contact time (*: $p<0.05$, ANOVA with Tukey HSD, error bars: s.e.m). (e) The final inter-nuclear distance (left) and membrane distance (right) between patterned pairs were significantly less compared to pairs that were not confined (****: $p<1e-4$, t-test, error bars: s.e.m). The dotted line indicates the maximum corner-to-corner distance within the adhesive microislands. All scale bars: 100 μm.

2.6.4 Supplementary Figure 4 – Additional Timelapse Montages to Show Analysis Framework

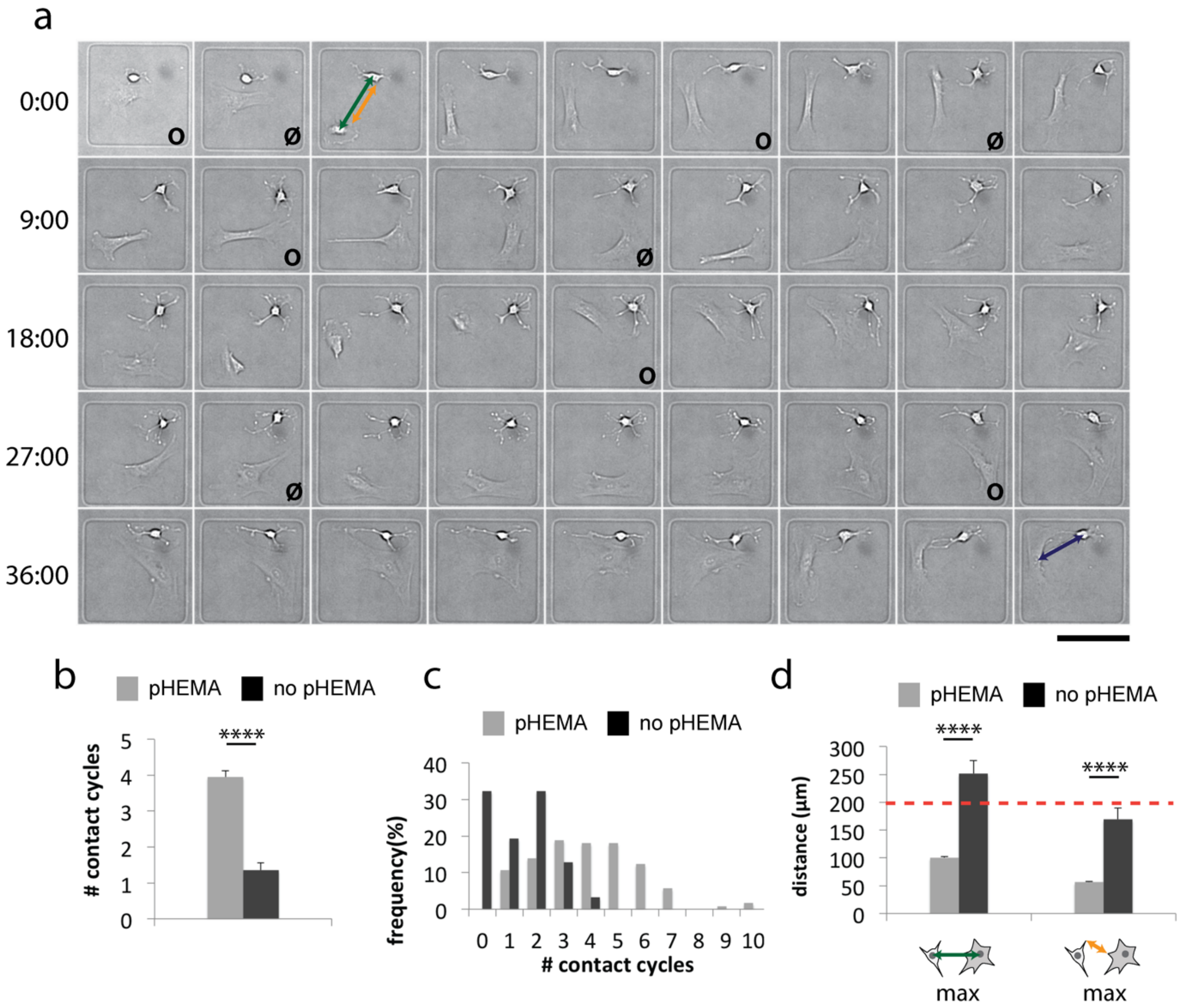

Supplementary Figure 2.4 (a) DNA-tethered NSC and astrocyte pairs in polyHEMA patterns make several apparent cycles of contact (O) and disengagement (Ø). The green arrow shows the maximum distance between nuclei, and the yellow arrow shows the maximum cell membrane distance over the course of the experiment. The blue arrow shows the final distance between nuclei at 44 hours and, in this case, the final cell distance was 0 since the membranes were in contact at 44 hours. Hours are denoted on the left. (b) PolyHEMA-bounded pairs experienced significantly more contact cycles over 44 hours compared to pairs without polyHEMA (where representative images for no polyHEMA are shown in Supplementary Figure 2.5) ($p<1e-13$, error bars: s.e.m.). (c) The histogram of contact cycles shows a wider spread for polyHEMA-bounded pairs. (d) The maximum nuclear and membrane distances (green and yellow) between pairs were also significantly lower for polyHEMA-bounded pairs ($p<1e-5$, error bars: s.e.m.). All scale bars: 100 µm.

2.6.5 Supplementary Figure 2.5 – Additional Timelapse Montages of Cells Patterned without PolyHEMA

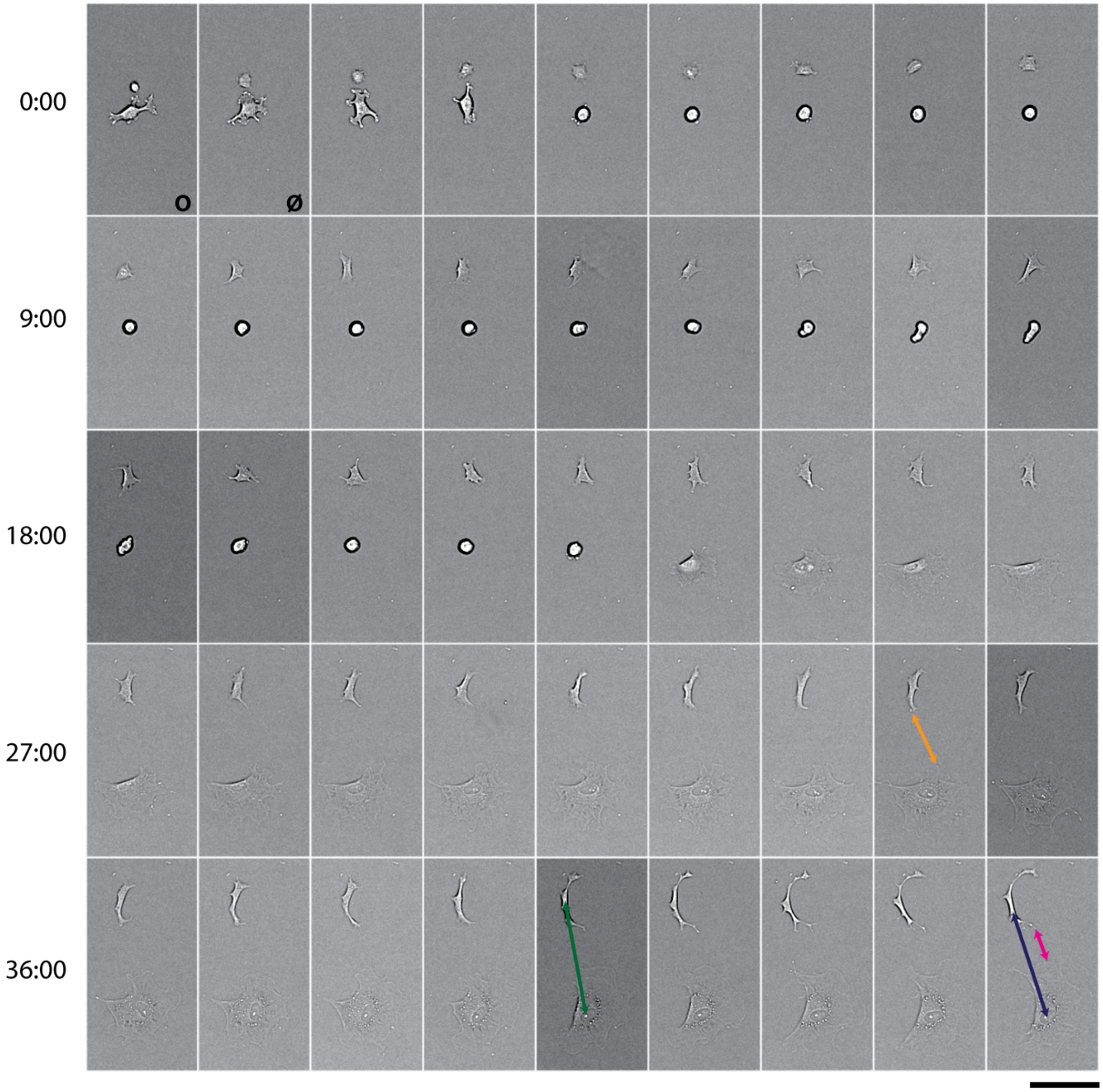

Supplementary Figure 2.5 Notated using the same strategy as described in Supplementary Figure 2.4. The magenta arrow shows the final cell membrane distance.

2.6.6 Supplementary Figure 2.6 – Additional Plots for NSCs Patterned with Naïve Astrocytes

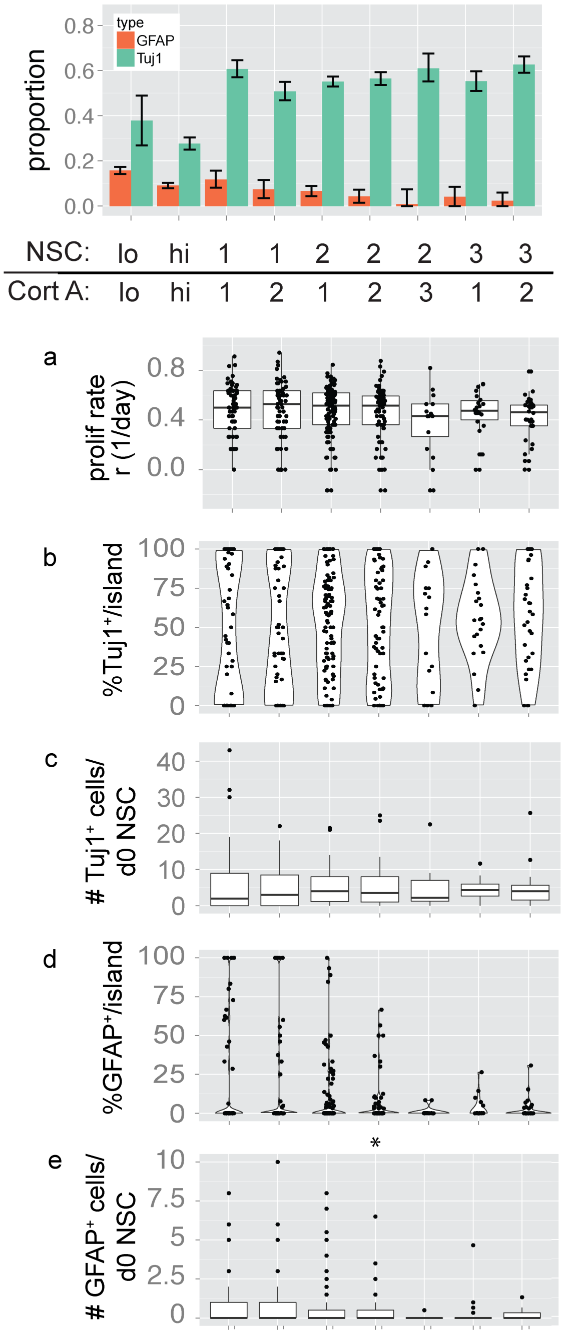

Supplementary Figure 2.6 NSCs patterned with 1, 2, and 3 astrocytes exhibited higher differentiation rates than NSCs patterned in bulk, at either high (5000 cells cm^{-2}) or low density (500 cells cm^{-2}). (a) Proliferation rates. (b) Distribution of % Tuj1^{+} island^{-1} shows that increasing the number of initial NSC progenitors cause wider bellies in the distributions, reflecting the lower likelihood that all progeny adopt the same fate. (c) Boxplot of the number of Tuj1^{+} cells generated from each initial NSC. (d) Violin plots of the distributions of % GFAP^{+} island^{-1}. (e) Boxplot of the number of GFAP^{+} cells (initial NSC)$^{-1}$. All error bars are 95% confidence intervals.

2.6.7 Supplementary Figure 7 – Plasmid Maps for Expression Vectors

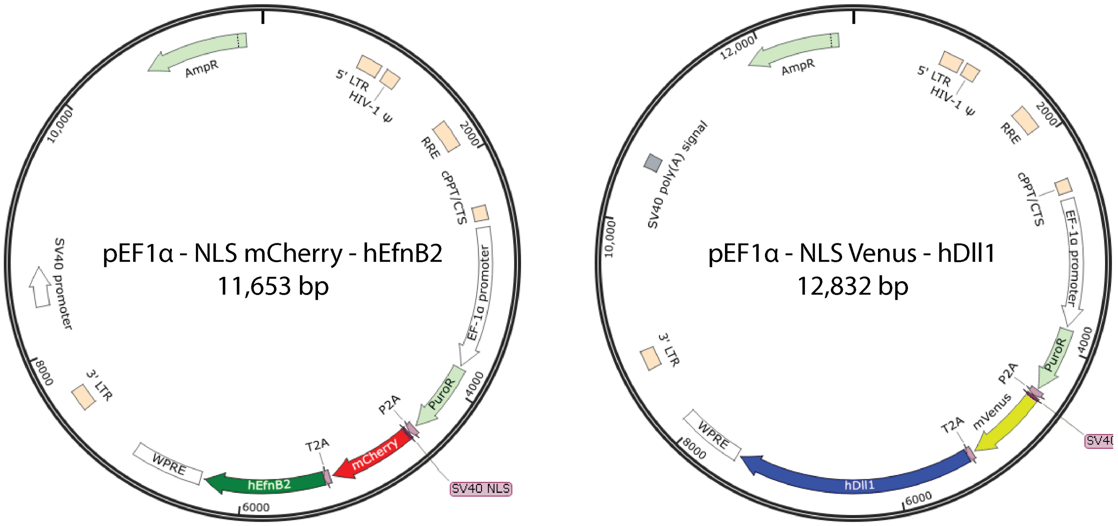

Supplementary Figure 2.7 Overview of plasmids for generating juxtacrine-expressing cortical astrocyte cell lines.

2.6.8 Supplementary Figure 2.8 – Two-Color Immunoflow Results Show Linear Relationship Between NLS-mCherry and Dll1 or EfnB2

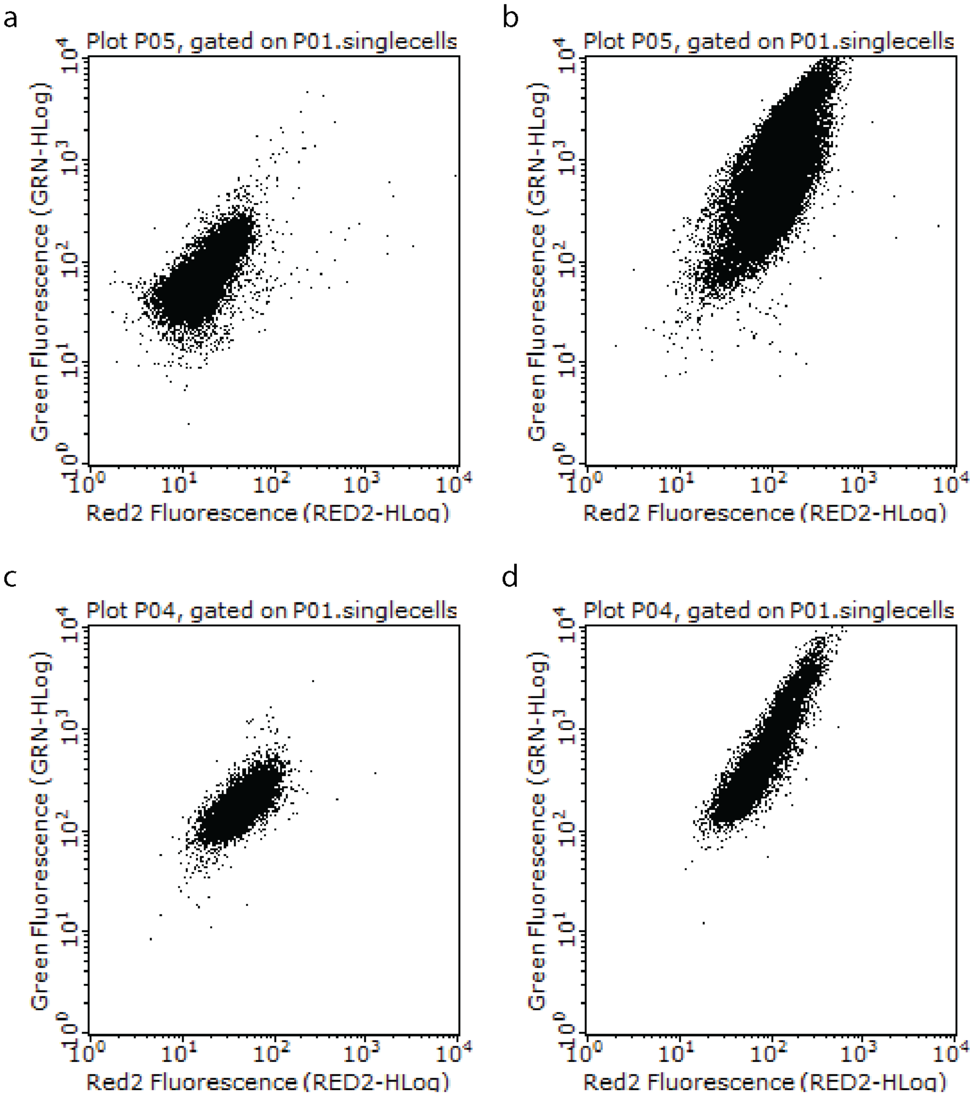

Supplementary Figure 2.8 (a) Naïve astrocytes stained with Dll1 antibody. (b) Dll1 lentivirus-infected astrocytes show linear relationship between mCherry fluorescence (Red2) and Dll1 488 antibody (Green). (c) and (d) show the same for naïve astrocytes and EfnB2-overexpressing astrocytes, each stained for EfnB2.

2.6.9 Supplementary Figure 2.9 – Additional Plots for NSCs Patterned with EfnB2-Expressing Astrocytes

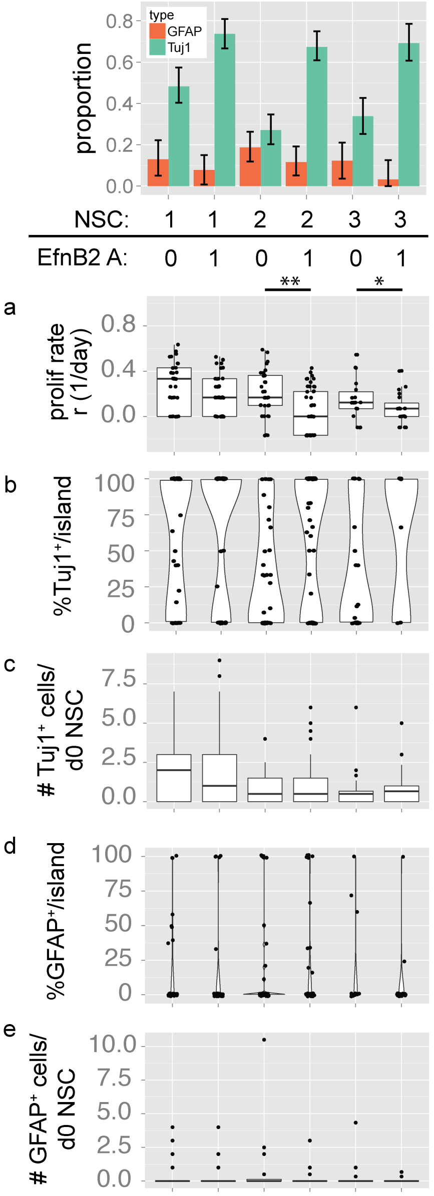

Supplementary Figure 2.9 NSCs patterned with single hEfnB2-overexpressing cells exhibited enhanced Tuj1$^+$ differentiation. (a) In the presence of an EfnB2-astrocyte, the mean proliferation rate decreases, which is statistical in the case of 2 initial NSCs (**, p=0.0012, t-test) and 3 initial NSCs (*, p=0.06, t-test). (b) NSCs exhibited enhanced Tuj1+ differentiation as evident in the wide distributions within the upper portion of the violin plots. (c) Boxplot of the number of Tuj1$^+$ cells generated (initial NSC)$^{-1}$. No differences in the mean number of Tuj1+ cells were observed with the addition of one EfnB2 expressing astrocyte (for NSC = 1, 2, and 3). EfnB2 thus functions by increasing the fraction of NSCs islands^{-1} that give rise to a high proportion of Tuj1$^+$ cells rather than increasing the number of Tuj1$^+$ cells NSC^{-1} within a microisland. (d) Distribution of % GFAP$^+$ island^{-1}. (e) Boxplot of the number of GFAP$^+$ cells (initial NSC)$^{-1}$ reveal that very few GFAP$^+$ cells are produced overall. All error bars are 95% confidence intervals.

2.6.10 Supplementary Figure 2.10 – Additional Plots for NSCs Patterned with Dll1-Expressing Astrocytes

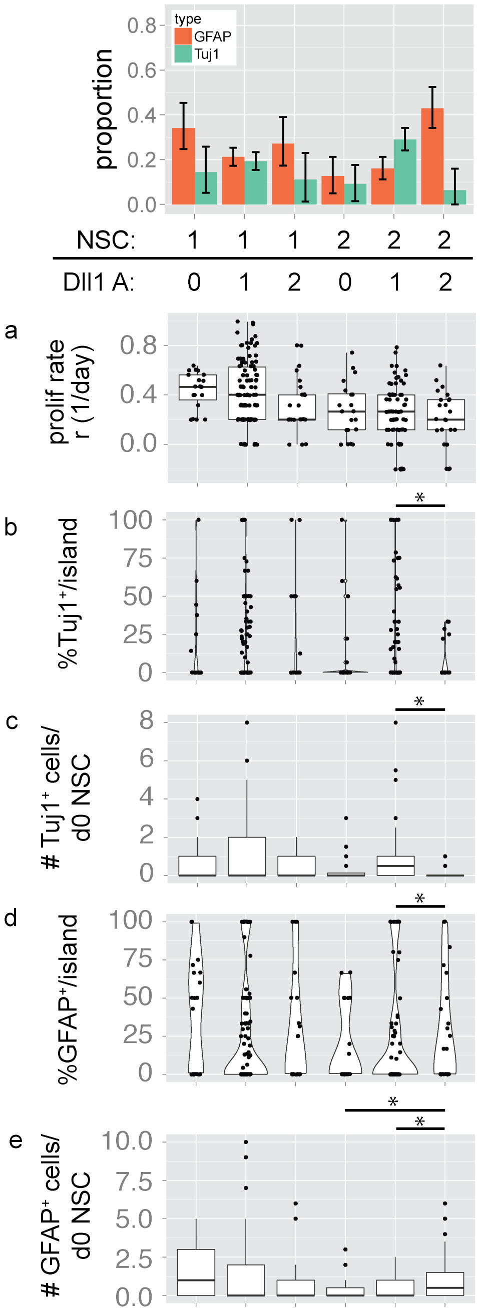

Supplementary Figure 2.10 NSCs patterned with single hDll1-overexpressing astrocyte exhibited reduced Tuj1. (a) Proliferation rates show no differences in the mean with the addition of Dll1-overexpressing astrocytes. (b) Narrow distributions for %Tuj1 island^{-1} reflect low Tuj1 differentiation rates. Asterisk indicates significant difference between samples. (c) Boxplot of the number of Tuj1^{+} cells generated (initial NSC)$^{-1}$. Asterisk indicates significant difference between samples. (d) Distribution of % GFAP island^{-1}. Asterisk indicates significant difference between samples. (e) Boxplot of the number of GFAP+ cells (initial NSC)$^{-1}$. Asterisk indicates significant difference between samples. All error bars are 95% confidence intervals; all p values obtained from ANOVA with Tukey HSD. $*p<0.05$.

2.6.11 Supplementary Figure 2.11 – Additional Plots for NSCs Patterned with EfnB2-Expressing and Dl1-Expressing Astrocytes

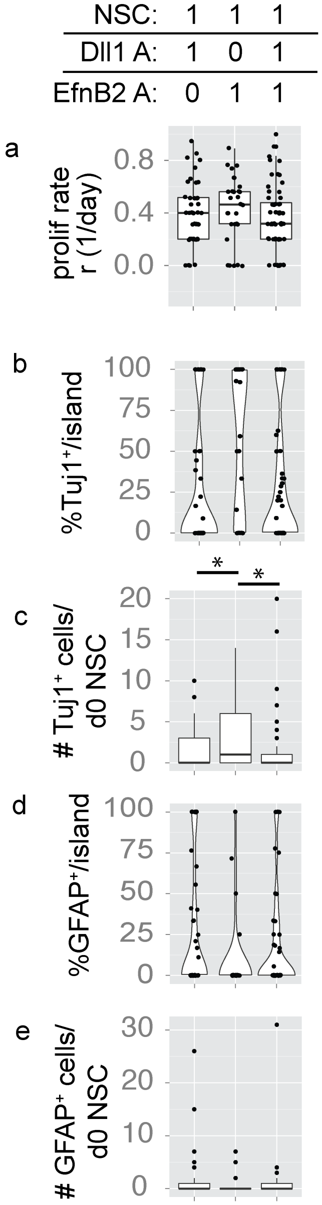

Supplementary Figure 2.11 (a) Proliferation rates show similar medians in patterns with only Dll1 and patterns with both signals. However, mean proliferation rates are not significantly different ($p=0.6$, ANOVA). (b) Violin plot showing similar distributions of %Tuj1 pattern^{-1} between patterns with only one Dll1-astrocyte and patterns with both types of astrocytes. By contrast, the %Tuj1 island^{-1} measurements with only one EfnB2 astrocyte were significantly elevated to higher levels ($p<0.0.5$, ANOVA with post-hoc Tukey Honest Significant Difference test). (c) Boxplot of the number of Tuj1^{+} cells with respect to initial NSC shows that islands with a Dll1-astrocyte and microislands with both a Dll1-astrocyte and a EfnB2-astrocyte produce significantly fewer Tuj1^{+} cells compared to microislands with only EfnB2 ($p=0.022$ and $p=0.024$ compared to the left and right columns, ANOVA with Tukey HSD). (d) Distribution of % GFAP island^{-1} does not reveal significant differences across samples ($p=0.16$, ANOVA). (e) Boxplot of the number of GFAP+ cells (initial NSC)$^{-1}$, with no significant differences across sample means ($p=0.44$, ANOVA). All error bars are 95% confidence intervals.

2.6.12 Supplementary Figure 12 – Matlab GUI to Facilities Manual Tabulation of Cell Counts

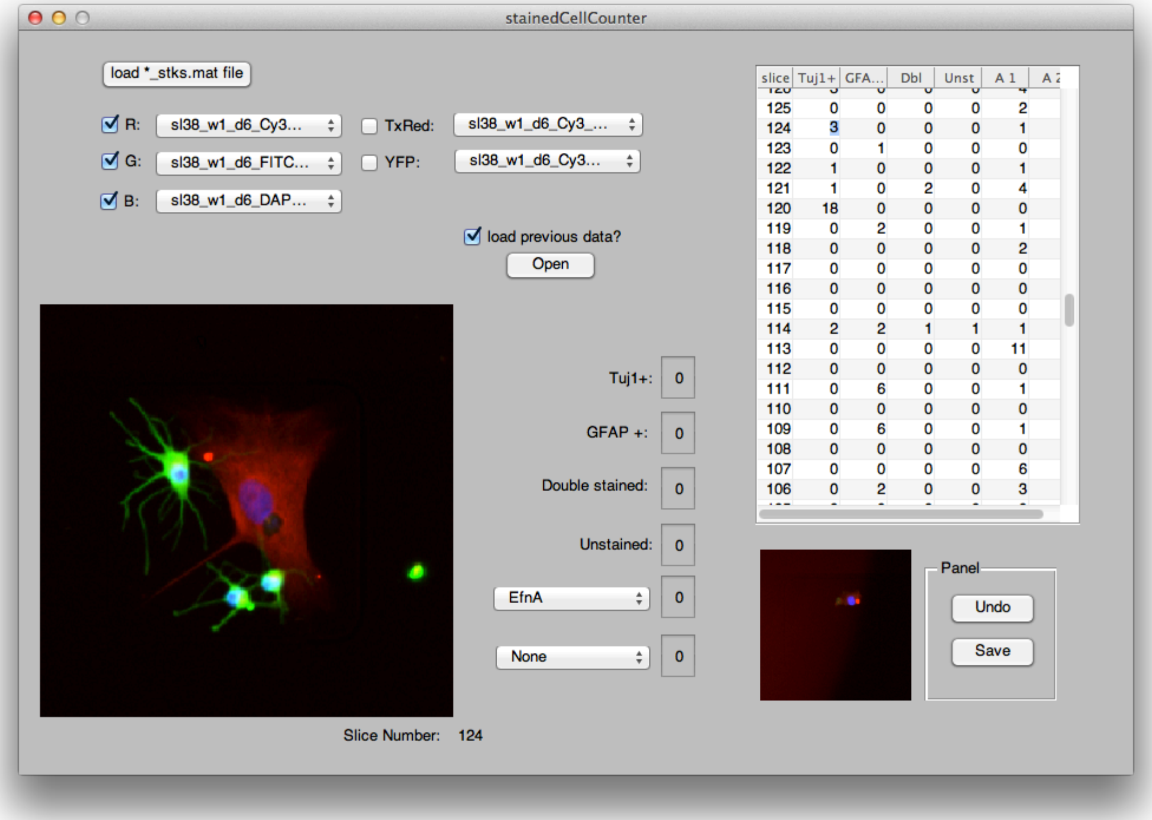

☑ R: sl38_w1_d6_Cy3...

☑ G: sl38_w1_d6_FITC...

☑ B: sl38_w1_d6_DAP...

☐ TxRed: sl38_w1_d6_Cy3_...

☐ YFP: sl38_w1_d6_Cy3...

☑ load previous data?

Tuj1+: 0

GFAP +: 0

Double stained: 0

Unstained: 0

EfnA: 0

None: 0

Slice Number: 124

slice	Tuj1+	GFA...	Dbl	Unst	A 1
125	0	0	0	0	2
124	3	0	0	0	1
123	0	1	0	0	0
122	1	0	0	0	1
121	1	0	2	0	4
120	18	0	0	0	0
119	0	2	0	0	1
118	0	0	0	0	2
117	0	0	0	0	0
116	0	0	0	0	0
115	0	0	0	0	0
114	2	2	1	1	1
113	0	0	0	0	11
112	0	0	0	0	0
111	0	6	0	0	1
110	0	0	0	0	0
109	0	6	0	0	1
108	0	0	0	0	0
107	0	0	0	0	6
106	0	2	0	0	3

Supplementary Figure 2.12 The software interface – described in greater detail in the Methods section – loads a series of images into red, green, and blue channels with optional extra channels for images of NLS-conjugated fluorescent proteins. Manually tabulated counts are entered into a table, which is stored in a data structure upon hitting 'save'. The editable table makes it easy to review and edit counts. To avoid bias, immunostaining counts are performed blinded to day 0 information on numbers and types of cells per island.

2.6.13 Supplementary Table 1 – Number of Samples for Each Type of Community Composition

#	community composition	n
1	1NSC + 1CortA	61
2	1NSC + 2CortA	59
3	2NSC + 1CortA	110
4	2NSC + 2CortA	67
5	2NSC + 3CortA	16
6	3NSC + 1CortA	22
7	3NSC + 2CortA	32
8	1NSC + 0EfnA	33
9	1NSC + 1EfnA	44
10	2NSC + 0EfnA	32
11	2NSC + 1EfnA	46
12	3NSC + 0EfnA	20
13	3NSC + 1EfnA	24
14	1NSC + 0DeltaA	19
15	1NSC + 1DeltaA	106
16	1NSC + 2DeltaA	21
17	2NSC + 0DeltaA	20
18	2NSC + 1DeltaA	65
19	2NSC + 2DeltaA	23
20	1NSC + 0EfnA + 1 DeltaA	45
21	1NSC + 1EfnA + 0 DeltaA	29
22	1NSC + 1EfnA + 1 DeltaA	57

2.6.14 Supplementary Table 2 – Complementary Pairs of Cell-Labeling and Surface-Printed DNA Sequences in Addition to the CoAnchor Sequence for Stabilizing Cell-Labeling Oligonucleotides

Sequence Name	DNA Sequences (5’ – 3’)
A	GTA ACG ATC CAG CTG TCA CT TTTTTTTTTT TTTTTTTTTT TTTTTTTTTT TTTTTTTTTT TTTTTTTTTT TTTTTTTTTT ACTG ACTG ACTG ACTG ACTG
A’	GTA ACG ATC CAG CTG TCA CT TTTTTTTTTT TTTTTTTTTT TTTTTTTTTT TTTTTTTTTT TTTTTTTTTT TTTTTTTTTT CAGT CAGT CAGT CAGT CAGT
B	GTA ACG ATC CAG CTG TCA CT TTTTTTTTTT TTTTTTTTTT TTTTTTTTTT TTTTTTTTTT TTTTTTTTTT TTTTTTTTTT TCATACGACTCACTCTAGGG
B’	GTA ACG ATC CAG CTG TCA CT TTTTTTTTTT TTTTTTTTTT TTTTTTTTTT TTTTTTTTTT TTTTTTTTTT TTTTTTTTTT CCCTAGAGTGAGTCGTATGA
F	GTA ACG ATC CAG CTG TCA CT TTTTTTTTTT TTTTTTTTTT TTTTTTTTTT TTTTTTTTTT TTTTTTTTTT TTTTTTTTTT AGA AGA AGA ACG AAG AAG AA
F’	GTA ACG ATC CAG CTG TCA CT TTTTTTTTTT TTTTTTTTTT TTTTTTTTTT TTTTTTTTTT TTTTTTTTTT TTTTTTTTTT TTC TTC TTC GTT CTT CTT CT
G	GTA ACG ATC CAG CTG TCA CT TTTTTTTTTT TTTTTTTTTT TTTTTTTTTT TTTTTTTTTT TTTTTTTTTT TTTTTTTTTT AGC CAG AGA GAG AGA GAG AG
G’	GTA ACG ATC CAG CTG TCA CT TTTTTTTTTT TTTTTTTTTT TTTTTTTTTT TTTTTTTTTT TTTTTTTTTT TTTTTTTTTT CTC TCT CTC TCT CTC TGG CT
CoAnchor	AGT GAC AGC TGG ATC GTT AC

2.6.15 Supplementary Table 3 – Assessment of DNA Incorporation into Cells

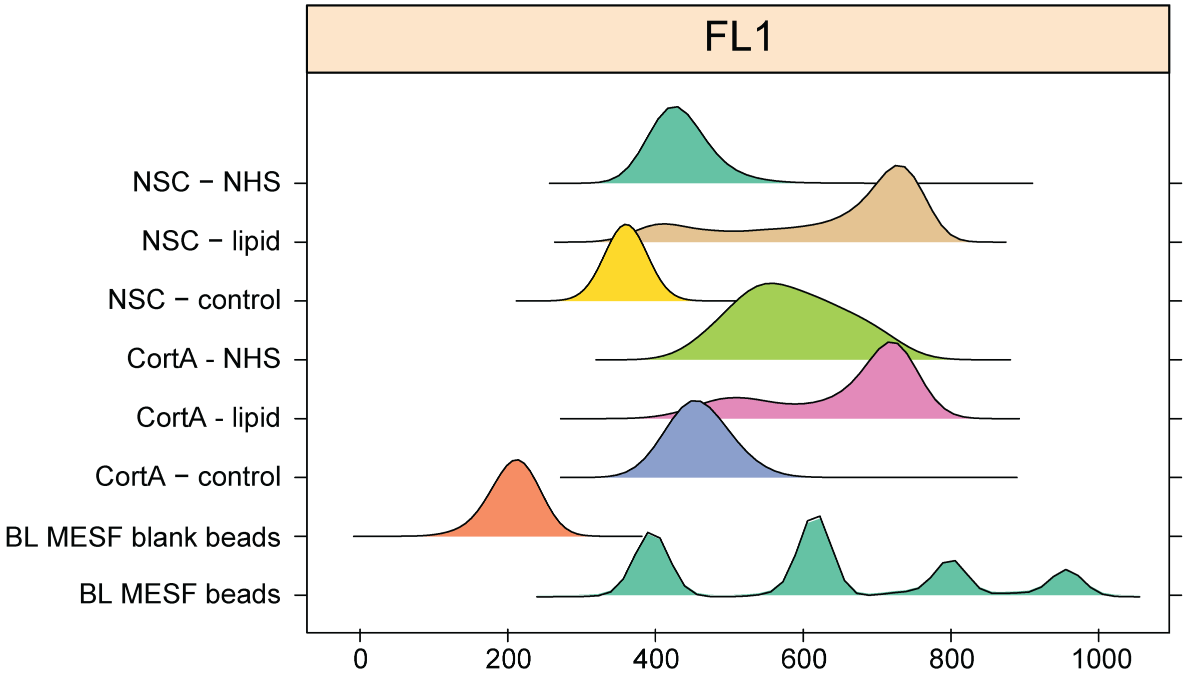

Type	Peak (strands cell^{-1})	5th percentile (strands cell^{-1})	95th percentile (strands cell^{-1})
NSC - NHS	4,606	3,125	10,727
NSC – lipid	107,809	3,701	139,626
NSC – control	2,437	1,808	3,556
CortA – NHS	18,355	7,498	84,914
CortA - lipid	90,136	7,498	135,521
CortA - control	5,732	3,666	13,619

Supplementary Table 2.3. After cell labeling by lipid DNA or NHS-DNA, cells were incubated with Alexa 488-conjugated complementary oligonucleotides and assessed by flow cytometry. Lipid DNA outperformed NHS-DNA for both NSCs (108k vs. 5k strands cell^{-1}) and astrocytes (90k vs. 18k strands cell^{-1}).

2.6.16 Supplementary Note 2.1

Our ability to measure many metrics from each patterned community yields data that can be displayed in a variety of ways. Here, we provide extensive descriptions of the supplementary plots from each experiment (below) with some guidelines for interpretation.

Proliferation rate: The proliferation rate is calculated as described in the Methods section. In these plots, a boxplot of the proliferation rate measurement is overlaid with jittered points, each representing a measurement from one island.

% Tuj1$^+$ island^{-1}: For each island, the %Tuj1$^+$ island^{-1} value is calculated by dividing the number of Tuj1$^+$ cells over total number of NSC-progeny at day 6. For each type of community composition, a violin plot of the %Tuj1$^+$ island^{-1} distribution is overlaid with jittered points, each representing a measurement from one island. For most plots there may be a large number of 0% Tuj1$^+$ measurements, making it impossible to infer an idea of the distribution from looking at the jittered points alone. Thus, the interpolated lines of the violin plot provide a better sense of the true distribution of values along the 0-100% y-axis.

 # Tuj1$^+$ cells (d0 NSC)$^{-1}$: For each microisland, the # Tuj1$^+$ cell at day 6 is divided by the total number of NSCs at day 0. This provides a measure of the average number of Tuj1$^+$ cells produced from each NSC. In communities with only one initial NSC, this is a measure of the absolute number of Tuj1$^+$ cells produced. These data are represented as a boxplot with the line designating the median, with upper and lower "hinges" corresponding to the first and third quartiles (the 25th and 75th percentiles).

% GFAP$^+$ island^{-1}: Similar to % Tuj1$^+$ island^{-1}. In general, since GFAP marker expression is less frequent than Tuj1 expression, we have less statistical power when analyzing GFAP data. Note that the GFAP+ NSC progeny can readily be distinguished from the cortical astrocytes (which are much larger and flatter) and, in many cases, by cortical astrocyte expression of a NLS fluorescent protein.

 # GFAP$^+$ cells NSC^{-1}: Similar to # Tuj1$^+$ (d0 NSC)$^{-1}$. For each of these plots, interesting and significant results are described in the figure legend. Plots without significant differences are presented without comment. For ANOVA, we subset the data based on the number of initial NSCs to assess the impact of additional astrocytes.

2.7 References

1. Klein, L., Kyewski, B., Allen, P. M. & Hogquist, K. A. Positive and negative selection of the T cell repertoire: what thymocytes see (and don't see). *Nature reviews. Immunology* **14**, 377-391, (2014).
2. Junttila, M. R. & de Sauvage, F. J. Influence of tumour micro-environment heterogeneity on therapeutic response. *Nature* **501**, 346-354, (2013).
3. Scadden, D. T. Nice neighborhood: emerging concepts of the stem cell niche. *Cell* **157**, 41-50, (2014).
4. Mirzadeh, Z., Merkle, F. T., Soriano-Navarro, M., Garcia-Verdugo, J. M. & Alvarez-Buylla, A. Neural stem cells confer unique pinwheel architecture to the ventricular surface in neurogenic regions of the adult brain. *Cell Stem Cell* **3**, 265-278, (2008).
5. Morrison, S. J. & Spradling, A. C. Stem cells and niches: mechanisms that promote stem cell maintenance throughout life. *Cell* **132**, 598-611, (2008).
6. Nusse, R. Wnts and Hedgehogs: lipid-modified proteins and similarities in signaling mechanisms at the cell surface. *Development* **130**, 5297-5305, (2003).
7. Fuchs, E., Tumbar, T. & Guasch, G. Socializing with the neighbors: stem cells and their niche. *Cell* **116**, 769-778, (2004).
8. Gage, F. H., Takahashi, J. & Palmer, T. D. The Adult Rat Hippocampus Contains Primordial Neural Stem Cells. *Molecular and Cellular Neuroscience* **8**, 389-404, (1997).
9. Palmer, T. D., Markakis, E. A., Willhoite, A. R., Safar, F. & Gage, F. H. Fibroblast growth factor-2 activates a latent neurogenic program in neural stem cells from diverse regions of the adult CNS. *The Journal of Neuroscience* **19**, 8487-8497, (1999).
10. Willhoite, A. R., Gage, F. H. & Palmer, T. D. Vascular niche for adult hippocampal neurogenesis. *The Journal of Comparative Neurology* **425**, 479-494, (2000).
11. Ashton, R. S. *et al.* Astrocytes regulate adult hippocampal neurogenesis through ephrin-B signaling. *Nat Neurosci* **15**, 1399-1406, (2012).
12. Gaiano, N. & Fishell, G. The role of notch in promoting glial and neural stem cell fates. *Annual Review of Neuroscience* **25**, 471-490, (2002).
13. Lie, D. C. *et al.* Wnt signalling regulates adult hippocampal neurogenesis. *Nature* **437**, 1370-1375, (2005).
14. Lai, K., Kaspar, B. K., Gage, F. H. & Schaffer, D. V. Sonic hedgehog regulates adult neural progenitor proliferation in vitro and in vivo. *Nat Neurosci* **6**, 21-27,(2003).
15. Ma, D. K., Ming, G. L. & Song, H. Glial influences on neural stem cell development: cellular niches for adult neurogenesis. *Current Opinion in Neurobiology* **15**, 514-520, (2005).
16. Kaji, H., Camci-Unal, G., Langer, R., Khademhoseeini, A. Engineering systems for the generation of patterned co-cultures for controlling cell-cell interactions. *Biochimica et Biophysica Acta* **1810**, 239-250, (2011).
17. Hui, E. E. & Bhatia, S. N. Micromechanical control of cell-cell interactions. *Proc Natl Acad Sci USA* **104**, 5722-5726, (2007).
18. Selden, N. S. *et al.* Chemically programmed cell adhesion with membrane-anchored oligonucleotides. *J Am Chem Soc* **134**, 765-768, (2012).
19. Weber R. J., Liang, S. I., Selden, N. S., Desai, T. A., Gartner, Z. J. Efficient targeting of fatty-acid modified oligonucleotides to live cell membranes through stepwise assembly. *Biomacromolecules* **15**, 4621-4626, (2014).

20. Todhunter, M. E. *et al*. Programmed synthesis of three-dimensional tissues. *Nat Methods* **12**, 975-981, (2015).
21. Gracz, A. D. *et al*. A high-throughput platform for stem cell niche co-cultures and downstream gene expression analysis. *Nature Cell Biology* **17**, 340-349, (2015).
22. Ables, J. L. *et al*. Notch1 is required for maintenance of the reservoir of adult hippocampal stem cells. *J Neurosci* **30**, 10484-92, (2010).
23. Kano, I., Darbouret, D., & Mabic, S. UV Technologies in Water Purification Systems. http://www.learnpharmascience.com/emd/docs/UV%20technologies%20in%20water%20purification%20systems.pdf, (2012).
24. Bonaguidi, M. A. *et al.* In vivo clonal analysis reveals self-renewing and multipotent adult neural stem cell characteristics. *Cell* **145**, 1142-1155, (2011).
25. Hsiao, S. C. *et al.* Direct cell surface modification with DNA for the capture of primary cells and the investigation of myotube formation on defined patterns. *Langmuir* **25**, 6985-6991, (2009).
26. Palmer, T. D., Ray, J. & Gage, F. H. FGF-2 responsive progenitors reside in proliferative and quiescent regions of the adult rodent brain. *Molecular and Cellular Neuroscience* **6**, 474-486, (1995).

Chapter 3: A Multiplexed, Lithographic DNA Approach to Recapitulate Complex Signaling Environments with Controlled Spatial Presentations

This chapter is in part a preprint of a paper currently under review.

Scheideler, O.J., Yang, C., Falcón-Banchs, R., Mosher, K.I., Ciminelli, E.C., Bremer, A.W., Chern, S.A., Schaffer, D.V., Sohn, L.L. A multiplexed, lithographic DNA approach to recapitulate complex signaling environments with controlled spatial presentations. Under Consideration.

3.1 Introduction

The biological processes that underlie both normal mammalian tissue function and pathological dysfunction originate from complex signaling interactions between constituent cells and their surrounding microenvironment *(1-3)*. Heterogeneous and dynamic in nature, this network of extrinsic signals – including soluble cues, cell-cell contact-dependent signals, and "solid-phase" matrix cues – encodes and transmits regulatory information that instruct single-cell behavior *(4, 5)*. While significant technological advances have enabled researchers to investigate cellular responses to these microenvironmental cues by recapitulating endogenous signaling scenarios *in vitro*, fundamental aspects of this signaling environment remain unaddressed – namely, that these cues are modulated by key microenvironmental features, such as temporal dynamics and spatial variation *(6-8)*. This realization that cell signaling events are far more complex than binary (i.e. either on or off) motivates the need for *in vitro* platforms capable of decoupling the roles of these parameters in signaling, thereby providing a complete understanding of how underlying cellular processes orchestrate tissue function.

Of these key contextual parameters, spatial presentation has drawn particular interest since the spatial heterogeneity of a signal alone is sufficient to drive changes in cell response *(9, 10)*. For example, variable spatial organizations of solid-phase extracellular matrix (ECM) components and sequestered cues are capable of altering cell migration velocity in fibroblasts (*11*) as well as influencing the mode of cell division (symmetric versus asymmetric) in single mouse embryonic stem cells (*12*). Similarly, spatial modulation of juxtacrine ligand presentation can tune both neurogenesis in adult neural stem cells (NSCs) (*13*) and invasiveness of breast cancer cells (*14*). The importance of spatial presentation also extends to the coordination among multiple ligands within a larger network of signals. Spatial interactions can occur at a bulk-tissue level, such as the canonical example of antagonizing gradients of bone morphogenic protein and Wnt against Sonic hedgehog that specify neural progenitor subtypes along the dorso-ventral axis of the developing neural tube (*15*). Additionally, spatial interactions can also occur within a more localized microenvironment, such as the adult NSC niche. In particular, heterogeneous distribution patterns of secreted and membrane-associated factors localize across different anatomical layers within the hippocampal dentate gyrus and regulate various stages of adult neurogenesis (*16-19*), offering further biological motivation that instructive cues are encoded in the spatial organization of regulatory signals.

Patterning-based platforms that enable control over cell and/or ligand positioning provide the means to dissect how biology encodes regulatory information through spatial organization. However, mapping the complex interactions between multiple signaling factors while still maintaining high spatial control remains a key challenge. Many current patterning techniques fall short as they lack the specificity to multiplex (i.e. pattern multiple ligands and/or cells). For example, cell-patterning methods – which range from active strategies that utilize microfluidic (*20, 21*), acoustic (*22, 23*), and dielectrophoretic forces (*24, 25*) for manipulating cells to indirect capture methods that modulate surface chemistries by changing surface charge (*26, 27*) or depositing cell-adhesive (*28*) or cell-resistive materials *(29, 30*) – are limited to patterning one or two cell components. On the other hand, direct-deposition methods – such as ink-jet printing (*31*), dip-pen lithography (*32*), and robotic-spot microarray technologies (*33-35*) – that can re-create multifactorial signaling scenarios often sacrifice micron-scale resolution, throughput, and/or rely on inaccessible or uneconomical tools. Furthermore, these methods are often focused on either cells or ligands, but not both.

To address these many limitations, we present a broadly applicable high-throughput DNA-based patterning platform that recapitulates and dissects spatially-regulated signaling events in vitro by directing the assembly of heterogeneous populations of both cells and solid-phase cues with high spatial resolution and precision. Using traditional photolithographic techniques, we engineered a high-throughput method to fabricate and register multicomponent patterns consisting of unique 20 base-pair, single-stranded oligonucleotides onto a glass substrate. These surface DNA patterns then hybridize with, and direct the spatial organization of, complementary oligonucleotides grafted to signaling ligands and/or cells, thereby enabling their surface presentation with lithographic resolution. The resulting highly specific, multiplexed ligand/cell patterns can be used to model and study spatial heterogeneity during cell-cell communication and cell-ligand signaling (Fig. 1a). To demonstrate this platform's unique ability to investigate the role of spatial signal organization within a tissue microenvironment, we use adult NSCs as a model system (36-39). Specifically, we investigate how two competing niche ligands that drive opposing cell fates, fibroblast growth factor-2 (FGF-2) which regulates NSC proliferation (40) and ephrin-B2 which drives NSC differentiation (41), coordinate spatially to instruct NSC-fate decisions at the single-cell level.

3.2 Results

3.2.1 Fabricating Instructive, Multicomponent Surface DNA Patterns with Spatial and Hierarchical Complexity using Photolithography

While DNA-instructed assembly provides a simple and robust solution to coordinate heterogeneous signaling components by capitalizing on the specificity and strong, rapid binding kinetics of Watson-Crick base pairing (*42-45*), we tackled the challenge of engineering a parallel approach to fabricate multicomponent DNA-instructive surfaces. Previously, as described in detail in Chapter 2, we employed a microcantilever-based printing technology to spot oligonucleotides as cell-sized circular features that then capture and assemble heterogeneous cell communities at the single-cell level (*45*). The reproducibility, throughput, and multiplexing capabilities of this method, however, were severely limited. DNA patterns were restricted to those comprised of spotted DNA features that were highly dependent on the humidity of the chamber enclosing the cantilever-based system and on human trial-and-error in identifying the appropriate printing conditions (i.e. printing speed, cantilever contact time, etc.). Furthermore, while the system was programmable to be semi-automated, the time required for complex printing of even a single oligonucleotide could be hours due to the method's inherently serial nature (*46, 47*), effectively precluding its application to printing and registering multiple oligonucleotides.

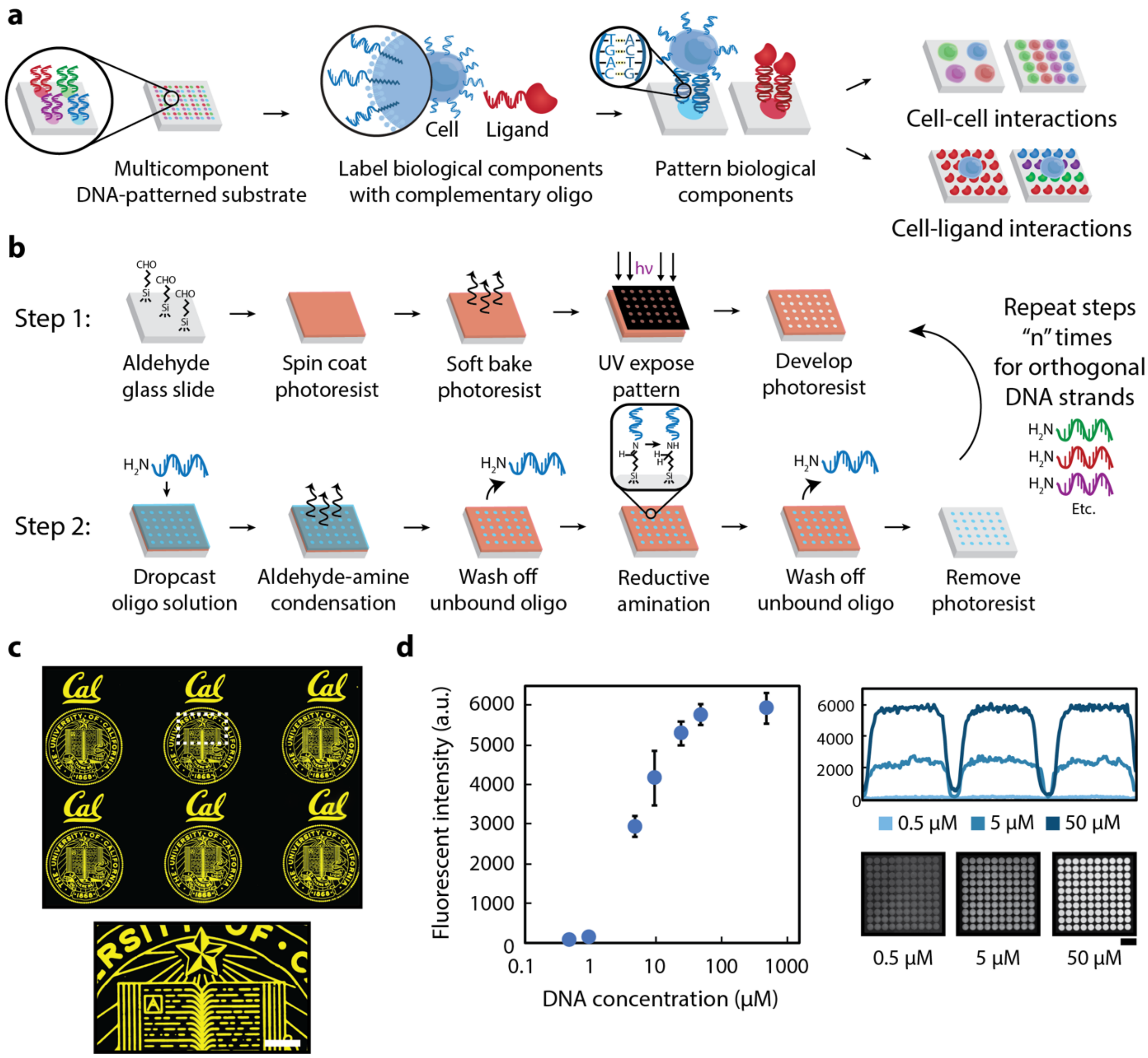

Figure 3.1 High-resolution surface DNA patterning using photolithography. (a) Multicomponent patterns of unique 20 base-pair oligonucleotides instruct the spatial organization of cells and ligands through the hybridization between surface-presented oligonucleotides and complementary oligonucleotide-labeled biological components. (b) Surface DNA patterns are fabricated through the successive utilization of, first, photolithography to define regions of reactive aldehyde groups for oligonucleotide conjugation (Step 1) and, second, a reductive amination step to react covalently the amine-terminated oligonucleotides to the aldehyde-functionalized glass surface (Step 2). Multicomponent DNA patterns are assembled by patterning a new layer of positive photoresist and repeating steps 1 and 2 using unique oligonucleotides. (c) The use of photolithography enables the fabrication of high-resolution, spatially complex DNA patterns. Patterned photoresist is utilized as a mask to conjugate selectively amine-terminated oligonucleotides, which can be visualized by hybridizing a complementary fluorescent oligonucleotide. (d) A dynamic range of surface DNA pattern intensities (left) can be achieved by tuning the DNA solution concentration. Representative fluorescent intensity profiles (right, top) and their corresponding images of a 40-μm DNA spot array (right, bottom) are illustrated

for a low (0.5 μM), medium (5 μM), and high (50 μM) DNA concentration. Error bars are standard deviation and *n*=3. All scale bars represent 100 μm.

Here, we present a major advance of the underlying surface DNA-patterning concept not only by expanding the patterning capabilities of DNA-based assembly to encompass both solid-phase ligands and cells but also by developing a high-throughput, parallel strategy that has increased multiplexing capabilities, flexibility to pattern any geometry, high spatial resolution, and ease in registering multiple DNA layers. Specifically, we engineered a strategy that uses patterned photoresist as a physical template – one that we demonstrate can be iteratively removed and re-patterned to conjugate numerous, orthogonal oligonucleotide strands. As illustrated in Fig. 1b, there are two key steps for achieving this multicomponent, DNA-patterned platform. The first involves traditional photolithography, where patterned photoresist serves to 1) expose selective areas of surface aldehyde groups for DNA conjugation, 2) act as a physical barrier to prevent conjugation to unexposed aldehyde groups, and 3) preserve protected, unconjugated aldehyde functionality for subsequent, multilayered DNA patterning steps. The second step covalently immobilizes 20 base-pair oligonucleotides to the glass substrate by reacting the primary amine group at the 5' end of the DNA with the surface-exposed aldehyde groups. See Methods for additional protocol details.

Our approach of UV-patterning photoresist offers the distinct advantage of defining, with great control and precision, complex spatial patterns across different length scales (i.e. from microns to millimeters and, in turn, from sub-cellular to bulk population) and over large areas (up to thousands of mm^2) within minutes. Fig. 1c shows the resulting high-resolution surface DNA patterns that can be achieved with this method, visualized by hybridizing a complementary, fluorescent-labeled oligonucleotide. In-depth characterization of DNA-patterning steps revealed that optimization of both the buffer composition and the combination of condensation time and temperature played critical roles in achieving robust surface DNA patterns (Supplementary Fig. 1). An additional key advantage of our method is the tunable control over DNA concentrations patterned onto the substrate. Such control enables variations in signal concentration, as is found with morphogen gradients during development (*48*). By varying the concentration of the oligonucleotide solution dropcast over the photoresist patterns, we achieved a >100-fold range of fluorescent intensities (Fig. 1d).

To highlight the utility of this DNA-based engineering approach for modeling spatial heterogeneity *in vitro*, we demonstrated that lithographically-defined DNA surfaces are highly functional. As shown in Fig. 2a, microfabricated DNA patterns were capable of organizing a bulk, oligo-labeled NSC population (*49, 50*) with high spatial precision, demonstrating the potential to re-create complex cell-based tissue structures, such as the hippocampal dentate gyrus (*51*), crypts of intestinal villi (*52*), or hepatic lobules (*53*). To determine the minimum DNA concentration necessary for cell patterning, we tested cell-capture efficiencies of 20 μm-diameter spot arrays over a concentration range from 0.5-100 μM. Our results show that a minimum concentration of 5 μM was necessary to capture at least one oligonucleotide-labeled NSC per spot (Fig. 2b). Above this concentration, we observed a high average capture rate of >90%. While DNA concentration can influence cell capture, so too can microfabricated pattern feature size. Increasing the diameter of DNA-patterned circle features resulted in a robust and reproducible increase in the number of cells captured per spot (Fig. 2c). Moreover, when the diameter was commensurate with the size of

NSCs (~15 µm), single-cell capture was achieved (Supplementary Fig. 2). As we demonstrate later, this capability enables high-throughput clonal analysis.

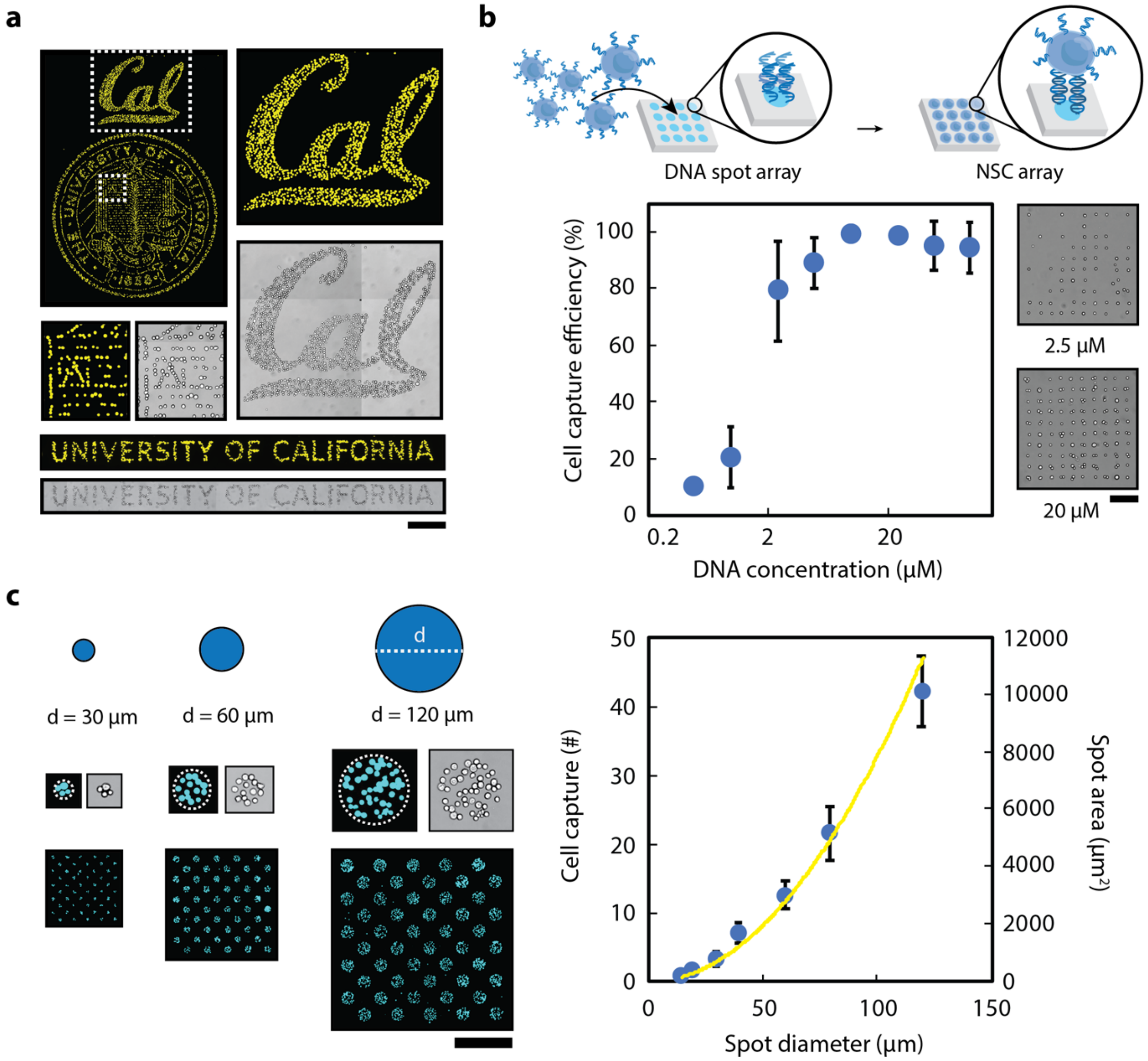

Figure 3.2 Microfabricated DNA patterns direct the capture of NSCs. (a) Patterned surface oligonucleotides organize a fluorescently-labeled population of NSCs with high spatial precision through Watson-Crick base pairing between the surface-conjugated DNA and the temporary lipid-modified DNA tethered to the cell membranes. (b) Cell-capture efficiency of 20 µm-diameter DNA-spot patterns was dependent upon the concentration of DNA solution with a significant drop of efficiency occurring at a concentration below 5 µM (left). This is seen in the representative NSC-patterned images of a 10 x 10 array of 20 µm-diameter DNA spots for a range of concentrations (right). (c) The number of DNA-captured cells can be controlled by tuning the feature size of the DNA patterns. Representative images (left) demonstrate DNA spots with different diameter dimensions capturing varying numbers of fluorescently-labeled NSCs. Moreover, an increase in diameter size of DNA-patterned spots (right) results in an increase in cell-capture number (blue dots) that follows a similar increasing trend in spot area (yellow line). All error bars are standard deviation and *n* values are reported in Table S3. Scale bars represent 500 µm.

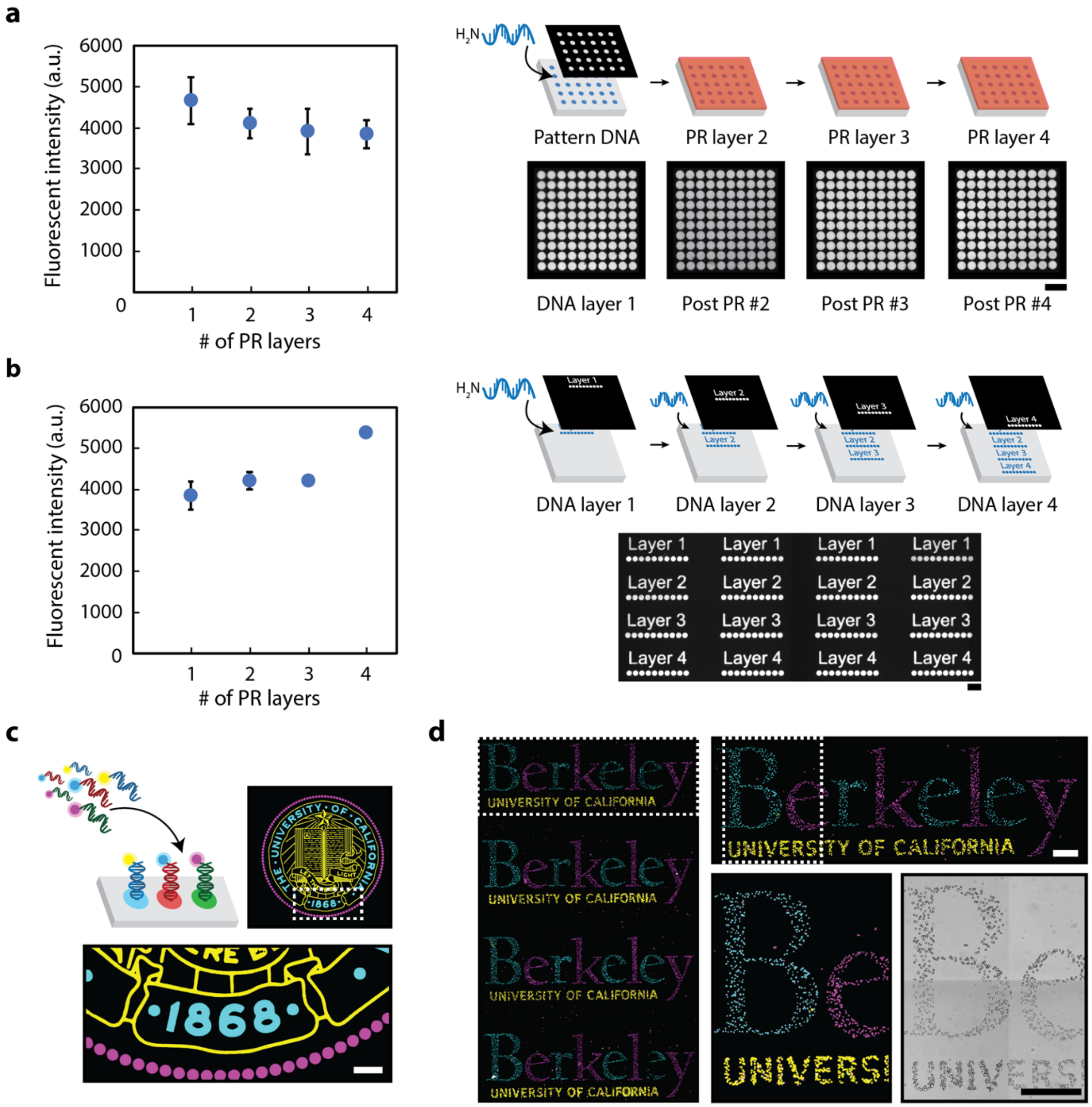

Figure 3.3 Scalable, multicomponent DNA patterns organize heterogeneous cell populations. Characterization of multiple fabrication steps highlight the compatibility of photolithography with DNA patterning. (a) The integrity of surface DNA patterns is preserved – as indicated by the ability to hybridize with its complementary, fluorescent oligo counterpart – when subjected to repeated photolithographic fabrication steps, as would occur when patterning multiple DNA layers (i.e. removal of photoresist (PR) with acetone and patterning of a new layer). Despite a slight initial drop upon the application of a second PR layer, the average fluorescent intensity of DNA-patterned features remains robust upon a third and fourth photolithography step. (b) The functionality of the surface-modified aldehyde groups, which is necessary for DNA conjugation, is also preserved during successive PR layer applications. Additional photolithography steps yield surface DNA patterns with robust fluorescent intensities. Scale bars represent 100 μm. All error bars are standard deviation and *n*=3. (c) Micron-scale registration of 3 complex DNA patterns were patterned and visualized with unique complementary fluorescent oligonucleotides. (d) To highlight their functionality, multicomponent DNA patterns assembled three distinct, fluorescently-tagged NSC populations with high spatial control and specificity by labeling each population with unique complementary, lipid-modified oligos that insert into the cell membrane. Scale bars represent 500 μm.

To fabricate multicomponent DNA patterns, we found that the aforementioned two-step process can be repeated after dissolving the patterned photoresist in acetone and spinning on a new photoresist layer to define a new spatial mask that then guides the conjugation of additional oligonucleotide strands. To validate the robustness and reproducibility of our engineering approach, we examined two key potential pitfalls. First, we demonstrated that the repeated application and patterning of a new photoresist mask does not adversely affect the first DNA-patterned layer. As Fig. 3a shows, the first DNA pattern retained functionality (i.e. the ability to hybridize) when subjected to iterative removal and application of three additional photoresist layers. In contrast, re-patterning the same photoresist layer for a second DNA pattern resulted in contamination of the first DNA layer (Supplementary Fig. 3). Thus, the application of new photoresist layers preserves the integrity of the previously-patterned DNA layers, while also allowing for the selective exposure of additional aldehyde regions for multicomponent conjugation. Second, we demonstrated that the actual photolithographic steps – particularly, 1) heating, 2) photoresist removal with acetone, and 3) resist development with a highly alkaline solution (pH > 10) – do not compromise the aldehyde groups on the glass substrate, as DNA patterns fabricated from subsequent layers retained high-intensity fluorescent values (Fig. 3b). Extensive characterization established that multilayer patterning can be extended to at least 10 layers without loss of fidelity (Supplementary Fig. 4) and that tunability of patterned DNA concentrations can also be achieved for multiplexed DNA patterns (Supplementary Fig. 5). Fig. 3c and d demonstrates the successful registration of three complex DNA patterns and the robust functionality of multiplexed surface DNA patterns, respectively.

3.2.2 Multicomponent DNA Patterns Instruct the Presentation of Heterogeneous Proteins with High Spatial Control

A key step for demonstrating the unique capabilities of our DNA-directed strategy is utilizing the surface DNA patterns to control the spatial organization of solid-phase ligands. Having such control would enable, for instance, emulating the presentation of ECM-sequestered or cell surface-tethered signals (*41, 54*). Our approach of using DNA as a programmable intermediary capture agent ensures that multiple ligands, each labeled with a different complementary oligonucleotide, can be assembled from a single mixed solution flowed across the DNA-patterned surface. To label ligands of interest with oligonucleotides, we utilized the heterobifunctional linker, dibenzocylcooctyene (DBCO)-polyethyleneglycol (PEG4)-maleimide (Fig. 4a). Briefly, ligands were designed to contain a free terminal cysteine to react with the maleimide group on the crosslinker, thereby introducing a DBCO moiety on the ligand that allowed for subsequent click chemistry reaction with an azide-modified oligonucleotide label. As a proof-of-concept, we conjugated an oligonucleotide to recombinant enhanced green fluorescent protein (eGFP) (Supplementary Fig. 6). Surface DNA patterns directed the spatial organization of eGFP and successfully maintained robust protein patterns over long-term cell culture (Supplementary Fig. 7a). In addition, neither eGFP lacking an oligonucleotide label nor eGFP containing a non-complementary label resulted in protein capture (Supplementary Fig. 7b), indicating that complementary DNA sequences were necessary to achieve high specificity of eGFP patterns. To visualize patterned ligands and to serve as a relative readout of patterned protein concentration, a Cy5 dye was included at the 3' end of the oligonucleotide label (Fig. 4b). Finally, to highlight that spatial control could be extended to multiple solid-phase cues, we conjugated a second oligo strand to mCherry and demonstrated tunable patterns of mCherry and eGFP (Fig. 4c).

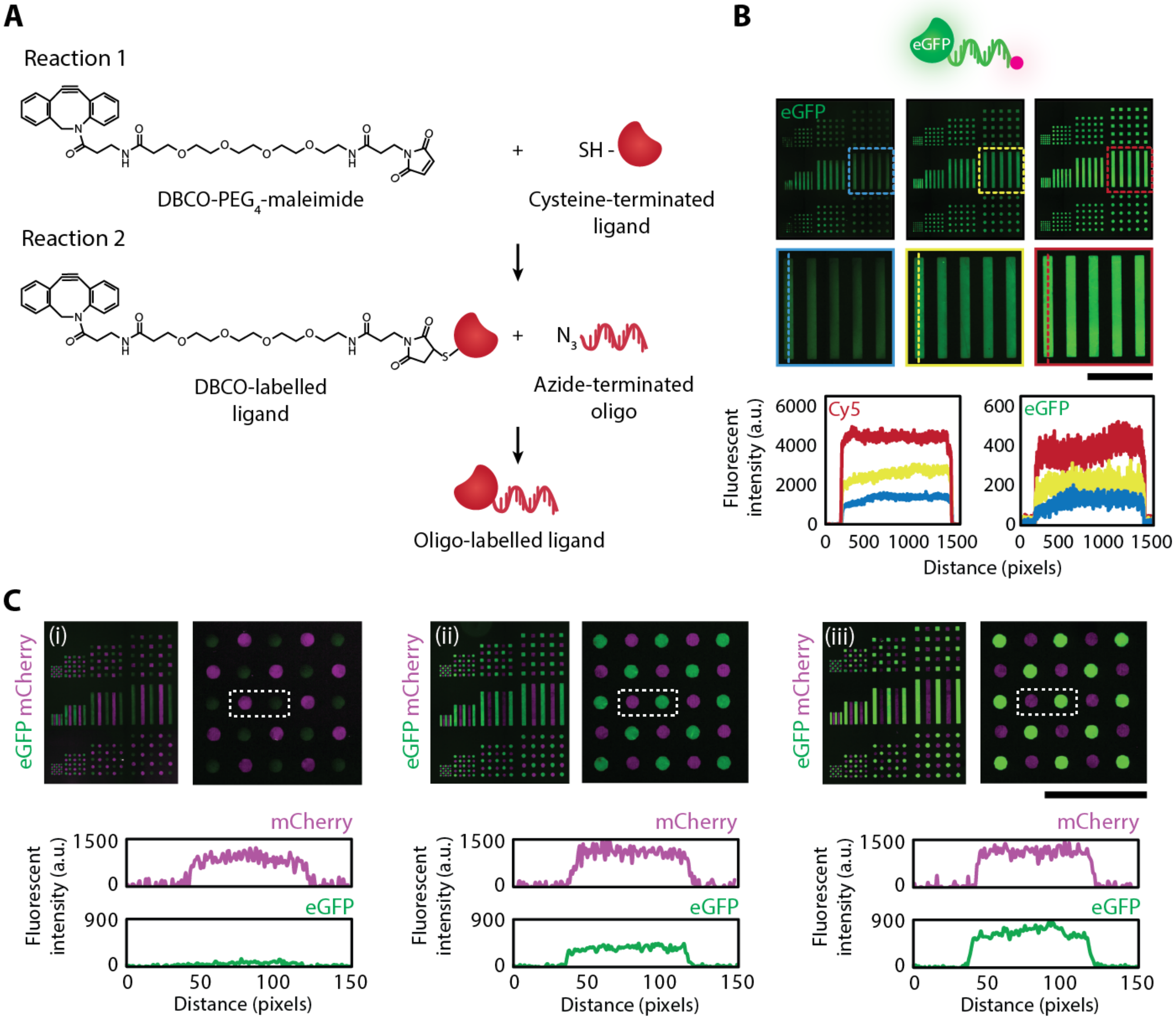

Figure 3.4 Microfabricated DNA patterns direct the spatial organization of solid-phase ligands. (a) The heterobifunctional linker, dibenzyocyclooctyne (DBCO) – polyethylene glycol (PEG4) – maleimide, enables covalent labeling of ligands of interest with an oligonucleotide label. A free sulfhydryl group on the protein is reacted first with the maleimide moiety on the crosslinker, introducing a DBCO functional group to the ligand that then reacts via click chemistry to an azide-terminated oligonucleotide. (b) The incorporation of an oligonucleotide label possessing a fluorescent tag enables imaging and monitoring of DNA-directed ligand patterns. For proof of concept, enhanced green fluorescent protein (eGFP) with a Cy5 tag was assembled using DNA surface patterns (top). Trends in fluorescent intensity profiles for the patterned protein and the fluorescent tag closely matched one other when tuning surface DNA concentrations, suggesting that the fluorescent oligonucleotide label can also be employed as a relative readout of patterned protein concentration (bottom). (c) Multicomponent DNA surface patterns enable tunable control over each ligand concentration as evident in the DNA assembly of eGFP and mCherry. mCherry concentration was held constant as eGFP concentration was tuned as quantified by the change in eGFP fluorescence intensity (bottom) and visualized in the fluorescent composite images (top). Scale bars represent 500 µm.

3.2.3 Applying Multiplexed Surface DNA Patterns to Dissect the Role of Spatial Organization on Competing NSC-Fate Decisions

As a first biological demonstration of the utility of our method, we focused on modeling complex signaling scenarios within the adult NSC niche. Stem cell niches are canonical examples of specialized microenvironments that coordinate the behavior (i.e. quiescence, activation, survival, migration, lineage commitment, etc.) of residing stem cells in response to physiological or pathological directives (*58-61*). Stem cells must decide whether to self-renew, thereby actively contributing to the reserve of stem cells within the niche, or to differentiate into specialized, mature progeny. The complex balance between these two competing fate choices ensures that a stem cell population can maintain homeostasis as well as respond to organismal needs. Here, we investigated how adult hippocampal NSCs resolve the competition between opposing fate cues and to what extent spatial organization of a signal offers biophysical context to inform this decision. We leveraged our technique's spatial control over both cells and solid-phase cues to recapitulate and modulate NSC interactions with two fate-conflicting niche signals, FGF-2 and ephrin-B2. While FGF-2 operates as both a soluble and ECM-sequestered cue to promote proliferation and stem cell maintenance (*40, 62*), ephrin-B2 is a key juxtacrine signal presented by neighboring hippocampal astrocytes that drives neuronal differentiation by signaling through the EphB4 receptor on NSCs (*13, 41*). We took advantage of the high spatial control of our DNA-based system to model solid-phase competition between FGF-2 and ephrin-B2, thereby exposing single-NSC cultures to distinct spatial organizations of the ligands and conducted time-lapse experiments over the course of differentiation to study the dynamics of the single-cell cultures and correlate them with endpoint cell fate.

To enable high-throughput clonal analysis in our DNA-based platform, we microfabricated arrays of 15 μm-diameter DNA spots to direct the capture of oligonucleotide-labeled single NSCs. We then used photolithography to pattern a cell-resistive, non-biofouling material, polyacrylamide (PA), to create "microisland" features that isolate single-cell patterns from each other during culture (Supplementary Fig. 8). The combination of DNA and PA patterns provided the high-throughput power of tracking 1000's of single NSCs over a 5-day differentiation period and subsequently performing clonal analysis by immunostaining to probe for cell fate (Supplementary Fig. 9). To investigate first the contribution of solid-phase presentation of the individual niche cues, FGF-2 or ephrin-B2, on NSC-fate decisions, we prepared both ligands with unique oligonucleotides labeled with a Cy3 and Cy5 fluorescent dye, respectively, for visualization (Supplementary Fig. 10 and 11) and patterned the complementary oligonucleotide within single NSC microislands to direct the subsequent ligand-oligo conjugate. Because of the challenge of producing recombinant ephrin-B2 in high yield, we replaced the full-length protein with a mimetic peptide, TNYLFSPNGPIARAW, that exhibits nanomolar binding affinity to its cognate EphB4 receptor (*60*). As expected, FGF-2 and the ephrin-B2 peptide individually promoted opposing cell fates (Supplementary Fig. 12). Interestingly, immobilized FGF-2 was a potent activator of high proliferation and low differentiation across all patterned ligand concentrations in contrast to the lower proliferation rate and higher differentiation observed with decreasing concentrations of soluble FGF-2 (Supplementary Fig. 9). Our results suggest that the activity of FGF-2 is more potent as a solid-phase than as a soluble cue, consistent with prior work on other immobilized growth factors (*61*). For the ephrin-B2 peptide, we found a minimum concentration threshold was necessary before observing high neuronal differentiation and low proliferation rate. Moreover,

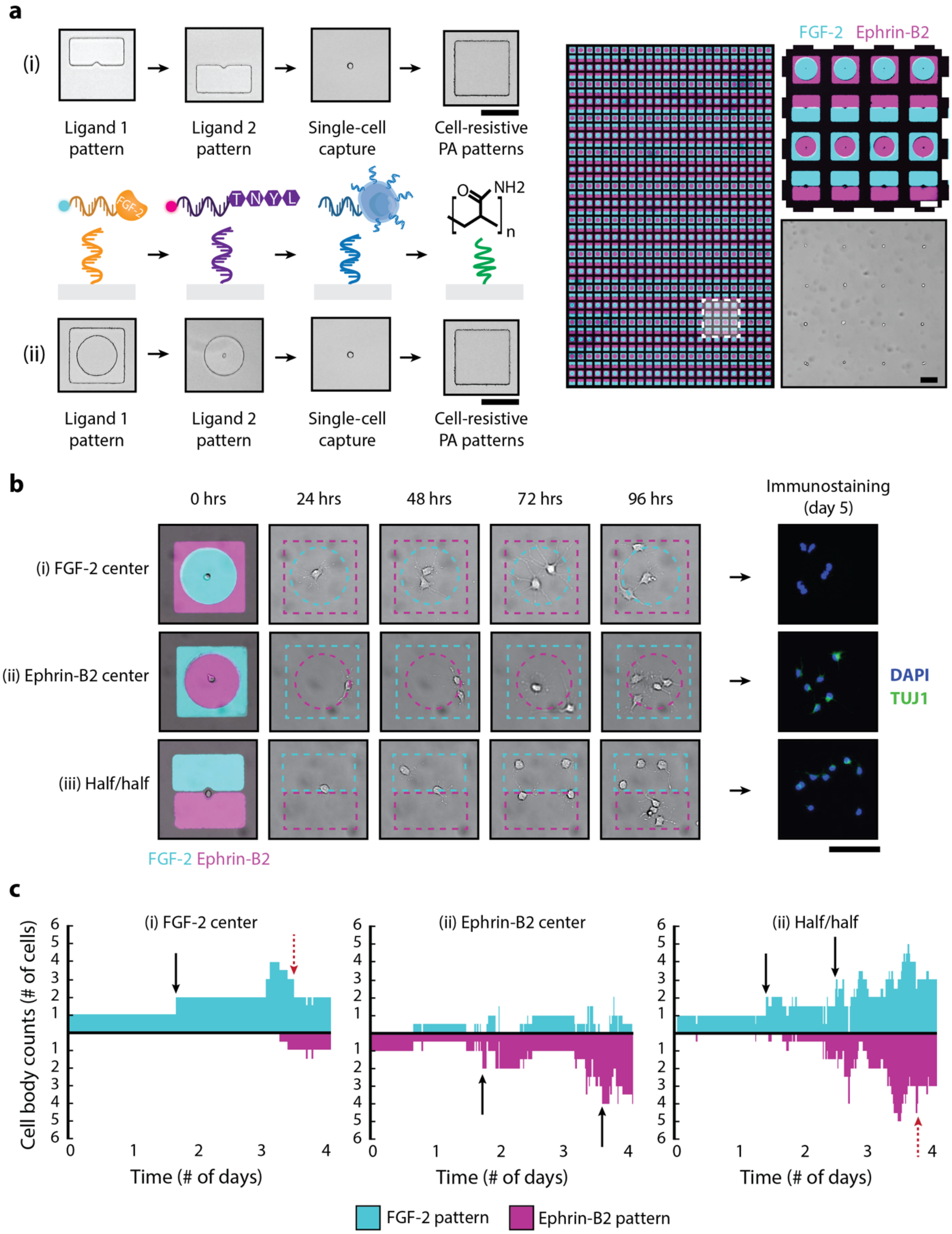

Figure 3.5 Multicomponent DNA patterns enable tight spatial control and investigation of the presentation of competing ligand cues, FGF-2 and ephrin-B2, on single NSC behavior. (a) Overview of two 4-layer DNA patterning schemes that direct the assembly of FGF-2, ephrin-B2-mimetic peptide, single NSCs, and PA patterns (left).

(i) The top PR patterns segregate each ligand to one half of the microisland, exposing the patterned single NSC to both solid-phase cues equally, while (ii) the bottom PR patterns forces the presentation of one ligand over the other. A representative image (right) of a large-area microisland array containing both presentation strategies; the patterned ligands are visualized by their respective fluorescent oligonucleotide labels (FGF-2 in cyan and ephrin-B2 in magenta). The zoomed-in insert highlights the simultaneous assembly of three different spatial presentation configurations: half/half, FGF-2 center, and ephrin-B2 center. (b) Representative time-lapse images illustrating cell proliferation and migration for 3 sample microislands of the different ligand spatial configurations and their corresponding day 5 immunostaining results: (i) FGF-2 center, (ii) ephrin-B2 center, (iii) half/half. (c) Quantification of cell body counts within FGF-2 (cyan) and ephrin-B2 (magenta) patterns over 4-day time-lapse utilizing custom analysis script, corresponding to the same 3 sample microislands in part (b). All scale bars represent 100 μm.

with increasing peptide concentrations, heterogeneity of single-cell microislands decreased, converging onto a similar end fate of a single differentiated neuron.

Having observed that FGF-2 and the ephrin-B2-mimetic peptide drive divergent cell fates in single NSCs, we next employed our DNA-based method to assemble and model scenarios in which NSCs are presented with both conflicting cues, thereby emulating the expression of both of these signals by hippocampal astrocytes contacting NSCs (*41, 62*). We capitalized upon our system's spatial control over both ligands and cells to modulate ligand presentation within single-cell microislands cultures. Two DNA patterning strategies were implemented in parallel (Fig. 5a). The first involved constraining single NSCs to the center of either an FGF-2 region or ephrin-B2 peptide region, with the second ligand patterned at the microisland periphery. The second strategy positioned single NSCs at the interface between two, half/half ligand patterns with equal access to both solid-phase signals. Thousands of microislands encompassing all three spatial arrangements were assembled simultaneously, as shown in Fig. 5a (right).

To assess whether variations in ligand spatial organization were sufficient to alter NSCs interactions with the two solid-phase signals and also whether this ultimately translated to differences in end-fate decisions, microislands were imaged over the course of a 4-day time-lapse (Supplementary Movies 1-3) to track cell body distributions across the ligand-patterned regions. Time-lapse snapshots of (i) FGF-2-center, (ii) ephrin-B2-center, and (iii) half/half microislands are provided in Fig. 5b (left) along with their corresponding day 5 immunostaining results (right). Custom computational analysis (Supplementary Fig. 13 and 14) provided the capability to map out the dynamic cell-ligand interactions of each microisland culture and track how the initial parent NSC and its subsequent progeny distributed themselves over time in response to the organization of these competing niche cues (Fig. 5c).

Harnessing these analytical capabilities, we first assessed how spatial modulation of FGF-2 and ephrin-B2 "domains" shaped the interactions of the single NSC cultures with these two competing niche ligands. For the FGF-2-center microislands, we observed high average cell occupancy within the FGF-2 domain that persisted over all four days (Fig. 6a(i)). In contrast, ephrin-B2-center microislands exhibited a much wider distribution of average cell occupancies in the ephrin-B2 region on the first day alone (Fig. 6a(ii)) and, by the second day, the majority of microislands no longer occupied ephrin-B2 substantially. This observation was further corroborated upon analyzing the half/half microislands, where single NSCs had the freedom to "choose" either protein-patterned region (Fig. 6a(iii)). Here, average cell occupancy within FGF-2 remained far greater than occupancy within ephrin-B2 or at the interface of both domains, mimicking the FGF-2-center microislands.

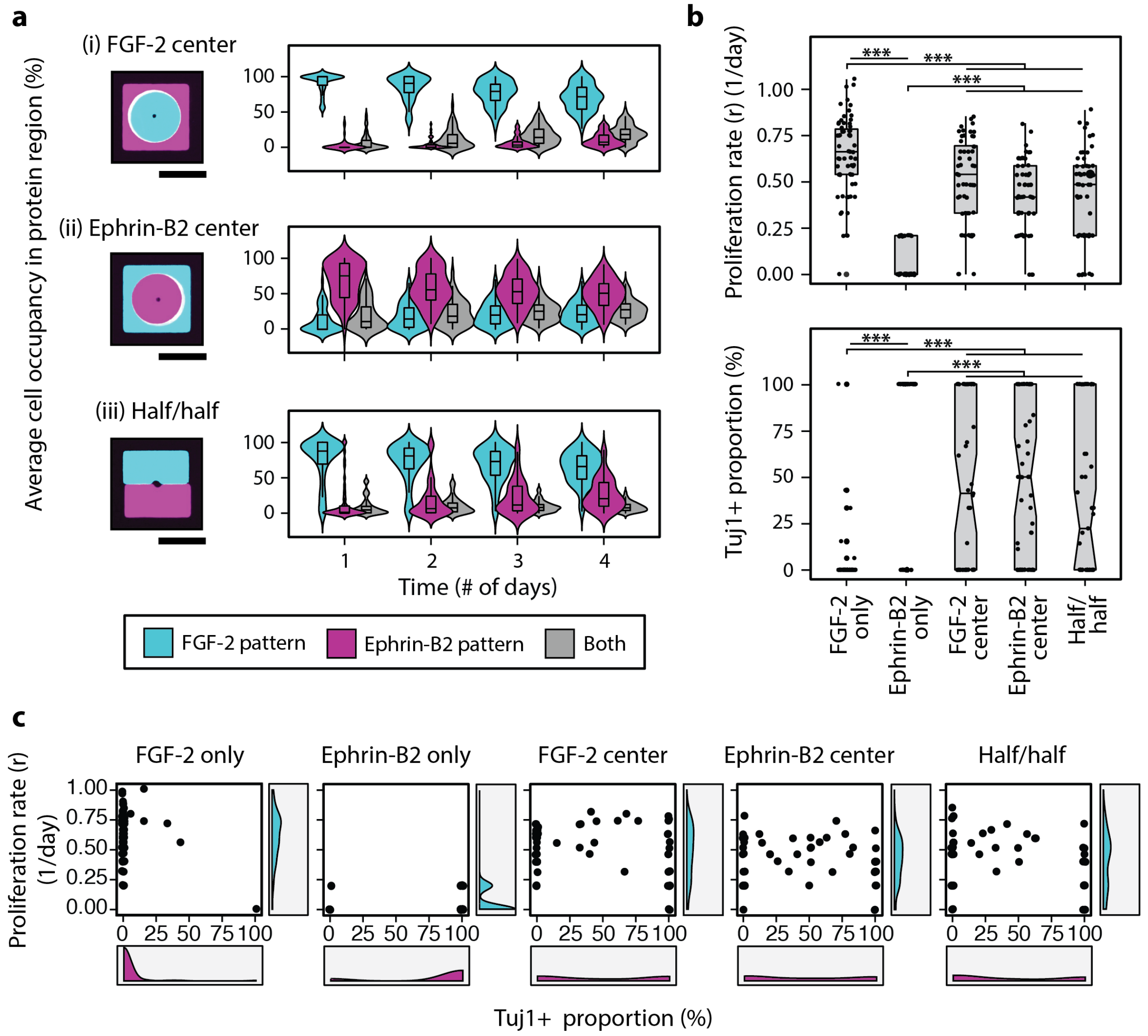

Figure 3.6 Cell occupancy in response to various ligand presentations of FGF-2 and ephrin-B2 and resulting end fate after 5-day differentiation. (a) Average cell occupancy of cell bodies within the FGF-2 (cyan), ephrin-B2 (magenta), and spanning both (grey) protein-patterned regions were tracked over time for each of the three ligand spatial presentations: (i) FGF-2 center, (ii) ephrin-B2 center, and (iii) Half/half. A strong spatial bias towards FGF-2 was observed. (b) Analysis of end fate through quantification of proliferation (top) and neuronal differentiation (bottom) reveal that, despite spatial preference towards FGF-2, some NSC microislands integrated both signals, generating significant heterogeneity. (c) The potential identification of distinct subpopulations that give rise to this heterogeneity was tested by comparing proliferation rate vs. Tuj1-positive differentiation on a per microisland basis. However, the heterogeneity in single NSC response to the presentation of both ligands was further highlighted as permutations of high/low differentiation and proliferation were present for all three competing ligand presentations. *n* = 55 for each ligand presentation. All p-values obtained from Tukey-Kramer test. ***$p<0.001$. All scale bars represent 100 µm.

Having observed NSC preference for FGF-2 over ephrin-B2, we then immunostained clonal microislands to investigate whether this cell-occupancy bias translated to cell-fate decisions. A comparison of the three different ligand spatial presentations against FGF-2-center and ephrin-B2-center microislands (Fig. 6b) revealed that one niche signal did not exclusively dominate over the other. The three different ligand-competition presentations displayed significantly higher proliferation rates over the ephrin-B2-only condition yet were still significantly lower than the FGF-2-only microislands. With regards to differentiation, we anticipated that the FGF-2 preference would result in cells in these microislands having a more proliferative, stem-like state. However, a surprisingly wide distribution of Tuj1-positive differentiation proportions was observed, including microisland subpopulations spanning both extremes of 100% and 0% neuronal differentiation as well as a few displaying partial neuronal differentiation.

To provide additional insight into this heterogeneity, we further investigated the relationship between differentiation and proliferation for each of the microisland patterns (Fig. 6c). We observed a clear phenotype for the FGF-2-center microislands in which an increase in Tuj1-positive differentiation correlated with a decrease in proliferation. In the case of the ephrin-B2-center microislands, we observed consistently low levels of proliferation for both high and low differentiation. However, for the microislands containing both ligands in competition, there was no clear trend as microislands exhibiting both high and low differentiation exhibited wide proliferation-rate distributions. Therefore, the observed mix of proliferation and differentiation strongly indicates that these cells are integrating both signals and that the added presence of either cue is insufficient to instruct or completely alter cell-fate decisions, despite NSC's spatial preference toward occupying FGF-2. This outcome highlights the inherent complexity and heterogeneity of NSC behavior and further motivates the need for additional in-depth single-cell analysis to identify potential contributing factors that give rise to this heterogeneity. The unique power of our platform is that it provides the very foundation to do so.

We next dissected the dynamics of individual microislands by tracking the changes in average cell-body occupancy within the FGF-2-patterned region over time and subsequently grouped microislands according to end fate. As shown in Supplementary Fig. 15a, each microisland's trajectory is represented by a line. However, rather than identifying unique consensus trajectories for the "Low (0%)", "Medium (0-100%)", and "High (100%)" neuronal differentiation bins or a minimum and/or maximum occupancy threshold that could be indicative of cell fate, we observed microislands with similar FGF-2-occupancy patterns spread across all three differentiation categories. More remarkably, we observed instances of single-NSC cultures that underwent differentiation despite having nearly 100% FGF-2 occupancy. A closer examination of these particular cases (Supplementary Fig. 15b) revealed a potential source for this paradox, as neurites were visualized extending across into the ephrin-B2 region, such that cells could potential sense and probe both protein patterns throughout differentiation. While it is unclear whether transient sampling of the ephrin-B2 differentiation cue by a short neurite is sufficient to drive a long-term cell-fate decision, future work to track neurite dynamics, which represents an additional computational image analysis challenge, and analyze temporal aspects of cell occupancy within each ligand-patterned region may help elucidate further how single NSCs sense and integrate conflicting instructive cues.

3.3 Discussion

Here, we introduced a photolithography-based strategy to fabricate instructive, multiplexed DNA surface patterns that enable the recapitulation and dissection of complex signaling scenarios *in vitro* by directing the assembly of heterogeneous cells and/or solid-phase ligands with high spatial precision. We demonstrated the use of patterned photoresist as a template to guide DNA conjugation and coordinate control over multiple DNA strands (i.e. multiplexing) without sacrificing spatial control and resolution. A key feature of this platform is that photoresist masks can be removed and new masks patterned to conjugate up to 10 oligonucleotide strands with prior DNA layers or patterns retaining their functionality.

The unique capabilities of this platform allow one to address complex biological questions, and as a first demonstration, we utilized our microfabricated DNA patterns to investigate how NSCs resolve conflicting solid-phase niche cues (i.e. FGF-2 and ephrin-B2) that drive opposing cell fates (i.e. proliferation and differentiation) and how spatial heterogeneity may offer information to direct this decision. We capitalized on our system's high spatial control over both cells and ligands to segregate and study 1000's of single NSCs within microislands containing various spatial arrangements of the two ligands. By modulating the spatial presentation of these two cues and subsequently tracking average cell-body occupancy within the ligand-patterned regions, we discovered a strong bias in spatial occupancy to the FGF-2-patterned regions. This bias may have been driven by the ephrin-B2-mimetic peptide acting as a repulsive cue, which aligns with previous findings of Eph/ephrin guiding tissue boundary formation and axon extension through cell repulsion (*63, 64*). However, further investigation into downstream end fate revealed that, despite their spatial preference for FGF-2, NSCs still "listened" to the ephrin-B2 differentiation cue. Simultaneous sensing of both may enable a stem cell clone to balance survival, proliferation, and differentiation to yield a desired number of new neurons while maintaining a stem cell reservoir.

Another fundamental strength of our DNA-based patterning system is that it offers a foundation to tease apart the underlying contributions to observed behavior – contributions that could have easily been obscured in bulk-population studies. While average cell regional occupancy alone may not be indicative of end fate, analysis of single microisland cultures revealed dynamic neurite processes extending across the ligand patterns, sometimes synchronized with cell-body occupancy and sometimes in opposition. Future work will include tracking of neurite-ligand interactions as well as investigating the temporal aspect of cell-ligand interactions to provide additional insight into key factors that push single NSC towards differentiation.

Although we focused on dissecting the influence of spatial presentation of cues within the adult NSC niche, our DNA-based patterning platform is broadly applicable to studying a host of other tissue systems. Moreover, increased pattern complexity is possible, given the ease and parallel nature of photolithography. Pattern resolution is diffraction limited to the wavelength of light used to pattern the resist (100's of nm), the numerical aperture of the lens utilized for patterning, and the type of resist, itself. For cases where submicron feature size is needed, electron-beam lithography may be used to create templates. Registration of one mask pattern to the next is dependent on the alignment-mark design and the photolithography tool (whether automated or manual). In general, our novel DNA platform's use of established photolithographic techniques affords a low-adoption barrier, where this system can be easily utilized to elucidate complex signaling logic for a broad range of cells and tissues, such as the nervous system, immune system, and tumors.

3.4 Methods

Micropatterning 20-base pair (bp) amine-terminated oligonucleotides with positive photoresist

Traditional photolithography was employed to pattern aldehyde glass substrates with positive photoresist. S1813 photoresist (Shipley) was spun onto aldehyde-functionalized glass slides (Schott Nexterion) at 3,000 RPM for 30 seconds and subsequently heated for 1.5 minutes on a 100°C hotplate. Photoresist-coated aldehyde slides were exposed selectively to UV light (365 nm; 260 mJ cm^{-2}) with a mask aligner (Karl Suss MJB 3) using a custom mylar mask (Fineline Imaging). Patterns were developed using MF-321 developer (Shipley), washed with 18 mΩ deionized (DI) water, and dried with dry nitrogen gas. Resolution of patterning is limited by the wavelength of light used in the exposure system.

Immediately following photolithography, a 5'-amine-modified, 20-bp oligonucleotide (IDT, Eurofins) solution prepared in 50 mM sodium phosphate buffer (pH = 8.5) was dropcast over the photoresist patterns. Slides were covered with a petri dish to prevent evaporation, and the DNA solution was allowed to incubate for 5 minutes. Slides were then heated for 1 hour in a 75°C oven to induce the formation of Schiff bonds (C=N) between the terminal amine on the DNA and the aldehyde on the glass surface. Slides were then briefly submerged in 0.4% sodium dodecyl sulfate (SDS) in DI water and rinsed with plain DI water to remove excess DNA. To conjugate covalently the DNA strands to the surface aldehyde groups – thereby, converting the hydrolysable Schiff base to single C-N bonds – reductive amination was conducted at room temperature for 15 minutes in 0.25% sodium borohydride (Sigma) in 1X PBS. Upon completion, a second rinse with DI water was performed. To remove the positive photoresist, slides were thoroughly rinsed first with acetone and then DI water, followed by drying with dry nitrogen gas.

The above steps were repeated to micropattern orthogonal DNA strands (as illustrated in Fig. 1b), starting with spinning on a new layer of positive photoresist. To align multiple DNA patterns, a microscope with a 10X objective was employed to register fiducial markers on subsequent mylar photomasks to pre-fabricated metal alignment markers on the DNA glass substrate. Completed DNA-patterned slides were stored under vacuum until ready for biopatterning. A complete list of DNA sequences is provided in Table S1.

Patterning metal fiducial markers for multicomponent DNA registration

Prior to all DNA patterning, metal alignment markers were fabricated on the aldehyde glass substrate using standard photolithography. Similar to DNA patterning, positive photoresist (Shipley 1813) was photopatterned using a mask aligner (Karl Suss MJB 3) followed by the deposition of a 100 Å thin film of titanium via electron-gun evaporation. Photoresist and excess metal were removed by acetone lift-off. Slides were then washed with DI water, dried with dry nitrogen gas, and stored under vacuum. Precision of DNA pattern registration is limited by lithographic alignment.

Characterizing DNA patterns with complementary fluorescent DNA

Substrates were blocked at room temperature in 2% bovine serum albumin (BSA, Sigma) in 1X phosphate buffered saline, pH 7.4 (PBS) for 1 hour to minimize nonspecific adsorption. Complementary, fluorescently-tagged oligonucleotides were prepared at 0.2 µM in 2% BSA and incubated for 5 minutes on a shaker at room temperature. The substrate surface was then washed 4x with PBS and imaged using an ImageExpress Micro (IXM) high-throughput, automated imager. Complementary oligonucleotide sequences and their conjugated fluorophores are listed in Table S1.

Cloning and expression of cysteine (Cys)-terminated recombinant proteins in Escherichia coli

The DNA fragments encoding enhanced green fluorescent protein (eGFP) and mCherry were subcloned into a T7 expression vector with a 6xHis-tag at the N-terminus to allow for downstream purification and a Cys residue at the C-terminus to enable conjugation with a single-stranded oligonucleotide label. A T7 plasmid containing 6xHis-fibroblast-growth-factor 2(FGF-2)-Cys was a gift from the UC Berkeley QB3 MacroLab facility. All constructs were confirmed via sequencing and subsequently transformed into Rosetta 2 (DE3) competent *E. coli* cells.

For protein production, 20 mL of an overnight culture was seeded into 1L of Terrific Broth (TB) supplemented with 100 µg/mL of ampicillin and allowed to grow at standard growing conditions (37°C, 220 rpm) until an OD_{600} = 0.6. The culture was then induced with isopropyl β-D-1-thiogalactopyranoside (Thermo Fisher Scientific) at a final concentration of 1 mM and allowed to shake for an additional six hours at 30°C prior to being harvested by centrifugation (5,000g, 20 min, 4°C). Bacterial pellets were stored at -80°C until ready for purification.

Recombinant protein purification using gravity flow chromatography

Frozen bacterial pellets were thawed on ice and re-suspended in 30 mL of lysis buffer (50 mM NaH_2PO_4, 300 mM NaCl, 10 mM Imidazole, pH = 8) supplemented with 1 mg/mL of lysozyme (Sigma), 200 µg/mL of phenylmethylsulfonyl fluoride (Sigma), and 20 mM of 2-mercaptoethanol (Sigma). After incubating on ice for 30 minutes, cells were sonicated for 2 minutes at 60 W (10-sec on/10-sec off) to ensure complete lysis, and cell debris was pelleted via centrifugation (28,000g, 1 hour, 4°C). The collected supernatant was purified using gravity flow chromatography with a bed of Ni-NTA agarose (Qiagen). Wash buffer containing 50 mM imidazole was used to remove nonspecific binding of background proteins, and elution buffer containing 250 mM imidazole was applied to the column to elute the His-tagged protein of interest. Elution fractions were separated using SDS polyacrylamide gel electrophoresis (NuPAGE 4-12% Bis-Tris Protein Gel, Thermo Fisher Scientific) and analyzed via Coomassie staining (R-250, Thermo Fisher Scientific). Fractions containing protein of interest were then pooled, and dialysis was performed using a 10 kDa Slide-A-Lyzer cassette (Thermo Fisher Scientific) overnight at 4°C with 2 solution changes to eliminate excess imidazole as well as desalt the collected protein into storage buffer (1X PBS, 0.5 mM EDTA, 10% glycerol, pH = 8). The Pierce BCA Protein Assay (Thermo Fisher Scientific) assay was employed for protein quantification.

Labeling of cysteine-terminated recombinant protein with azide-terminated oligonucleotide label using dibenzylcyclooctyne (DBCO)-PEG$_4$-maleimide heterobifunctional crosslinker

Immediately before use, a 10 mM solution of DBCO-PEG$_4$-Maleimide (Jena Bioscience) was prepared in anhydrous dimethyl sulfoxide (DMSO) and reacted, at a 4-fold molar excess, with the protein-of-interest (i.e. eGFP, mCherry, or FGF-2) diluted to 0.1 mM in Conjugation Buffer (1X PBS with 1 mM EDTA (pH = 7)). The conjugation was reacted overnight at 4°C on a tube rotator. The next day, excess DBCO was removed, and the buffer was exchanged to 1X PBS (pH = 7) using a 10 kDa Amicon Ultra-0.5 mL Centrifugal Filter (EMD Millipore). The DBCO-reacted protein-of-interest was then reacted, at a 3-fold molar excess, with an azide-terminated oligonucleotide label overnight at 4°C on a tube rotator. Reaction efficiency was assessed by running the product on a reducing SDS polyacrylamide gel (NuPAGE 4-12% Bis-Tris Protein Gels, ThermoFisher Scientific) and subsequently imaging the gel using a flat-bed fluorescent scanner (Typhoon 8600, Molecular Dynamics), probing for the fluorescent tag modifying the oligonucleotide label (Supplementary Fig. 5, Supplementary Fig. 11). Protein-oligonucleotide conjugate was stored at -20°C until ready to use.

Labeling of cysteine-terminated EphB4-binding peptide with azide-terminated oligonucleotide label using dibenzylcyclooctyne (DBCO)-PEG$_4$-maleimide heterobifunctional crosslinker

Because of its small size, the EphB4-binding peptide (TNYLFSPNGPIARAWC, approx. 2 kDa) (*63*) was reacted, at a 2-fold excess, with the DBCO-PEG$_4$-Maleimide (Jena Bioscience) crosslinker, as outlined in the previous protocol for conjugating proteins of interest with an oligo label. The conjugation was reacted overnight at 4°C on a tube rotator. The resulting DBCO-reacted peptide was reacted again, at a 3-fold molar excess, with an azide-terminated oligo label overnight at 4°C on a tube rotator. Completion of the reaction was confirmed through visualization of a band shift on a 20% polyacrylamide gel (Supplementary Fig. 11). Oligonucleotide-labeled peptide was stored at -20°C until ready to use.

DNA-directed patterning of oligonucleotide-labeled proteins

Similar to the above protocol for characterizing surface DNA patterns with a complementary fluorescent oligonucleotide, substrates were first blocked at room temperature with 2% BSA in PBS for 1 hour to minimize nonspecific adsorption. Complementary, oligonucleotide-labeled fluorescent proteins were prepared at 0.2 μM in 2% BSA and incubated for 5 minutes on a shaker at room temperature. The substrate surface was then washed 4x with PBS and imaged using an ImageExpress Micro (IXM) high-throughput, automated imager.

Patterning polyacrylamide (PA) for high-throughput single-cell cultures over 5-day differentiation

Upon completion of DNA patterning, a PA grid was fabricated onto the substrates to enable clonal analysis of thousands of single-cell cultures over the course of differentiation. This was achieved by first photopatterning a large-scale array of 141 μm x 141 μm square features (i.e. “microislands”) arranged with a 200-μm pitch using positive photoresist (Shipley 1813). The photoresist squares were patterned such that the surface DNA patterns were positioned and protected beneath the square features. Subsequently, linear polyacrylamide was dropcast across the substrate surface, reacting with exposed aldehyde groups within unpatterned photoresist areas (Supplementary Fig. 8) (*65*). Specifically, a 10% PA solution in 10 mM 4-(2-hydroxyethyl)-1-piperazineethanesulfonic acid) (HEPES, pH=7) was first degassed in a desiccator for 10 minutes to remove dissolved oxygen. Upon activation of the PA solution with 1.5% tetramethylethylenediamine (Bio-Rad) and 0.225% ammonium persulfate (Bio-Rad), 250 µL of the PA mixture was dropcast immediately over the photoresist features, and a Gel Slick (Lonza)-treated glass coverslip was used to spread out the PA solution over the entire DNA-patterned substrate. Following 1 hour of polymerization, the coverslip was removed, and the slide was rinsed with DI water to remove unreacted PA. Finally, the photoresist defining the PA patterns and protecting the DNA were removed by dissolving in acetone. The slide was rinsed with DI water, dried with dry nitrogen gas, and stored under vacuum.

To characterize the nonbiofouling nature of the patterned PA, substrates were incubated with 1 mg/mL of BSA-AlexaFluor 488 conjugate (Thermo Fisher Scientific) at room temperature for 2 hours on a shaker. Loosely bound protein was removed by washing substrates 4x with PBS. Selective protein adsorption to the square microisland features was revealed upon imaging with a FITC filter.

Polydimethylsiloxane (PDMS) stamping of flow cells onto DNA-patterned glass slide

PDMS flow cells were fabricated using standard soft lithography in which a 10:1 Sylgard 184 prepolymer base: curing agent mixture (Dow Corning) was degassed, poured onto a negative silicon master containing 150 µm-high SU8 channels, and cured for 1 hour in an 80°C oven. Upon complete curing, PDMS flow cells were excised from the negative-relief master using a razor blade and trimmed to fit within one well of a Millicell EZ 4-well chamber (EMD Millipore). To ensure strong attachment of the flow cell during both cell/protein patterning as well as long-term culture, PDMS flow cells were bonded to the DNA-patterned glass substrate using a PDMS stamping protocol (Supplementary Fig. 16). Briefly, degassed 10:1 PDMS mixture was spin coated onto a blank glass slide at 4,000 RPM for 30 seconds to create a thin PDMS film. The prepared PDMS flow cell was subsequently stamped onto this uncured PDMS film such that the flow cell walls were "inked" with uncured PDMS. The flow cell was subsequently affixed over each well of the DNA-patterned glass substrate. The slide was heated at 65°C for 1 hour to cure the PDMS "ink" – thus, creating a strong adhesive bond between the flow cell and DNA substrate. Completed slides were stored under vacuum until ready for biopatterning.

Cell culture

Adult rat hippocampal neural stem cells (NSCs) were isolated previously from 6-week-old female Fischer 344 rats (*43*). To promote monolayer adhesion, NSCs were cultured on polystyrene plates coated with 10 µg/mL poly-L-ornithine hydrobromide (Sigma) in sterile DI water overnight at room temperature and 5 µg/mL of laminin (Invitrogen) in sterile PBS overnight at 37°C. NSCs were maintained in Dulbecco's Modified Eagle Medium/Nutrient Mix F-12 (DMEM/F-12, Invitrogen) with 1% (v/v) N-2 Supplement (Invitrogen) and 20 ng/mL of basic fibroblast growth factor (FGF-2, Peprotech) and incubated at 37°C and 5% CO_2. NSCs were passaged upon 80% confluency using Accutase (Innovative Cell Technologies). For mixed differentiation studies, NSCs were cultured in normal culture media supplemented with 1% fetal bovine serum

(Invitrogen), 1 μM retinoic acid (Enzo Life Sciences), and 1% penicillin-streptomycin (Gibco) in DMEM/F-12 + N-2 Supplement. For studies involving protein patterns, NSCs were cultured in maintenance media (DMEM/F-12 + N-2) supplemented with 0.1 ng/mL of FGF-2 to promote low proliferation.

Fluorescent labeling of NSC populations using CellTracker dyes

NSCs were prepared as a suspension in PBS at 8 x 10^6 cells/mL. CellTracker Violet BMQC (2,3,6,7-tetrahydro-9- bromomethyl-1H,5H-quinolizino(9,1-gh)coumarin), CellTracker Green CMFDA (5-chloromethylfluorescein diacetate), CellTracker Red CMTPX, and CellTracker Deep Red (Thermo Fisher Scientific) were added to a final concentration of 2.5 μM, 2.5 μM, 2.5 μM, and 1 μM, respectively, and allowed to incubate with the cells for 15 minutes at room temperature with occasional agitation. To remove excess dye, cells were spun down and re-suspended 3x in 1 mL of PBS. All subsequent steps involving labeled cells were performed in the dark.

Labeling of NSC membrane with lipid-DNA

NSCs were detached using Accutase (Innovative Cell Technologies) and prepared at 8 x 10^7 cells/mL in PBS. Cells were incubated with 5 μM lipid-DNA for 10 minutes at room temperature and followed immediately by a second incubation with 5 μM of a co-anchor lipid-DNA strand for another 10 minutes to stabilize the first DNA strand. NSCs were then washed 3x via centrifugation at 3000 RPM for 3 minutes with PBS and stored on ice until ready for patterning. Lipid oligo sequences are listed in Table S1.

Single NSC patterning and culture

Prior to cell-patterning experiments, DNA-patterned substrates were sterilized in a laminar flow tissue culture hood under ultraviolet light for 15 minutes then blocked with 2% BSA in PBS for 1 hour to minimize non-specific cell attachment. Oligo-labeled NSCs were re-suspended in 2% BSA at 4 x 10^7 cells/mL, and 20 uL was injected into the PDM flow cell. The high cell concentration ensured that the entire DNA-patterned area was covered with oligo-labeled NSCs. Cells were then cycled by pipetting 5 uL of the cell suspension into the inlet of the flow channel and removing 5 uL from the outlet. This action was repeated 10-20x to increase the chance of hybridization between the cell-tethered oligos and complementary, surface-tethered oligos. Unpatterned cells were washed away with PBS (Supplementary Fig. 17). For experiments involving protein patterns, the above steps were repeated with a 0.2 μM solution of the protein(s) of interest in 2% BSA. Upon complete cell and/or protein patterning, 250 μL of the appropriate culture media supplemented with 10 μg/mL laminin was added to each well, and the slide was cultured for 5 days with half media changes (minus laminin) every other day to prevent cells from lifting off of the surface.

Immunostaining of NSC differentiation

Following 5 days of differentiation, NSCs were fixed for 5 minutes at room temperature with 4% (w/v) paraformaldehyde and washed 3x for 5 minutes with PBS. Cells were then blocked and permeabilized at room temperature in PBS containing 5% donkey serum (Sigma) and 0.1% Triton X-100 (PBS-DT) for 1 hour prior to being incubated overnight at 4°C with the primary antibodies, 1:1000 mouse monoclonal IgG for tubulin III (Sigma, T8578) and 1:1000 chicken polyclonal IgG for glial fibrillary acidic protein (Abcam, ab4674), diluted in PBS-DT. The following day, cells were washed 3x for 5 minutes with PBS and incubated in the dark with secondary antibodies, 1:250 Alexa Fluor 488 donkey anti-mouse IgG (H+L) (Thermo Fisher Scientific, A-21202) and 1:250 Cy3 or Alexa Fluor 647 donkey anti-chicken IgG (H+L) (Jackson ImmunoResearch, 703-605-155), diluted in PBS-DT on a shaker at room temperature. Cells were subsequently washed 3x for 5 minutes in PBS with 1:1000 4',6-Diamidino-2-Phenylindole, Dihydrochloride (DAPI) added during the second wash. Samples were stored in PBS before and during imaging.

Statistical analysis

All statistical analysis was performed in MATLAB (R2018a). One-way Analysis of Variance (ANOVA) was used to test for significant differences between variable means. A p-value of less than 0.05 for ANOVA was considered significant. For data with a significant ANOVA result, we used the Tukey-Kramer method to compared between individual groups and test for significance. A p-value of less than 0.05 for the Tukey-Kramer method was considered significant. Details on replicates, ANOVA results, and Tukey-Kramer comparisons are provided in the figure captions.

3.5 Acknowledgements

We thank Dr. Junghyun Kim, Dr. Nahyun Cho, and Phil Kang for helpful discussions, Dr. Mary West at UC Berkeley's CIRM/QB3 Shared Stem Cell Facility for assistance with microscopy, Dr. Chris Jeans at UC Berkeley's QB3 MacroLab for assistance with recombinant protein purification, and Professor Zev Gartner's lab for synthesizing lipid-conjugated oligonucleotides. This work was supported by the following NIH grants: 1R01CA190843-01, 1R21EB019181-01A1, and 1R21CA182375-01A1. O.J.S. and R.F.B. were supported by the National Science Foundation Graduate Research Fellowship. O.J.S. was supported by a Siebel Scholarship and PEO Scholarship.

3.6 Supplemental Information

3.6.1 Supplemental Figure 3.1 – Characterization and Optimization of DNA Patterning Steps

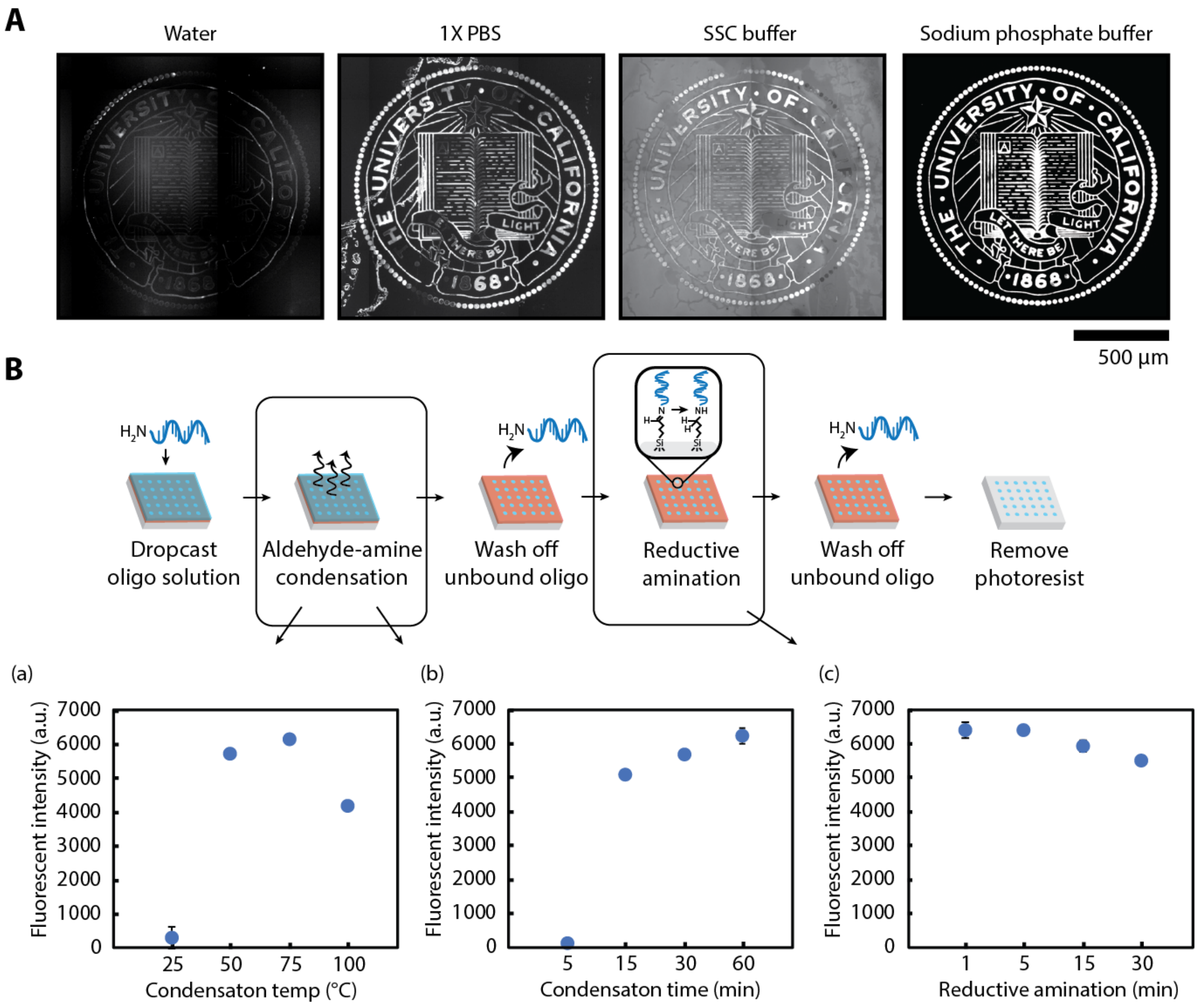

Supplementary Figure 3.1 (A) Surface patterning of amine-terminated oligonucleotides is strongly influenced by the composition of the buffer used to dilute the DNA. To visualize and characterize resulting DNA patterns, the fluorescent signal from a complementary fluorescent oligonucleotide that had been flowed across, and hybridized onto, the surface DNA patterns is imaged and quantified. The use of water as the dilution buffer resulted in a weak fluorescent signal. Adding salt to the buffer improved the fluorescence intensity of the patterns; however, an excess of salt, e.g. 1X PBS buffer, resulted in undesirable background signal. Saline-sodium citrate (SSC) buffer, commonly employed for DNA microarray technologies, partially dissolved the positive photoresist, contributing to even higher background fluorescence. Thus, the ideal buffer is one that 1) incorporates low salt concentration and 2) preserves the integrity of the patterned photoresist. In the reported experiments, 50 mM sodium phosphate buffer (pH = 8.0) was determined to be the ideal candidate for generating robust DNA patterns with minimal background. Scale bars represent 500 µm. (B) Two key steps in the DNA-patterning process were investigated further. For the aldehyde-amine condensation step, various (a) oven temperatures (25°C, 50°C, 75°C, 100°C) were tested for a 30-min incubation as well as a range of (b) incubation times (5 min, 15 min, 30 min, and 1 hour) at 75°C. Results from both highlight the necessary balance in selecting an appropriate temperature/time to ensure complete condensation. At the highest temperature (i.e. 100°C), we observed increased coffee-ring effect with higher DNA concentrations accumulating at the edge of the dropcast DNA; thus, we selected a condensation temperature of 75°C and incubation time of 30 minutes. (C) For the reductive amination step, all tested incubation times (1 min, 5 min, 15 min, and 30 min) generated high-intensity DNA patterns. Longer incubation times, however, resulted in a slight drop in intensity values. Error bars represent standard deviation and *n*=4.

3.6.2 Supplemental Figure 3.2 – Optimization of DNA-Patterned Features for High Efficiency Single-Cell Capture

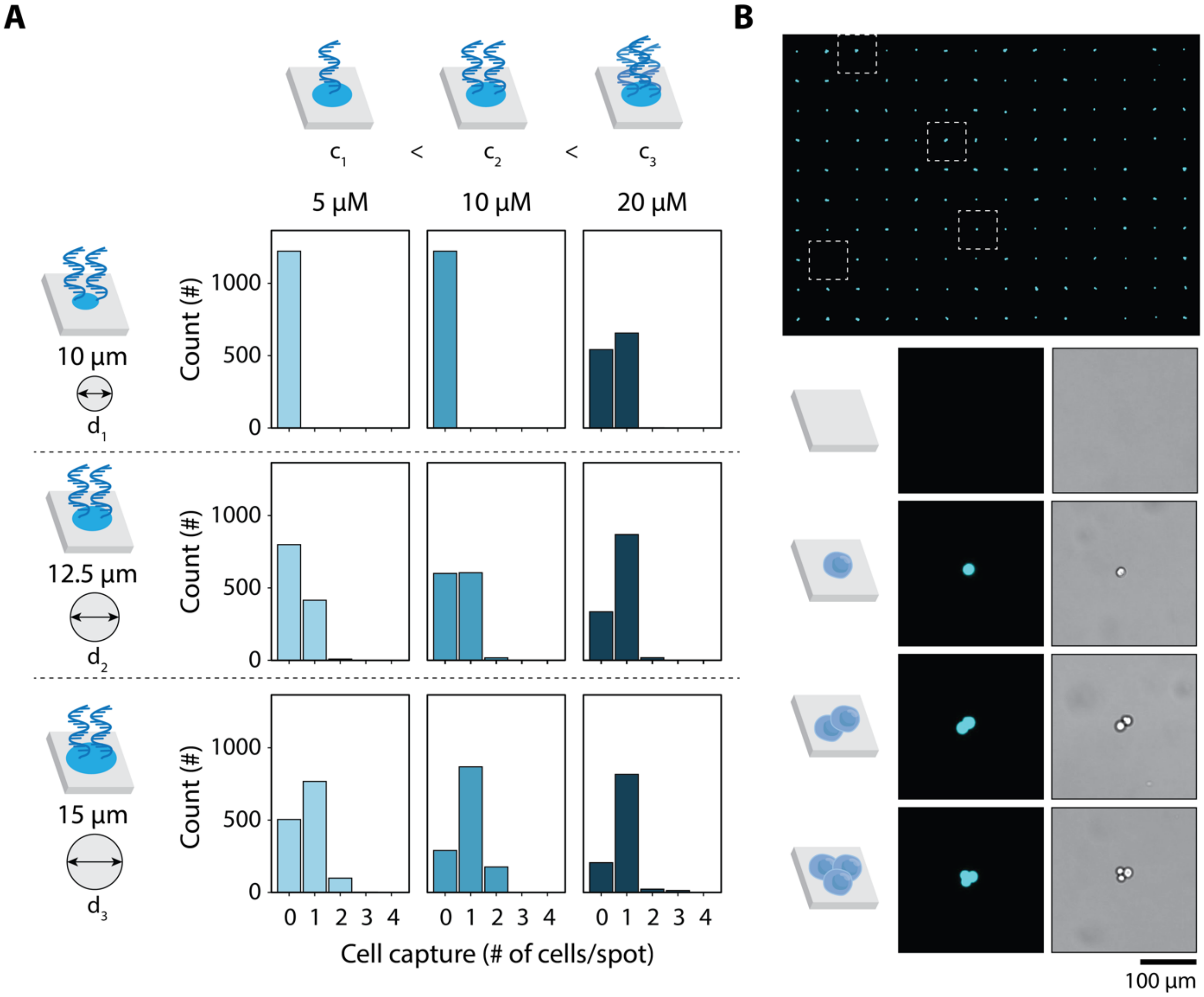

Supplementary Figure 3.2 DNA spot features were microfabricated onto a surface to capture single adult neural stem cells labeled with a lipid-oligonucleotide containing the complementary sequence. (A) To achieve high efficiency single-cell capture, we screened a combination of DNA-patterned spot size diameters and DNA concentrations, identifying a 15 μm-diameter spot size and 20 μM DNA concentration as the optimal condition. (B) Representative images of efficient and inefficient single-cell capture of fluorescently-labeled adult neural stem cells by photolithographic surface DNA patterns.

3.6.3 Supplemental Figure 3.3 – Re-Use of Photoresist (PR) Layer vs. New PR Layer for Multicomponent DNA Patterning

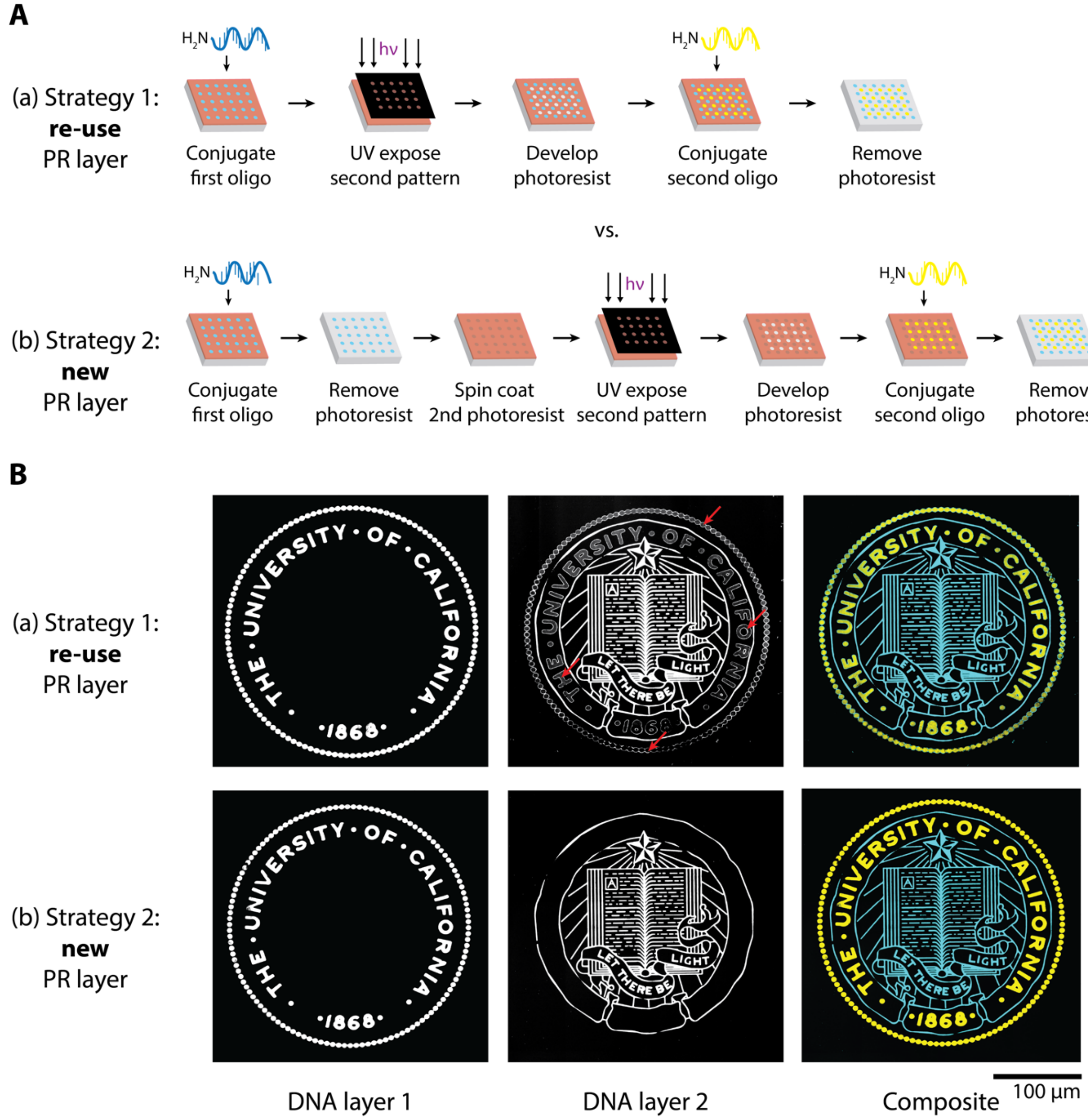

Supplementary Figure 3.3 (A) Two strategies were investigated for fabricating multicomponent surface DNA patterns. The (a) first strategy involved re-using the same PR layer that was employed to pattern the first DNA layer to conjugate a second oligo. The (b) second strategy involved removing the first PR layer upon the successful conjugation of the first oligo and applying a new PR layer on which to perform photolithography to define surface patterns for a second oligo. (B) Both strategies were capable of generated two-component DNA surface patterns as illustrated in the composite images (right). However, the (a) first strategy resulted in undesired contamination of the first DNA layer pattern with the second oligonucleotide (red arrows), most likely a result of the second oligo reacting with residual unconjugated aldehyde groups from the first DNA pattern region. In the case of the (b) second strategy, distinct and separate patterns with no bleed through of fluorescent signal between the layers was achieved.

3.6.4 Supplemental Figure 3.4 – Robustness of Photolithographic Approach for Assembling Multiplexed DNA Patterns

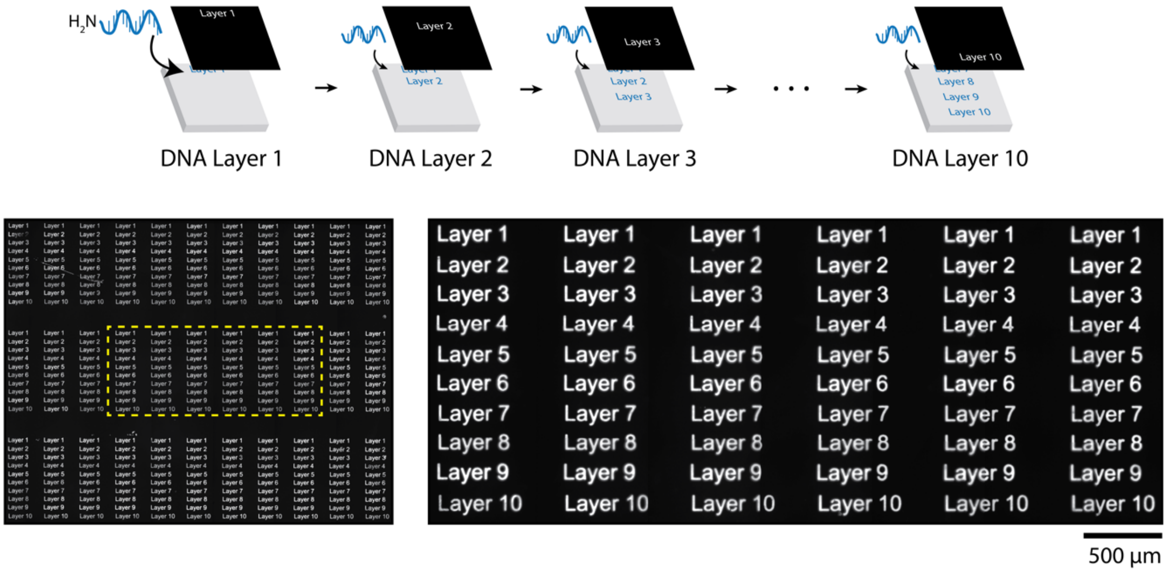

Supplementary Figure 3.4 The repeated application of multiple patterned photoresist layers was tested for up to 10 DNA layers. Hybridization with a complementary fluorescent oligonucleotide revealed that each layer retained its functionality.

3.6.5 Supplemental Figure 3.5 – Tunable Multicomponent DNA Patterns within the Same and Distinct Layers

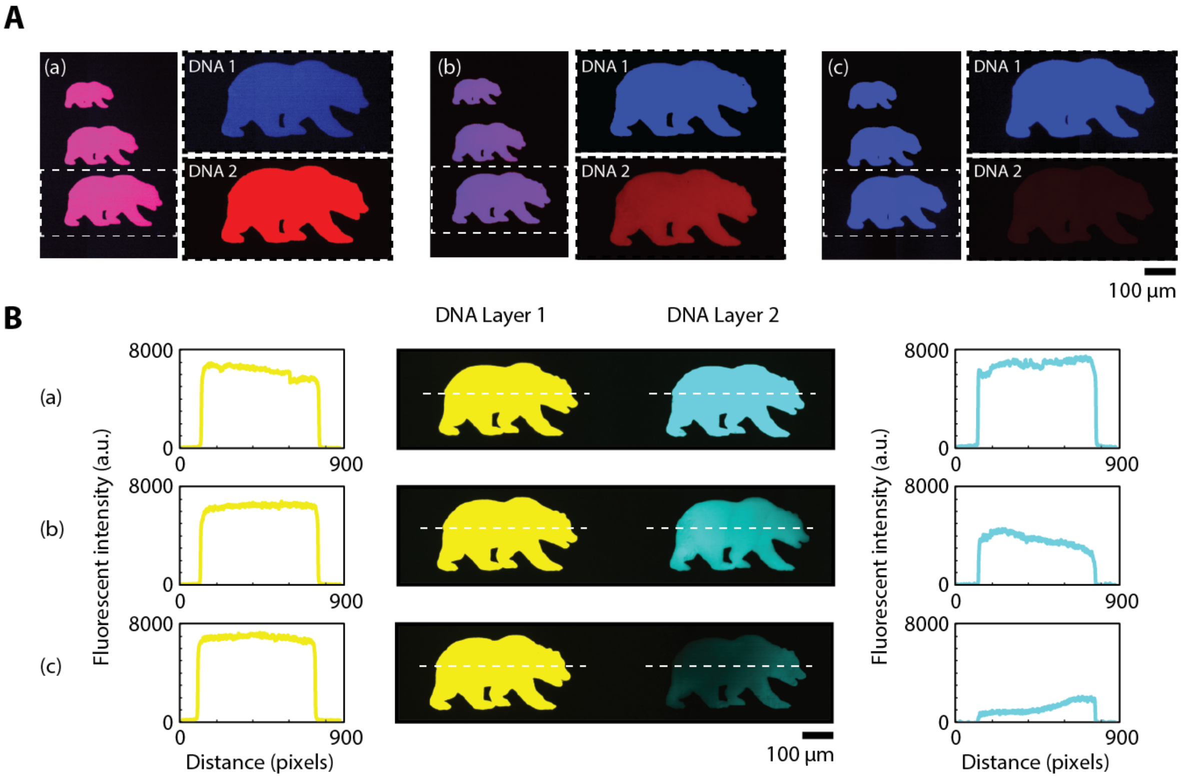

Supplementary Figure 3.5 Surface DNA concentrations can be controlled for multiple DNA components when patterned (A) within the same layer as demonstrated by the two-component, mixed bear patterns in which the concentration of one DNA strand (i.e. DNA 1) is held constant while a second strand (i.e. DNA 2) is tuned across (a) high, (b) medium, and (c) low concentrations, or (B) across separate layers as each layer contains a unique oligonucleotide and, similarly, one layer (i.e. DNA Layer 1) is held constant while the concentration of the other (i.e. DNA Layer 2) is varied across (a) high, (b) medium, and (c) low concentrations.

3.6.6 Supplemental Figure 3.6 – Characterization of Labeling Reaction of Recombinant Fluorescent Protein, eGFP, with a Fluorescently-Tagged Oligonucleotide Label using Dibenzocyclooctyne (DBCO) Heterobifunctional Cross-linker

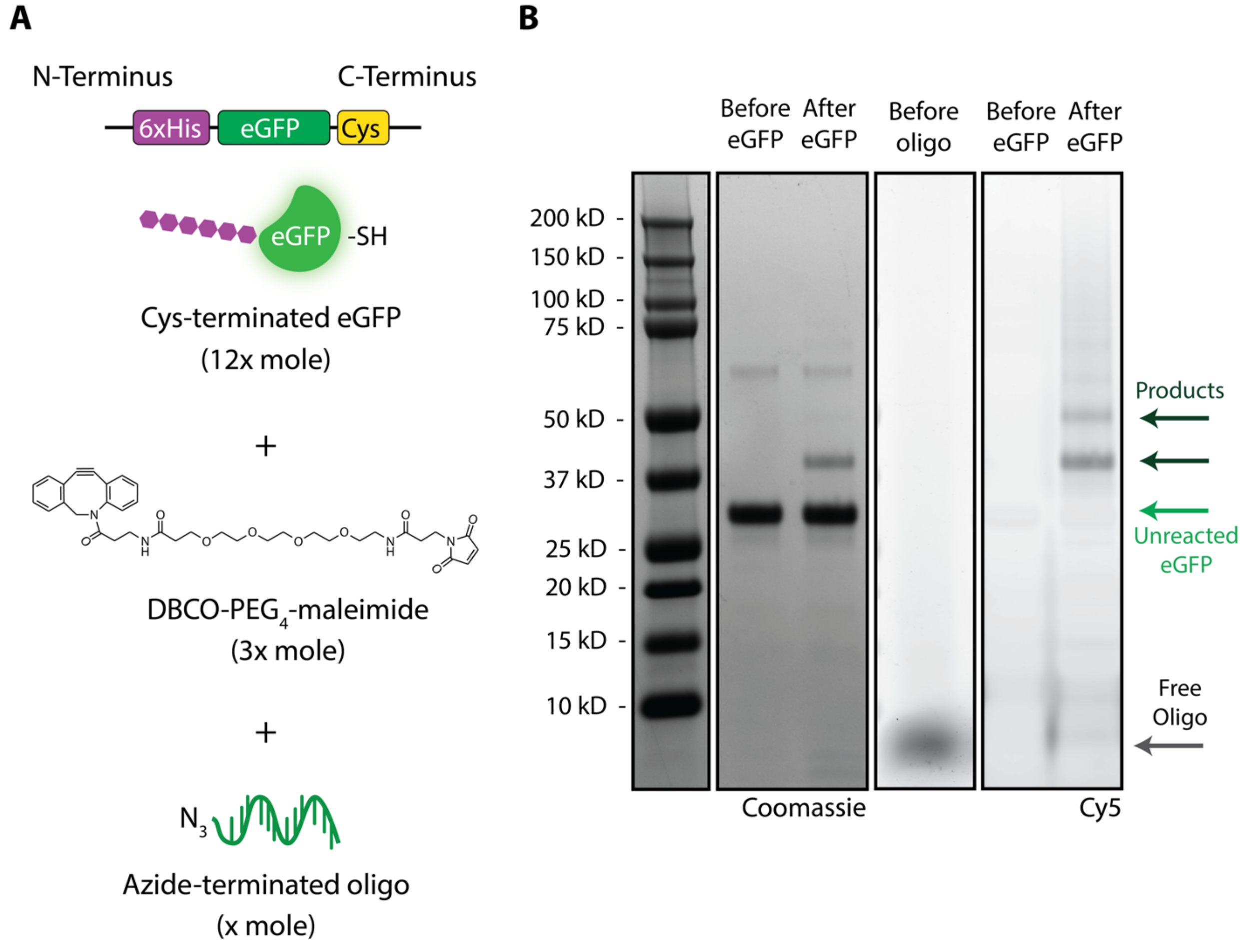

Supplementary Figure 3.6 eGFP was produced and purified from *E. coli* and subsequently reacted with a fluorescent oligonucleotide label to enable DNA-directed solid-phase ligand patterning. (A) eGFP was cloned with the following terminal tags: 1) histidine tag at the N-terminus to enable purification using a Ni-NTA column and 2) cysteine tag at the C-terminus to enable oligonucleotide conjugation via click chemistry. The two-step labeling reaction involved first reacting the fluorescent protein with a 4x molar excess of the heterobifunctional cross-linker, DBCO-PEG$_4$-maleimide, forming a stable thioether linkage between the maleimide group on the cross-linker and the sulfhydryl group on the C-terminal cysteine of the protein. The second step then involved reacting the DBCO-labeled protein at a 3x molar excess with the fluorescent oligo label via the terminal azide on the oligo and the DBCO moiety on the protein. (B) SDS-PAGE was utilized to assess the reaction efficiency. Coomassie staining of eGFP revealed a product band shifted ~7 kDa, corresponding to the molecular weight of the fluorescent oligonucleotide. To validate that this product was labeled with DNA, the gel was imaged for fluorescence as the oligonucleotide label possesses a Cy5 fluorescent tag at the 3' end. A fluorescent band with a molecular weight matching the Coomassie-stained bands was detected and, importantly, no fluorescent band was detected at ~7 kDa, suggesting that all of the oligos were conjugated to eGFP.

3.6.7 Supplemental Figure 3.7 – Stability and Specificity of DNA-Directed Enhanced Green Fluorescent (eGFP) Protein Patterns

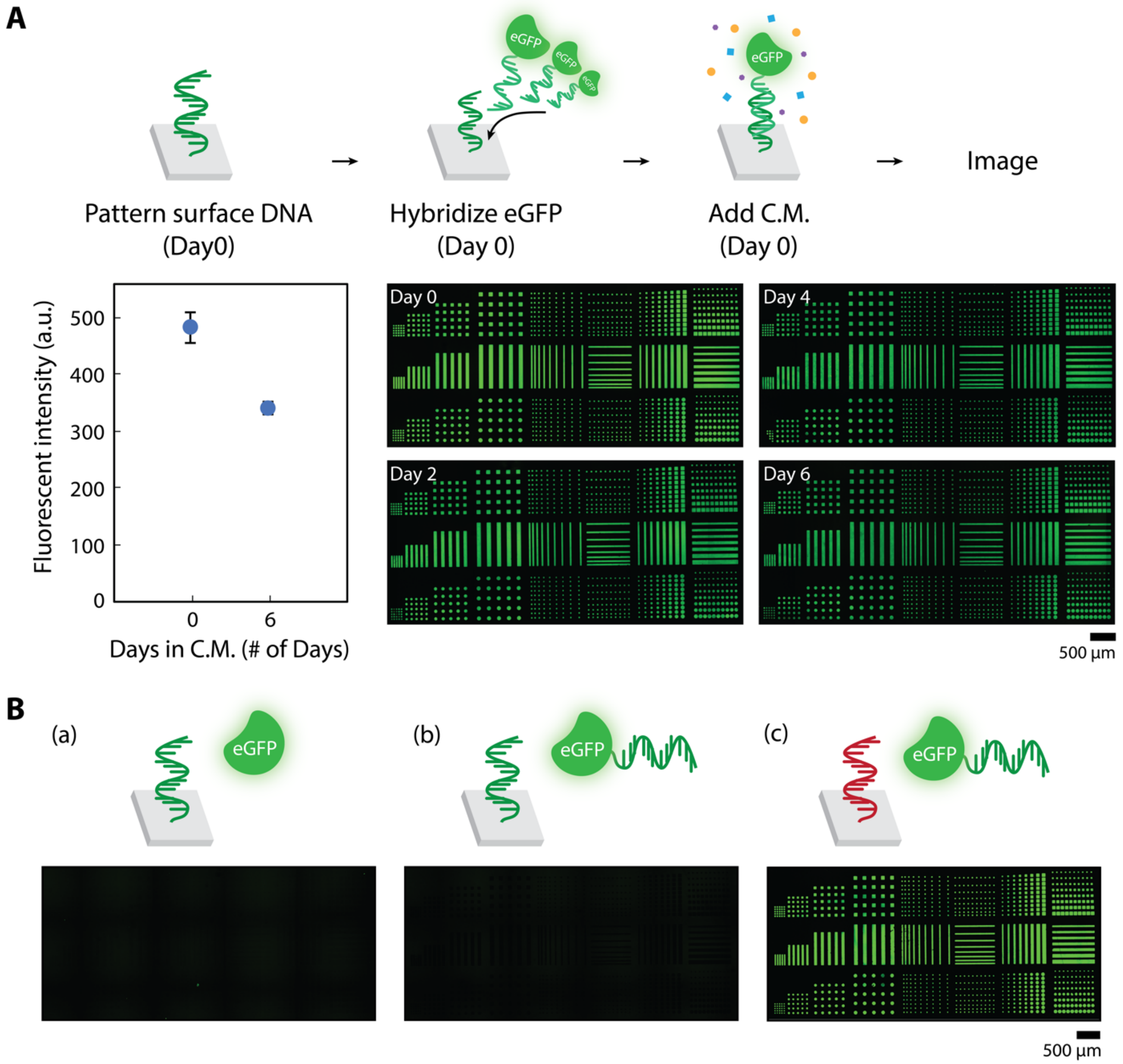

Supplementary Figure 3.7 (A) To characterize the stability of DNA-directed ligand patterns for use in long-term differentiation studies, an oligonucleotide label was conjugated to recombinant eGFP, and the conjugate was hybridized to its complementary, surface-patterned DNA. eGFP patterns were monitored over the course of a 6-day time-course with conditioned media (C.M.) changes occurring every other day. The fluorescent intensity emitted from eGFP was quantified on Days 0 and 6 (left). Despite a slight decrease in intensity, eGFP patterns continued to be well defined and stable, as illustrated in the representative images on days 0, 2, 4 and 6. Error bars are standard deviation and *n*=3. (B) To highlight the specificity of DNA-directed ligand patterning, a combination of patterning controls was tested using eGFP as the ligand of interest. No eGFP signal was detected for conditions in which there was (a) an absence of an oligonucleotide label conjugated to eGFP or (b) noncomplementary surface-patterned DNA. Only when (c) an oligonucleotide label on the eGFP is complementary to the surface DNA patterns was there detectable eGFP fluorescent patterns.

3.6.8 Supplemental Figure 3.8 – Optimization of Polyacrylamide (PA) Patterning using Photolithography

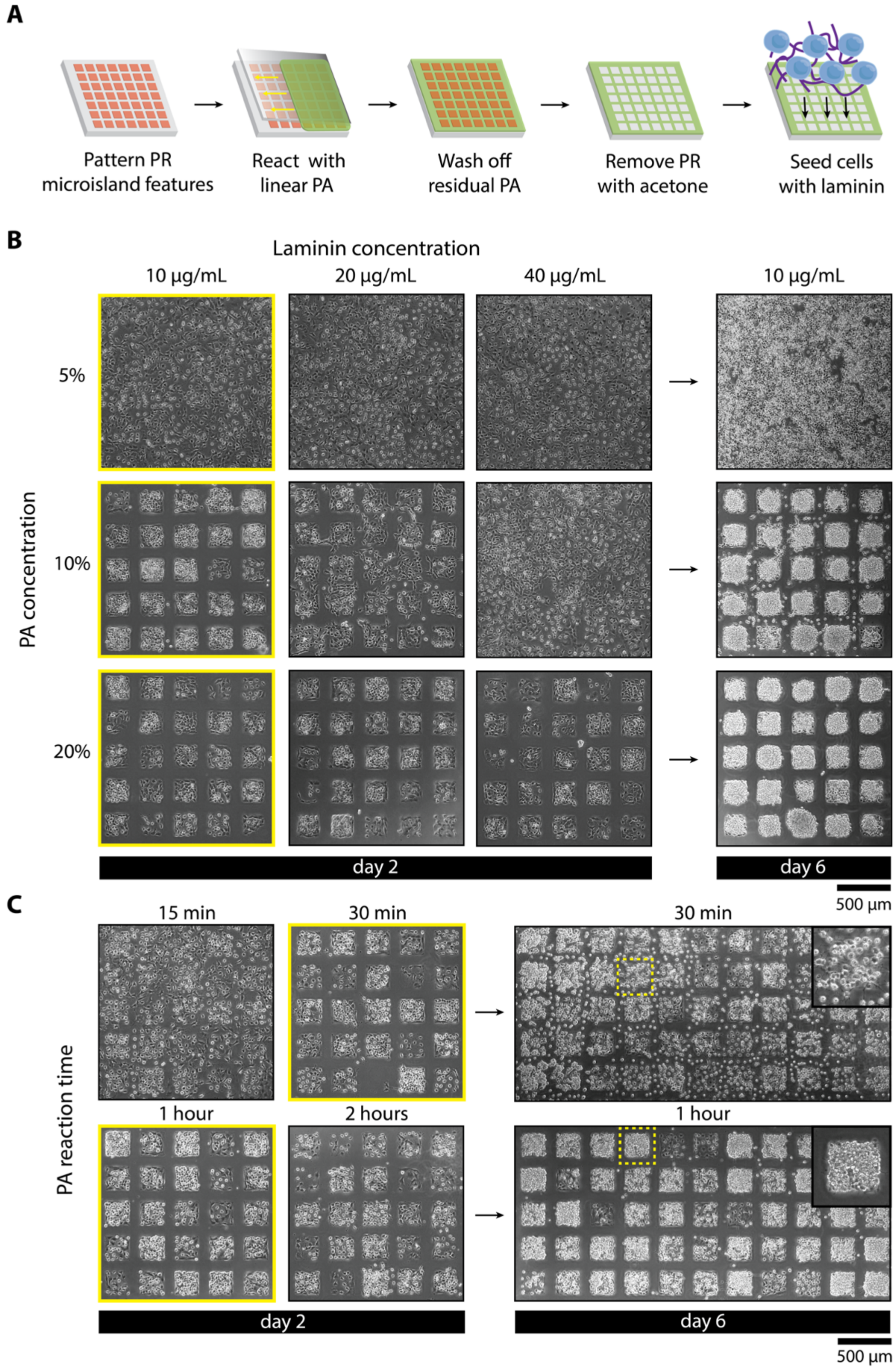

Supplementary Figure 3.8 In addition to directing the spatial assembly of DNA onto a substrate, patterned positive photoresist was used to fabricate PA grids (*65*), generating an array of cell-contained 141 µm x 141 µm microislands. Each microisland accommodates a single adult neural stem cell (NSC) and enables high-throughput clonal analysis. The PA grid restricts each patterned single cell to within a microisland over the course of differentiation. (A) To achieve high-fidelity, non-biofouling PA patterns, various combinations of PA percentages and laminin concentrations were tested by seeding 50,000 NSCs and observing the integrity of cells patterned within the micro-island features over the course of 6 days. A low percentage of PA (i.e. 5% PA) was insufficient to retain NSCs within the microislands across all of the different laminin concentrations tried. A 10% PA composition with low 10 µg/mL laminin concentration demonstrated non-biofouling properties for the first two days but, by days 4 and 6, NSCs were observed escaping the microisland features. Although 20% PA resulted in robust non-biofouling grids for all laminin concentrations for up to 6 days, washing off excess PA was difficult. Thus, 10% PA was optimized further by (B) testing the reaction time of the persulfate-induced grafting of the linear PA to the surface aldehydes. A minimum reaction time of 1 hour was necessary to retain cells within the microislands over the course of 6 days. This condition was utilized for all subsequent experiments.

3.6.9 Supplemental Figure 3.9 – Microfabricated DNA and PA Patterns Support High-Throughput Clonal Analysis of Adult Neural Stem Cells (NSCs)

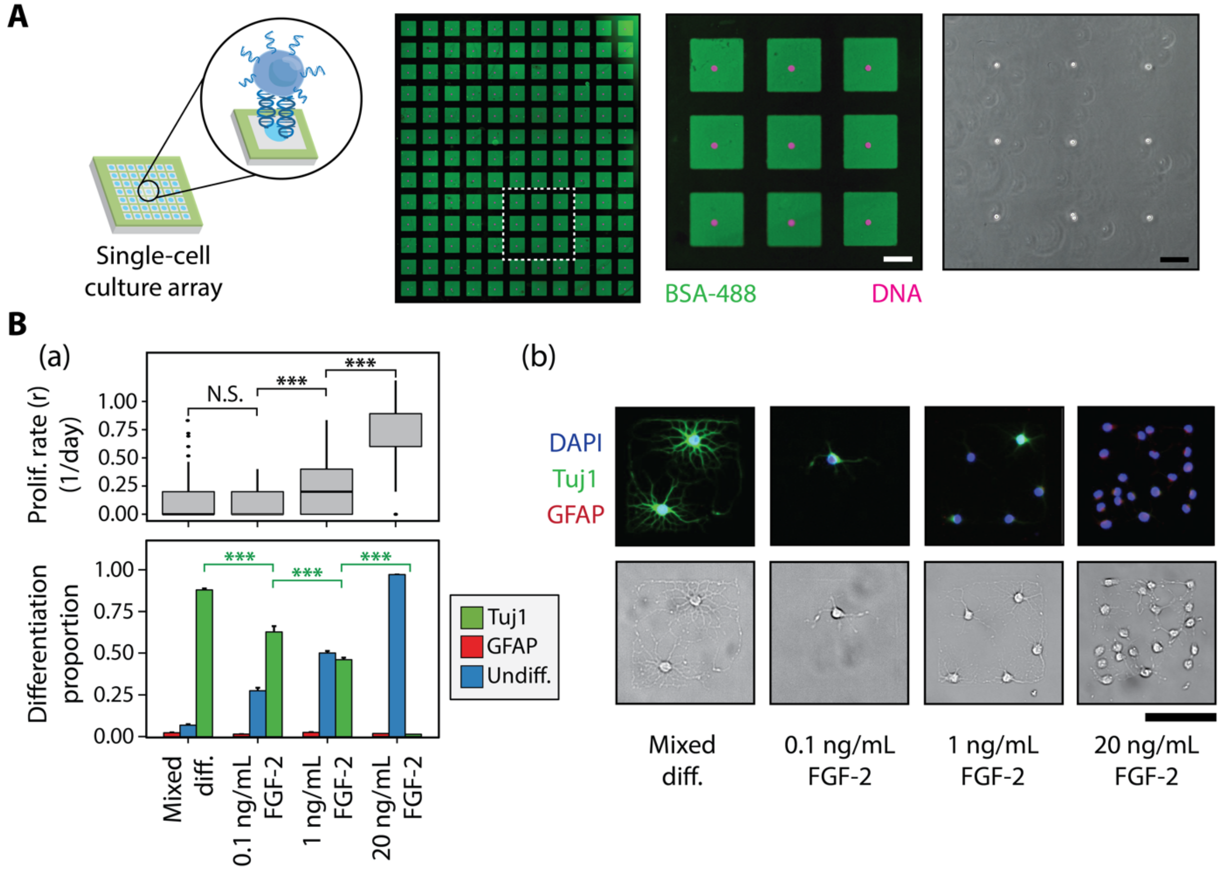

Supplementary Figure 3.9 (A) An array of 15 μm-diameter DNA spots (top left, blue circles) was microfabricated in combination with PA patterns (top left, green) to enable, first, the high-throughput capture of oligo-labeled single NSCs and, second, long-term biological studies of 1000's of single-cell cultures in parallel. Compatibility of DNA and PA patterning was evident as DNA patterns could be visualized with a complementary fluorescent oligo (magenta), while PA grid patterns were evident upon incubation with bovine serum albumin (BSA)-AlexaFluor488 as the PA is non-biofouling and excluded BSA to square microisland features. A representative grid of DNA-directed single NSC patterns are evident (right). (B) The combination of PA and DNA patterns enabled NSC clonal analysis following 5-day treatment with various soluble media conditions. (a) As anticipated, 20 ng/mL of FGF-2 promoted high proliferation with low levels of differentiation. As FGF-2 concentration decreased, proliferation rates also decreased as neuronal differentiation increased, while mixed differentiation containing 1% fetal bovine serum and 1 μM retinoic acid exhibited the highest neural differentiation as visualized by the high Tuj1 expression in the (b) representative immunostaining images of microislands for the different soluble conditions. Error bars are standard deviation and *n* values can be found in Table S3. All p-values obtained from Tukey-Kramer test. ***$p<0.001$. All scale bars represent 100 μm.

3.6.10 Supplemental Figure 3.10 – Purification of Recombinant Fibroblast Growth Factor-2 (FGF-2) and 5-Ethynyl-2'-Deoxyuridine (EdU) Pulse-Chase Experiment to Validate Protein Activity in Adult Neural Stem Cells (NSCs)

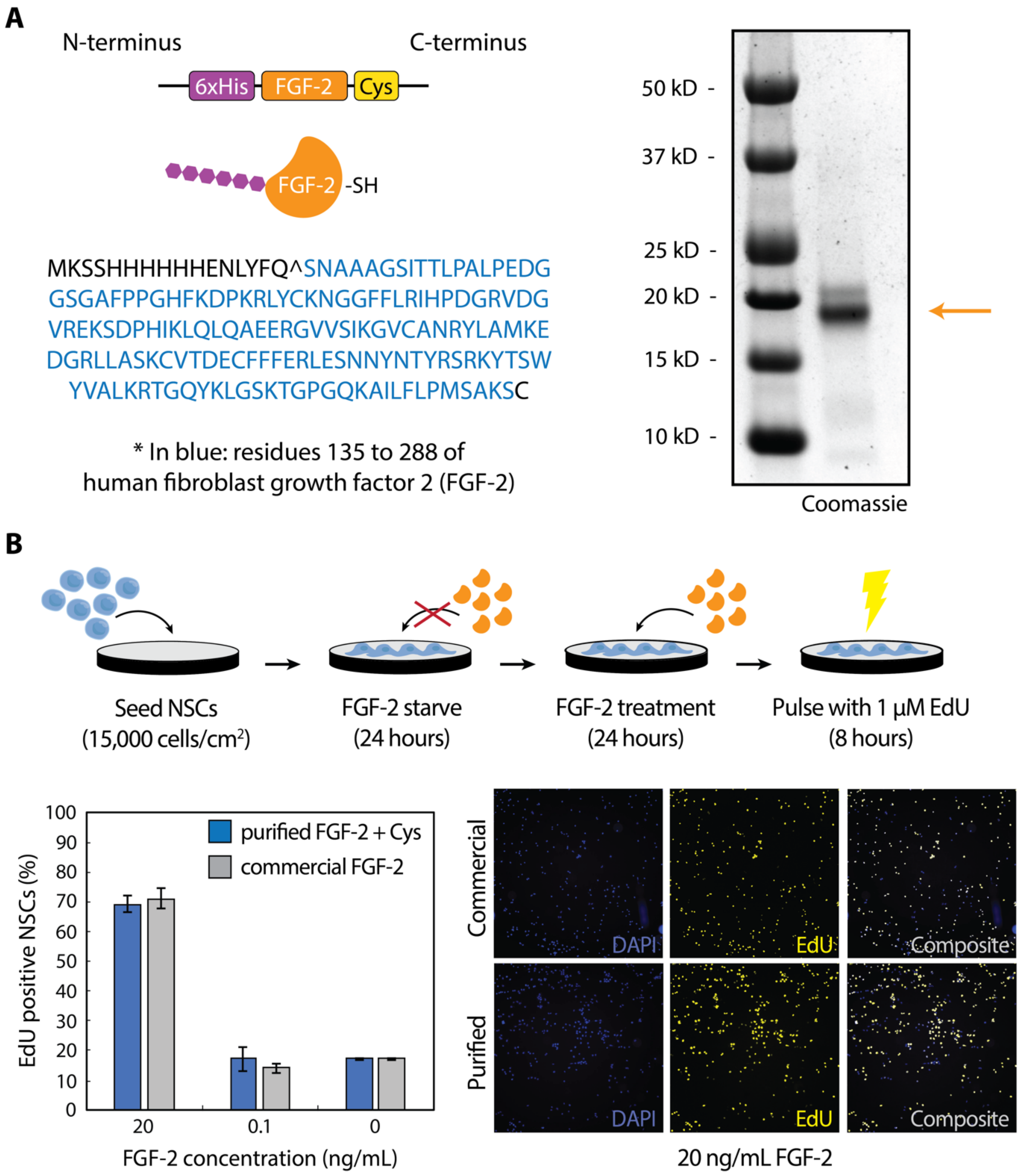

Supplementary Figure 3.10 (A) A T7 vector containing the ectodomain of human FGF-2 with a N-terminal histidine tag and a C-terminal cysteine was a gift from University of California – Berkeley Macrolab and subsequently cloned and purified from Rossetta2 *E. coli* (orange arrow highlights Coomassie band corresponding to purified FGF-2). (B) To validate the bioactivity of the aforementioned recombinant cysteine-terminated FGF-2, an EdU pulse-chase experiment was conducted with NSCs, comparing the proliferation of cells treated with recombinant FGF-2 versus commercially-available FGF-2 commonly used for stem cell maintenance. Cells were plated at 15,000 cells/cm^2, starved from FGF-2 for 24 hours to deplete residual FGF-2 added during NSC subculture, treated with either commercial or recombinant FGF-2 for 24 hours, pulsed with 1 uM EdU for 8 hours, fixed/stained, and imaged. Recombinant FGF-2 induced similar proliferation in comparison to commercial FGF-2 at both high (20 ng/mL) and low (0.1 ng/mL) concentrations (left), which can also be visualized by similar EdU staining for both cultures (right). Error bars are standard deviation and *n*=3.

3.6.11 Supplemental Figure 3.11 – Characterization of Oligo Labeling Reaction of Niche Ligands, Fibroblast Growth Factor-2 (FGF-2) and EphB4-Binding Peptide, using Click Chemistry

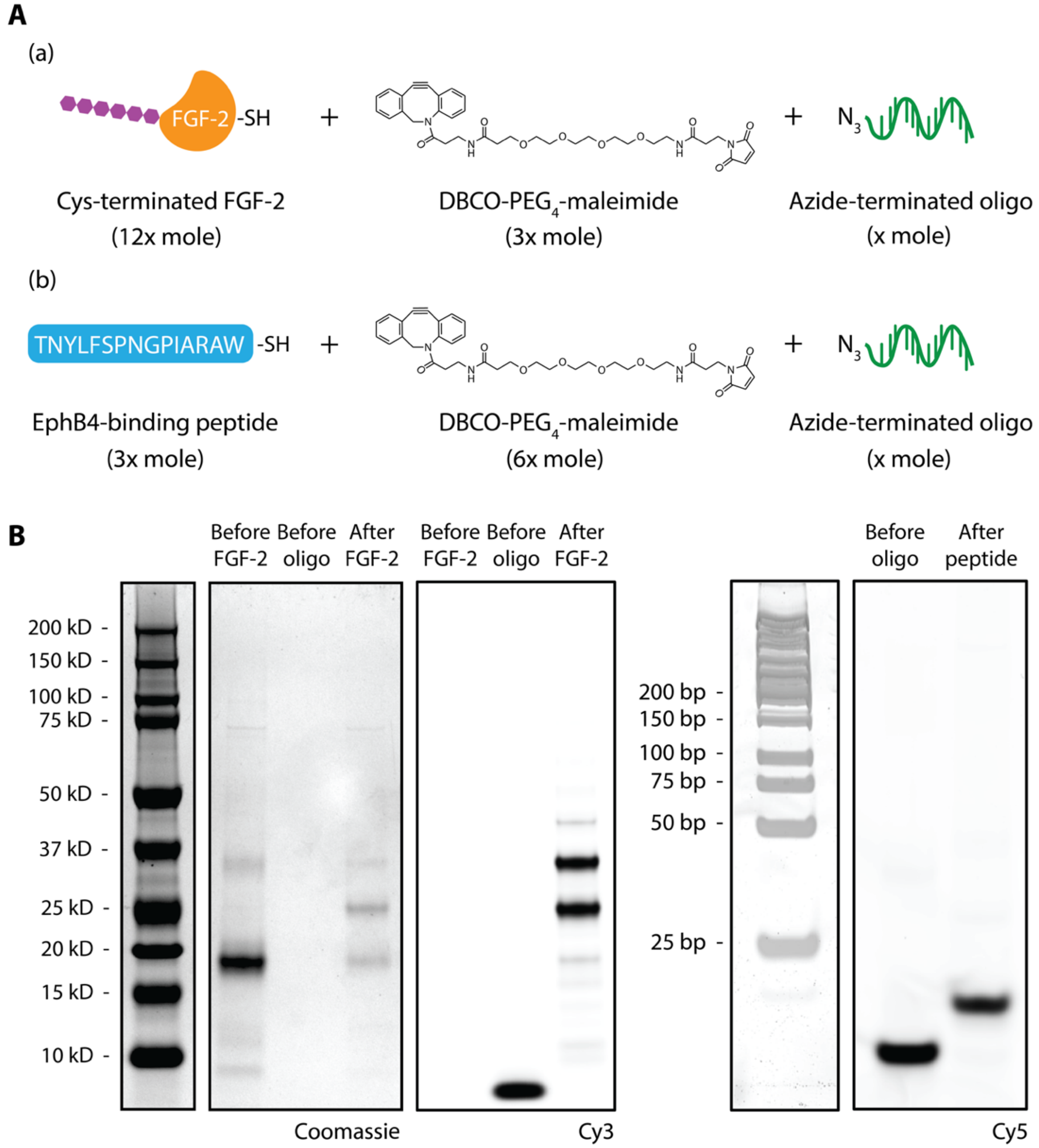

Supplementary Figure 3.11 (A) The strategy for labeling the niche ligand, FGF-2, is identical to that of labeling the fluorescent proteins; however, in order to conjugate an oligo to the short EphB4 peptide, TNYLFSPNGPIARAW, a slight variation in the reaction stoichiometries was made to accommodate the small peptide size (~2 kDa), which made it difficult to remove excess DBCO crosslinker via a spin column. (B) SDS-PAGE was used to assess FGF-2 reaction efficiency (left), and a 20% PA gel was employed to analyze the peptide reaction (right). For both scenarios, no unlabeled oligo was detected, suggesting that all of the fluorescent oligo label was reacted to the niche ligand of interest.

3.6.12 Supplemental Figure 3.12 – Multicomponent DNA Patterns Enable Controlled, High-Throughput Studies of Adult Neural Stem Cell (NSC) Niche Solid-Phase Ligand Cues, Fibroblast Growth Factor-2 (FGF-2) and Ephrin-B2, at the Single-Cell Level

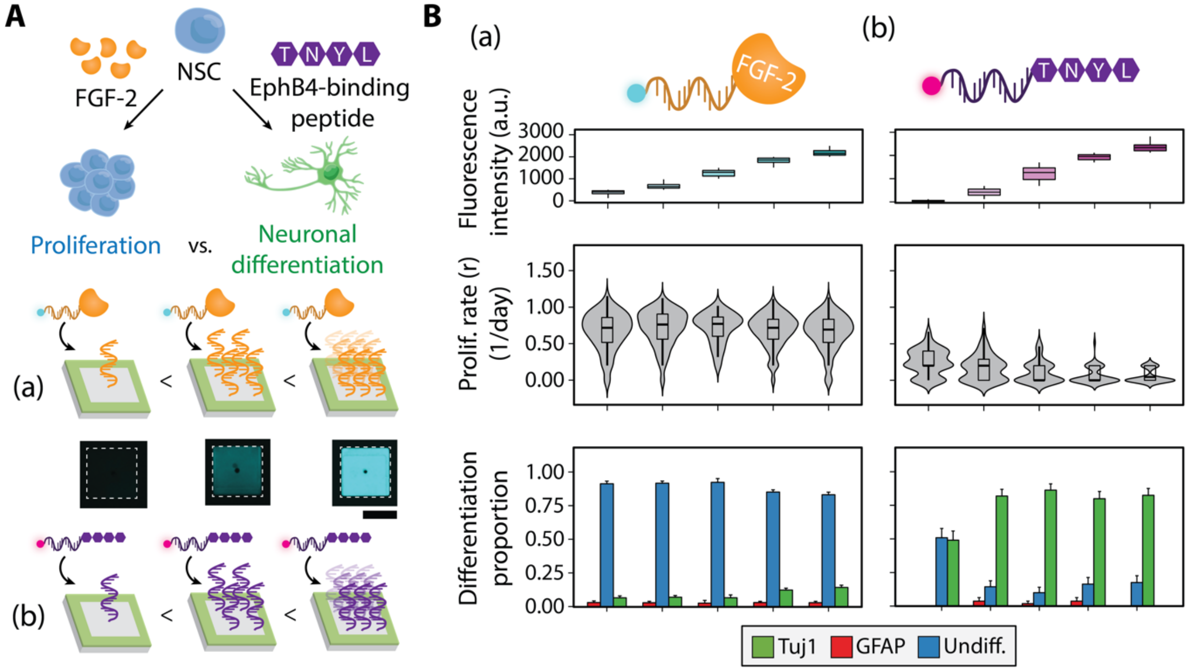

Supplementary Figure 3.12 (A) Adult NSCs reside within a dynamic niche where they receive and integrate a wide variety of extrinsic cues that ultimately instruct NSC fate decisions. FGF-2 and ephrin-B2 are two niche cues that promote opposing cell fates, where FGF-2 induces self-renewal, and ephrin-B2 promotes neuronal differentiation (top). The spatial presentation of (a) FGF-2 and (b) an ephrin-B2-mimetic peptide, TNYLFSPNGPIARAWC, can be controlled via DNA-directed assembly. Tunable solid-phase presentation can be achieved by modulating the concentration of surface-patterned DNA as visualized by the representative microislands with increasing fluorescent intensities. (B) Single NSC microislands were assembled containing a range of patterned ligand concentrations of either FGF-2 or ephrin-B2 peptide (a) Different concentrations of patterned FGF-2 resulted in similar proliferation and differentiation profiles, even at low concentrations. (b) For the ephrin-B2 peptide, however, a minimum ligand concentration was necessary to drive high neuronal differentiation (right). Error bars are standard deviation and n values can be found in Table S3. All scale bars represent 100 µm.

3.6.13 Supplemental Figure 3.13 – Cell Body Segmentation using ilastik Software

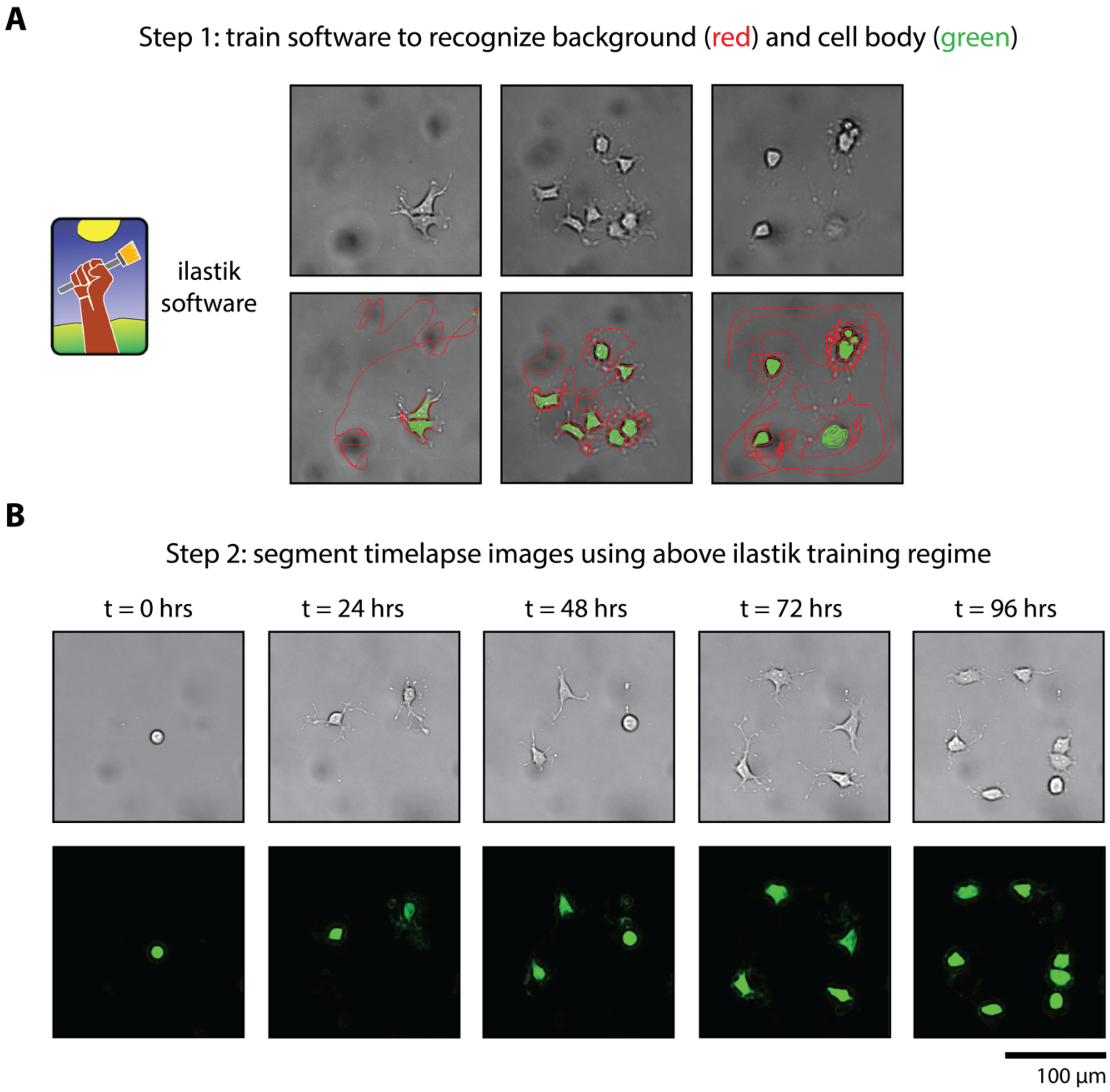

Supplementary Figure 3.13 One of the key challenges faced when analyzing our time-lapse experiments was processing the large number of microisland samples and their even larger associated time-lapse data sets. To address this challenge, we developed a custom computational analysis pipeline to detect and quantify cells within each protein region at each timepoint. In short, ilastik software (*66*) was employed to enable high-throughput segmentation and identification of cell bodies. (A) A pipeline was established based on user training of the software to distinguish between cell bodies (green) and background (red). Specifically, a handful of timepoints were analyzed manually, which included more challenging case scenarios in which cells were closely associated, spread out, more transparent, etc. Three example time-lapse frames (top) and their associated user-defined training segmentation (bottom) are displayed. (B) The established pipeline was then applied via batch processing to every frame of a 4-day time-lapse video. Representative images of bright field images (top) and their segmentation results (bottom) are provided.

3.6.14 Supplemental Figure 3.14 – Overview of Custom Fiji Script for Counting Cells

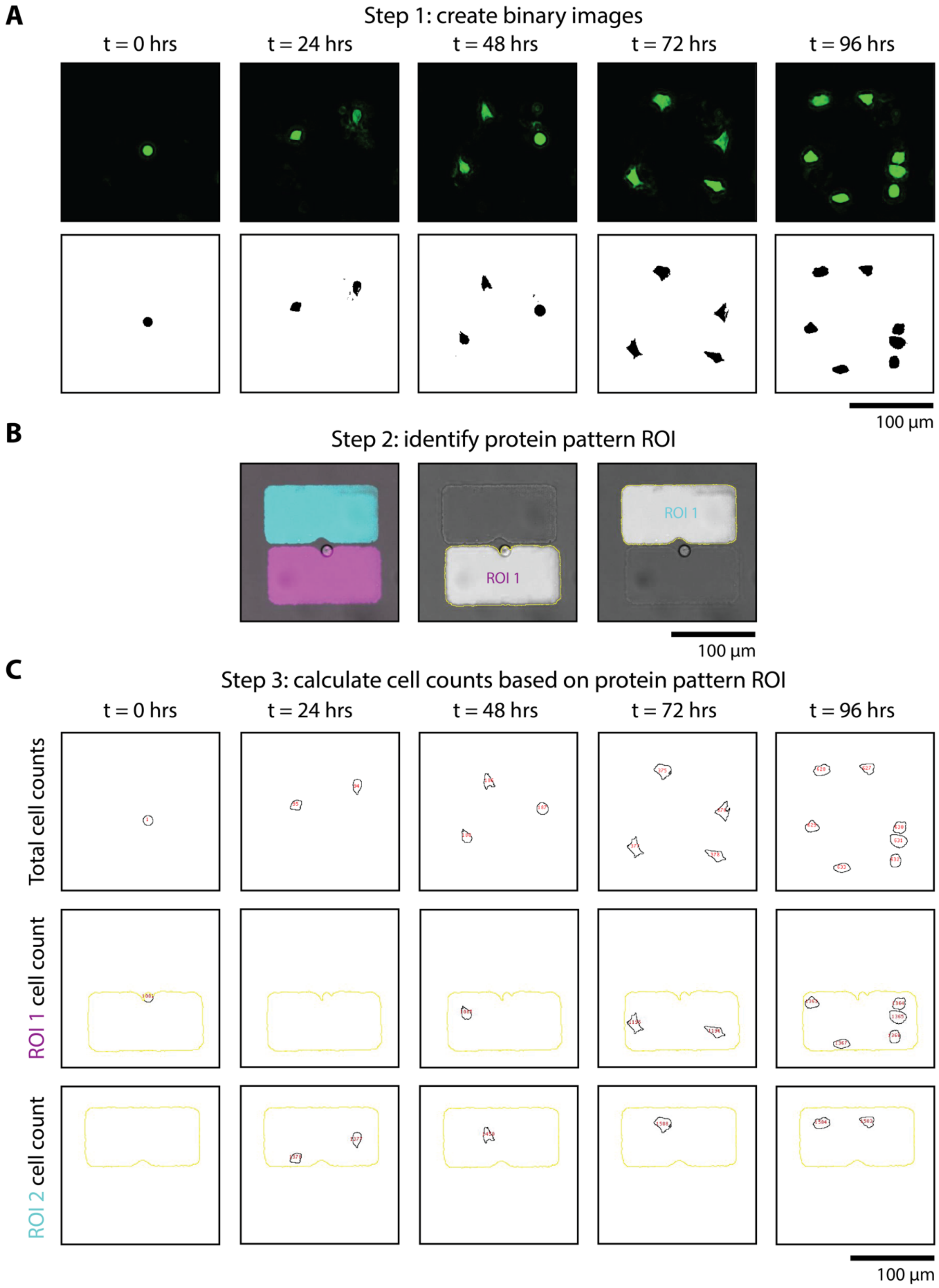

Supplementary Figure 3.14 The segmented time-lapse videos achieved using ilastik were then imported and analyzed via a custom macro script in Fiji. (A) The first step included converting the segmentation images into binary images and subsequently conducting post processing by filling holes and watershedding. Example timepoints from Days 0, 1, 2, 3, and 4 are provided. (B) The second step involved generating regions of interest (ROIs) based upon the fluorescent signal that is coupled to the protein patterns. (C) Finally, particle analysis was then conducted for three scenarios: 1) total cell body counts within the entire frame of view, 2) cell body counts within ROI 1, and 3) cell body counts within ROI 2. Based on these counts, the number of cell bodies within each of the protein regions as well as those that span both regions could be extrapolated for each timepoint.

3.6.15 Supplemental Figure 3.15 – Tracking Changes in Average Cell Occupancy within FGF-2 over Time for Each Individual Microisland

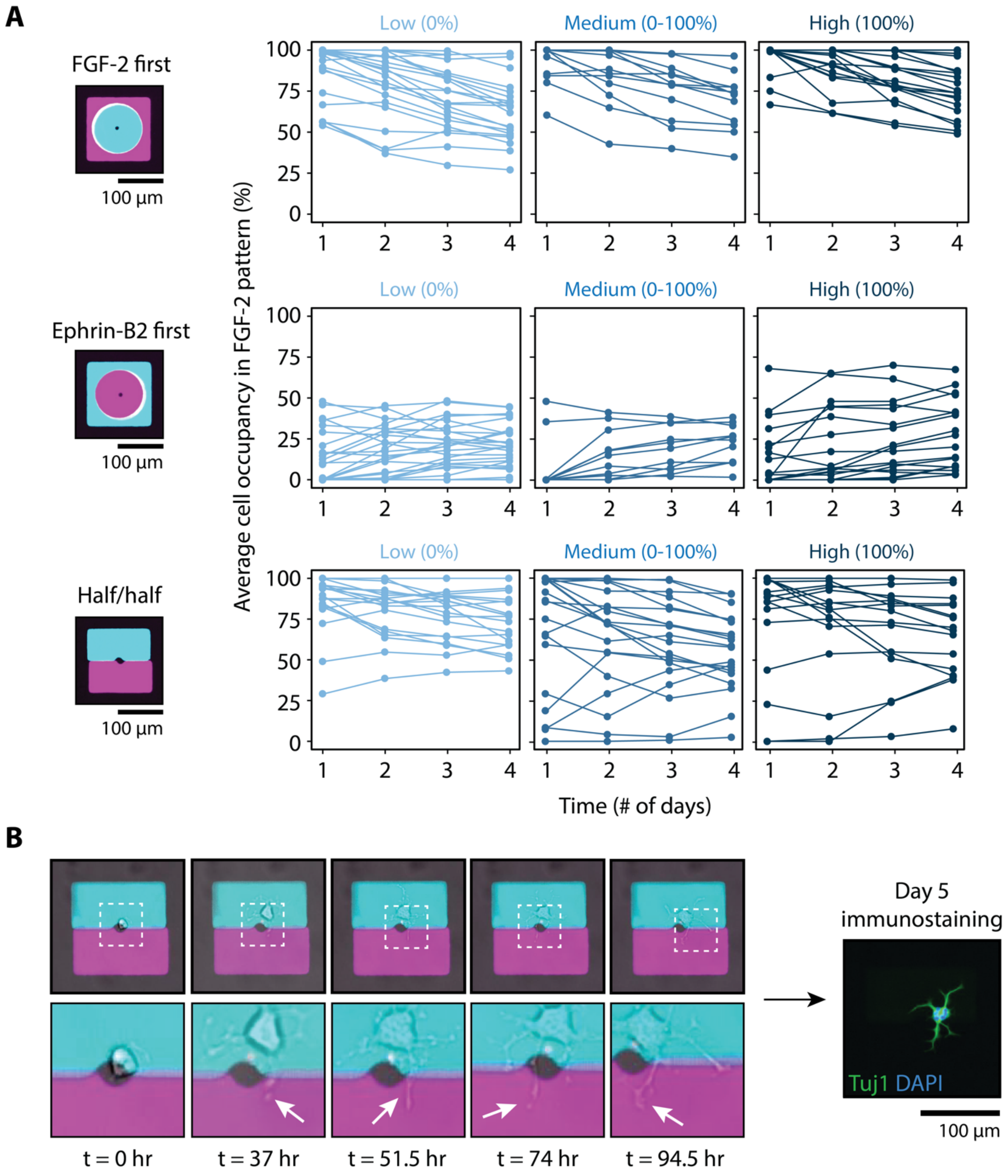

Supplementary Figure 3.15 (A) Microislands were binned into one of three categories based on Day 5 immunostaining results: "Low (0%)", "Medium (0-100%)", and "High (100%)" Tuj1+ neuronal differentiation. For each microisland, average cell occupancy within FGF-2 was then monitored for each day of the 4-day time-lapse. The microisland's trajectory is depicted as a line connecting each of these 4 points. (B) Time-lapse snapshots (left) of a microisland exhibiting 100% neuronal differentiation (right) despite having near 100% FGF-2 occupancy throughout the 4-day culture reveals dynamic neurite processes occupying both FGF-2 and ephrin-B2 patterns.

3.6.16 Supplemental Figure 3.16 – Polydimethylsiloxane (PDMS) Stamping Protocol to Enable Cell Patterning

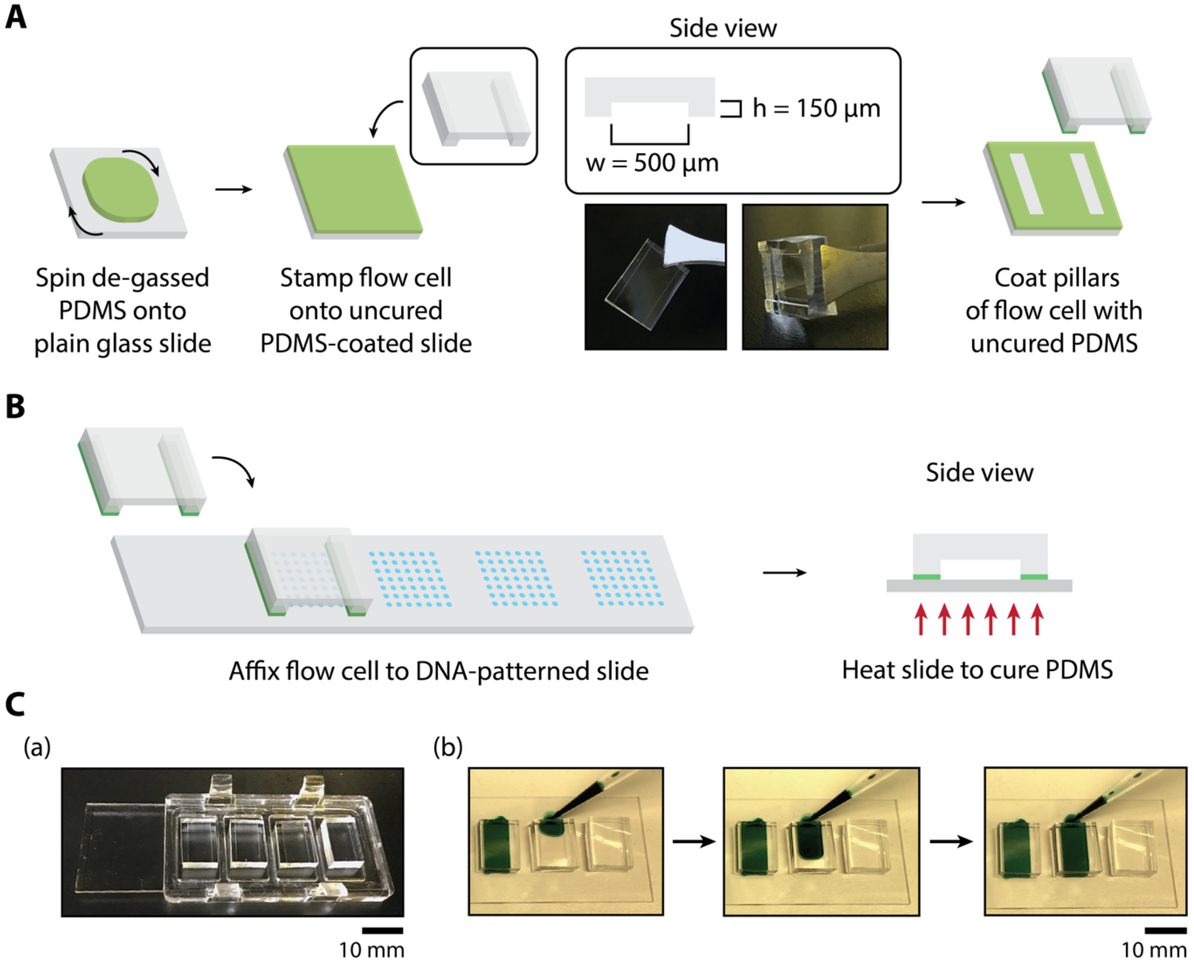

Supplementary Figure 3.16 PDMS flow cells are affixed within each well of a 4-well chamber slide to enable cycling of an oligo-labeled cell suspension across the DNA-patterned surface. The PDMS flow cell concentrates the cells to the surface as well as increases the probability of hybridization between the complementary cell-bearing and surface-patterned oligos. The latter of which is achieved by the repeated action of removing 5 µL of the cell suspension from the outlet and re-injecting into the inlet, thereby slowly cycling the cells across the surface until cells are patterned efficiently. In order to secure PDMS flow cells to the glass slide, a PDMS stamping protocol was employed. (A) Degassed PDMS was spun onto a plain glass slide at 4,000 RPM for 30 seconds to generate a thin film of PDMS. The flow cell was then stamped against this surface, coating only the pillars of the flow cell. (B) The flow cell is then positioned carefully over the DNA-patterned wells to ensure that, not only are the DNA patterns contained within the flow cell chamber, but also the flow cell must fit within the 4-well gasket chamber. The glass slide assembly is then heated at 65°C for 1 hour to cure the PDMS "glue", creating a bond strong enough to secure the flow cell throughout both the cell patterning steps as well as the 5-day differentiation experiment. (C) (a) A representative image of PDMS flow cells positioned within each well and (b) demonstration of capillary action drawing food coloring through the flow cell without the need of plasma treatment due to the tall flow channel height of 150 µm.

3.6.17 Supplemental Figure 3.17 – DNA-Directed Cell Patterning using Photolithographically-Defined Surface DNA Patterns

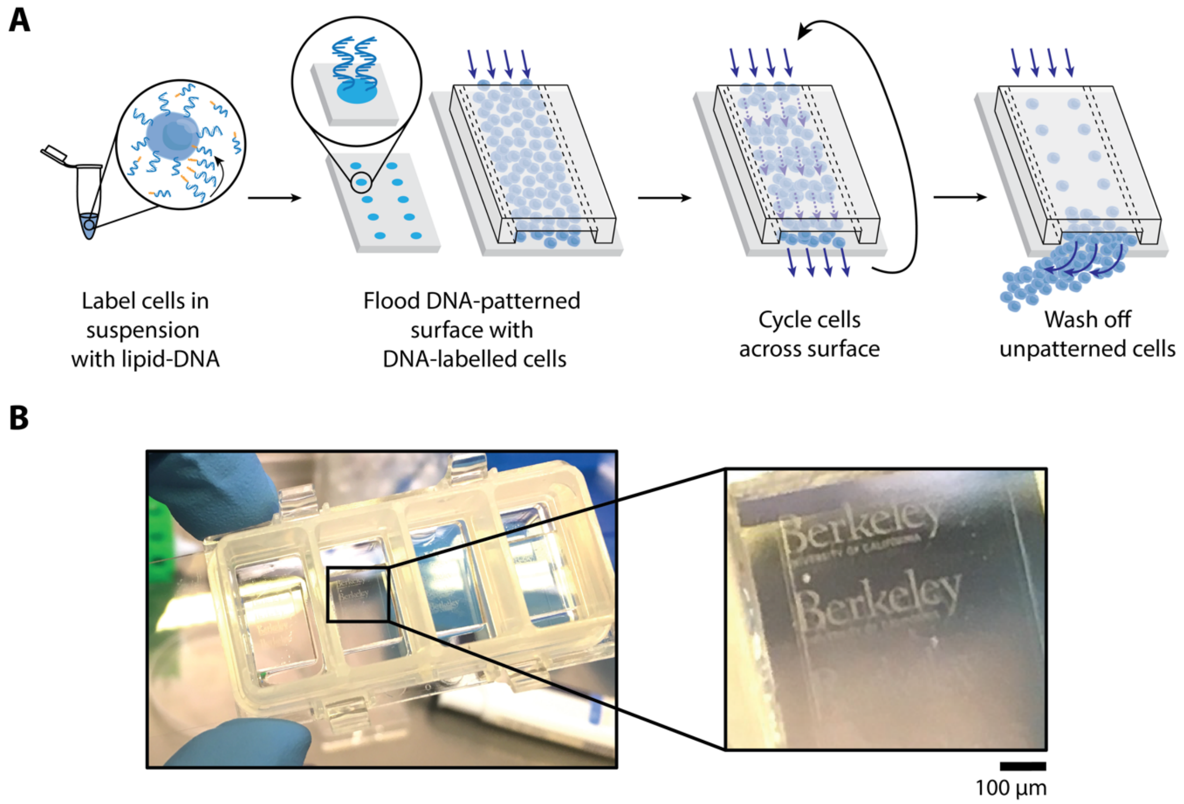

Supplementary Figure 3.17 (A) Microfabricated patterns of 20-bp single-stranded oligonucleotides direct the assembly of cell types of interest with high spatial precision via hybridization between complementary surface-conjugated and cell-labeling oligo strands. Cells are labeled with DNA through two successive incubation steps with lipid-modified oligo strands. While the first DNA imparts specificity, as the sequence of this strand is complementary to that of the DNA patterned onto the substrate, the second lipid-modified "co-anchor" strand tethers the first strand into the cell membrane. To achieve high patterning efficiencies, DNA-labeled cells are flooded first, via a PDMS flow cell, onto the surface of the DNA-patterned substrate. The cell suspension is then cycled slowly across the surface via the repeated action of pipetting cells into the flow cell inlet, retrieving the cells from the outlet, and re-pipetting into the inlet. Excess cells are washed off by flooding the flow cell with PBS multiple times, revealing cell patterns. (B) The resulting bulk adult neural stem cell patterns can be discerned by eye when DNA patterns are on the order of 100's of microns, as is the case for the displayed "Berkeley" patterns.

3.6.18 Supplemental Table 3.1 – Overview of Surface-Patterned DNA Sequences and their Complementary Fluorescent, Cell-Labeling, and Ligand-Labeling Oligonucleotides

Oligo Name	Sequence (5’ – 3’)
1. A-NH_2	[AminoC6] ACTGACTGACTGACTGACTG
2. A’-Cy3	[Cy3] CAGTCAGTCAGTCAGTCAGT
3. Azide-A’-Cy5	[Azide] CAGTCAGTCAGTCAGTCAGT [Cy5]
4. A’-Lipid	[Lipid] GTAACGATCCAGCTGTCACT TTTTTTTTTTTTTTTTTTTTTTTTTTTTTT TTTTTTTTTTTTTTTTTTTTTTTTTTTTTT CAGTCAGTCAGTCAGTCAGT
5. F-NH_2	[AminoC6] AGAAGAAGAACGAAGAAGAA
6. F’-NH_2	[AminoC6] TTCTTCTTCGTTCTTCTTCT
7. F’-AlexaFluor 488	[AlexaFluor488] TTCTTCTTCGTTCTTCTTCT
8. F-Lipid	[Lipid] GTAACGATCCAGCTGTCACT TTTTTTTTTTTTTTTTTTTTTTTTTTTTTT TTTTTTTTTTTTTTTTTTTTTTTTTTTTTT AGAAGAAGAACGAAGAAGAA
9. F’-Lipid	[Lipid] GTAACGATCCAGCTGTCACT TTTTTTTTTTTTTTTTTTTTTTTTTTTTTT TTTTTTTTTTTTTTTTTTTTTTTTTTTTTT TTCTTCTTCGTTCTTCTTCT
10. G-NH_2	[AminoC6] AGCCAGAGAGAGAGAGAGAG
11. Azide-G’-Cy3	[Azide] CTCTCTCTCTCTCTCTGGCT [Cy3]
12. G’-Cy5	[Cy5] CTCTCTCTCTCTCTCTGGCT
13. G’-Lipid	[Lipid] GTAACGATCCAGCTGTCACT TTTTTTTTTTTTTTTTTTTTTTTTTTTTTT TTTTTTTTTTTTTTTTTTTTTTTTTTTTTT CTCTCTCTCTCTCTCTGGCT
14. CoAnchor Lipid	[Lipid] AGTGACAGCTGGATCGTTAC

3.6.19 Supplemental Table 3.2 – Overview of Complementary Pairs of DNA Strands used for Characterization, Cell Patterning, Ligand Patterning, and Biological Experiments

Experiment	Oligo Name
1. DNA Patterning Characterization	G-NH_2, G'-Cy5
2. Cell Patterning	
a. one component	A-NH_2, A'-Lipid
b. two components	A-NH_2, A'-Lipid F'-NH_2, F'-Lipid
c. three components	A-NH_2, A'-Lipid F-NH_2, F'-Lipid G-NH_2, G'-Lipid
3. Fluorescent Protein Patterning	
a. one component (eGFP)	A-NH_2, Azide-A'-Cy5
b. two components (eGFP and mCherry)	A-NH_2, Azide-A'-Cy5 F-NH_2, Azide-F'
4. FGF-2 vs. Peptide Biology Experiments	
a. FGF-2 only	G-NH_2, Azide-G'-Cy3
b. EphB4-binding peptide only	A-NH_2, Azide-A'-Cy5
c. FGF-2 vs. EphB4-binding peptide	G-NH_2, Azide-G'-Cy3 A-NH_2, Azide-A'-Cy5
Note: F'-NH_2 and F-Lipid were utilized for patterning single cells in 4(a-c)	

3.6.20 Supplemental Table 3.3 – In-Depth Report of Experimental Sample Number "n"

Experiment	n
1. DNA Concentration vs. Cell Capture (Fig. 3B)	
a. 0.5 µM	83 arrays across 3 slides
b. 1 µM	82 arrays across 3 slides
c. 2.5 µM	78 arrays across 3 slides
d. 5 µM	73 arrays across 3 slides
e. 10 µM	74 arrays across 3 slides
f. 25 µM	73 arrays across 3 slides
g. 50 µM	25 arrays across 1 slide
h. 100 µM	18 arrays across 1 slide
2. DNA Spot Size vs. Cell Capture (Fig. 3C)	
a. d = 15 µm	200 spots
b. d = 20 µm	200 spots
c. d = 30 µm	340 spots
d. d = 40 µm	150 spots
e. d = 60 µm	250 spots
f. d = 80 µm	300 spots
g. d = 120 µm	125 spots
3. Soluble Media Conditions (Fig. S13B)	
a. Low FGF-2 (0.1 ng/mL)	177 microislands
b. Low FGF-2 (1 ng/mL)	832 microislands
d. Proliferation FGF-2 (20 ng/mL)	1331 microislands
e. Mixed Differentiation (1% FBS + 1 uM RA)	595 microislands
4. Single Solid-Phase Ligand Patterns (Fig. S17B)	
a. FGF-2 Only	1249 microislands
b. EphB4-Binding Peptide Only	273 microislands
5. Competing Solid-Phase Ligand Patterns (Fig. 7)	
a. Half/Half Patterns	55 microislands
b. FGF-2-Center	55 microislands
c. Ephrin-B2-Center	55 microislands

3.7 References

1. Sachs, P. C., Mollica, P. A., & Bruno, R. D. Tissue specific microenvironments: a key tool for tissue engineering and regenerative medicine. *J. Biol. Eng.* **11,** 34-45 (2017).
2. Scadden, D. T. The stem-cell niche as an entity of action. *Nature* **441,** 1075-1079 (2006).
3. Klemm, F. & Joyce, J. A. Microenvironmental regulation of therapeutic response in cancer. *Trends Cell Biol.* **25,** 198-213 (2015).
4. Quail, D. F. & Joyce, J. A. Microenvironmental regulation of tumor progression and metastasis. *Nat. Med.* **19,** 1423–1437 (2013).
5. Morrison, S. J. & Spradling, A. C. Stem cells and niches: mechanisms that promote stem cell maintenance throughout life. *Cell* **132,** 598-611 (2008).
6. Keung, A. J., Kumar, S., & Schaffer, D.V. Presentation counts: microenvironmental regulation of stem cells by biophysical and material cues. *Annu. Rev. Cell Dev. Biol.* **26,** 535-556 (2010).
7. Choi, C. K., Breckendridge, M. T., & Chen, C. S. Engineered materials and the cellular microenvironment: a strengthening interface between biology and bioengineering. *Trends Cell Biol.* **12,** 705-714 (2012).
8. Wheeldon, I., Farhadi, A., Bick, A. G., Jabbari, E., & Khademhosseini, A. Nanoscale tissue engineering: spatial control over cell-material interactions. *Nanotechnology* **21,** 212001 (2011).
9. Rompolas, P., Mesa, K. R., & Greco, V. Spatial organization within a niche as a determinant of stem-cell fate. *Nature* **502,** 513-518 (2013).
10. McBeath, R., Pirone, D. M., Nelson, C. M., Bhadriraju, K., & Chen, C. S. Cell shape, cytoskeletal tension, and RhoA regulate stem cell lineage commitment. *Dev. Cell* **6,** 483-495 (2004).
11. Maheshwari, G., Brown, G., Lauffenburger, D. A., Wells, A., & Griffith, L. G. Cell adhesion and motility depend on nanoscale RGD clustering. *J. Cell Sci.* **113,** 1677-1686 (2000).
12. Habib, S. J. *et al*. A localized Wnt signal orients asymmetric stem cell division in vitro. *Science* **6126,** 1445-1448 (2013).
13. Conway, A. *et al*. Multivalent ligands control stem cell behavior in vitro and in vivo. *Nat. Nanotechnol.* **8,** 831-8 (2013).
14. Shaw, A. *et al*. Spatial control of membrane receptor function using ligand nanocalipers. *Nat. Methods* **11,** 841-846 (2014).
15. Le Dréau, G. & Martí, E. Dorsal-ventral patterning of the neural tube: a tale of three signals. *Dev Neurobiol* **72,** 1471-1481 (2012).
16. Gonçalves, J. T., Schafer, S. T., & Gage, F. H. Adult neurogenesis in the hippocampus: from stem cells to behavior. *Cell* **167,** 897-914 (2016).
17. Chumley, M. J., Catchpole, T., Silvany, R. E., Kernie, S. G., & Henkemeyer, M. EphB receptors regulate stem/progenitor cell proliferation polarity during hippocampal neurogenesis. *J. Neurosci.* **27,** 13481-13490 (2007).
18. Pathania, M., Yan, L. D., & Bordey, A. A symphony of signals conducts early and late stages of adult neurogenesis. *Neuropharmacology* **58,** 865-876 (2010).
19. Lie, D. C. *et al*. Wnt signaling regulates adult hippocampal neurogenesis. *Nature* **437,** 1370-1375 (2005).

20. Frimat, J. P. *et al*. A microfluidic array with cellular valving for single cell co-culture. *Lab Chip* **11,** 231-237 (2011).
21. Hong, S., Pan, Q., & See, L. P. Single-cell level co-culture platform for intercellular communication. *Integr. Biol. (Camb)* **4,** 374-380 (2012).
22. Collins, D. J. *et al*. Two-dimensional single-cell patterning with one cell per well driven by surface acoustic waves. *Nat. Commun.* **6,** 8686 (2015).
23. Guo, F. *et al*. Controlling cell-cell interactions using surface acoustic waves. *Proc. Natl. Acad. Sci. U S A* **112,** 43-48 (2015).
24. Lin, R. Z., Ho, C. T., Liu, C. H., & Chang, H. Y. Dielectrophoresis based-cell patterning for tissue engineering. *Biotechnol. J.* **9**, 949-957 (2006).
25. Mittal, N., Rosenthal, A., & Voldman, J. nDEP microwells for single-cell patterning in physiological media. *Lab Chip* **7,** 1146-1153 (2007).
26. Junkin, M. *et al*. Plasma lithography surface patterning for creation of cell networks. *J. Vis. Exp.* **52,** 3115 (2011).
27. Khademhosseini, A. *et al.* Layer-by-layer deposition of hyaluronic acid and poly-l-lysine for patterned cell co-cultures. *Biomaterials* **25,** 3583-3592 (2004).
28. Fukuda, J. *et al.* Micropatterned cell co-cultures using layer-by-layer deposition of extracellular matrix components. *Biomaterials* **27,** 1479-1486 (2006).
29. Ruiz, A. *et al.* Microcontact printing and microspotting as methods for direct protein patterning on plasma deposited polyethylene oxide: application to stem cell patterning. *Biomed. Microdevices* **3,** 495-507 (2013).
30. Kung, F. H., Sillitti, D., Shreiber, D. I., Zahn, J. D., & Firestein, B. L. Microfluidic device-assisted etching of p-HEMA for cell or protein patterning. *Biotechnol. Prog.* **34,** 243-248 (2018).
31. Park, J. A. *et al*. Freeform micropatterning of living cells into cell culture medium using direct inkjet printing. *Sci. Rep.* **7,** 14610 (2017).
32. Lee, S. W. *et al*. Biologically active protein nanoarrays generated using parallel dip-pen nanolithography. *Adv. Mater.* **18,** 1133-1136 (2006).
33. Flaim, C. J., Chien, S., & Bhatia, S. N. An extracellular matrix microarray for probing cellular differentiation. *Nat. Methods* **2,** 119-125 (2005).
34. Ranga, A. *et al*. 3D niche microarrays for systems-level analyses of cell fate. *Nat. Commun.* **5,** 4324 (2014).
35. LaBarge, M. A. *et al*. Human mammary progenitor fate decisions are products of interactions with combinatorial microenvironments. *Integr. Biol. (Camb)* **1,** 70-79 (2009).
36. Gage, F. H. Mammalian Neural Stem Cells*. Science* **287,** 1433-1438 (2000).
37. Goh, E. L., Ma, D., Ming, G. L., & Song, H. Adult neural stem cells and repair of the adult central nervous system. *J. Hematother. Stem Cell Res.* **12,** 671-679 (2003).
38. Doetsch, F. A niche for adult neural stem cells. *Curr. Opin. Genet. Dev.* **13,** 543–550 (2003).
39. Bond, A. M., Ming, G. L., & Song, H., Adult mammalian neural stem cells and neurogenesis: five decades later. *Stem Cell* **17,** 385–395 (2015).
40. Palmer, T. D., Ray, J., & Gage, F. H. FGF-2-responsive neuronal progenitors reside in proliferative and quiescent regions of the adult rodent brain*. Mol. Cell Neurosci.* **6,** 474-486 (1995).
41. Ashton, R. S. *et al*. Astrocytes regulate adult hippocampal neurogenesis through ephrin-B signaling. *Nat. Neurosci*. **15,** 1399-1406 (2012).

42. Chandra, R. A., Douglas, E. S., Mathies, R. A., Bertozzi, C. R., & Francis, M. B. Programmable cell adhesion encoded by DNA hybridization. *Angew. Chem. Int. Ed. Engl.* **45,** 896-901 (2006).
43. Hsiao, S. C. *et al*. Direct cell surface modification with DNA for the capture of primary cells and the investigation of myotube formation on defined patterns. *Langmuir* **25,** 6985-6991 (2009).
44. Onoe, H. *et al*. Cellular microfabrication: observing intercellular interactions using lithographically-defined DNA capture sequences. *Langmuir* **28,** 8120-8126 (2012).
45. Chen, S. *et al*. Interrogating cellular fate decisions with high-throughput arrays of multiplexed cellular communities. *Nat. Commum.* **7,** 10309 (2016).
46. Belaubre, P. *et al*. Fabrication of biological microarrays using microcantilevers. *Appl. Phys. Lett.* **82,** 3122 (2003).
47. Dixit, C. K. & Aguirre, G. R. Protein microarrays with novel microfluidic methods: current advances. *Microarrays (Basel)* **3,** 180-202 (2014).
48. Tabata, T. & Takei, Y. Morphogens, their identification and regulation. *Development* **131**, 703-712 (2004).
49. Selden, N. S. *et al*. Chemically programmed cell adhesion with membrane- anchored oligonucleotides. *J. Am. Chem. Soc*. **134,** 765-768 (2012).
50. Weber, R. J., Liang, S. I., Selden, N. S., Desai, T. A., & Gartner, Z. J. Efficient targeting of fatty- acid modified oligonucleotides to live cell membranes through stepwise assembly. *Biomacromolecules* **15,** 4621-4626 (2014).
51. Pilz, G. A. *et al*. Live imaging of neurogenesis in the adult mouse hippocampus. *Science* **359,** 658-662 (2018).
52. Clevers, H. The intestinal crypt, a prototype stem cell compartment. *Cell* **154,** 274-284 (2013).
53. Bhatia, S. N., Underhill, G. H., Zaret, K. S., & Fox, I. J. Cell and tissue engineering for liver disease. *Sci. Transl. Med.* **6,** 245sr2 (2014).
54. Gaiano, N. & Fishell, G. The role of notch in promoting glial and neural stem cell fates. *Annu. Rev. Neurosci.* **25,** 471-490 (2002).
55. Voog, J. & Jones, D. L. Stem cells and the niche: a dynamic duo. *Cell Stem Cell* **6,** 103-115 (2010).
56. Chacón-Martínez, C. A., Koester, J., & Wickström, S. A. Signaling in the stem cell niche: regulating cell fate, function, and plasticity. *Development* **145,** dev165399 (2018).
57. Rezza, A., Sennett, R., & Rendl, M. Adult stem cell niches: cellular and molecular components. *Curr. Top. Dev. Biol*. **107,** 333-372 (2014).
58. Moore, K. A. & Lemischka, I. R. Stem cells and their niches. *Science* **311,** 1880-1885 (2006).
59. Kerever, A. *et al*. Novel extracellular matrix structures in the neural stem cell niche capture the neurogenic factor fibroblast growth factor 2 from the extracellular milieu. *Stem Cells* **25,** 2146-2157 (2007).
60. Koolpe, M., Burgess, R., Dail, M., & Pasquale, E. B. EphB receptor-binding peptides identified by phage display enable design of an antagonist with ephrin-like affinity. *J. Biol. Chem.* **17,** 17301-17311 (2005).
61. Kuhl, P. R. & Griffith-Cima, L. G. Tethered epidermal growth factor as a paradigm for growth factor-induced stimulation from the solid phase. *Nat. Med.* **2,** 1022-1027 (1996).

62. Kirby, E. D. *et al*. Acute stress enhances adult rat hippocampal neurogenesis and activation of newborn neurons via secreted astrocytic FGF2. *eLife* **2,** e00362 (2013).
63. Laussu, J., Khuong, A., Gautrais, J., & Davy, A. Beyond boundaries – Eph:ephrin signaling in neurogenesis. *Cell Adh. Migr.* **8,** 349-359 (2014).
64. Taylor, H., Campbell, J., & Nobes, C. D. Ephs and ephrins. *Curr. Biol.*, **27,** R90-R95 (2017).
65. Guo, W. -H. & Wang, Y. -L. Micropatterning cell-substrate adhesions using linear polyacrylamide as the blocking agent. *Cold Spring Harb. Protoc.*, doi: 10.1101/pdb.prot5582 (2011).
66. Strähle, C., Köthe, U., & Hamprecht, F. A. ilastik: Interactive Learning and Segmentation Toolkit. C. Sommer, 8th IEEE International Symposium on Biomedical Imaging (ISBI), 230-233 (2011).

Chapter 4: DNA-Based Approaches for Temporal Regulation of Ligand Presentation

4.1 Introduction

Biological systems are driven and tuned by the spatiotemporal fluctuations of external stimuli in which complex signaling dynamics orchestrate tissue function and instruct cell behavior (*1,2*). Within the temporal dimension of biology, the timing and strength of a signal – as well as the mode of temporal presentation (i.e. transient, sustained, oscillatory, etc.) – can modulate cell response. In the former case, the importance of signal timing (i.e. "when") was highlighted in human pluripotent stem cell differentiation into cardiomyocytes, where early beta-catenin-induced Wnt signaling coupled with Wnt suppression at a later timepoint synergistically yielded high cardiac potential (up to 98%) (*3*). Importantly, canonical Wnt suppression was pinpointed to a target, narrow window of 36-hrs post-differentiation, and mis-timing resulted in half the number of functional, contracting cardiomyocytes. A similar temporal window was also identified within adult hippocampal neural stem cells (NSCs), wherein the first 12-36 hours of differentiation were identified to be the most mechanoplastic. After which, NSCs were insensitive to changes in mechanical stimuli (*4*).

With regards to the importance of signal persistence or strength, increasing duration of stiff moduli pulses (E ~ 10 kPa) triggered longer periods of mechanical "memory" in hMSCs through the persistence of YAP/TAZ within the nucleus despite exposing cells to soft substrates (E ~ 2 kPa) immediately afterwards. While relatively short pulses (< 7 days) resulted in the eventual deactivation of YAP/TAZ by translocation back to the cytoplasm, increasing mechanical dosing to 10 days resulted in irreversible mechanical memory, revealing a stiffness threshold in which YAP/TAZ remained in the nucleus (*5*). Finally, the temporal pattern of signal presentation has also been demonstrated to be a key determinant in guiding cell behavior. Oscillations of cAMP as opposed to stable increases are necessary to modulate regional targeting of retinal neuronal processes via ephrin-A5-induced collapse and retraction during the establishment of the retinotopic map (*6*). These patterns are also important for multiple cues as, for example, the phase shift between Wnt and Notch oscillations mediate mesoderm segmentation (*7*). Temporal fluctuations also drive a host of other key biological processes, including metabolism, cell cycle, and circadian rhythms, to name but a few (*8*).

This increasing realization of the importance of temporal parameters in signaling motivates the development of a diverse toolbox of engineering methods for imparting temporal control, which the traditional genetic approaches for constitutive knockdown/knockouts and overexpression to perturb signaling dynamics does not provide (*9,10*). Optogenetics utilizes light-sensitive proteins to perturb specific nodes of a signaling pathway through the dimerization of two components or receptor clustering in response to light (*11*). Though offering high temporal and spatial resolution, this approach requires engineering a new protein for every pathway. Ligand-conjugated magnetic nanoparticles have also been proposed to concentrate signaling components of interest with quick on-off kinetics through the application of a magnetic field, generating dynamic signaling hotspots (*12*). However, magnetic nanoparticles require highly specialized equipment that may not be easily accessible. Finally, microfluidic devices impart tight manipulation of fluids, which is particularly well-suited for controlling the frequency and duration of soluble cues to cell culture (*13*). Similar to the magnet nanoparticle approach, specialized pump systems are required also.

Here, we contribute a DNA-based solution to achieve temporal control over solid-phase ligand presentation. As described in Chapter 3, we previously engineered a platform that utilizes photolithography to generate multiplexed surface DNA patterns comprised of unique 20-base pair oligonucleotides tethered to a glass substrate (*14*). The surface-tethered oligonucleotides direct and organize heterogenous cell types as well as solid-phase ligands by hybridizing with their complementary DNA strands, each conjugated with a signaling component of interest. While the use of photolithography imparts high spatial control with lithographic resolution, in this Chapter, I describe how we expanded the capabilities of our platform to incorporate *temporal control* for investigating in-depth how spatiotemporal patterns of extrinsic cues converge into cell fate decisions. Specifically, we demonstrate various DNA-based strategies that can be incorporated to achieve rapid cleavage of a patterned single ligand or multiplexed cleavage over multiple signaling ligands of interest. We highlight the applicability of these approaches with adult NSCs as our model system.

4.2 Results

4.2.1 DNase-Induced Cleavage of Single Ligand Presentation

DNA assumes a versatile and powerful role as a nanobiomaterial, storing inheritable information as well as orchestrating RNA and protein production to maintain homeostasis or, in some cases, initiate pathological signaling cascades. More recently, DNA has proven to be useful also as a materials engineering building block due to its ease in programmability, precise nanoscale geometry, and robust hybridization. A range of DNA-based applications have been demonstrated that span nanoscale robots or dynamic delivery constructs generated by DNA origami (*15*), DNA-based sensors for diagnostics (*16*), molecular characterization tools (*17*), and even applications in the field of microelectronics (*18*). Inspired by DNA's unique properties, we have leveraged the use of photolithography to pattern multiplexed DNA nanofilms that are highly functional as they assemble and recapitulate complex signaling environments in a controlled, bottom-up manner. Furthermore, we continue to draw inspiration from biology by utilizing enzymes that recognize and manipulate DNA to strengthen further our platform by incorporating the ability to impart temporal control over patterned signaling components. As illustrated in Figure 4.1(a), our first strategy to engineer temporal modulation into our system involves the use of deoxyribonuclease (DNase), which acts by cleaving the phosphodiester linkages of the DNA backbone, releasing DNA-hybridized ligands, and followed by a washing step to remove cleaved products. Due to this enzyme's lack of specificity, this particular approach enables a complete removal of all presented ligands, regardless of patterned DNA sequence. To enable visualization and quantification of DNase-based cleavage kinetics, we hybridized our surface DNA patterns to a fluorescent complementary oligonucleotide. We, then, introduced different concentrations of DNase (1 U, 10 U, and 100 U) and analyzed residual fluorescence after various incubation times (1 min, 5 min, and 15 min). As expected, we observed tunable cleavage kinetics by either increasing incubation time or increasing the concentration of DNase (Figure 4.1(b)). Particularly, at 100 units of DNase, we were able to achieve rapid cleavage of all patterned DNA within minutes.

To provide a proof-of-concept demonstration of DNase-based cleavage within a biological system, we highlighted temporal control over the presentation of fibroblast growth factor-2 (FGF-2), a key signaling ligand that promotes proliferation, and demonstrated that different degrees of ligand persistence directed various proliferation rates in NSCs. We employed our DNA-patterning platform to address single NSCs (Supplementary Figure 4.1) within microisland features containing patterned FGF-2. As illustrated in Figure 4.2(a), a fluorescent tag was included at the 3’ end of the oligonucleotide labeling FGF-2 to serve as a readout of protein localization, and the use of photolithography generated a large array of 100’s of single-cell/FGF-2 microislands. To achieve temporal control over FGF-2 presentation, we introduced DNase at different timepoints post-cell patterning to vary the persistence of ligand exposure and subsequently assessed its effects on single NSC proliferation rate. To avoid removing DNA-patterned NSCs upon the introduction of DNase, cells were incubated with laminin for one hour to allow for cells to adhere to the laminin-coated microislands and no longer rely on the DNA-tether (Supplementary Figure 4.2). The removal of FGF-2 at different time points throughout the 4-day culture resulted in a spectrum of proliferation rates (Figure 4.2(b)(i)) that increased from NSCs that lacked patterned FGF-2 to those that had immediate cleavage on Day 0, and cleavage on Day 2. These differences in proliferation rate can also be visualized through DAPI staining (Figure 4.2(b)(ii)). Other key advantages of using DNase include its low cytotoxicity and minimal effect on NSC differentiation (Supplemental Figure 4.3).

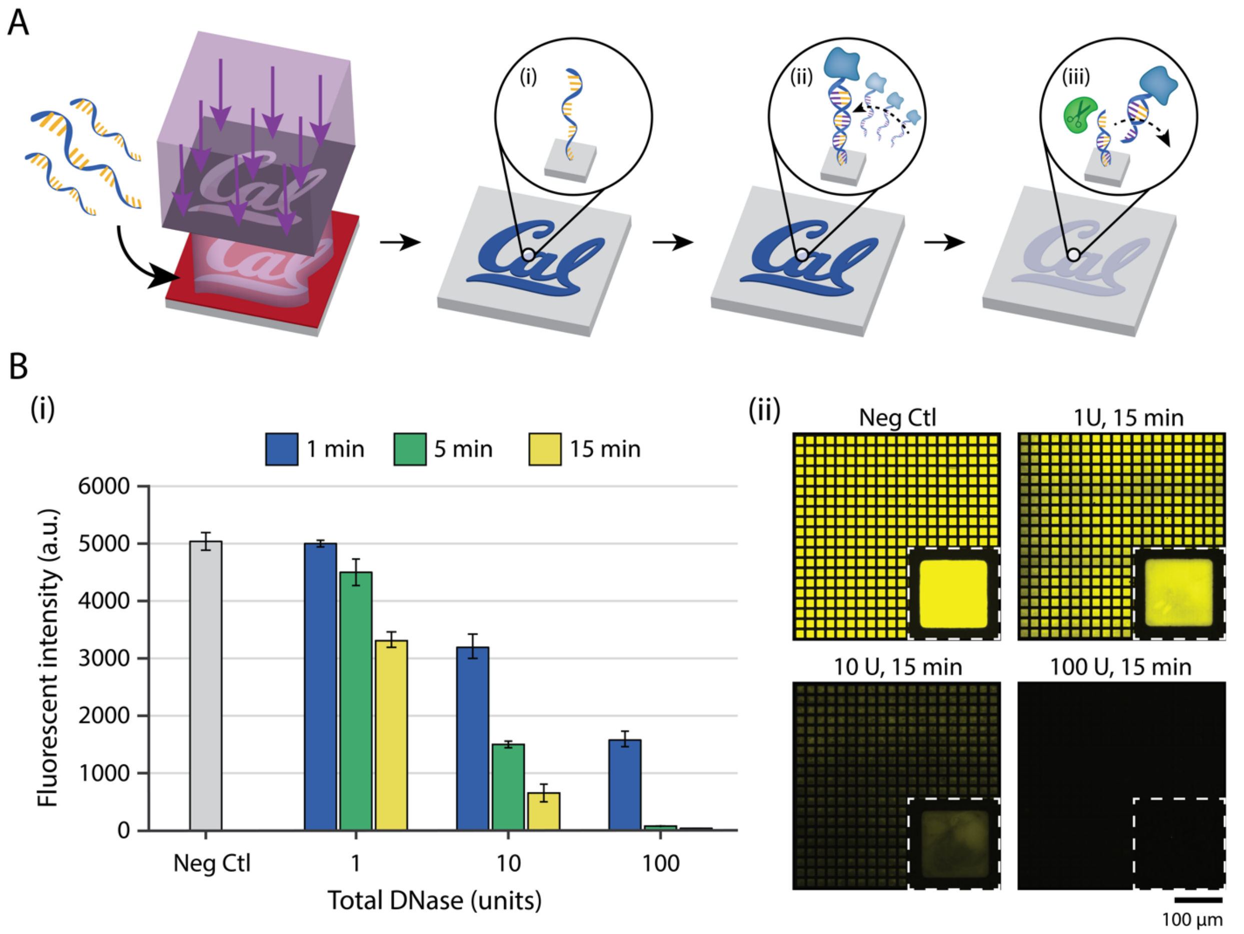

Figure 4.1 DNase-based strategy to achieve rapid, one-pot cleavage. (A) Temporal control over DNA-assembled ligands was achieved through incubation with DNase. (i) A 20 base-pair, single-stranded oligonucleotide was conjugated with high spatial control onto an aldehyde-functionalized glass slide using photolithographic techniques. (ii) Surface-tethered oligonucleotides instructed ligand assembly via hybridization with complementary oligonucleotides labeling a ligand of interest. (iii) The addition of DNase to DNA-assembled ligands induced hydrolysis of phosphodiester bonds, resulting in cleavage and subsequent release of the patterned ligand. (B) (i) Release kinetics of a hybridized fluorescent oligonucleotide were tested at different timepoints (1 min, 5 min, and 15 min) with different enzyme units (1 U, 10 U, and 100 U) of DNase prepared in NSC media (n=3; error bars represent standard deviation). (ii) Representative images of fluorescent DNA patterns 15 minutes post-incubation with different enzyme units of DNase. Scale bar represents 100 μm.

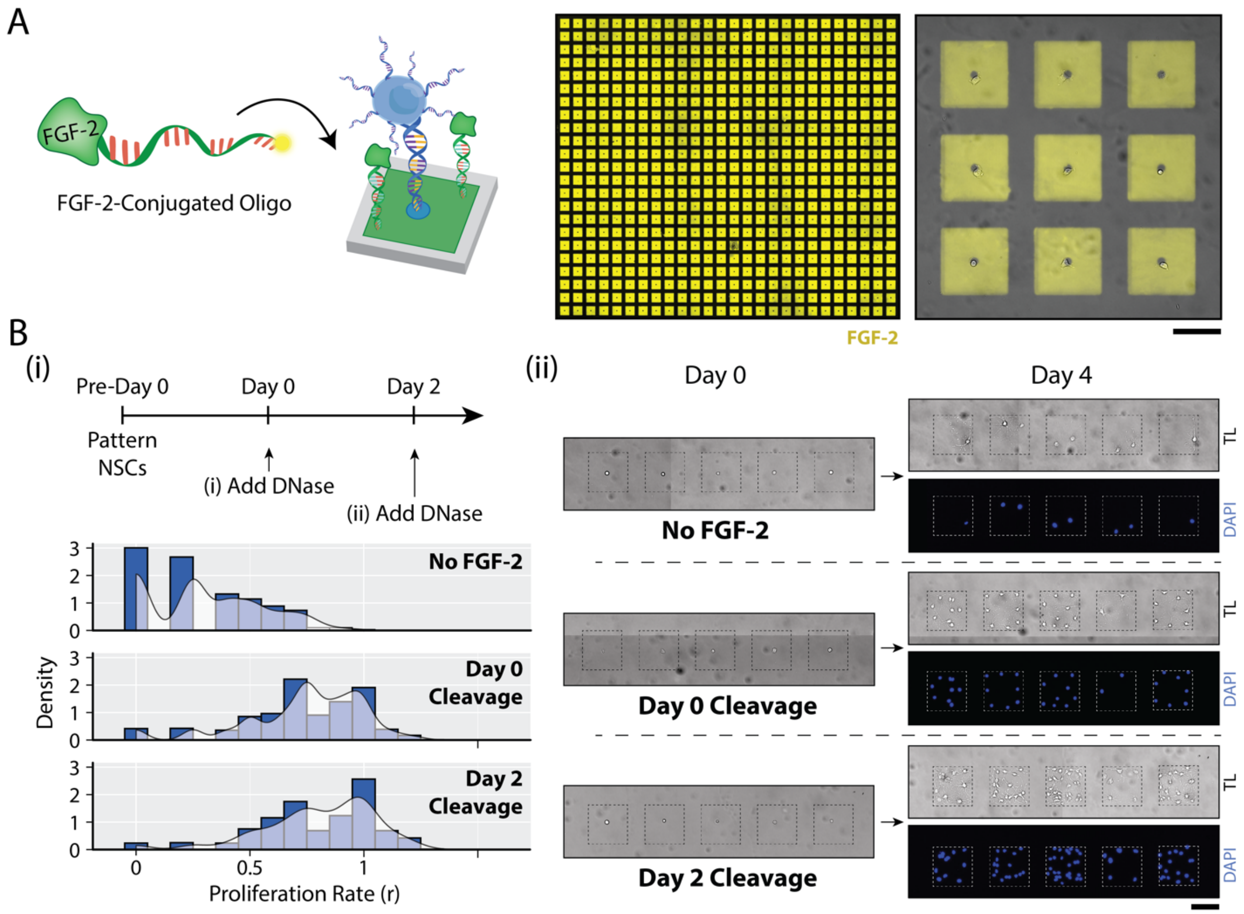

Figure 4.2 DNase-based cleavage of patterned fibroblast growth factor-2 (FGF-2) induced changes in single NSC proliferation. (A) A fluorescent oligonucleotide was conjugated to FGF-2 using click chemistry, and the conjugate was patterned within a large array of microisland features containing single NSCs using DNA-based assembly. FGF-2 patterns were visualized by imaging the fluorescent tag. Zoomed-in, overlay image shows representative 3x3 array of single-cell microislands patterned within FGF-2 (right). (B) (i) FGF-2 was patterned and cleaved with DNase at controlled timepoints (Day 0 and Day 2) during a 4-day culture, and proliferation rate was compared between conditions. (ii) Representative images of transmitted light (TL) and DAPI-stained microislands on Day 4 highlight different proliferation rates for various cleavage conditions. Scale bar represents 100 μm.

4.2.2 Encoding Cleavage Specificity with Restriction Sites

Though the application of DNase achieves temporal control over single DNA-presented ligands, biological systems are often comprised of multiple cues cooperating synergistically or antagonistically. Multicomponent control is required to resolve the temporal parameters governing these complex interactions. The use of orthogonal surface oligonucleotide strands programmed with unique sequences provides a solution for coordinating the DNA-based assembly of multiple signaling ligands. However, in order to obtain cleavage specificity, we propose programming restriction sites into patterned oligonucleotides, as demonstrated in Figure 4.3(a), and subsequently incubating the corresponding restriction enzyme.

To assess the feasibility of this approach, we designed and tested two DNA strands, one encoded with a *Bam* HI restriction site (GGATCC) and another with an *Eco* RI restriction site (GAATTC). We then hybridized complementary fluorescent oligos and quantified cleavage following incubation with different concentrations of the high-fidelity restriction enzymes. As highlighted in Figure 4.3(b)(ii), one of the key determinants of cleavage efficiency was the incubation buffer used during cleavage. A comparison of 1X CutSmart buffer, which is commonly employed for molecular cloning, against 1X PBS and NSC media (i.e. N2 media) revealed that CutSmart buffer was far more efficient for both enzymes. However, in the case of high *Bam* HI concentration at 1000 U, this discrepancy was negligible, as nearly complete cleavage was achieved for all three buffers after a one-hour incubation. Given the discrepancy in cutting kinetics for the different buffers, we investigated the effects of incubating 1X CutSmart buffer prepared in N2 media with adult NSCs. For a one-hour incubation, cell viability remained high (Supplemental Figure 4.4), and there was little to no effect on subsequent NSC proliferation and differentiation (Supplemental Figure 4.5).

Another key finding from these characterization experiments was the heterogeneity of restriction enzyme cleavage activity. Specifically, *Bam* HI demonstrated faster cutting kinetics while also demonstrating more tolerance to buffer composition. *Eco* RI exhibited far poorer cutting in N2 media across the different concentrations – a result most likely attributed to sub-optimal concentration of magnesium, which serves as a necessary co-factor for restriction enzyme activity, and/or the presence of high salt concentration. As shown in Supplemental Figure 4.6, these results were recapitulated in a gel format upon repeating the buffer and concentration conditions using a plasmid as a substrate, one that contained two *Bam* HI and two *Eco* RI cut sites. Therefore, when selecting appropriate restriction enzymes and buffer conditions, a rapid gel cleavage screen can be conducted to inform optimal oligo sequence design and ensure appropriate cleavage conditions. The robust specificity of restriction enzymes was highlighted further by testing the addition of *Bam* HI enzyme to a surface-patterned DNA strand containing a restriction site that closely resembles the correct *Bam* HI sequence yet deviates by one base pair (Supplemental Figure 4.7). Little to no cutting was detected across different *Bam* HI concentrations.

Thus, the strategy of programming restriction sites into patterned DNA strands imparts the necessary specificity to achieve multiplexed temporal control. More complex temporal ligand presentation logic can be achieved by extending the length of the surface-tethered oligonucleotide, such that partial DNA cleavage occurs upon the introduction of a restriction enzyme, leaving a residual 20-bp functional strand that can re-hybridize with a new ligand-conjugated oligo. An example of more complex temporal logic is demonstrated in Figure 4.3(c), where three unique fluorescent oligonucleotides were patterned initially, and the subsequent introduction of *Eco* RI and *Bam* HI removed the fluorescent oligos depicted by the yellow and purple patterns, respectively. Both cleavages exposed residual oligo strands that were then hybridized to new complementary strands that inverted the initial fluorophore presentation. Finally, the introduction of DNase removed all DNA-presented fluorophores. In-depth illustration of the DNA sequences employed for this cleavage and re-hybridization approach can be visualized in Supplemental Figure 8. The combined use of restriction sites/restriction enzymes with our lithographic DNA-patterning platform provides a systematic and controlled approach to explore the temporal dimension of solid-phase ligand signaling.

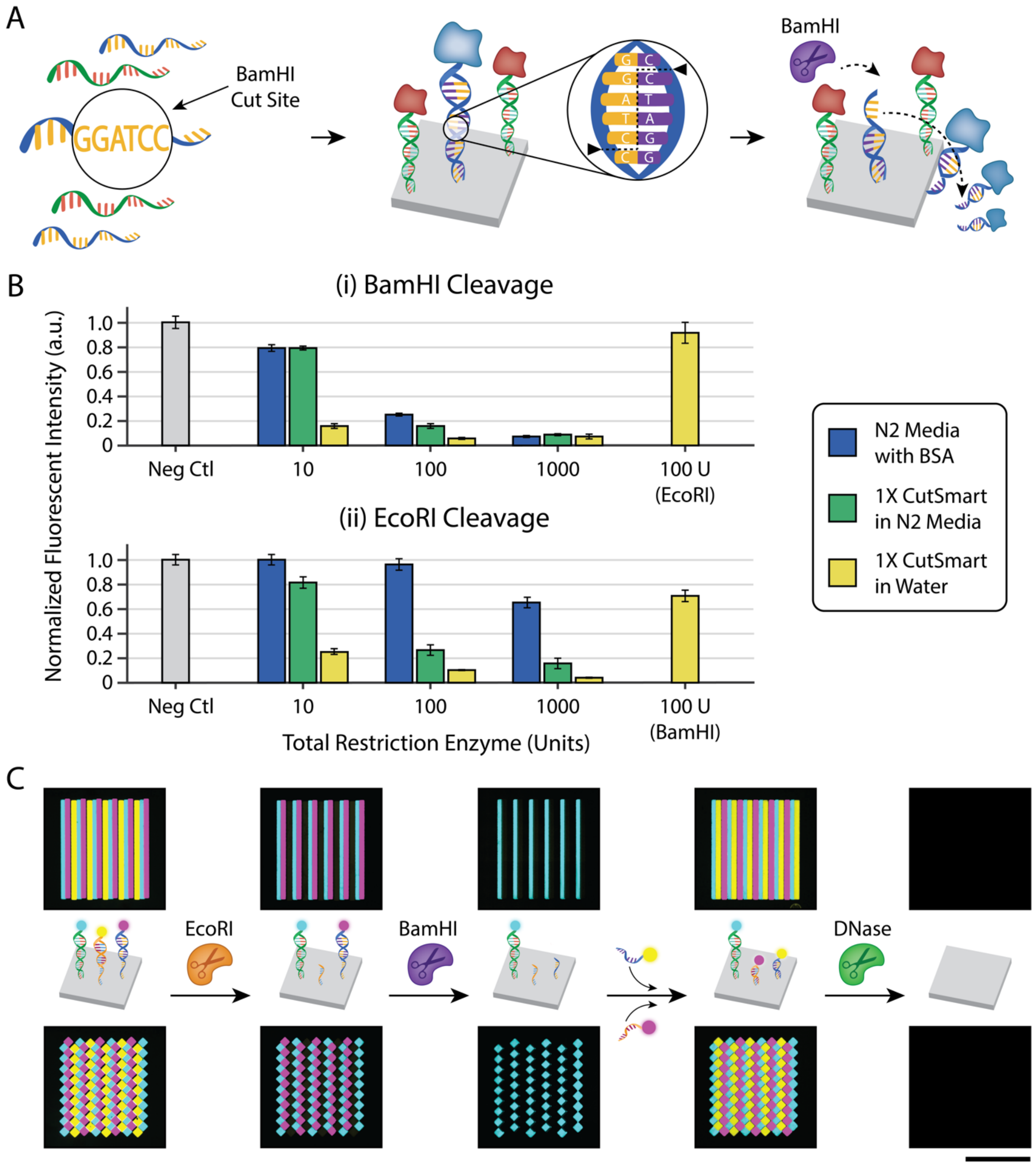

Figure 4.3 Encoding DNA cleavage specificity with restriction sites. (A) The incorporation of restriction sites into patterned DNA strands enabled targeted, site-specific cleavage upon incubation with a restriction enzyme. (B) Cleavage kinetics of different enzyme units (10 U, 100 U, and 1000 U) of (i) *Eco* RI and (ii) *Bam* HI prepared in different media conditions (N2 + 0.1 mg/mL BSA, 1X CutSmart in N2, and 1X CutSmart in water) were tested when incubated with hybridized fluorescent oligos containing either *Eco* RI or *Bam* HI cut sites for 1 hour at 37°C (n=3; error bars represent standard deviation). (C) The combined use of unique restriction sites and DNase enabled temporal control over multiple DNA-assembled signals as shown by the sequential cleavage of a (i) Cy5-hybridized oligonucleotide possessing an *Eco* RI cut site, (ii) Cy3-hybridized oligonucleotide possessing a *Bam* HI cut site, and (iii) AlexaFluor488-hybridized oligonucleotide with the use of DNase. The first cleaved DNA strand was designed to retain functionality post-cleavage, enabling the re-hybridization of a new Cy3-fluorescent oligo. Scale bar represents 100 µm.

4.2.3 A Parallel Approach for Rapid, Specific Cleavage using *Streptococcus pyogenes* Cas9 (SpCas9) Ribonucleoprotein

The discovery of CRISPR/Cas9 has revolutionized gene-editing therapeutics by enabling targeted Cas9-mediated gene correction. A single guide RNA (gRNA) directs a Cas9 endonuclease to a genomic site of interest, inducing site-specific cleavage that results in disruption of the mutated locus through insertions/deletions (INDELs) or correction via homology-directed repair (*19-21*). Motivated by the demonstrated specificity and robustness of CRISPR-Cas9, we investigated whether *Streptococcus pyogenes* (SpCas9) ribonucleoproteins (RNPs) could be applied to our DNA patterning system in a parallel approach to our previously described restriction enzyme strategy to achieve temporal control over patterned ligands. Analogous to type II restriction endonucleases, which assemble as homodimers that each recognize and cleave within symmetric recognition sequences, spCas9 contains two nuclease domains that together generate double-stranded breaks. Thus, when implemented into our system, Cas9-mediated cleavage releases the DNA-presented ligand that can then be washed away.

As illustrated in Figure 4.4(a), we designed and patterned a single-stranded oligonucleotide amenable to spCas9 cleavage as it contains a 20-bp target sequence located directly adjacent to the SpCas9 protospacer adjacent motif (PAM). 15-bp flanking regions were included to accommodate the bulky ~160 kDa Cas9 protein, providing both accessibility to the surface-tethered oligo and adequate length for R-loop formation by base-pair hybridization between the gRNA and target DNA sequence. To validate that our assembled Cas9 RNP could target and cleave our designed oligos, we first screened cleavage efficiencies in a gel format similar to the previously described restriction enzyme strategy, identifying rapid cleavage for both 10-fold and 100-fold excess of RNP (Supplemental Figure 4.9). We then patterned our CRISPR oligo using photolithography. Upon hybridizing the fluorescent complementary oligo, we investigated the kinetics of SpCas9 RNP-mediated surface DNA cleavage, testing incubation times that ranged from 1 min to 15 minutes (Figure 4.4(b)). We discovered a cutting saturation effect – which most likely can be attributed to a lack of SpCas9 RNP displacement post-cleavage – and that this saturation was reached within minutes, which highlights the rapid yet titratable action of SpCas9 RNP. This is in contrast to the previous restriction enzyme strategy that demonstrated increased cutting of DNA-presented ligand upon increased incubation times. To achieve various degrees of cutting, we conducted an initial proof-of-concept experiment, where we tested multiple doses at a fixed RNP concentration. As shown in Figure 4.4(c), repeated application of Cas9 RNP (1x, 2x, and 3x) resulted in increased cleavage. Interestingly, preliminary experiments revealed that increasing the RNP concentration does not result in increased cleavage efficiencies. Future work will focus on teasing apart the contributing factors for this observation. Other key experiments include identifying the number of required doses to achieve total cleavage of surface-hybridized DNA, characterizing RNP activity in different biological buffers, and demonstrating CRISPR multiplexing with multiple patterned DNA strands by incorporating orthogonal gRNAs.

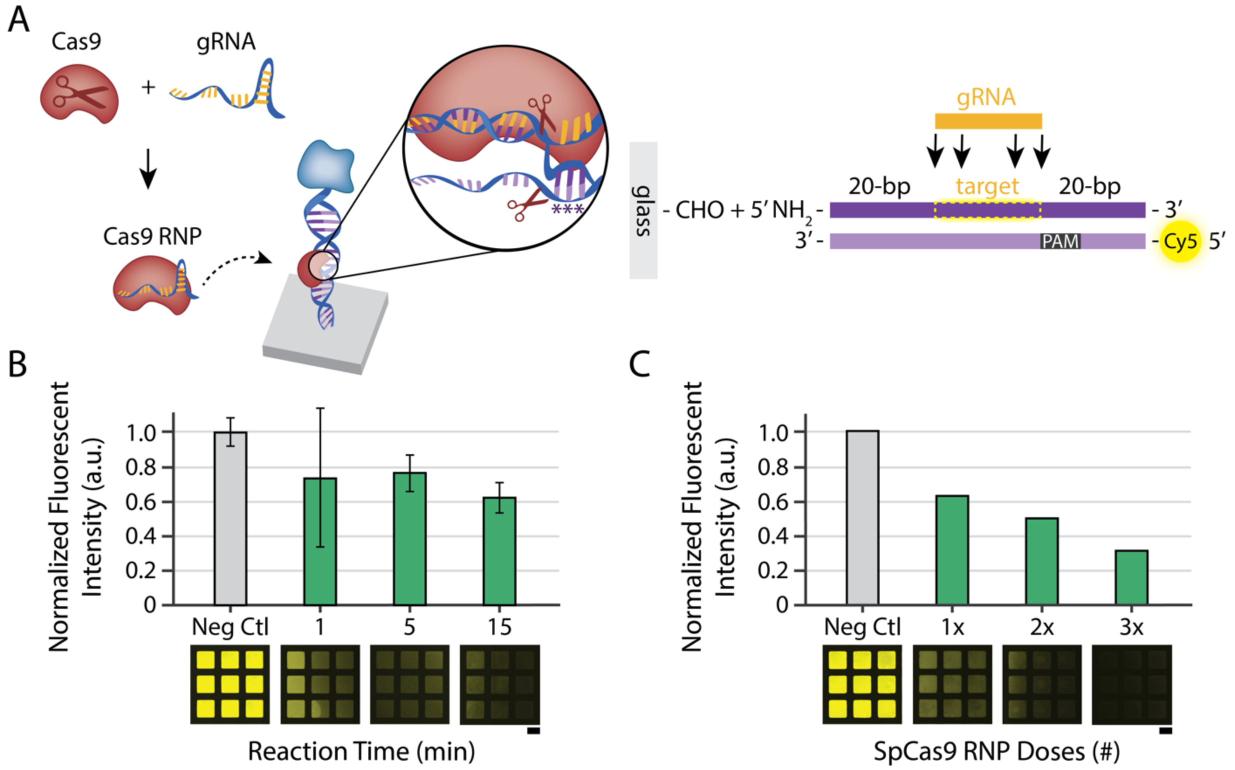

Figure 4.4. RNA-guided, site-specific cleavage with *Streptococcus pyogenes* Cas9 (spCas9) ribonucleoprotein (RNP). (A) spCas9 RNP is assembled with a 20-base pair (bp) gRNA targeting a surface-patterned DNA oligo that has been hybridized with a ligand of interest (left). The target sequence is immediately adjacent to the spCas9 PAM sequence, NGG, and contains 15-bp flanking sequences (right). For characterization experiments, a complementary DNA strand with a Cy5 modification at the 3’ end was employed for visualization and quantification. (B) Cas9 RNP cleavage kinetics of 50 nmole was tested for different incubation times (1, 5, and 15 min) in RNP buffer at 37°C. n=3 and error bars represent standard deviation. (C) Initial studies (i.e. one replicate) suggest that titratable cleavage can be achieved through multiple 15-min RNP doses. Scale bar represents 100 µm.

4.3 Discussion

Here, we describe multiple DNA-based strategies for engineering temporal control over presented solid-phase ligands – strategies that enable recapitulating and dissecting how temporal parameters modulate ligand action. Our platform harnesses photolithography to fabricate surface DNA patterns comprised of multiplexed oligonucleotide strands which, in turn, assemble heterogeneous ligands through the hybridization between surface-tethered oligos and ligands labelled with the unique, complementary oligos. While we previously demonstrated that employing photolithography imparts tight spatial control over ligand presentation, we proposed integrating temporal control into our system by capitalizing on biology’s natural toolbox of nucleases to cleave DNA-presented ligands. One of the key advantages of adopting nucleases is their biocompatibility, which is in contrast to previous strategies that apply UV light, induce pH changes, or tune temperature to achieve temporal modulations – thus, inducing cytotoxicity and/or altering normal cell behavior (*22*). A second key advantage of nuclease-mediated temporal control is the cleavage tunability by selecting different classes of nucleases. With DNase, we demonstrated nonspecific yet rapid, one-pot cleavage of hybridized ligands, which is particularly well suited for controlling solid-phase ligand persistence of a single ligand and investigating the effects of timing and strength/duration on cell behavior. For signaling environments in which multiple signals are operating together, both restriction endonucleases and SpCas9 RNP's can be utilized to achieve cleavage specificity or multiplexed temporal control. Even more sophisticated strategies can be engineered to model more complex networks by designing longer oligo strands such that there remains a functional portion of the surface-patterned DNA post-cleavage upon which new strands labeling additional ligands can be hybridized and controlled. Together, these three DNA-targeting enzymes provide a facile, yet robust, approach to explore the temporal space of biology.

4.4 Methods

Surface DNA patterning using photolithography

20 base-pair, single-stranded oligonucleotides (IDT) were patterned onto an aldehyde glass slide (Schott Nexterion). In short, microfabricated positive photoresist (Shipley S1813) served as a physical mask, selectively exposing aldehyde surface regions and subsequently guiding the conjugation of amine-terminated oligonucleotides with high spatial control. An oligonucleotide solution prepared in 50 mM sodium phosphate buffer (pH = 8.5) was dropcast over the patterned photoresist, heated to induce condensation, and treated with 0.05% sodium borohydride in 1X PBS for 10 minutes to conjugate covalently the amine-terminated oligonucleotide to the aldehyde substrate. Photoresist was removed by rinsing slides with acetone, followed by DI water, and dried under a dry nitrogen stream. Slides were stored under vacuum until ready to use. DNA sequences are provided in Supplementary Table 4.1.

To visualize patterns, Millicell EZ 4-well chambers (Millipore) were first secured onto the glass slide, and the surface was blocked for 1 hour on a shaker by adding 1 mL of blocking buffer (2% bovine serum albumin (BSA) in 1X PBS) to each well. The 2% BSA was exchanged using a pipette with 250 µL/well of a 0.2 µM solution comprised of the complementary oligonucleotide containing a fluorescent tag prepared in the same blocking buffer. Following a 5-minute incubation on a shaker to allow for hybridization, wells were rinsed 4x with 1X PBS to remove unbound fluorescent oligonucleotides and stored in fresh 1X PBS during imaging (*14*).

Cell culture

Adult rat hippocampal neural stem cells (NSCs) were isolated previously from 6-week-old female Fischer 344 rats (*23*). To promote monolayer adhesion, NSCs were cultured on polystyrene plates coated with 10 µg/mL poly-L-ornithine hydrobromide (Sigma) in sterile DI water overnight at room temperature and 5 µg/mL of laminin (Invitrogen) in sterile PBS overnight at 37°C. NSCs were maintained in Dulbecco's Modified Eagle Medium/Nutrient Mix F-12 (DMEM/F-12, Invitrogen) with 1% (v/v) N-2 Supplement (Invitrogen) and 20 ng/mL of basic fibroblast growth factor (FGF-2, Peprotech) and incubated at 37°C and 5% CO_2. NSCs were passaged upon 80% confluency using Accutase (Innovative Cell Technologies). For differentiation studies, NSCs were cultured in normal culture media supplemented with 1% fetal bovine serum (Invitrogen), 1 µM retinoic acid (Enzo Life Sciences), and 1% penicillin-streptomycin (Gibco) in DMEM/F-12 + N-2 Supplement. For studies involving protein patterns, NSCs were cultured in maintenance media (DMEM/F-12 + N-2) supplemented with 0.1 ng/mL of FGF-2 to promote low proliferation and differentiation.

DNA-based single NSC patterning

High-throughput capture of thousands of single NSCs is achieved by first labeling cell membranes with lipid-conjugated oligonucleotides containing the complementary sequence to surface-patterned, 15 µm-diameter DNA spot features. The prepared DNA-tethered cell suspension is then flowed 10-20x across the DNA substrate with the aid of a polydimethoxysilane (PDMS) flow chamber to promote hybridization between surface-bearing and cell-labeling oligos – thus, achieving cell capture. Both the cell-labeling process and flow steps are described previously in detail (*14*).

DNase-based cleavage experiments

Deoxyribonuclease I (DNase) (Worthington, LS002138) was supplied by the manufacturer as a lyophilized power and was re-suspended in NSC media (DMEM/F-12 + 1% N-2 Supplement) at 1,000 Kunitz units/mL. For DNase-cleavage characterization experiments, stock DNase was diluted further to the appropriate Kunitz units in 250 μL of media and subsequently incubated at 37°C within each DNA-patterned well for the designated amount of time. Wells were then rinsed 4x with 1X PBS to remove cleaved DNA.

For DNase-cleavage experiments of DNA-hybridized fibroblast-growth factor 2 (FGF-2), patterned single NSCs were first incubated with 20 μg/mL of laminin for 1 hour at 37°C to ensure that cells no longer rely on DNA to be tethered to the surface and, thus, not removed upon the introduction of DNase. 1000 units of DNase was then introduced to cells by pipetting into the PDMS flow cell and allowed to incubate for 15 minutes at 37°C. Wash steps were conducted by cycling PBS into and out of the flow cell 10x. A total of three DNase treatment was conducted to ensure complete cleavage of patterned FGF-2 and validated upon imaging as an observed loss of Cy3 signal.

Restriction enzyme-based cleavage experiments

For DNA-patterning experiments, high-fidelity *Bam* HI and *Eco* RI (NEB) were prepared in the following buffers: 1X CutSmart (NEB) diluted in water, 1X CutSmart diluted in NSC media (DMEM/F-12 + 1% N-2 Supplement), and/or NSC media supplemented with 0.1 mg/mL bovine-serum albumin (BSA). 250 μL of prepared restriction enzyme solution containing the desired units and buffer were then added to fluorescently-hybridized DNA-patterned slides, prepared as described above.

For restriction enzyme digest characterization experiments, 20 units of high-fidelity *Bam* HI and *Eco* RI were prepared in the aforementioned buffers and incubated with 500 ng of a 11.6 kb plasmid containing two *Eco* RI cut sites and two *Bam* HI cut sites in a total volume of 50 μL for 5 min, 30 min, or 60 min at 37°C. Digest efficiency was assessed by running products on a 1% Tris-Acetate-EDTA (TAE) agarose gel, and DNA bands were visualized using SyberSafe (Thermo Fisher Scientific).

Streptococcus pyogenes Cas9 (SpCas9) ribonucleoprotein (RNP)-based cleavage experiments

To assemble the RNP, recombinant SpCas9 was diluted to 10 μM in RNP buffer (20 mM Tris-HCl, 100 mM KCl, 5% (v/v) glycerol, 5 mM $MgCl_2$, 1 mM TCEP, 50 μg/mL, pH=7.5) and added to 12 μM of folded single guide RNA (sgRNA) prepared in folding buffer (20 mM HEPES, 150 mM NaCl, pH=7.5), which was transcribed and purified in the Doudna Lab as described previously (*21*). The two components were incubated at 37°C for 10 minutes and subsequently diluted further in RNP buffer at the desired concentration prior to being added to DNA-patterned substrate.

4.5 Acknowledgements

We thank Dr. Molly Kozminsky, Dr. Nahyun Cho, Thomas Carey, Sabrina Sun, Christina Fuentes, Andy Lopez, Dr. Shakked Halperin, and Dr. Kira Mosher for helpful discussions as well as Connor Tsuchida and the Doudna Lab for assistance in designing and assembling SpCas9 RNP.

4.6 References

1. Behra, M., & Hoffmann, A. Understanding the temporal codes of intracellular signals. Curr Opin Genet Dev. 20(6), 684-93 (2019).
2. Purvis, J. E., & Lahav, G. Encoding and decoding cellular information through signaling dynamics. Cell. 152(5), 945-56 (2013).
3. Lian et al. Robust cardiomyocyte differentiation from human pluripotent stem cells via temporal modulation of canonical Wnt signaling. Proc Natl Acad Sci U S A. 109(27), E1848-E1857 (2012).
4. Rammensee et al. Dynamics of mechanosensitive neural stem cell differentiation. Stem Cells. 35(2), 497-506 (2017).
5. Yang, C., Tibbitt, M. W., Basta, L., Anseth, K. S. Mechanical memory and dosing influence stem cell fate. Nat Mater. 13(6), 645-52 (2014).
6. Nicol, X., Voyatzis, S., Muzerelle, A., Narboux-Neme, N., Sudhf, T. C., Miles, R., Gaspar, P. cAMP oscillations and retinal activity are permission for ephrin signaling during the establishment of the retinotopic map. Nat Neurosci 10(3), 340-7 (2007).
7. Sonnen, K. F. et al. Modulation of phase shift between Wnt and Notch signaling oscillations controls mesoderm segmentation. Cell. 172(5), 1079-90 (2018).
8. Ganesan, A., & Zhang, J. How cells process information: quantification of spatiotemporal signaling dynamics. Protein Sci. 21(7), 918-28 (2012).
9. Ross, B., Mehta, S., Zhang, J. Molecular tools for acute spatiotemporal manipulation of signal transduction. Curr Opin Chem Biol. 34, 135-142 (2016).
10. Handly, L. N., Yao, J., Wollman, R. Signal transduction at the single-cell level: approaches to study the dynamic nature of signaling networks. J Mol Biol. 428(19), 3669-82 (2016).
11. Repina, N. A., Rosenbloom, A., Mukherjee, A., Schaffer, D. V., Kane, R. S. At light speed: advantages in optogenetic systems for regulating cell signaling and behavior. Annu Rev Chem Biomol Eng. 8, 13-39 (2017).
12. Etoc, F., Lisse, D., Bellaiche, Y., Piehler, J., Coppey, M., Dahan, M. Subcellular control of Rac-GTPase signaling by magnetogenetic manipulation inside living cells. Nat Nanotechnol. 8(3), 193-8 (2013).
13. Sonnen, K. F. & Merten, C. A. Microfluidics as an emerging precision tool in development biology. Dev Cell. 48(3), 293-311 (2019).
14. Scheideler et al. A multiplexed, lithographic DNA approach to recapitulate niche ligand competition with controlled spatial presentations. Submitted to Nature Methods.
15. Li et al. A DNA nanorobot functions as a cancer therapeutic in response to a molecular trigger in vivo. Nat Biotechnol. 36(3), 258-264 (2018).
16. Park, S. J., Taton, T. A., Mirkin, C. A. Array-based electrical detection of DNA with nanoparticle probes. Science. 295(5559), 1503-6 (2002).
17. Nickels et al. Molecular force spectroscopy with a DNA-origami based nanoscopic force clamp. Science. 354(6310), 305-7 (2016).
18. Sha et al. Charge splitters and charge transport junctions based on guanine quadruplexes. Nat Nanotechnol. 13(4), 316-21 (2018).
19. Jinek et al. A programmable dual-RNA-guided DNA endonuclease in adaptive bacterial immunity. Science. 337(6096), 816-21 (2012).

20. Sternberg, S. H., Redding, S., Jinek, M., Greene, E. C., Doudna, J. A. DNA interrogation by the CRISPR RNA-guided endonuclease Cas9. Nature. 507, 62-67 (2014).
21. Sternberg, S. H., LaFrance, B., Kaplan, M., Doudna, J. A. Conformational control of DNA target cleavage. Nature. 527(7576), 110-3 (2015).
22. Scheideler, O. J., Sohn, L. L., Schaffer, D. V. Emerging engineering strategies to study the stem cell niche. In: Turksen K. (eds) Biology in Stem Cell Niche. Stem Cell Biology and Regenerative Medicine. Springer, Cham.
23. Palmer, T. D., Ray, J., & Gage, F. H. FGF-2-responsive neuronal progenitors reside in proliferative and quiescent regions of the adult rodent brain. *Mol. Cell Neurosci.* 6**,** 474-486 (1995).

4.7 Supplementary Materials

4.7.1 Supplemental Figure 4.1. DNA-Patterned, High-Throughput Single Neural Stem Cell (NSC) Array

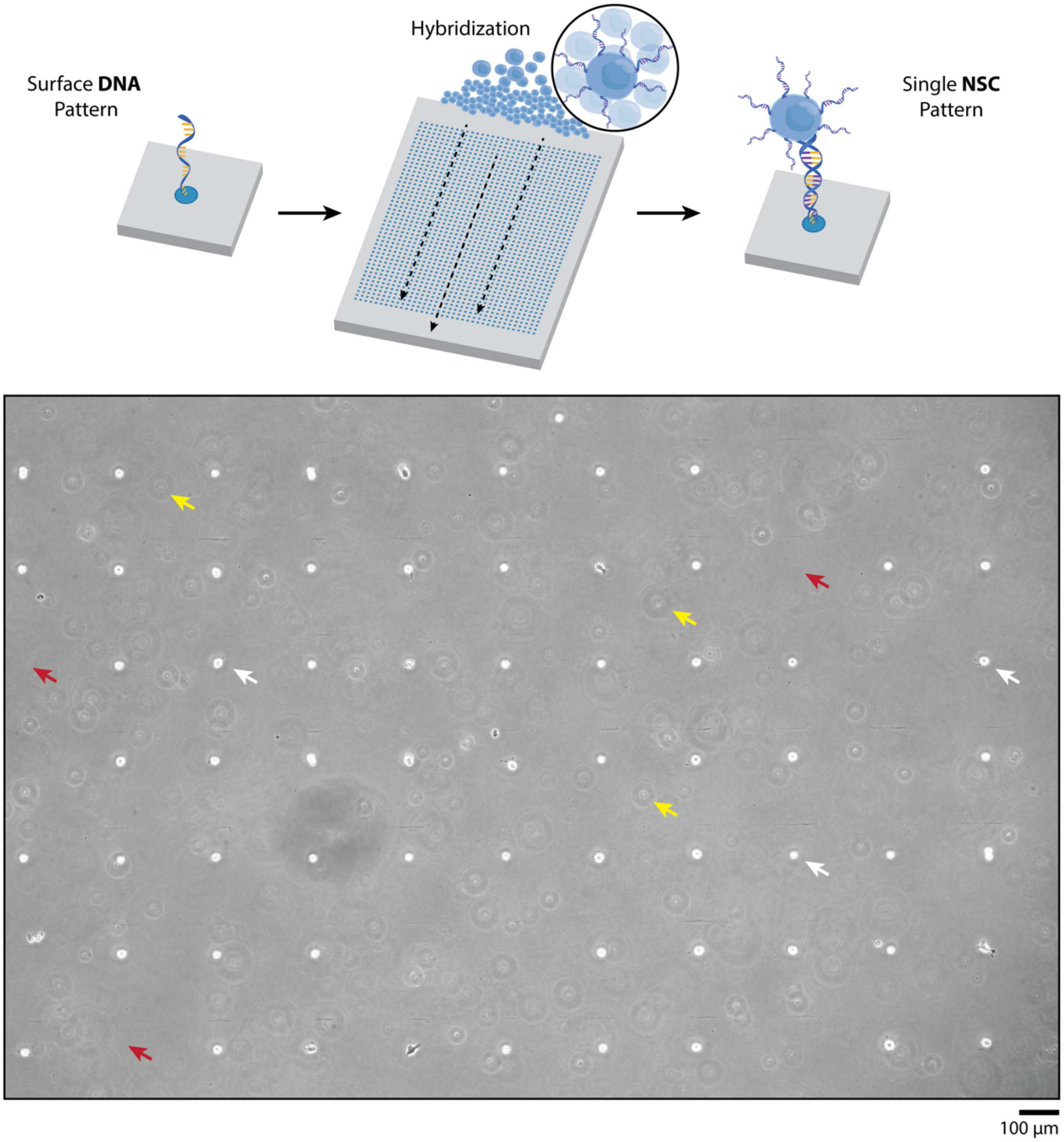

Supplemental Figure 4.1 Surface DNA patterns instruct high-throughput arrays of single adult neural stem cells (NSCs) via hybridization between surface-tethered and cell-bearing complementary oligonucleotides. White arrows highlight single NSC capture, red arrows highlight no capture, and yellow arrows highlight floating cells not in-plane.

4.7.2 Supplemental Figure 4.2. DNA-Patterned Single Neural Stem Cell (NSC) Retention Following Laminin Incubation and DNase Treatment

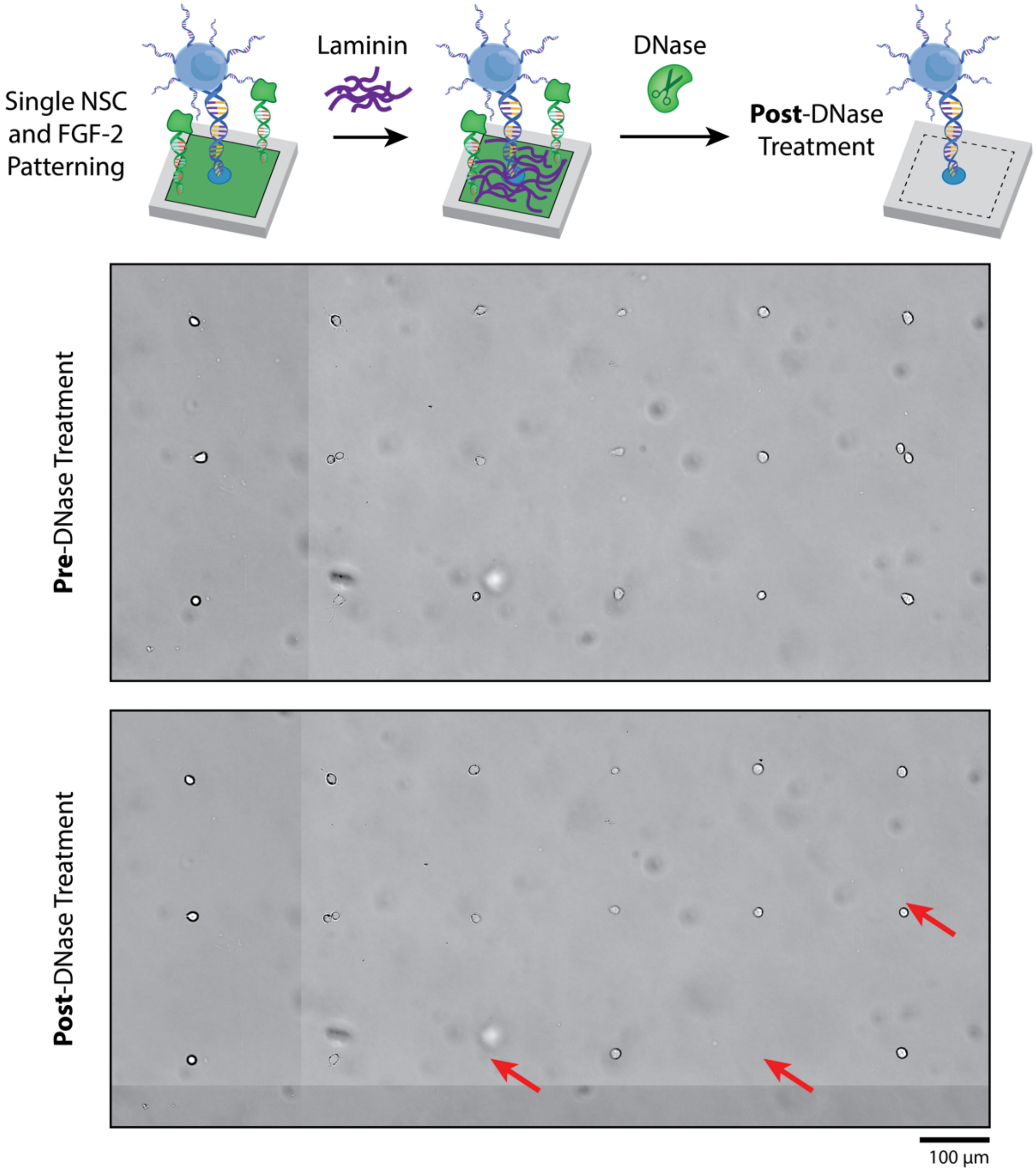

Supplemental Figure 4.2 A one-hour incubation step with 10 µg/mL of laminin was conducted prior to DNase treatment to allow cells to attach to the laminin-coated glass substrate and no longer rely on its surface-tethered oligonucleotides to position it onto the surface. An average single-cell pattern retention rate of 75-80% was observed. Of the cells that were removed, the majority were located at the inlet of the polydimethoxysilane flow cell where they experienced the most shear. Red arrows highlight cells that were removed during the DNase treatment.

4.7.3 Supplemental Figure 4.3. Effects of DNase Treatment on Adult Neural Stem Cell (NSC) Differentiation

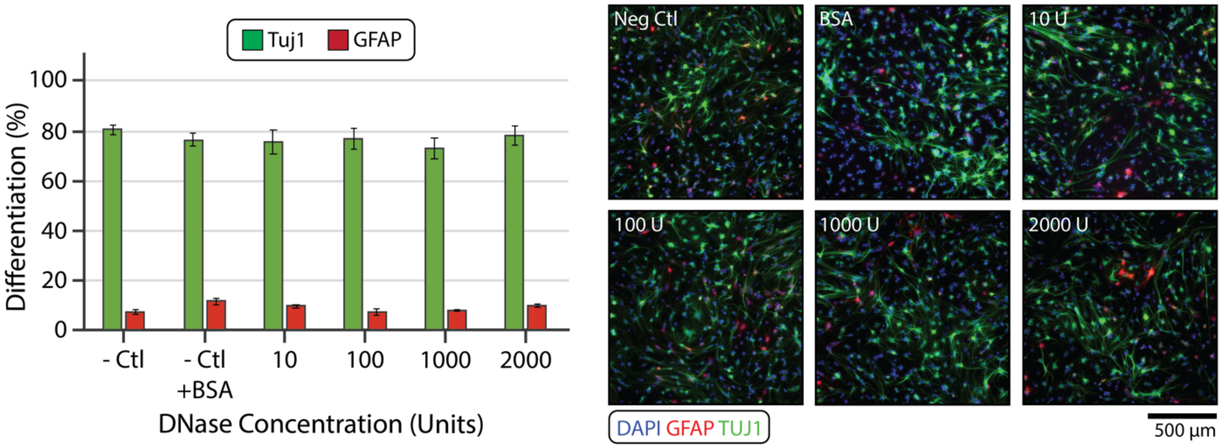

Supplemental Figure 4.3. Effects of DNase treatment on adult neural stem cell (NSC) differentiation. NSCs were treated for 30-minutes at 37ºC with different concentrations of DNase prepared in NSC media (i.e. N2 media) prior to inducing mixed differentiation for 5 days. Immunostaining analysis of neuronal and astrocytic fate commitment revealed similar differentiation proportions for each condition. n=4 and error bars are standard deviation.

4.7.4 Supplemental Figure 4.4. Live/Dead Assessment of Adult Neural Stem Cells (NSCs) Following 1X CutSmart Treatment in N2 Media for Various Incubation Times.

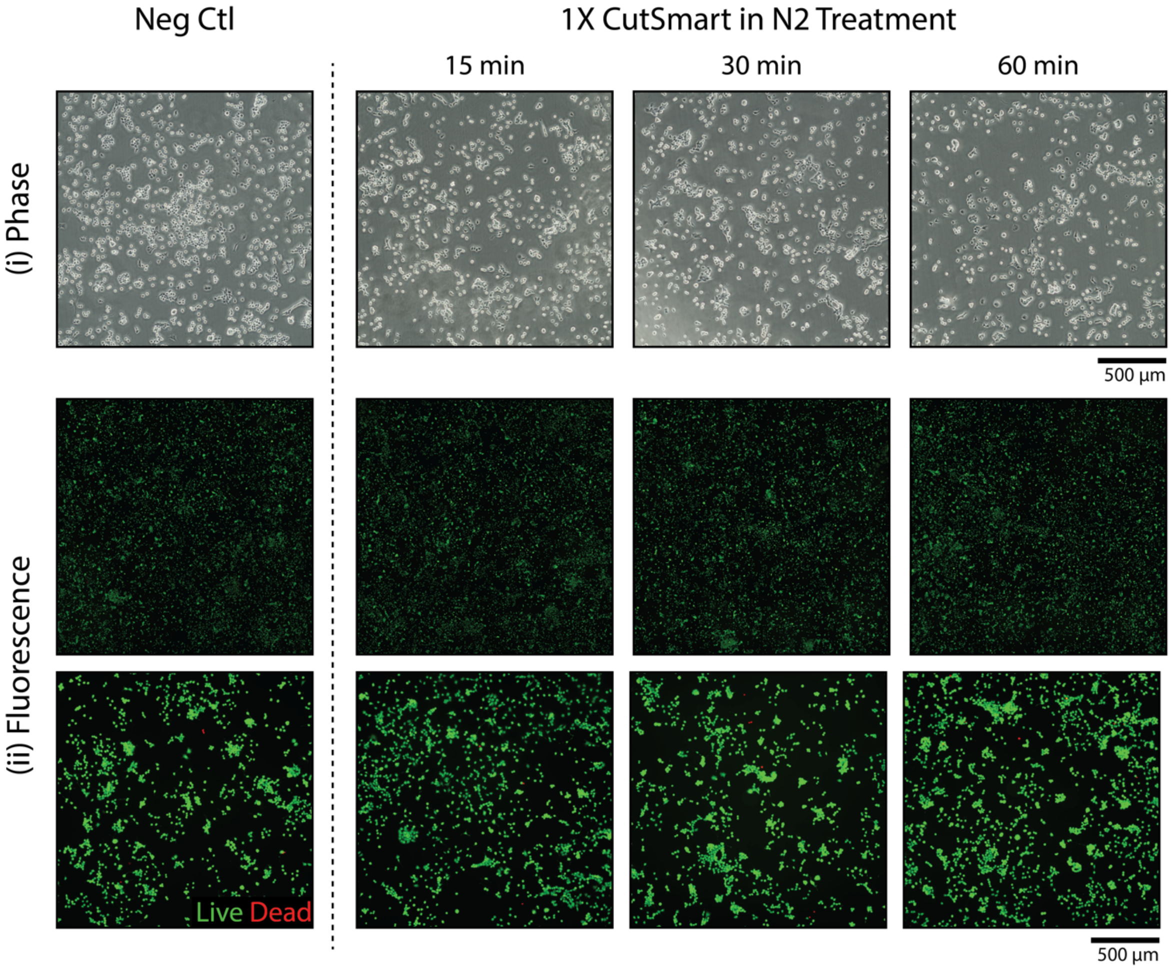

Supplemental Figure 4.4. Live/dead assessment of adult neural stem cells (NSCs) following 1X CutSmart treatment in N2 media for various incubation times.

4.7.5 Supplemental Figure 4.5 Effects of 1X CutSmart Buffer on NSC Behavior

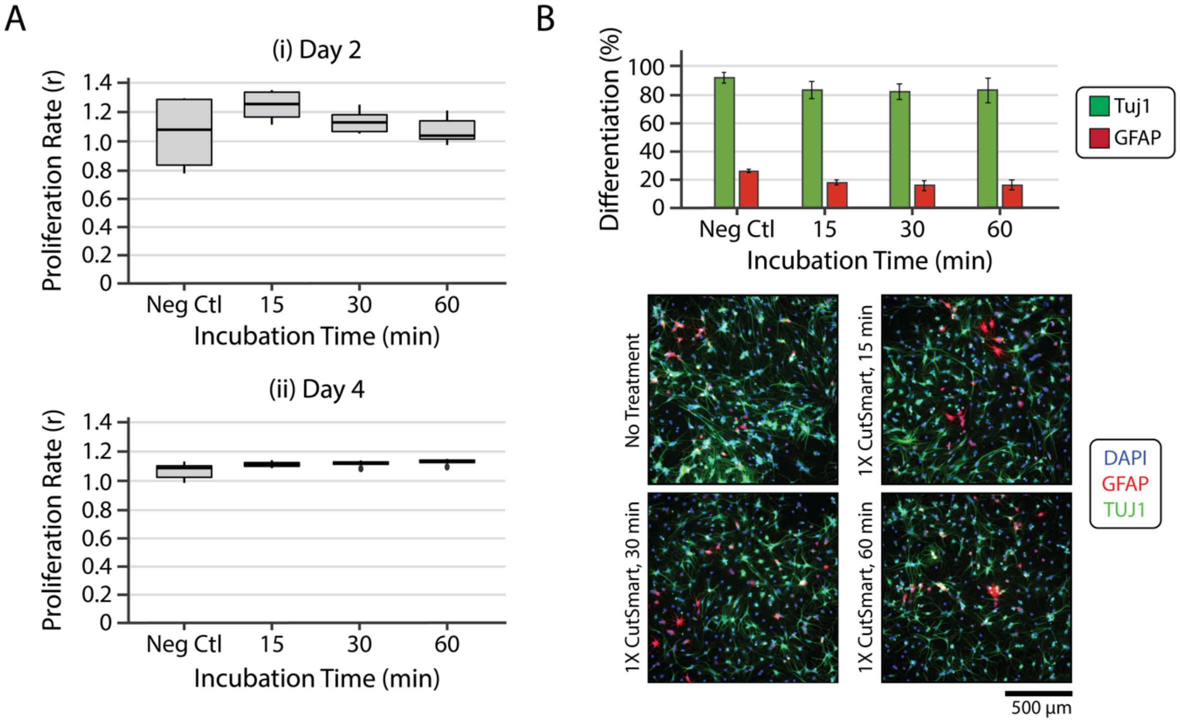

Supplemental Figure 4.5 Effects of 1X CutSmart buffer prepare in N2 Media on NSC differentiation and proliferation. n=4 and error bars are standard deviation.

4.7.6 Supplemental Figure 4.6 Cleavage Kinetics of Plasmid in Different Buffer Conditions using Gel Format

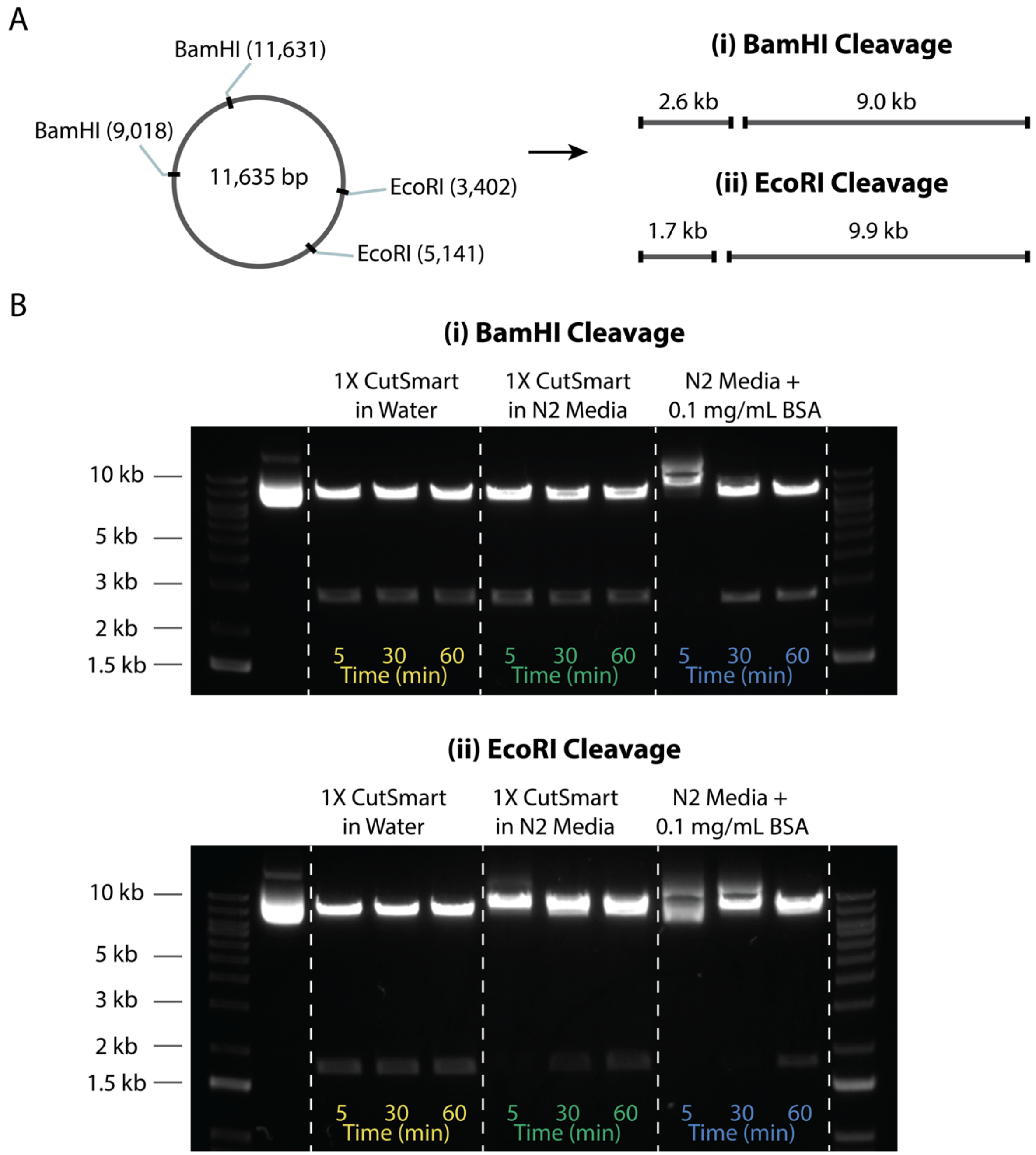

Supplemental Figure 4.6 (a) A ~11.6 kbp plasmid containing two (i) *Bam* HI and (ii) *Eco* RI cut sites was employed to screen restriction enzyme cleavage kinetics. (b) Restriction enzymes, (i) *Bam* HI and (ii) *Eco* RI, were incubated for different incubation times (5 min, 30 min, 60 min) in various buffer conditions (1X CutSmart in water, 1X CutSmart in N2 media, and N2 media + 0.1 mg/mL BSA) prior to running out the cleavage products on a 1% agarose TAE gel and imaged with SyberSafe.

4.7.7 Supplemental Figure 4.7 Specificity of Restriction Enzyme-Based Cleavage

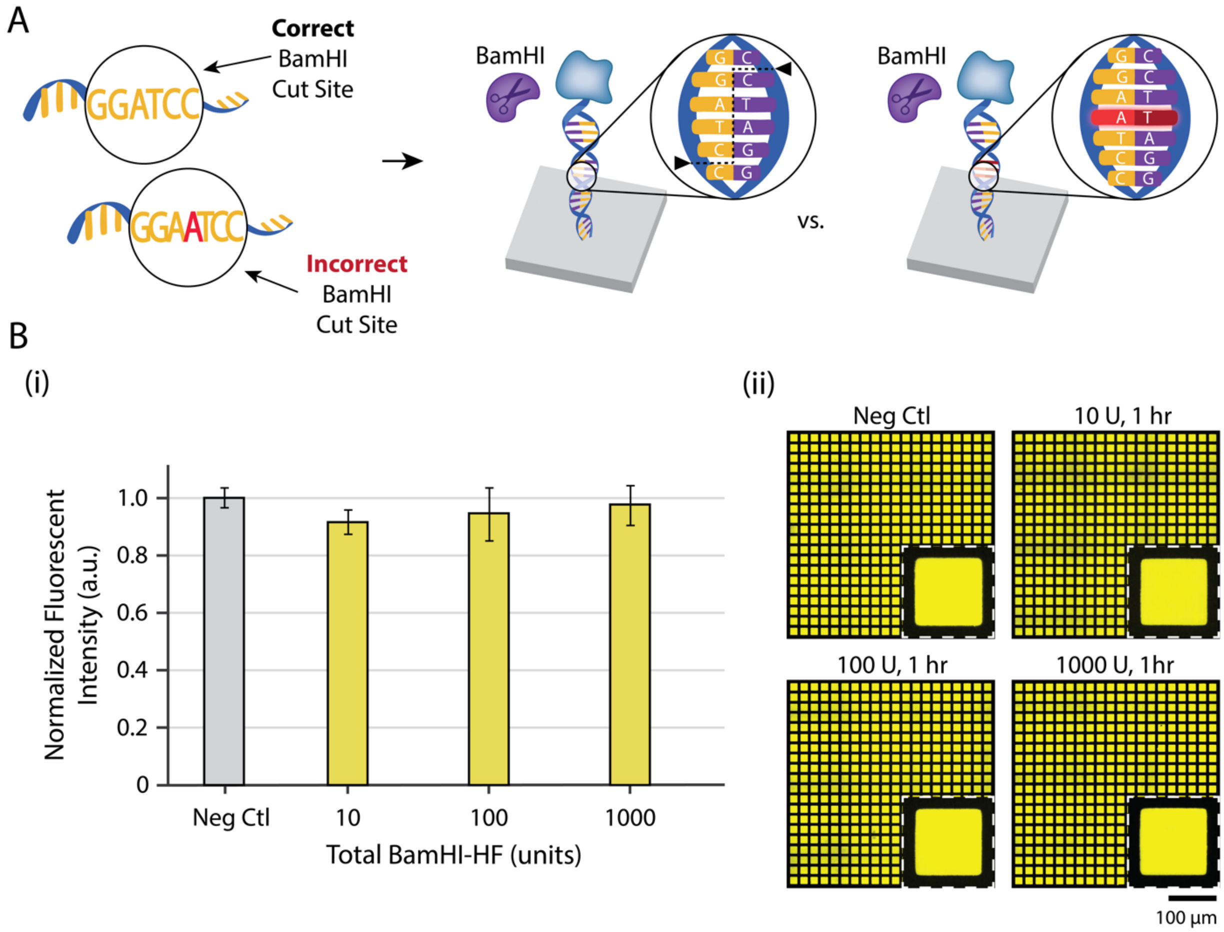

Supplemental Figure 4.7 (a) To demonstrate the specificity of restriction enzyme-based cleavage, an incorrect *Bam* HI oligo was patterned onto an aldehyde glass substrate using photolithography. (b) Different concentrations of *Bam* HI prepared in 1X CutSmart buffer were incubated for one hour following the hybridization of a fluorescent complementary oligo, revealing little to no cleavage between conditions. n=3 and error bars are standard deviation.

4.7.8 Supplemental Figure 4.8 In-Depth Visualization of Rehybridization Strategy Post Restriction Enzyme-Based Cleavage

Supplemental Figure 4.8 (i) *Eco* RI oligo is conjugated to a glass substrate by reacting the terminal amine modification on the oligo to the aldehyde group functionalized to the glass substrate. (ii) A 20-bp complementary oligo containing an *Eco* RI cut site (GAATTC) and Cy5 fluorescent modification is hybridized to the surface-tethered oligo. (iii) The addition of *Eco* RI restriction enzyme releases the hybridized fluorescent DNA portion. (iv) The unhybridized surface DNA can then hybridize a new fluorescent oligo strand.

4.7.9 Supplemental Figure 4.9 SpCas9 RNP Cleavage Kinetics Screen in Gel Format

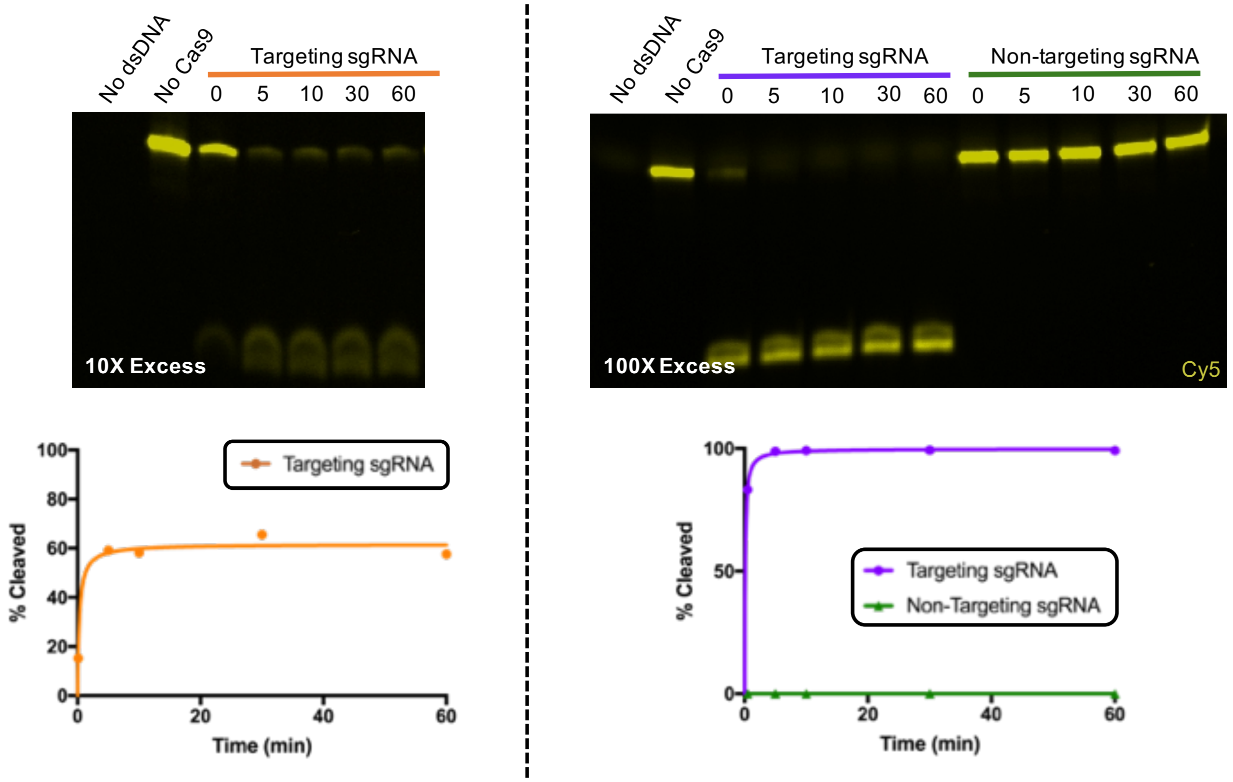

Supplemental Figure 4.9 SpCas9 RNP cleavage kinetics were tested on the same surface-patterned and complementary fluorescent DNA strands utilized for DNA patterning. Both a 10-fold molar excess of SpCas RNP (right) and 100-fold molar excess (right) were investigated as well as specificity of cleavage through the incorporation of a non-targeting single-guide RNA (sgRNA). Gel images courtesy of Doudna Lab.

4.7.10 Supplemental Table 4.1 Overview of DNA Sequences

Oligo Name	Sequence (5’ to 3’)	Notes
1. A-BamHI-NH_2	[AminoC6] ACTGACTGACTGACTGACTGCCATAAGGATCCCTAAGCA	Surface oligo for *Bam* HI
2. A’-BamHI-Cy3	[Cy3] CAGTCAGTCAGTCAGTCAGT	Fluorescent oligo for *Bam* HI
3. A’-Cy5	[Cy5] CAGTCAGTCAGTCAGTCAGT	Fluorescent oligo post *Bam* HI cleavage
4. F-NH_2	[AminoC6] AGAAGAAGAACGAAGAAGAA	Surface oligo for single NSC patterns
5. F’-AlexaFluor 488	[AlexaFluor488] TTCTTCTTCGTTCTTCTTCT	Fluorescent oligo
6. F’-Lipid	[Lipid] GTAACGATCCAGCTGTCACT TTTTTTTTTTTTTTTTTTTTTTTTTTTTTT TTTTTTTTTTTTTTTTTTTTTTTTTTTTTT TTCTTCTTCGTTCTTCTTCT	Lipid oligo for labeling single NSC
7. G-NH_2	[AminoC6] AGCCAGAGAGAGAGAGAGAG	Surface oligo for DNase
8. Azide-G’-Cy3	[Azide] CTCTCTCTCTCTCTCTGGCT [Cy3]	Click Chemistry oligo for labeling FGF-2
9. G’-Cy5	[Cy5] CTCTCTCTCTCTCTCTGGCT	Fluorescent oligo for DNase
10. G’-Cy3	[Cy3] CTCTCTCTCTCTCTCTGGCT	Fluorescent oligo post *Eco* RI cleavage
11. G-EcoRI-NH2	[AminoC6] AGCCAGAGAGAGAGAGAGAGCTAAGC AGAATTCCCATAAG	Surface oligo for *Eco* RI
12. G’-EcoRI-Cy5	[Cy5] CTTATGGGAATTCTGCTTAG	Fluorescent oligo for *Eco* RI
13. B-Cas9-PAM-D’-NH2	[AminoC6] TCATACGACTCACTCGTCACCTCCAATGACTAGGGTGGGTAACGATC CAG	Surface oligo for Cas9 RNP
14. B’-Cas9-PAM-D-Cy5	[Cy5] CAGCTGGATCGTTACCCACCCTAGTCATTGGAGGTGACGAGTGAGTC GTATGA	Fluorescent oligo for Cas9 RNP
15. CoAnchor Lipid	[Lipid] AGTGACAGCTGGATCGTTAC	Locking lipid DNA for single NSC

Chapter 5: Conclusions & Future Directions

5.1: Overview

In this dissertation, we discuss the development of various DNA-based engineering strategies that can be employed to recapitulate complex signaling environments through multiplexed spatiotemporal control. Though we focus our applications on teasing apart dynamic niche-driven signals that regulate single adult neural stem cell (NSC) fate decisions, these engineering tools are broadly applicable to other cellular or tissue-based systems. In this final chapter, we review our current patterning capabilities and the exciting directions that this DNA platform can enable in the future.

5.2: DNA-Based Assembly of Heterotypic Cell-Cell Interactions

Chapter 2 highlights the fine-tuned, DNA-based control in assembling heterogeneous cellular communities through printed DNA spot patterns with feature sizes on the order of single cells (~10-15 μm). Multiplexed cellular control is achieved by utilizing unique oligonucleotide sequences and tagging each cell population with the appropriate complementary strand. While we previously demonstrated communities comprised of single NSCs patterned alongside two different astrocytes that express different juxtacrine cues (i.e. three-component cell patterns), the foundation laid here places us in prime position to emulate and dissect NSC interactions with other key niche neighboring cell types, such as microglia and neurons or even other NSCs. Moreover, this method can define further the degree of cellular interaction – paracrine vs. juxtacrine – through the strategic patterning of cell-resistive materials, such as polyacrylamide. As highlighted in the experiment shown in Figure 5.1, paracrine signaling between NSC-astrocyte pairs can be emulated by fabricating DNA features such that each DNA pattern responsible for capturing either a single NSC or astrocyte is isolated within its own distinct polyacrylamide microisland. Upon cell capture, both cell types are chemically isolated from one another, restrained within unique spatial domains, yet the distance between the two cells can be tuned (Figure 5.1(a)) to heighten or reduce the diffusion of paracrine signals. The integration of this platform into a microfluidic device would enable additional temporal control by introducing fresh media into the system to remove paracrine signals at designated timepoints. To model juxtacrine signaling, which relies upon cell-cell contact, surface DNA patterns are positioned within the same polyacrylamide microisland. Unlike the paracrine case, cells actively engage with one another over the imaging time-course. Similarly, the degree of juxtacrine interaction can be modulated by the initial positioning of the astrocyte-NSC pair. One interesting future study would be to develop cell tracking software to quantify cell-cell physical contact, such as number of contacts and duration of contact, to determine whether or not a minimum threshold of contact is necessary to induce downstream juxtacrine signaling.

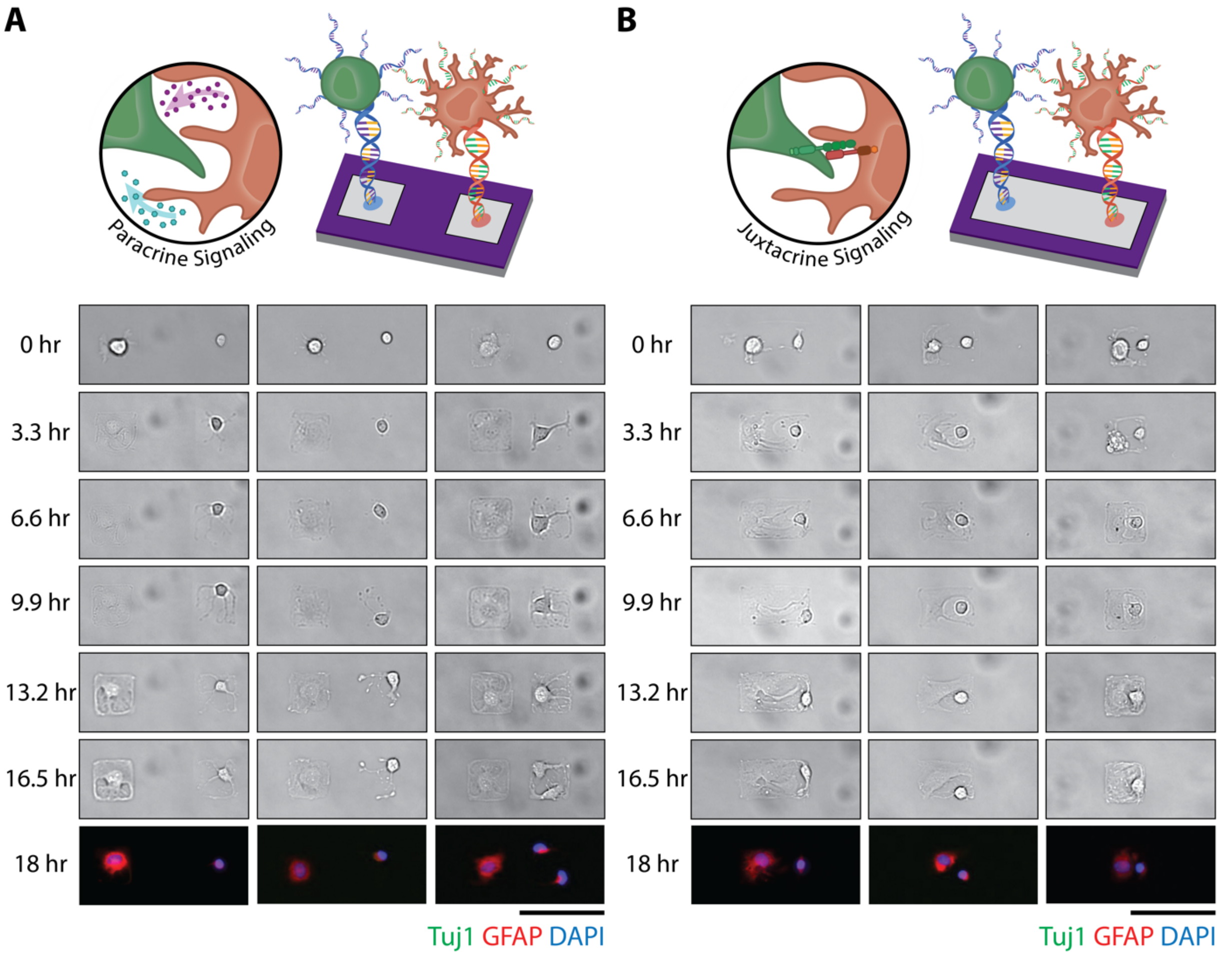

Figure 5.1 Modeling Heterotypic Cell-Cell Interactions Between Adult Neural Stem Cells (NSCs) and Glial Fibrillary Acidic Protein (GFAP)-Positive Niche Astrocytes *In Vitro*. Microfabricated surface DNA patterns enable recapitulating intercellular interactions between NSCs and their astrocyte neighbors. The incorporation of non-biofouling, polyacrylamide patterns along with DNA patterns provides additional control in (a) constraining both cell types within their own square microisland feature to study the effects of paracrine signaling over the course of NSC differentiation or (b) constraining both cell types together within the same microisland to study the fate-inducing results of juxtacrine signaling. Scale bars represent 100 μm.

Expanding cellular communities beyond 3 or 4 cell types, however, can be time intensive due to the serial nature of depositing DNA using BioForce's Nano eNabler. Chapter 3 presents a solution to this challenge by using photolithography to pattern photoresist masks that guide the conjugation of DNA to a surface – a mask that remarkably can be stripped and re-patterned using UV light and a transparency mask to build up multiple DNA layers without sacrificing the fidelity of previously patterned layers or damaging the aldehyde functional groups that are necessary for DNA conjugation. With this approach, we demonstrated that at least 10 DNA layers can be registered, which theoretically can assemble 10 heterogeneous cell types and capture better a more mimetic NSC *in vitro* niche model.

An additional key advantage of using photolithography to direct the formation of cellular communities is the high-throughput generation of features with increased pattern complexity, flexibility, and resolution that transcends the previous approach of arraying small DNA circular features to construct larger patterns. Thus, cellular communities can be organized not only at the single-cell level but also at a bulk-tissue scale. The latter capability, in particular, allows for recapitulating the cyto-architecture of tissues, such as the hippocampal dentate gyrus, where cells are organized into distinct anatomical layers as illustrated in Figure 5.2. Moreover, 100-1000's of these assemblies can be fabricated simultaneously due to the parallel nature of photolithography.

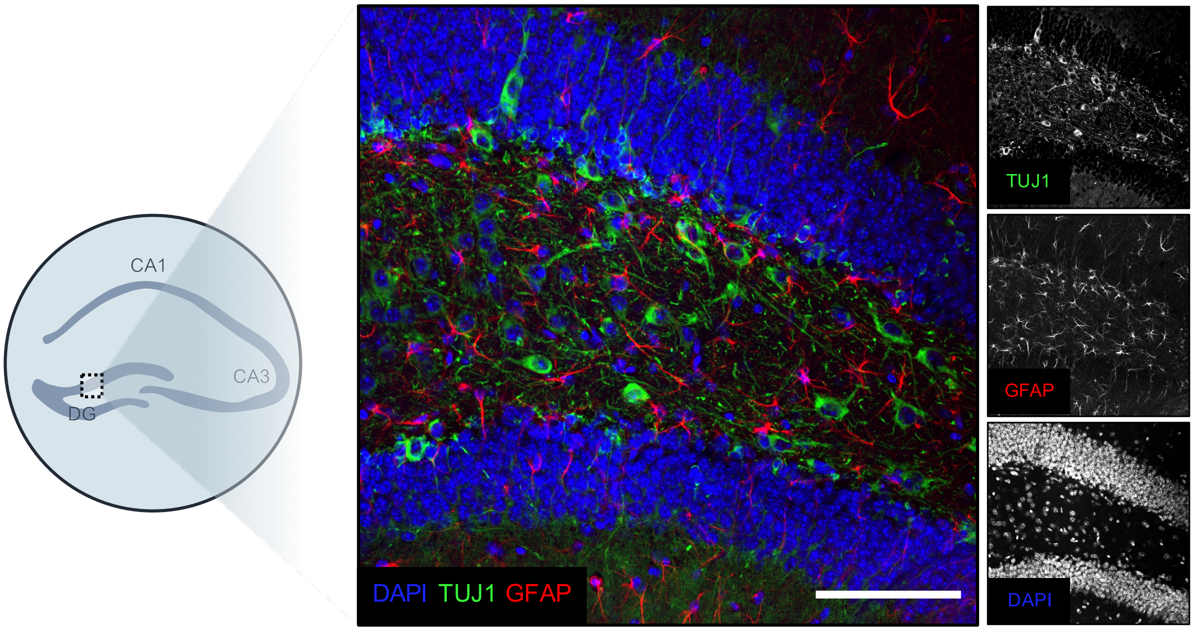

Figure 5.2 Cytoarchitecture of the Mouse Hippocampal Dentate Gyrus. Immunostaining of GFAP-positive astrocytes (red), Tuj1-positive neurons (green), and DAPI (red) reveal anatomically-defined layers within the adult NSC niche. Scale bar represents 100 µm.

5.3: DNA-Based Assembly of Heterotypic Cell-Ligand Interactions

In addition to studying the effects of ligand presentation on the surface of niche astrocytes by patterning genetically engineered astrocytes alongside single NSCs, we also expanded our DNA-based strategy to isolate and pattern solid-phase ligands directly onto a cell-culture surface, recapitulating the presentation of ECM-sequestered or surface-tethered signals (Chapter 3). Doing so offers the key advantage of isolating the niche signal and eliminating confounding effects of other potential contributing cell-cell contact-mediated and/or secreted signal from patterned cells as well as enables addressing how niche cues are modulated by key microenvironmental parameters – namely, spatial presentation and temporal dynamics.

Photolithography affords robust spatial control over ligand presentation at both the micron and millimeter scale, where minimum obtainable feature size is dependent on: 1) photomask type (i.e. transparency vs. chrome), 2) lithographic exposure system, and 3) wavelength of light. Ligand-receptor signaling, however, is fundamentally a nanoscale phenomenon. One proposed future direction to increase the power of our ligand patterning DNA platform is pushing sub-micron resolution. One potential approach is utilizing e-beam lithography, which can achieve sub-10 nm feature size, to define masks that guide DNA conjugation. One key challenge associated with this approach is determining whether the electron-sensitive resist or the electron beam itself compromises the aldehyde functional group on the surface. This could be resolved potentially by including an extra aldehyde silanization step following resist patterning. Another challenge that would need to be addressed is the low-throughput of e-beam lithography as it is a direct-write technology that slowly rasters a focused electron beam to generate patterns and is not generally utilized for large-area patterning.

A second alternative approach for nanoscale control over ligand presentation is to take advantage of the predictable structure of double-stranded DNA. In its most common and stable form (i.e. B form as opposed to A or Z form), DNA has a 3.4 nm pitch for every 10 base pairs. With this knowledge, short complementary sequences can be designed to hybridize ligands onto a long, surface-patterned oligo such that the distances between neighboring ligands can be precisely designed. Unknowns that would need to be addressed include how long the complementary strands needs to be in order for robust ligand hybridization as well as whether or not there are limitations in the length of patterned DNA oligonucleotide (i.e. can a DNA strand be too long where it forms undesired secondary structures that prohibit hybridization?).

5.4: Expanding DNA-Based Assembly to Other Biomolecules

While this dissertation highlights the use of surface DNA patterns as a means to program control over both cells and solid-phase ligands, the concept of DNA-based assembly can be extended to other biomolecules by simply modifying the molecule attached to the DNA label. Here, we provide the initial proof-of-concept experiments that antibody patterning can also be obtained with our lithographically defined DNA substrates.

Antibodies are of great interest to the biomedical field due to their inherent ability to bind target antigens with high affinity. Controlling antibody positioning has particular applications for the development of sensors and diagnostic tools in addition to the capture of key and/or rare cell types. As illustrated in Figure 5.3, we demonstrate that an oligonucleotide label can be introduced to antibodies via a similar heterobifunctional crosslinker used to label ligands in Chapter 3. Rather than utilizing a maleimide functional group that can react with free thiols on the protein, however, we opted for a N-hydroxysuccinimide (NHS) ester-terminated cross-linker to react with free amines on the antibody. One potential concern for this type of reaction is disrupting antibody conformation where antigen binding is impaired; therefore, we tested a range of reaction stoichiometries for an AlexaFluor 488-conjugated donkey anti-mouse secondary antibody (Figure 5.3 (a, right)). Specifically, we varied the excess amount of crosslinker in relation to antibody (i.e. Reaction 1). A Cy5 tag was also included on the oligonucleotide label to enable monitoring of reaction efficiencies upon separating products on a protein gel, where unreacted oligo could be assessed in addition to the degree of labeling of both the heavy and light chains (Figure 5.3 (b(i))). To determine how reaction stoichiometries affected antigen binding, a 555-modified mouse IgG isotype was incubated with antibody-hybridized DNA patterns, and the 555 signal was subsequently quantified (Figure 5.3 (b(ii))). Despite having multiple oligonucleotide strands labeling both heavy and light chains, the 1:32 reaction stoichiometry exhibited both the highest amount of antibody patterned onto the DNA substrate (as suggested by the 488 signal) as well as the highest antigen binding (from the 555 signal). This can most likely be attributed to a minimal amount of free oligos that compete with antibody hybridization, maximizing the amount of surface-tethered antibody. One future optimization experiment includes investigating whether excess, unreacted oligo can be removed either through filtration or size-exclusion chromatography. Additional reaction stoichiometries can also be tested to determine whether there exists a threshold for oligonucleotide saturation that disrupts antibody structure, forcing the molecule to precipitate out of solution and/or lose the ability to bind to its cognate antigen (i.e. 1:64, 1:128, etc.).

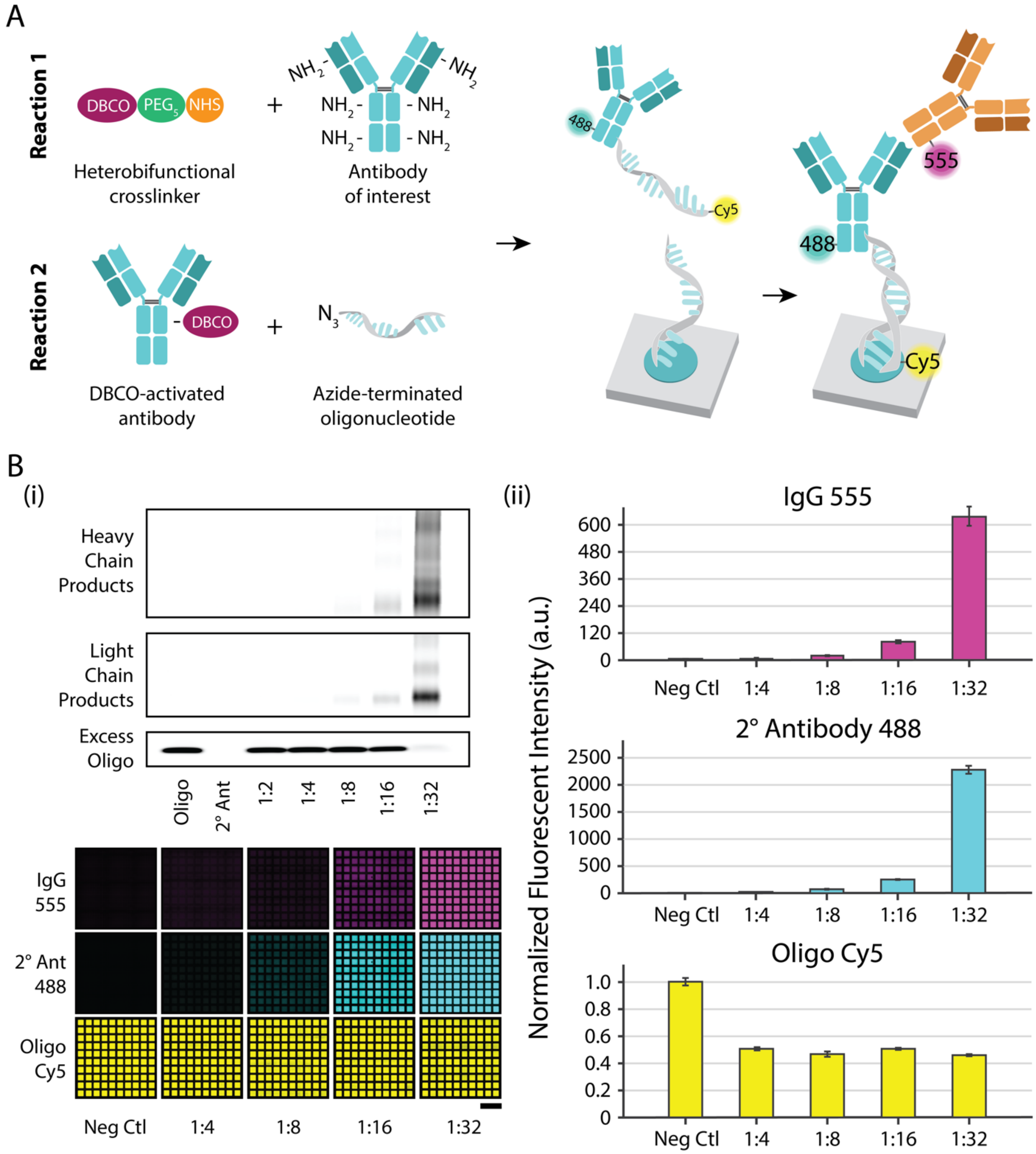

Figure 5.3 DNA-Directed Antibody Patterning. (a) DNA-labeling of antibodies is achieved through the use of the bi-functional cross-linker, dibenzocyclooctyene (DBCO)-polyethylene glycol (PEG)-N-hydroxysuccinimide (NHS) ester. The NHS ester reacts with free amines on the antibody, which then enables the use of click chemistry between

the DBCO-functionalized antibody and azide-terminated oligonucleotide. For characterization experiments, we conjugated an AlexaFluor 488 donkey anti-mouse secondary antibody with a Cy5-tagged oligonucleotide. Antigen binding was assessed with a 555-modified mouse IgG molecule. (b) (i) Antibody labeling efficiency was investigated by separating reaction products using a denaturing sodium dodecyl sulfate polyacrylamide gel and imaging the Cy5 tag on the oligo. (ii) Multiple fluorescent tags were incorporated to enable monitoring of the oligo label (Cy5), antibody (488), and antigen (555) for the different reaction stoichiometries (n=3 and error bars are standard deviation). Scale bar represents 500 µm.

Another major advantage of DNA-based antibody assembly is that DNA is remarkably robust as we discovered that it is able to withstand multiple heating steps (up to 100ºC), the alkalinity of photoresist developer, acetone washes, etc. Antibodies, in contrast, are more prone to dehydration and denaturation. The key advantage of patterning DNA as an intermediary is being able to preserve antibody function as, during the final step, oligo-labeled antibodies simply need to be flown across the DNA-patterned substrate and, thus, can be assembled in solution. Not only is DNA amenable to patterning using photolithography but also, once it is tethered onto a glass substrate, it remains highly stable and functional. Initial tests indicate that DNA patterns retain the ability to hybridize with oligo-conjugated antibodies when stored under vacuum for a month and potentially longer (Figure 5.4). While there appears to be a significant drop in the amount of antibody patterned onto the surface, the amount of hybridized DNA (as indicated by the Cy5 signal) as well as the amount of bound antigen (as indicated by the 555 signal) remain high.

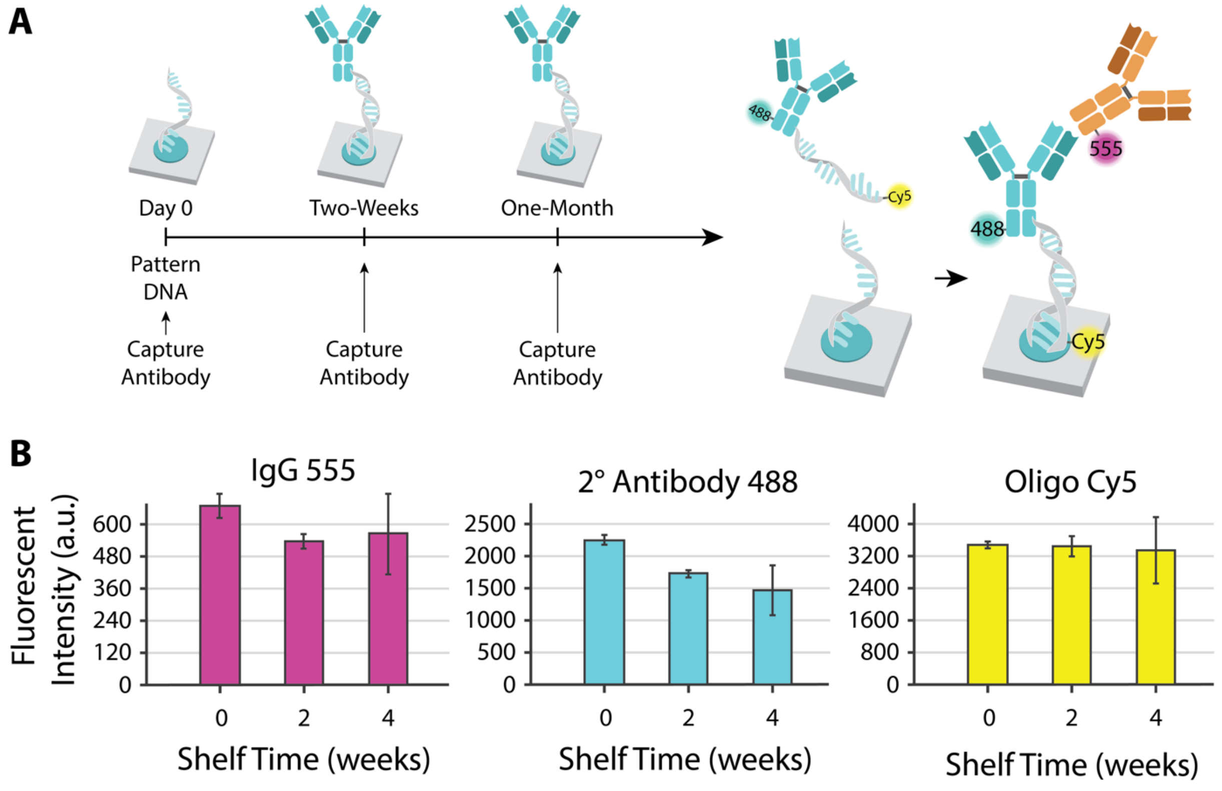

Figure 5.4 Long-Term Stability of Lithographically-Defined Surface DNA for Antibody Patterning. (a) DNA-patterned substrates were stored for up to one-month under vacuum and were tested at designated timepoints (0 days, 2 weeks, and 4 weeks) for the ability to capture an AlexaFluor 488-conjugated donkey anti-mouse antibody and bind 555-modified mouse IgG. (b) Fluorescence indicative of each biological component (oligo = Cy5, antibody = 488, and antigen = 555) was quantified and compared across timepoints (n=3 and error bars are standard deviation).

5.5: Final Conclusions

DNA is a programmable biomaterial that provides the functional code that gives rise to the extraordinary diversity of living organisms within our ecosystem and, more recently, has found exciting *ex vivo* applications as a robust nano-building material for a diverse set of engineering tools. In this dissertation, we highlight further how DNA can transcend its traditional role of orchestrating protein production in cells to enabling precise multiplexed control over biological components of interest (i.e. cells and solid-phase ligands). Furthermore, we demonstrate DNA's amenability to being patterned by photolithography in addition to the incorporation of DNA-specific enzymes into our platform, the combination of which provide the added, spatiotemporal control necessary to model the inherent, dynamic signaling scenarios of complex tissues, such as the stem cell niche. Looking forward, these DNA-based engineering strategies afford exciting, unprecedented opportunities across many disciplines to enable novel biological insights – knowledge that will provide a more fundamental understanding of the key biological processes that drive the regulation and/or dysregulation of tissues and also inform the development of powerful, new therapeutics.